

Relativistic laser pulse compression and focusing in stratified plasma-vacuum systems

Inaugural-Dissertation

zur

Erlangung des Doktorgrades der
Mathematisch-Naturwissenschaftlichen Fakultät
der Heinrich-Heine-Universität Düsseldorf

vorgelegt von

Christoph Karle
aus Dinslaken

Dezember 2007

Aus dem Institut für theoretische Physik I
der Heinrich-Heine-Universität Düsseldorf

Gedruckt mit der Genehmigung der Mathematisch-Naturwissenschaftlichen Fakultät der
Heinrich-Heine-Universität Düsseldorf

Referent: Prof. Dr. K.-H. Spatschek
Korreferentin: Prof. Dr. M. Hochbruck

Tag der mündlichen Prüfung: 25.01.2008

Relativistic laser pulse compression and focusing in stratified plasma-vacuum systems

Christoph Karle
December 2007

Institut für Theoretische Physik I
Heinrich-Heine-Universität Düsseldorf

Contents

1	Introduction	7
2	Model equations	10
2.1	Reduced Fluid-Maxwell equations	10
2.2	Equations for the weakly relativistic regime	13
2.3	Slowly varying envelope approximation	16
3	Pulse compression in one dimension	18
3.1	Model equations in 1D	18
3.2	Numerical methods	20
3.3	Accuracy and efficiency of the numerical scheme	24
3.4	Pulse dynamics in 1D	32
4	Pulse compression in two dimensions	44
4.1	Numerical Methods	44
4.2	Accuracy and efficiency of the over-all 2D scheme	52
4.3	Pulse dynamics in 2D	56
4.4	Transversal filamentation instability	64
4.5	Other 2D / 3D instabilities	76
5	Transversal focusing with plasma layers	82
5.1	Focusing properties of plasma layers	82
5.2	Boundaries between vacuum and plasma	87
5.3	Propagation of short vs. long wavelength transversal modes in vacuum	90
6	Stratified plasma-vacuum systems	95
6.1	Advantages of multiple plasma layers	96
6.2	Optimization of transversal focusing	98
6.3	Controlling transversal filamentation	105
7	Conclusion	116
A	VAM model for pulse compression in 2D	119
B	Transversal filamentation instability	122
B.1	Stationary solution of the cubic nonlinear wave equation	122
B.2	Growth rate of the instability	123

Contents

C 3D instabilities	125
Bibliography	129

1 Introduction

Since the invention of the laser in 1960, the use of laser technology has become ubiquitous. Lasers today are used for optical communication, digital data storage applications, material processing, welding, numerous medical applications from diagnostics to surgery and have become an indispensable tool in scientific research due to the coherent nature of laser radiation.

During the first two decades the laser intensities were increased rapidly through the introduction of Q -switching and mode locking. The pulse length decreased accordingly, from microseconds to nanoseconds with Q -switching and femtoseconds with mode locking. This allowed intensities to reach $I \sim 10^{14} W/cm^2$ and already lead to relativistic effects for electrons oscillating in the field of infrared lasers, as the necessary intensity for relativistic electrons is $I \lambda_0^2 \sim 10^{18} W \mu m^2/cm^2$. If a laser pulse at this intensity propagates through a gas, it is directly ionized and a plasma is created. The relativistic mass increase then leads to nonlinear effects, like self-modulation and self-focusing, similar to nonlinear optics for bound electrons in a medium.

Since typical amplification media show strong nonlinear effects for intensities this high, intensities could not be increased further until the technique of chirped pulse amplification (CPA) was developed in 1985. This technique enabled a considerable further increase in laser intensity. Large laser facilities world wide now reach intensities well over one Petawatt. CPA also reduced the cost of high power lasers significantly and allowed universities to build μm lasers (e.g. using Ti:sapphire crystals) that reach intensities above $I \sim 10^{18} W/cm^2$ and thus allow to study relativistic effects in plasmas.

The basic mechanism of CPA is the stretching of the pulse by a factor of thousand to a hundred thousand by inducing a linear chirp. This can be achieved by letting the pulse propagate through a medium with large group velocity dispersion like an optical fiber or by reflection at a grating, which has the same effect. After stretching the frequencies, the front of the pulse is red-shifted, while the back of the pulse is blue-shifted (or vice versa). The stretched pulse can then be amplified without reaching the saturation limit of the amplification medium. After amplification, the chirp is reversed and the pulse is thus compressed to its original length. Amplification by 6 to 12 orders of magnitude were achieved in this way. To reach amplification factors this high, the stretcher and compressor have to be matched exactly, otherwise the chirp is not fully compensated. This gets more complicated for shorter pulses as higher order dispersion terms become important, which have to be compensated, too. Still, it is possible to achieve very short pulses in the range of 10 to 30 femtoseconds with high quality wave fronts by using holographic gratings, deformable mirrors and acousto-optic temporal phase correctors (Dazzler).

A variant of CPA is the so called optically parametric CPA (OPCPA). This method

1. Introduction

uses a nonlinear crystal in which the pulse is amplified through the interaction with a pump pulse. Because of the nonlinear amplification mechanism, that is necessarily in the saturated range of the medium, the efficiency is lower than for standard CPA. The gain bandwidth, on the other hand, is larger than for CPA.

Focusing the ultraintense pulses produced in this way on solid or gaseous targets results in the formation of overdense (which reflect the pulse) or underdense plasmas (which allow pulse propagation) respectively. The huge amount of coherent radiation in a small volume produces many interesting nonlinear effects with interesting applications. The overdense plasma surface of a solid irradiated by a short, high contrast pulse, strongly oscillates and produces higher harmonics of the laser frequency. More than 100keV harmonics can be produced in this way with resulting pulse lengths in the attosecond or even zeptosecond range [26, 3]. These pulses can be used for the diagnostics of ultrafast physical processes. Irradiation of a thin metal foil by an intense laser pulse leads to a large electrostatic field between the foil and thermal electrons behind the foil that were produced by the currents induced by the pulse. Protons or ions adherent to the back of the foil are easily accelerated by this field up to tens of MeV [31, 58, 21]. These protons can be used for time resolved imaging, because protons produced at different times have different energies. Protons of a certain energy can be selected and focused by a laser irradiated cylindrical metal foil [63, 24]. In the future the acceleration of light ions, for example carbon, to several hundred MeV is likely possible.

In gaseous targets the pulse can induce a large amplitude plasma waves, called the wakefield of the pulse, that can be used to accelerate electrons [18, 32, 21]. Wakefields are especially suited for particle acceleration, because in the process of the wakefield production the huge transversal electromagnetic field of the laser is transformed into a longitudinal electrostatic field. Because the plasma is ionized by definition, there are no problems due to material breakdown at $\sim 20\text{MV}/\text{m}$ as for conventional accelerators. Electrostatic fields of $100\text{GV}/\text{m}$ and more can be sustained and electron energies of up to 1GeV have been reached [42]. In undulators the accelerated electrons can then be used to generate very short and intense coherent X-rays (X-ray free electron lasers, XFEL). Overviews of laser technology and the whole field of nonlinear laser-plasma interaction can be found, for example, in [6, 52, 65], with many further references.

Numerical simulations have been vital to understand the nonlinear effects that occur in laser-plasma interaction. They are also indispensable for the design of experiments. Mostly particle-in-cell (PIC) codes are used for this simulations, because they include most of the relevant physics and can be scaled to a large number of processors [55]. In PIC simulations, electrically charged macroparticles are used to model the electrons and ions in the plasma. From their positions and velocities the current density is calculated on a grid. This current density is used as a source term for the Maxwell equations that are solved on the same grid. The updated electromagnetic fields are then interpolated to the positions of the macroparticles to update their positions and velocities. The number of macroparticles is usually much smaller than the number of particles in a real plasma, hence their name. This leads to relatively high noise levels in PIC simulations. Because the macroparticles only interact through the grid, binary collisions are not included, but

can be added by means of Monte Carlo methods.

For parameter regimes, where kinetic effects are negligible, fluid-dynamical codes can be used instead. They assume a fixed velocity distribution for electrons and ions, e.g. a cold or an isothermal plasma. Since they are not particle based, simulations with fluid codes are generally less noisy than with PIC codes. The computational cost of fluid simulations is also significantly lower. For the study of a particular parameter regime, further simplifications of the fluid-dynamical model can be possible. This again reduces the computational cost of simulations and enables the investigation of a large range of parameters in the particular regime.

In this thesis we study the pulse compression properties of plasma layers. Due to the relativistic interaction with the plasma, a laser pulse can be longitudinally compressed down to a single laser cycle in length, with a corresponding increase in intensity. PIC simulations show that energy efficient pulse compression is limited to weakly relativistic intensities [59], at least for the uncompressed initial pulse. In this range of intensities the main source of nonlinearity is the relativistic mass increase due to the quiver motion of the electrons in the field of the laser. The ponderomotive force of the laser only causes small perturbations in the electron density. We will derive model equations that include the relevant nonlinearities and develop efficient numerical methods for them.

To fully assess the potential of relativistic pulse compression, the transversal dynamics of the pulse has to be included into the simulations, both during propagation in a plasma layer and in vacuum [9, 56]. Transversal instabilities play an important role, too. Thus numerical codes for 2D/3D geometries are necessary. With this codes we will study the propagation of a pulse through one or more plasma layers with vacuum in between. Such layered plasma-vacuum systems are a promising concept to produce very short and intense pulses. With further improvement of the stretcher / compressor gratings it might be possible in the future to further amplify the resulting pulses with OPCPA due to its large gain bandwidth.

The thesis is organized as follows. In the next chapter the model equations for the weakly relativistic parameter regime will be derived. In chapter 3 pulse dynamics in 1D will be discussed. The numerical methods for 1D simulations will be developed in this chapter, too. The necessary modifications for 2D simulations are developed at the beginning of chapter 4, after which the compression dynamics and instabilities in 2D are investigated. The lens-like transversal focusing properties of a plasma layer are studied in chapter 5. Chapter 6 about pulse compression with stratified plasma-vacuum systems combines the ideas developed in the preceding chapters.

2 Model equations

The starting point for the derivation of the different model equations that we will later use for numerical simulations and analytical descriptions of pulse propagation, are the cold fluid equations coupled to the Maxwell equations for the fields \mathbf{A} and ϕ . This Fluid-Maxwell-equations do not include kinetic effects that change the microscopic velocity distribution and thus can not model particle acceleration and heating of the plasma. But they allow for much lower runtimes of simulations that have much less numerical noise than e.g. PIC-simulations. First we will derive a reduced version of the Fluid-Maxwell equations by assuming that the plasma is curl-free where $\mathbf{A} = 0$. A further simplification is possible for laser intensities that only cause a weak relativistic mass increase of the plasma electrons. The resulting equations for the weakly relativistic regime form the basis for most numerical simulations in the present work. Most analytical models will be based on the cubic nonlinear Schrödinger equation that is derived at the end of this chapter using the slowly varying envelope approximation.

2.1 Reduced Fluid-Maxwell equations

The Maxwell-equations for the potentials \mathbf{A} and ϕ in Coulomb gauge are

$$\frac{1}{c^2} \frac{\partial^2}{\partial t^2} \mathbf{A} - \Delta \mathbf{A} = \frac{1}{c} \frac{\partial}{\partial t} \nabla \phi + \left(\frac{4\pi}{c} \right) \mathbf{j} \quad (2.1)$$

$$\Delta \phi = 4\pi \rho . \quad (2.2)$$

To couple the fluid equations for density and momentum of a two component plasma of electrons and Z_i -times charged ions, we use the following definitions

$$\begin{aligned} \mathbf{j} &= e(Z_i n_i \mathbf{v}_i - n_e \mathbf{v}_e) , \\ \rho &= e(Z_i n_i - n_e) . \end{aligned}$$

For a fixed ion background ($\mathbf{v}_i = 0$) with $Z_i n_i^0 = n_e^0 \equiv n_0$ this simplifies to

$$\begin{aligned} \mathbf{j} &= -en_e \mathbf{v}_e , \\ \rho &= e(n_0 - n_e) . \end{aligned}$$

Combined with the continuity equation and momentum balance of a cold ($T = 0$) electron fluid

$$\frac{\partial}{\partial t} n_e + \nabla \cdot (n_e \mathbf{v}_e) = 0 \quad (2.3)$$

$$\left(\frac{\partial}{\partial t} + \mathbf{v}_e \cdot \nabla \right) \mathbf{P}_e = e \left[-\nabla \phi - \frac{1}{c} \frac{\partial \mathbf{A}}{\partial t} + \frac{1}{c} \mathbf{v}_e \times (\nabla \times \mathbf{A}) \right] \quad (2.4)$$

2.1. Reduced Fluid-Maxwell equations

this yields a closed system of equations. We can thus distinguish two types of nonlinearity in the wave equation for \mathbf{A} . Because of

$$\mathbf{v}_e = \frac{\mathbf{P}_e}{m_e \gamma_e}, \quad (2.5)$$

with

$$\gamma_e = \frac{1}{\sqrt{1 - \left(\frac{\mathbf{v}_e}{c}\right)^2}} = \sqrt{1 + \left(\frac{\mathbf{P}_e}{m_e c}\right)^2}. \quad (2.6)$$

there is a relativistic mass increase of the electrons, as well as oscillations in plasma density. The momentum balance can be rewritten as an equation for the canonical momentum

$$\frac{\partial}{\partial t} \left(\mathbf{P}_e - \frac{e}{c} \mathbf{A} \right) = e \nabla \phi - mc^2 \nabla \gamma_e + \frac{1}{m_e \gamma_e} \mathbf{P}_e \times \left[\nabla \times \left(\mathbf{P}_e - \frac{e}{c} \mathbf{A} \right) \right]. \quad (2.7)$$

To normalize the equations, we use the inverse wave frequency ω_0^{-1} of the laser as the unit of time and the inverse wave number k_0^{-1} as the unit of length with $\omega_0 = ck_0$. In this normalization the laser wavelength in vacuum is $\lambda_0 = 2\pi$ and the laser frequency $\nu_0 = 1/2\pi$. The potentials are measured in units of $m_e c^2/e$, velocities in units of c and momentum in units of $m_e c$. The density is measured in units of the critical plasma density for a given laser carrier frequency, defined as

$$\frac{4\pi n_c e^2}{m_e} = \omega_0^2. \quad (2.8)$$

Additionally we extract a constant factor out of the electron density

$$\frac{n_e(\mathbf{r}, t)}{n_c} = \frac{n_0}{n_c} \frac{n_e(\mathbf{r}, t)}{n_0} \equiv \frac{n_0}{n_c} n_e(\mathbf{r}, t).$$

A logical choice for n_0 is the maximum of the ion background density. To allow for propagation of a laser pulse through the plasma $\frac{n_0}{n_c}$ has to be less than unity.

The dimensionless Fluid-Maxwell-equations in Coulomb gauge are thus given by

$$\frac{\partial^2}{\partial t^2} \mathbf{A} - \Delta \mathbf{A} - \frac{\partial}{\partial t} \nabla \phi = -\frac{n_0}{n_c} n_e \frac{\mathbf{P}}{\gamma} \quad (2.9)$$

$$\Delta \phi = \frac{n_0}{n_c} (n_i - n_e) \quad (2.10)$$

$$\frac{\partial}{\partial t} n_e + \nabla \cdot \left(n_e \frac{\mathbf{P}}{\gamma} \right) = 0 \quad (2.11)$$

$$\frac{\partial}{\partial t} (\mathbf{P} - \mathbf{A}) - \frac{\mathbf{P}}{\gamma} \times \{ \nabla \times (\mathbf{P} - \mathbf{A}) \} = \nabla (\phi - \gamma) \quad (2.12)$$

$$\gamma = \sqrt{1 + \mathbf{P}^2} \quad (2.13)$$

2. Model equations

with the additional gauge condition $\nabla \cdot \mathbf{A} = 0$. The restriction to a cold plasma and a fixed ion background limits the applicability of the equations to the descriptions of short, fast¹ pulses. In the time span such a pulse needs to propagate the distance of its own length, neither can the much heavier ions move, nor can the plasma thermalize the energy transmitted by the pulse.

We define the projection operators Π_c and Π_g such that any field \mathbf{u} is decomposed into $\mathbf{u} = \mathbf{v} + \mathbf{w}$ with the following properties

$$\begin{aligned} \Pi_g \mathbf{u} = \mathbf{v} &\equiv \mathbf{u}_g & \nabla \times \mathbf{v} &= 0, & \text{but generally } \nabla \cdot \mathbf{v} &\neq 0, \\ \Pi_c \mathbf{u} = \mathbf{w} &\equiv \mathbf{u}_c, & \nabla \cdot \mathbf{w} &= 0, & \text{but generally } \nabla \times \mathbf{w} &\neq 0, \end{aligned}$$

with

$$\Pi_c + \Pi_g = \mathbf{1}.$$

as long as the manifold X , on which the operators are defined, is star shaped.

Clearly, \mathbf{v} is a gradient field, and \mathbf{w} is a curl field. The operators can be represented as

$$\Pi_g = \nabla \Delta^{-1} \nabla \cdot \quad \text{and} \quad \Pi_c = 1 - \nabla \Delta^{-1} \nabla \cdot .$$

Applying $\mathbf{1} = \Pi_c + \Pi_g$ to the momentum balance

$$\{\Pi_c + \Pi_g\} \left[\frac{\partial}{\partial t} (\mathbf{P} - \mathbf{A}) - \frac{\mathbf{P}}{\gamma} \times \{\nabla \times (\mathbf{P} - \mathbf{A})\} = \nabla(\phi - \gamma) \right], \quad (2.14)$$

allows to split the equation in a divergence-free and a curl-free part. The equation

$$\frac{\partial}{\partial t} (\mathbf{P}_c - \mathbf{A}) - \Pi_c \left[\frac{\mathbf{P}}{\gamma} \times \{\nabla \times (\mathbf{P}_c - \mathbf{A})\} \right] = 0 \quad (2.15)$$

describes the convective transport of the divergence-free part of the canonical momentum $\mathbf{P}_{\text{can}} = \mathbf{P} - \mathbf{A}$. This implies that for the initial condition $\mathbf{P}_c = \mathbf{A}$, the canonical momentum stays curl-free for all times.

$$\mathbf{P}_{\text{can}} = \mathbf{P}_g + \mathbf{P}_c - \mathbf{A} = \mathbf{P}_g . \quad (2.16)$$

This initial condition simplifies the curl-free part to

$$\frac{\partial}{\partial t} \mathbf{P}_g - \Pi_g \left[\frac{\mathbf{P}}{\gamma} \times \{\nabla \times (\mathbf{P}_c - \mathbf{A})\} \right] = \nabla(\phi - \gamma) \quad (2.17)$$

$$\frac{\partial}{\partial t} \mathbf{P}_g = \nabla(\phi - \gamma) \quad (2.18)$$

Since $\nabla \times \mathbf{P}_g = 0$, \mathbf{P}_g can be written as a Clebsch-potential, $\mathbf{P}_g = \nabla\psi$. The momentum balance can then be integrated to yield

$$\frac{\partial}{\partial t} \psi = \phi - \gamma + 1 . \quad (2.19)$$

¹ $v_g \propto c$ with $v_g = \sqrt{1 - n_0/n_c}$, which implies densities not too close to n_c

2.2. Equations for the weakly relativistic regime

This set of equations already has a simpler structure than the original Fluid-Maxwell equations. Numerically, though, they are still hard to tackle, because they include the development of shocks in the density and velocity distribution that can produce unphysical negative densities and lead to numerical instability. This occurs because of the convective nonlinearity that can lead to a crossing of the characteristics of the equations. There are no physical mechanism included in the equations that could prevent this trajectory crossing. Simply including artificial viscosity has the unwanted side effect of qualitatively altering the solution of the equations even in regions where it is smooth. For schemes using Lax-stabilization, e.g. [4] the same objections are valid [43]. Developing a Riemann-solver based numerical scheme (see e.g. [46]) for relativistic laser-plasma interaction, which could cope with shocks in the solution is beyond the scope of this work. Some work has been done in [53] on flux corrected transport methods (FCT, see [36, 67]), but the resulting scheme has the restriction that the grid constants for all coordinates have to be in the same range.

2.2 Equations for the weakly relativistic regime

As we will see in the next chapter, energy efficient pulse compression is limited to weakly relativistic intensities. We will now derive equations for this particular parameter regime. Applying the splitting via Π_g and Π_c to the wave equation for \mathbf{A} , yields for the divergence-free part

$$\frac{\partial^2}{\partial t^2} \mathbf{A} - \Delta \mathbf{A} = -\frac{n_0}{n_c} (1 - \nabla \Delta^{-1} \nabla \cdot) \left\{ \frac{n_e}{\gamma} (\mathbf{A} + \nabla \psi) \right\} \quad (2.20)$$

and for the curl-free part

$$\frac{\partial}{\partial t} \nabla \phi = -\frac{n_0}{n_c} \nabla \Delta^{-1} \nabla \cdot \left\{ \frac{n_e}{\gamma} (\mathbf{A} + \nabla \psi) \right\} . \quad (2.21)$$

The right-hand-side of both equations includes the curl-free part of the current density $\Pi_g \mathbf{j}$. This part can be rewritten in a form with two terms, where the inverse Laplace operator acts only on one of them.

$$\frac{n_c}{n_0} \Pi_g \mathbf{j} = \nabla \Delta^{-1} \nabla \cdot \left\{ \frac{n_e}{\gamma} (\mathbf{A} + \nabla \psi) \right\} \quad (2.22)$$

$$= \Delta^{-1} \left\{ \nabla \left(\mathbf{A} \cdot \nabla \frac{n_e}{\gamma} \right) + \nabla \nabla \cdot \frac{n_e}{\gamma} \nabla \psi \right\} \quad (2.23)$$

$$= \Delta^{-1} \left\{ \nabla \left(\mathbf{A} \cdot \nabla \frac{n_e}{\gamma} \right) + \Delta \left(\frac{n_e}{\gamma} \nabla \psi \right) + \nabla \times \nabla \times \left(\frac{n_e}{\gamma} \nabla \psi \right) \right\} \quad (2.24)$$

$$= \frac{n_e}{\gamma} \nabla \psi + \Delta^{-1} \left\{ \nabla \left(\mathbf{A} \cdot \nabla \frac{n_e}{\gamma} \right) + \nabla \times \left[\left(\nabla \frac{n_e}{\gamma} \right) \times (\nabla \psi) \right] \right\} . \quad (2.25)$$

2. Model equations

Substituted into the equations for \mathbf{A} and $\nabla\phi$ we get

$$\frac{\partial^2}{\partial t^2}\mathbf{A} - \Delta\mathbf{A} = -\frac{n_0}{n_c} \left\{ \frac{n_e}{\gamma}\mathbf{A} - \Delta^{-1} \left\{ \nabla \left(\mathbf{A} \cdot \nabla \frac{n_e}{\gamma} \right) + \nabla \times \left[\left(\nabla \frac{n_e}{\gamma} \right) \times (\nabla\psi) \right] \right\} \right\} \quad (2.26)$$

$$\frac{\partial}{\partial t}\nabla\phi = -\frac{n_0}{n_c} \left\{ \frac{n_e}{\gamma}\nabla\psi + \Delta^{-1} \left\{ \nabla \left(\mathbf{A} \cdot \nabla \frac{n_e}{\gamma} \right) + \nabla \times \left[\left(\nabla \frac{n_e}{\gamma} \right) \times (\nabla\psi) \right] \right\} \right\} . \quad (2.27)$$

The two terms that Δ^{-1} acts on have a simple interpretation: multiplying the divergence-free \mathbf{A} or the curl-free $\nabla\psi$ with $\frac{n_e}{\gamma}$ leads to new divergence and curl components in those terms, respectively. These two terms are necessary to cancel the corresponding components of $\frac{n_e}{\gamma}\mathbf{A}$ and $\frac{n_e}{\gamma}\nabla\psi$, to get the actual curl-free and divergence-free parts of the current density.

Both terms are identical to zero in the one dimensional case², so it is natural to assume that in the three dimensional case they can be neglected, too, if the dependency on the perpendicular coordinate is sufficiently slow. But in this case the perpendicular Laplace operator would also be negligibly small, because for $\mathbf{A}(\mathbf{r}) = \mathbf{A}(z, \alpha\mathbf{r}_\perp)$ it yields a factor α^2 , while $\nabla \left(\mathbf{A} \cdot \nabla \frac{n_e}{\gamma} \right)$, even with the assumption $A_z \equiv 0$, only yields a factor α . We thus have to derive the scaling more thoroughly to arrive at the correct equations.

We choose the following ansatz for the weakly relativistic scaling

$$\mathbf{A}(\mathbf{r}, t) = \varepsilon \{ \mathbf{A}_\perp(z, \alpha\mathbf{r}_\perp) + \mu \mathbf{e}_z A_\parallel(z, \alpha\mathbf{r}_\perp) \} \quad (2.28)$$

$$n_e(\mathbf{r}, t) = n_e^0 + \beta n_e^1(z, \alpha\mathbf{r}_\perp) \quad (2.29)$$

$$\phi(\mathbf{r}, t) = \rho \phi^1(z, \alpha\mathbf{r}_\perp) \quad (2.30)$$

$$\psi(\mathbf{r}, t) = \delta \psi^1(z, \alpha\mathbf{r}_\perp) \quad (2.31)$$

$$\gamma(\mathbf{r}, t) = 1 + \frac{\varepsilon^2}{2} |\mathbf{A}|^2 . \quad (2.32)$$

The different smallness parameters are of course interrelated. First we will derive the conditions for a consistent relation between these parameters.

From Coulomb gauge we get

$$\nabla \cdot \mathbf{A} = \varepsilon \{ \alpha \nabla_\perp \cdot \mathbf{A}_\perp + \mu \partial_z A_\parallel \} = 0 \Rightarrow \mu = \alpha .$$

The Laplace equation for ϕ yields

$$\rho \Delta \phi^1 = \frac{n_0}{n_c} (n_e - n_e^0) = \frac{n_0}{n_c} \beta n_e^1 \Rightarrow \rho = \beta .$$

The reduced momentum balance

$$\delta \partial_t \psi^1 = \rho \phi^1 - (\gamma - 1) = \rho \phi^1 + \mathcal{O}(\varepsilon^2)$$

² $A_z = 0, \nabla_\perp \frac{n_e}{\gamma} = 0, \nabla_\perp \psi = 0 \Rightarrow \mathbf{A} \cdot \nabla \frac{n_e}{\gamma} = 0, \left(\nabla \frac{n_e}{\gamma} \right) \times (\nabla\psi) = 0$

2.2. Equations for the weakly relativistic regime

and the continuity equation

$$\rho \nabla \cdot \partial_t \nabla \phi^1 = \beta \partial_t n_e^1 = -\frac{n_0}{n_c} n_e^0 \delta \Delta \psi^1 + \text{h.o.t.}$$

are consistent with

$$\delta = \rho = \beta = \varepsilon^2 .$$

This scaling is also consistent with the wave equation for \mathbf{A}

$$\varepsilon \left\{ \partial_t^2 \mathbf{A} - \partial_z^2 \mathbf{A} - \alpha^2 \Delta_{\perp} \mathbf{A} \right\} = -\varepsilon \left\{ \frac{n_0}{n_c} (n_e^0 + \beta n_e^1) \left[1 - \frac{\varepsilon^2}{2} |\mathbf{A}|^2 \right] \mathbf{A} \right\} + \dots .$$

Under this assumption, because of

$$\nabla \frac{n_e}{\gamma} = \varepsilon^2 (\nabla n_e^1 + n_e^0 \nabla \frac{|\mathbf{A}|^2}{2})$$

and

$$\mathbf{A} \cdot \nabla = \mathbf{A}_{\perp} \cdot (\alpha \nabla_{\perp}) + \alpha A_{\parallel} \partial_z$$

we have

$$\nabla \left(\mathbf{A} \cdot \nabla \frac{n_e}{\gamma} \right) = \mathcal{O}(\varepsilon^3 \alpha)$$

and

$$\nabla \times \left[\left(\nabla \frac{n_e}{\gamma} \right) \times (\nabla \psi) \right] = \mathcal{O}(\varepsilon^4 \alpha^2) .$$

The inverse Laplace operator does not change the order of these terms, because

$$\Delta^{-1} = \mathcal{F}^{-1} \frac{1}{k_{\parallel}^2 + \alpha^2 k_{\perp}^2} \approx \mathcal{F}^{-1} \frac{1}{k_{\parallel}^2} \left(1 - \alpha^2 \frac{k_{\perp}^2}{k_{\parallel}^2} \right) = \left(\frac{\partial^2}{\partial z^2} \right)^{-1} + \mathcal{O}(\alpha^2) ,$$

where \mathcal{F}^{-1} is the inverse Fourier transform. To get consistent equations, we have thus to include all terms up to order ε^3 and $\varepsilon \alpha^2$, while neglecting terms of order $\varepsilon^3 \alpha$ and higher. Linearizing in the density fluctuation allows for a further simplification of the equations by differentiating the continuity equation in time

$$\frac{\partial^2}{\partial t^2} n_e^1 = -\frac{n_0}{n_c} n_e^0 \frac{\partial}{\partial t} \Delta \psi^1 ,$$

and applying the Laplace operator the equation for ψ^1

$$\frac{\partial}{\partial t} \Delta \psi^1 = \Delta \phi^1 - \Delta \gamma .$$

Substituting ψ^1 in this way, we get

$$\frac{\partial^2}{\partial t^2} n_e^1 + \frac{n_0}{n_c} n_e^0 n_e^1 = n_e^0 \Delta \gamma . \quad (2.33)$$

2. Model equations

Combined with the wave equation of the correct order in the scaling coefficients

$$\partial_t^2 \mathbf{A} - \Delta \mathbf{A} = -\frac{n_0}{n_c} \left\{ n_e^0 \left(1 - \frac{\varepsilon^2}{2} |\mathbf{A}|^2 \right) + n_e^1 \right\} \mathbf{A} \quad (2.34)$$

we have a complete system of equations. Since a component of \mathbf{A} that is initially zero will stay zero, we can construct a pulse with $A_{\parallel} \equiv 0$ and only use \mathbf{A}_{\perp} in the equations. It is convenient for numerics to write $\mathbf{A}_{\perp}(\mathbf{r}, t)$ as a complex field $a(\mathbf{r}, t)$ by defining

$$\mathbf{A}_{\perp}(\mathbf{r}, t) = \frac{1}{2} a(\mathbf{r}, t) \{ \mathbf{e}_x \pm i \mathbf{e}_y \} + \text{c.c.} \quad (2.35)$$

for a circular polarized laser, where the \pm denotes left or right circular polarization.

2.3 Slowly varying envelope approximation

We can further simplify the wave equation (2.34) by introducing the so called slowly varying envelope approximation (SVEA). We first transform into a comoving frame with the new variables

$$\zeta = z \text{ and } \tau = \frac{1}{\beta} z - t, \quad (2.36)$$

where $\beta = \sqrt{1 - n_0/n_c}$ is the linear group velocity of the pulse.

Transforming the derivatives in (2.34) accordingly results in

$$\left\{ \frac{\partial^2}{\partial \zeta^2} + \frac{1 - \beta^2}{\beta^2} \frac{\partial^2}{\partial \tau^2} + \frac{2}{\beta} \frac{\partial^2}{\partial \tau \partial \zeta} + \Delta_{\perp} \right\} \mathbf{A}(\mathbf{r}_{\perp}, \zeta, \tau) = \frac{n_0 n_e}{n_c \gamma} \mathbf{A}(\mathbf{r}_{\perp}, \zeta, \tau). \quad (2.37)$$

Defining the envelope ansatz

$$\mathbf{A}(\mathbf{r}_{\perp}, \zeta, \tau) = \frac{1}{2} a(\mathbf{r}_{\perp}, \zeta, \tau) \{ \mathbf{e}_x \pm i \mathbf{e}_y \} e^{-i \frac{1 - \beta^2}{\beta^2} \zeta + i \tau} + \text{c.c.} \quad (2.38)$$

and insertion into (2.37) yields

$$i \frac{\partial}{\partial \zeta} a + \frac{1 - \beta^2}{2 \beta^3} \frac{\partial^2}{\partial \tau^2} a + \frac{1}{2 \beta} \Delta_{\perp} a = \frac{1 - \beta^2}{2 \beta} \left\{ \frac{n_e}{\gamma} - 1 \right\} a, \quad (2.39)$$

under the assumption that the envelope function $a(\mathbf{r}_{\perp}, \zeta, \tau)$ varies slowly compared to the carrier wave and $\frac{\partial^2}{\partial \tau \partial \zeta}$ and $\frac{\partial^2}{\partial \zeta^2}$ can be neglected.³ Setting $n_e = \text{const.}$ and expanding the γ -factor leads to the well known cubic nonlinear Schrödinger equation (cubic NLSE).

Under the same variable transformation and envelope approximation, the density equation becomes

$$\frac{\partial^2}{\partial \tau^2} n_e^1 + \frac{n_0}{n_c} n_e^0 n_e^1 = n_e^0 \left\{ \frac{1}{\beta^2} \frac{\partial^2}{\partial \tau^2} + \Delta_{\perp} \right\} \gamma. \quad (2.40)$$

³For two or three dimensional wave equations this is also called the paraxial approximation [61].

2.3. Slowly varying envelope approximation

Note that this equation represents an initial value problem in ζ , not in τ as the NLSE. This complicates the numerical solution of the coupled system (2.39), (2.40).

For very short pulses of only a few laser cycles, the envelope approximation breaks down. Another drawback of the NLSE is that the transition of the laser pulse from vacuum to plasma is not described self-consistently by this equation. The NLSE is thus less well suited for the numerical simulation of pulse compression than the full wave equation. We mainly derived the NLSE here for use in analytical models based on the variation-of-action method (VAM).

3 Pulse compression in one dimension

The propagation of a pulse that is short in the longitudinal direction and wide in the transversal direction will at first be close to the propagation of a one dimensional pulse that is transversally constant. If and when the dynamics in 2D/3D changes significantly from 1D will be discussed in the later chapters. In this chapter we will study the influence of pulse and plasma parameters on longitudinal pulse compression and instabilities that already occur in 1D. First we will derive the 1D versions of the equations from chapter 2 and then develop a numerical scheme to handle the fast time and space dependence of the wave equation. This part of the chapter was published in [39].

3.1 Model equations in 1D

It is instructive to derive the model equations (2.33) and (2.34) again in 1D. We start with the normalized equations (2.9), (2.11) and (2.12) and assume that all quantities depend spatially only on the z -coordinate. Coulomb gauge implies the purely transverse nature of the wave ($\mathbf{A} = \mathbf{A}_\perp$). The wave equation (2.34) for the transverse component \mathbf{A}_\perp now reads

$$\frac{\partial^2}{\partial t^2} \mathbf{A}_\perp - \frac{\partial^2}{\partial z^2} \mathbf{A}_\perp = -\frac{n_0}{n_c} n_e \frac{\mathbf{P}_\perp}{\gamma}. \quad (3.1)$$

The longitudinal part of the wave equation simplifies to

$$\frac{\partial^2 \phi}{\partial t \partial z} + \frac{n_0}{n_c} n_e \frac{P}{\gamma} = 0. \quad (3.2)$$

Either this equation or the continuity equation is redundant, because derivation with respect to z yields the 1D continuity equation.

The same splitting was achieved in 3D by decomposing the equations into a curl-free and a divergence-free part.

The momentum balance (2.12) can be split into its longitudinal and transversal components. The transversal electron momentum balance

$$\frac{\partial}{\partial t} (\mathbf{P}_\perp - \mathbf{A}_\perp) + \left(\frac{P_z}{\gamma} \right) \frac{\partial (\mathbf{P}_\perp - \mathbf{A}_\perp)}{\partial z} = 0 \quad (3.3)$$

has the special solution

$$\mathbf{P}_\perp = \mathbf{A}_\perp. \quad (3.4)$$

3.1. Model equations in 1D

This special initial condition corresponds to the 3D condition $\nabla \times (\mathbf{P} - \mathbf{A}) = 0$, which is the local version of the global 1D condition. In 3D the local longitudinal direction is given by the direction of the \mathbf{k} -vector and the momentum components perpendicular to this direction are equal to \mathbf{A}_\perp . The component of \mathbf{A} parallel to \mathbf{k} is equal to zero because of Coulomb gauge.

The longitudinal electron momentum balance

$$\frac{\partial P_z}{\partial t} - \mathbf{P}_\perp \cdot \frac{\partial (\mathbf{P}_\perp - \mathbf{A}_\perp)}{\partial z} = \frac{\partial (\phi - \gamma)}{\partial z}, \quad (3.5)$$

can be simplified by the special solution, too. Thus we directly have only a scalar equation for the momentum in 1D, without using a Clebsch potential ψ with $\mathbf{P} = \nabla\psi$. This leads to the basic set of 1D equations:

$$\frac{\partial^2}{\partial t^2} \mathbf{A}_\perp - \frac{\partial^2}{\partial z^2} \mathbf{A}_\perp = -\frac{n_0}{n_c} n_e \frac{\mathbf{A}_\perp}{\gamma}, \quad (3.6)$$

$$\frac{\partial^2 \phi}{\partial t \partial z} + \frac{n_0}{n_c} n_e \frac{P_z}{\gamma} = 0, \quad (3.7)$$

$$\frac{\partial^2 \phi}{\partial z^2} = \frac{n_0}{n_c} (n_e - n_e^0), \quad (3.8)$$

$$\frac{\partial P_z}{\partial t} = \frac{\partial (\phi - \gamma)}{\partial z}, \quad (3.9)$$

where n_e^0 is the time-independent part of n (which is identical to the fixed ion background) and $\gamma = \sqrt{1 + |\mathbf{A}_\perp|^2 + P_z^2}$.

The scaling for the weakly nonlinear regime is much simpler in 1D, too. We assume that

$$\mathbf{A}_\perp \propto \varepsilon \ll 1 \text{ and } n_e = n_e^0 + \alpha n_e^1.$$

Equations (3.8) and (3.7) then directly tell us that $\phi^1 \propto \alpha$ and $P_z^1 \propto \alpha$ ($\phi^0 = P_z^0 = 0$). Inserting

$$\gamma \approx 1 + \frac{\varepsilon^2}{2} |\mathbf{A}_\perp|^2 + \frac{\alpha^2}{2} (P_z^1)^2$$

into (3.9) suggests $\alpha = \varepsilon^2$ and that P_z^1 can be neglected in the γ -factor.

The correctly scaled wave equation then is

$$\frac{\partial^2}{\partial t^2} \mathbf{A}_\perp - \frac{\partial^2}{\partial z^2} \mathbf{A}_\perp = -\frac{n_0}{n_c} \left\{ n_e^0 \left(1 - \frac{1}{2} |\mathbf{A}_\perp|^2 \right) + n_e^1 \right\} \mathbf{A}_\perp. \quad (3.10)$$

Derivation of (3.7) with respect to time and inserting (3.9) and the scalings for n_e and P_z yield an equation for the electrostatic part of the \mathbf{E} -field $E_z^1 \equiv \partial_z \phi^1$

$$\frac{\partial^2}{\partial t^2} \partial_z \phi^1 + \frac{n_0}{n_c} n_e^0 \partial_z \phi^1 = -\frac{1}{2} \frac{n_0}{n_c} n_e^0 \frac{\partial}{\partial z} |\mathbf{A}_\perp|^2. \quad (3.11)$$

This equation allows for an arbitrary dependence of n_e^0 on z . The full 3D version of this equation has three components and thus is better substituted with a scalar equation

3. Pulse compression in one dimension

for n_e^1 by using $\Delta\phi = \frac{n_0}{n_c} n_e^1$. If we assume n_e^0 to be piecewise constant or only slowly dependent on z , as we did in the derivation of the 3D equations, we can transform the above equation into

$$\frac{\partial^2}{\partial t^2} n_e^1 + \frac{n_0}{n_c} n_e^0 n_e^1 = -\frac{1}{2} n_e^0 \frac{\partial^2}{\partial z^2} |\mathbf{A}_\perp|^2. \quad (3.12)$$

The equations thus have the same form as in 3D, only the Laplace operator is restricted to the z -coordinate.

Comparison of 1D simulations with these two equations for the density response show no significant differences for density profiles with density jumps or smooth ramps of several λ_0 length. For 1D simulations we will use the equation for E_z^1 and for the 2D simulations in the following chapters the equation for n_e^1 .

A significant difference can occur between simulations with the full γ -factor and the expanded γ , because the scaling only tells us the order of ε of a term in the equations, but not the constant in front of it. In all following simulations we will use the full γ -factor, if not explicitly stated otherwise.

3.2 Numerical methods

Numerically solving the wave equation (3.10) poses the problem that the carrier wave of a laser pulse has a fast time and space dependency. The discretization of the spatial grid and the stepsize in time have to be chosen accordingly small. This is even the case for circular polarization and a pulse envelope that changes slowly compared to the laser wavelength (so that the nonlinearity varies smoothly), because the restriction is caused by the properties of the linear operator on the left-hand-side of the equation. We will discuss two methods that will allow us to attenuate the restrictions, Gautschi-type numerical schemes to handle the fast time dependence and the quasi-envelope approach (QEA) to reduce the number of grid points.

3.2.1 Spatial discretization

Due to the finite energy assumption on the physical solution it is possible to consider periodic boundary conditions for the discretization as long as the simulation box is big enough and one takes care of reflected pulses at the boundaries. For long time simulations this can be combined with a moving window technique.

Semi-discretization in space is done by a pseudospectral method with N Fourier modes on a space interval $z \in z_0 + [-L, L]$. This leads to the following system of coupled ordinary differential equations in time (the prime denotes time-derivative):

$$a'' = -D^2 a + g(a, n_e^1), \quad g(a, n_e^1) = -\frac{n_0}{n_c} (n_e^0 + n_e^1) \frac{1}{\gamma} a, \quad (3.13)$$

$$E'' = -\omega^2 E + f(a), \quad f(a) = -n_e^0 i D \sqrt{1 + |a|^2}. \quad (3.14)$$

3.2. Numerical methods

Here, $D^2 = \mathcal{F}_N^{-1} \mathcal{D}^2 \mathcal{F}_N$, where \mathcal{F}_N is the discrete Fourier-transform operator, and

$$\mathcal{D} = \frac{\pi}{L} \text{diag}\left(-\frac{N}{2}, -\frac{N}{2} + 1, \dots, -1, 0, 1, \dots, \frac{N}{2} - 1\right).$$

The j th component of the vectors $a(t)$ and $E(t)$ are approximations to $a(z_j, t)$ and $E(z_j, t)$ at $z_j = z_0 + j \frac{2L}{N}$, and $\omega^2 = \frac{n_0 n_e^0}{n_c}$.

3.2.2 A two-step Gautschi-type exponential integrator for time discretization

As a solver for these equations we use a modification of a Gautschi-type exponential integrator [34]. This integrator is motivated as follows: By the variation-of-constants formula, the exact solution of

$$y'' = -\Omega^2 y + F(y) \tag{3.15}$$

satisfies

$$\begin{aligned} y(t + \tau) = & 2 \cos(\tau\Omega) y(t) - y(t - \tau) \\ & + \int_0^\tau \Omega^{-1} \sin((\tau - s)\Omega) (F(y(t + s)) + F(y(t - s))) ds. \end{aligned} \tag{3.16}$$

For a constant inhomogeneity F this yields

$$y(t + \tau) = 2y(t) - y(t - \tau) + \tau^2 \psi(\tau\Omega) (-\Omega^2 y(t) + F),$$

where

$$\psi(x) = 2 \frac{1 - \cos x}{x^2}.$$

In the general case, a numerical scheme is obtained by substituting a suitable approximation of $F(y(t \pm s))$ into (3.16). This leads to approximations $y_k \approx y(t_k)$, $t_k = k\tau$, defined by

$$y_{k+1} = 2y_k - y_{k-1} + \tau^2 \psi(\tau\Omega) (-\Omega^2 y_k + F_k).$$

The simplest choice, originally proposed by Gautschi [22], is to set $F_k = F(y_k)$. However, the convergence analysis in [34] shows that in order to obtain second-order error bounds, which are independent of the product of the step size with the frequencies, it is necessary to evaluate the nonlinearity F at a filtered position, i.e. $F_k = F(\phi(\tau\Omega)y_k)$. If this *filter function* ϕ is omitted, then large errors are expected in the case when the product of the step size τ with one of the frequencies of the problem (the eigenvalues of Ω) is an integer multiple of π . The filter function is a suitably chosen real function whose purpose is to filter out resonant frequencies, e.g.

$$\phi(x) = \left(\frac{\sin x}{x}\right)^2, \quad \text{or} \quad \phi(x) = \left(\frac{\sin x}{x}\right)^2 \left(1 + \frac{1}{2}(1 - \cos x)\right).$$

3. Pulse compression in one dimension

The integrator applied to (3.15) then reads

$$y_{k+1} = 2y_k - y_{k-1} + \tau^2 \psi(\tau\Omega) (-\Omega^2 y_k + F_k), \quad F_k = F(\phi(\tau\Omega)y_k). \quad (3.17)$$

In addition it is also possible to obtain approximations to the “velocities” y' via

$$y'_{k+1} = y'_{k-1} + 2\tau\sigma(\tau\Omega)(-\Omega^2 y_k + F_k), \quad (3.18)$$

where $\sigma(x) = \sin x/x$. Note that approximating the “velocities” by standard finite differences will lead to inaccurate results due to the oscillatory behavior of y .

For $\Omega = 0$ the Gautschi-type integrator reduces to the well known leap-frog or Störmer-Verlet method. We will use (3.17) and, if desired, (3.18) for the integration of (3.13) for the vector potential.

The accuracy of the integrator may be further improved if approximations to the inhomogeneity are available at additional times. This is only true if we solve the equations (3.14) for the electrical field because there the inhomogeneity only depends on a . If we solve the equation for a first, we have approximations $a_j \approx a(t_j)$ for $j = k-1, k$, and $k+1$. We then replace $f(a)$ by an interpolation polynomial of degree two interpolating in $(t_{k-1}, f(a_{k-1}))$, $(t_k, f(a_k))$, and $(t_{k+1}, f(a_{k+1}))$. Note that we consider the circular polarized case, in which f is a smooth function. Using this interpolation polynomial instead of $F(y(t \pm s))$ in (3.16) yields

$$E_{k+1} = 2E_k - E_{k-1} + \tau^2 \psi(\tau\omega) (-\omega^2 E_k + f(a_k)) + \tau^4 \chi(\tau\omega) (f(a_{k+1}) - 2f(a_k) + f(a_{k-1})) \quad (3.19)$$

for (3.14), where

$$E_k \approx E(t_k) \quad \text{and} \quad \chi(x) = 2 \frac{\cos x - 1 + \frac{1}{2}x^2}{x^4}.$$

The scheme (3.19) is of order four, if a_j , $j = k-1, k, k+1$ are exact or sufficiently accurate approximations of $a(t_j)$. However, the coupled scheme (3.17), (3.19) cannot be better than second order.

3.2.3 Choice of operators

For solving (3.13) the obvious choice would be using (3.17) with $\Omega = D$. By construction, the Gautschi-type integrator then solves equations $y'' = -\Omega^2 y + F$ with constant F exactly. Due to the special form of the nonlinearity g , we can enlarge the part which is integrated exactly by writing

$$g(a, n_e^1) = -\alpha a + \tilde{g}(a, n_e^1)$$

and setting $\Omega^2 = D^2 + \alpha$ for a suitable α . If the pulse is inside the plasma, the dominant term of g is linear in a , which suggests to choose $\alpha = n_0/n_c$. Outside the plasma (where $n_e^0 = 0$) the nonlinearity is negligible so that one should set $\alpha = 0$.

3.2.4 Quasi-envelope approach

The motivation behind the quasi-envelope approach (QEA) is illustrated on a numerical result shown in Fig. 3.1: the spectrum of the vector potential splits into two parts. The important part is concentrated around a certain characteristic wave number depending on whether the pulse propagates inside or outside of the plasma. In addition there is another peak resulting from reflection which is not of interest in our physical application, because the reflection can be nearly completely avoided by using a soft vacuum-plasma boundary (which is a more realistic model for an experimental setup). Therefore, it is sufficient to resolve the part of the spectrum with positive k -values around the carrier only, without problems due to aliasing that could occur if we do not handle the reflections correctly. The number of spatial grid points required can be reduced significantly by shifting the spectrum appropriately, i.e. we replace the vector potential a by

$$a(z, t) = \tilde{a}(z, t)e^{i\kappa z}$$

and solve (3.10) for \tilde{a} instead of a . This yields

$$\frac{\partial^2}{\partial t^2}\tilde{a} = \frac{\partial^2}{\partial z^2}\tilde{a} + 2i\kappa\frac{\partial}{\partial z}\tilde{a} - \kappa^2\tilde{a} - \frac{n_0}{n_c}(n_e^0 + n_e^1)\frac{1}{\gamma}\tilde{a}, \quad \gamma^2 = 1 + |\tilde{a}|^2.$$

Note that in the ‘‘classical’’ envelope approximation $\partial^2\tilde{a}/\partial z^2$ is neglected, leading to a Schrödinger type equation in z . In the spatially discretized equation (3.13), \mathcal{D}^2 has to be replaced by $(\mathcal{D} + \kappa)^2$. The value of κ can be varied for different positions of the pulse (inside/outside of the plasma or at the boundary), so we choose $\kappa = \sqrt{1 - n_0/n_c}$, $\kappa = 1$ or the mean value of both.

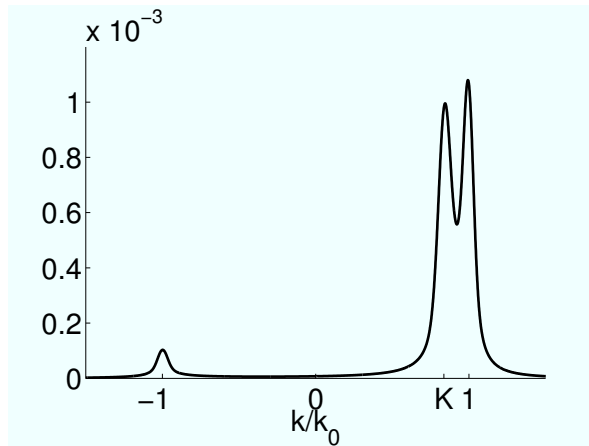


Figure 3.1: Spectrum of the wavenumbers of the vector potential while entering the plasma, $K = \sqrt{1 - n_0/n_c}$ (arbitrary units).

3.2.5 Multilevel approach

Obviously, the spatial grid size is determined by the necessity of resolving reflections arising at jumps of the plasma density. If we have a sharp jump, then the reflections

3. Pulse compression in one dimension

require small spatial grid sizes only when the pulse enters or leaves the plasma. This can be exploited in a standard way by using two (or more) different grids. In our case we used a fine grid in transitions between vacuum and plasma and a coarse one in the remaining simulation. Switching between coarse and fine grid is done by interpolation and from the fine to the coarse grid by restriction (both in Fourier space). Note that this switch requires to recompute the differential operator and hence the matrix operators required for the Gautschi-type integrator.

3.2.6 Overall numerical method

The complete numerical method combines the strategies described above. This requires the computation of three or more sets of operators: one in vacuum ($\alpha_v = 0, \kappa_v = 1$, coarse grid), one in plasma ($\alpha_p = n_0/n_c, \kappa_p = \sqrt{1 - n_0/n_c}$, coarse grid), and one in the transition ($\alpha_t = 0.5 n_0/n_c, \kappa_t = (1 + \sqrt{1 - n_0/n_c})/2$, fine grid), and possibly additional sets if the pulse gets too steep to be resolved on the coarse grid in plasma due to nonlinear pulse compression. If background density is small (so that the difference between vacuum and plasma wavelength is also small) and the density profile has no sharp jump (so that no reflection occurs), it is most of the time sufficient to use the same set of operators for both the transitional region and the plasma region on the same coarse grid, with a κ halfway between vacuum and plasma wave-number. Recall that in vacuum, there is no nonlinearity, and thus the Gautschi-type integrator solves the problem exactly for arbitrary time steps. Obviously, it is not necessary to compute filter functions in this case.

3.3 Accuracy and efficiency of the numerical scheme

3.3.1 Description of the simulated example problem

For runtime comparison we chose a simulation box of length $1000 \lambda_0$. As density profile we used a piecewise linear function which is 0 for z smaller than $100 \lambda_0$ and greater than $810 \lambda_0$, 1 for $105 \lambda_0 < z < 805 \lambda_0$ and linear in between. In this case, the multilevel approach is not necessary, because nearly no reflection occurs at the plasma boundaries. To simplify the simulational setup for the runtime comparison further, for methods with QEA, only one set of operators is used with a mean value of vacuum and plasma wavelength. With an additional set of operators for the plasma part, the results discussed below would be even better. But for a low background density like $n_0 = 0.3 n_c$, which we used, the results are already very good. For denser plasmas (e.g. $n_0 = 0.6 n_c$), switching of operators between plasma boundary and plasma parts of the density profile becomes a necessity. For the multilevel tests we used a rectangular density profile beginning at $105 \lambda_0$ and ending at $805 \lambda_0$, and we included the different operators discussed in Sec. 3.2.6.

3.3. Accuracy and efficiency of the numerical scheme

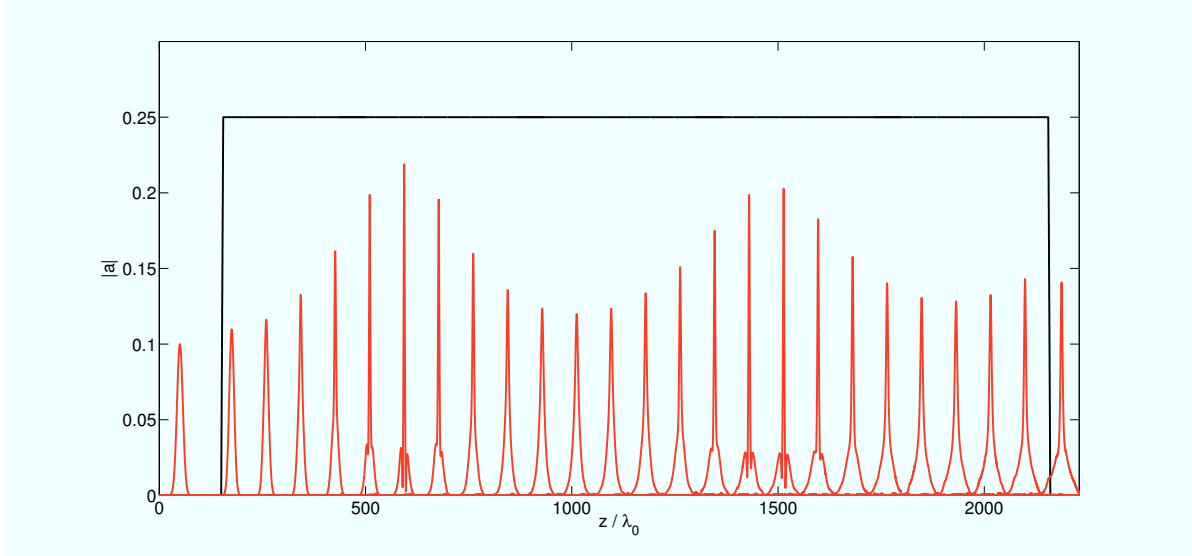


Figure 3.2: Propagating pulse at different times in red, background density profile in black for $a_0 = 0.1$, $L_0 = 10 \lambda_0$ and $n_0 = 0.3 n_c$.

The initial conditions for the vector potential in vacuum were calculated from

$$a(z, t) = a_0 e^{-\frac{(z-z_0-t)^2}{L_0^2}} e^{i(z-t)} \quad (3.20)$$

at $t = 0$ and $t = \tau$. The parameters were $z_0 = 35 \lambda_0$, $L_0 = 10 \lambda_0$, and $a_0 = 0.1$ or $a_0 = 0.12$. Due to the normalization $\lambda_0 = 2\pi$.

As an example, the time evolution for two different initial amplitudes is shown in Fig. 3.2 and in Fig. 3.3. For the lower amplitude, first a compression and then a widening of the pulse can be seen. In the case of the higher amplitude, the pulse first compresses, and then splits off a part of its energy into a prepulse. If we calculate the amplitude for the single soliton state of the Schrödinger model for a $L_0 = 10 \lambda$ wide $\text{sech}(z/L_0)$ pulse (see [59]), we get $a_0 \approx 0.038$. A simulation of such a pulse verifies that the soliton state of our model equations is close to this. For the two amplitudes above, this implies that we are well within the nonlinear regime. It also suggests that the initial condition with $a_0 = 0.1$ is close to a bound two solution state, while for $a_0 = 0.12$ it is clearly above. In the latter case the pulse compresses more and earlier, and more energy is radiated away from the core of the pulse after the compression.

As benchmarks for the accuracy of the different numerical schemes, we used two error measures. Since we do not have an analytical solution of the nonlinear model equations, we computed a reference solution on a very fine grid ($N = 2^{17}$) with very small time steps. We then used it to measure the error in maximum amplitude squared (amplitude error) and its position (phase error) at different times of the simulation results. Since the simulations were computed on coarser grids (especially the QEA solutions) we first Fourier interpolated to the same number of grid points as the reference solution.

3. Pulse compression in one dimension

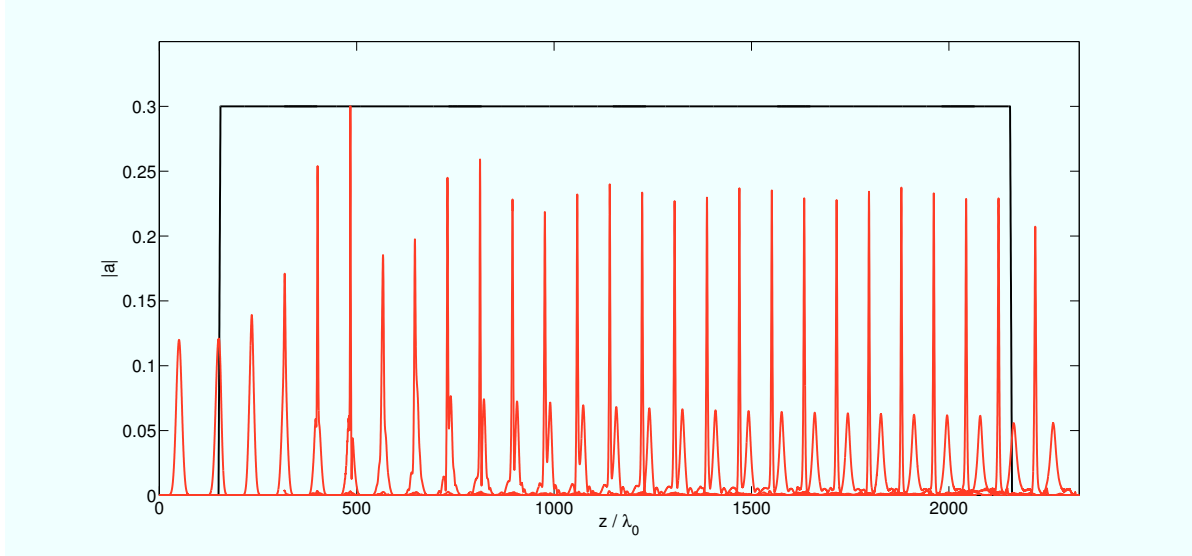


Figure 3.3: Propagating pulse at different times in red, background density profile in black for $a_0 = 0.12$, $L_0 = 10 \lambda_0$ and $n_0 = 0.3 n_c$.

3.3.2 Effect of different time-integration schemes

If the vector potential is held in Fourier space and only transformed back for the evaluation of the nonlinearity/inhomogeneity, one has to compute six fast Fourier transforms per time step for the leap-frog method (two for the nonlinearity of the wave equation, two for the inhomogeneity of the plasma response, and two for the transformation of E). There is one more Fourier transform needed for the Gautschi-type integrator since in each step the filtered as well as the nonfiltered vector potential is required in real space. In addition, one has to compute the products with the matrix functions ψ , ϕ , and possibly σ . Obviously computing a single time step with the Gautschi-type integrator is more expensive than one time step with the leap-frog method. But it turns out that the Gautschi-type method allows larger time steps in order to reach the same accuracy.

In Fig. 3.4 and Fig. 3.5 maximum relative amplitude error (left) and maximum phase error in λ (right) are plotted over computational time. Each curve represents one integrator on one spatial grid with different time steps.

For a given tolerance for the relative amplitude error the leap-frog method (dotted+triangles) needs two times smaller time steps than the Gautschi-type integrator (solid+diamonds) on the same spatial grid ($N = 2^{12}$). In our examples this reduces the computational time by a factor of 1.5 (see table 3.1). If the phase error is taken into account, too, the gain in computational time is even greater.

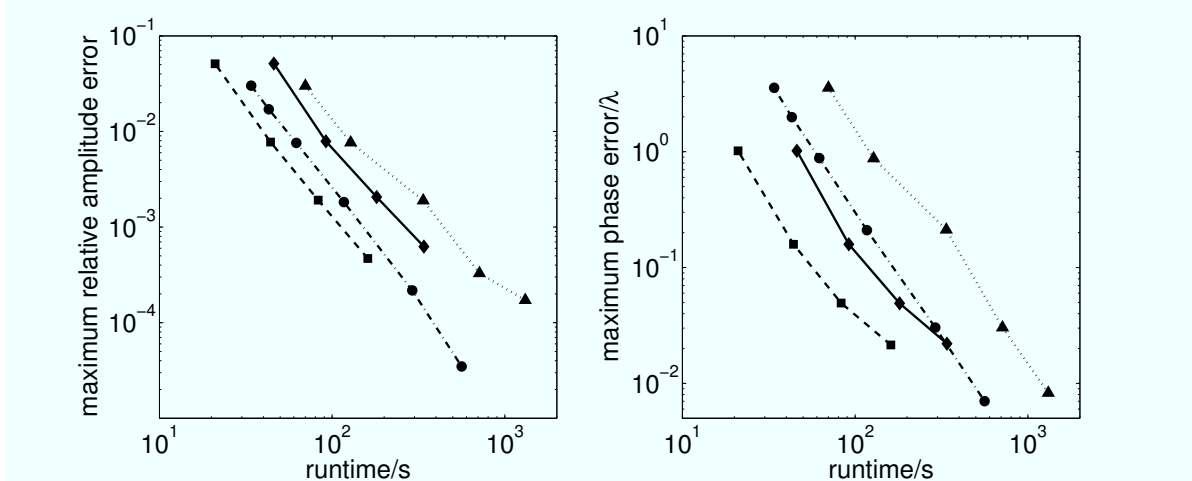


Figure 3.4: Maximum amplitude and phase error vs. runtime ($a_0 = 0.1$) for varying τ for leap-frog (dotted+triangles), Gautschi (solid+diamonds), leap-frog + QEA (dash-dotted+circles) and Gautschi + QEA (dashed+squares). We used $N = 2^{12}$ for methods without QEA and $N = 2^{11}$ for methods with QEA (see also table 3.1).

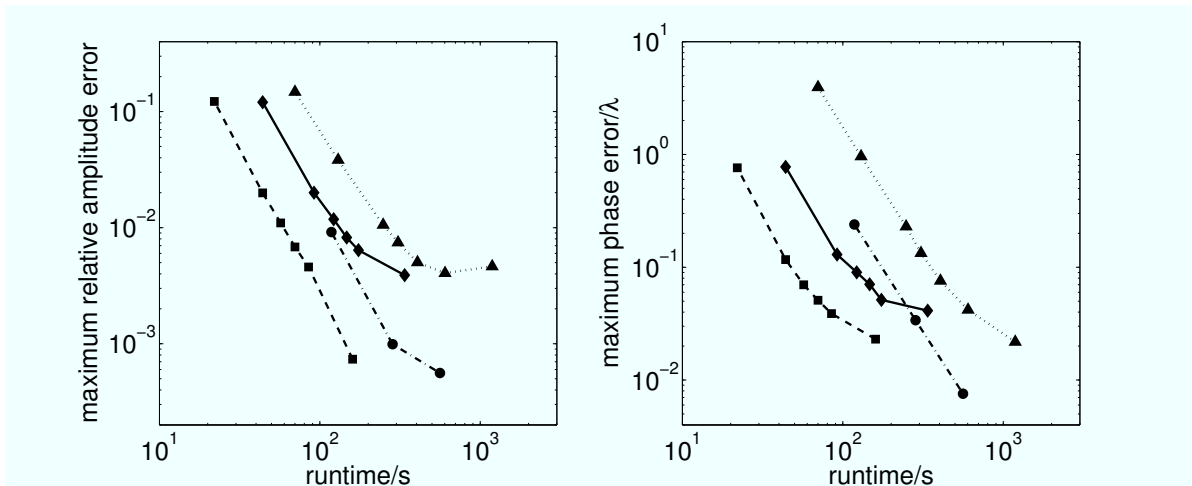


Figure 3.5: Same as Fig. 3.4, but for $a_0 = 0.12$.

3.3.3 Effect of choice of operators

The effect of the choice of operators is illustrated in Fig. 3.6 for the case $a_0 = 0.1$. It is observed that the choice of $\alpha = n_0/n_c$ within the plasma reduces the phase error significantly while the error in the amplitude is only slightly larger. However, for $a_0 = 0.12$ switching between the operators did not pay off. The reason for this might be the increased density variation compared to the smaller amplitude. The results in Fig. 3.6 were computed including QEA of Section 3.2.4, but the method showed the same behavior when combined with other variants described above. The phase error is given in terms of λ whereas the amplitude error is given relatively compared to the

3. Pulse compression in one dimension

reference amplitude. In both cases the error is averaged over pulses at 100 different positions spread evenly over the computation interval.

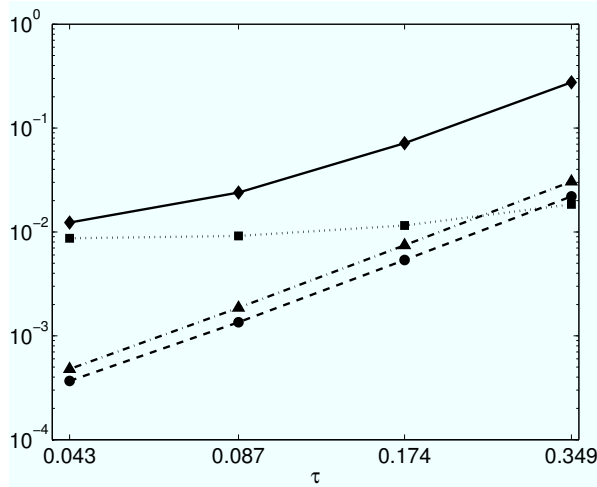


Figure 3.6: Amplitude and phase error plotted over the time step τ for the Gautschi-type integrator including quasi-envelope approach with and without the variant described in Section 3.2.3. Phase/amplitude error with $\alpha = 0$ (solid/dashed line) and $\alpha = n_0/n_c$ within the plasma (dotted/dash-dotted line) for $a_0 = 0.1$.

3.3.4 Effect of quasi-envelope approach

By applying the quasi-envelope approach to the leap-frog method as well as the Gautschi-type integrator, the number of spatial grid points can be significantly reduced without loss of accuracy (see curves with and without QEA in Fig. 3.4 and Fig. 3.5). Since the major part of computational time is spent on Fast Fourier transforms, which cost $\mathcal{O}(N \log N)$ operations, the reduction of grid points by a factor of 2 again leads to a saving in computational time of more than a factor of 2. Another reason for a more than linear reduction in computational time is that smaller arrays are more likely to fit into the cache of the processor. For small enough arrays, a whole time step can run from CPU cache. We observed that QEA is more effective in reducing the amplitude error, while the Gautschi-type method is more effective in reducing the phase error.

The parameters for the discretization needed to achieve a maximum relative amplitude error of 10^{-2} are summarized in table 3.1. Exemplary runtimes for one specific hardware/software setup are also given.

If one compares the standard leap-frog method to the new variant of the Gautschi-type integrator combined with QEA, the computational time is reduced by a factor of 3 in the first and even by a factor of 4.5 in the second example. If we set a bound lower than 10^{-2} for the amplitude error, we see that without QEA this error bound cannot be reached by only reducing τ . This is because the error due to the coarse spatial resolution limits the accuracy that can be reached. Thus a finer grid is needed, which results in

3.3. Accuracy and efficiency of the numerical scheme

	$a_0 = 0.1$			$a_0 = 0.12$		
	N	τ	time/min.	N	τ	time/min.
LF	2^{12}	0.1	2:10	2^{12}	0.04	5:07
LF + QEA	2^{11}	0.1	1:03	2^{11}	0.05	1:57
Gautschi	2^{12}	0.2	1:32	2^{12}	0.12	2:28
Gautschi + QEA	2^{11}	0.2	0:44	2^{11}	0.12	1:10

Table 3.1: Runtimes for maximum one percent relative amplitude error. N is the number of spatial grid points, τ is the time step size. Computational details: Pentium 4, 3.0 GHz, Intel C++ 8.1, FFT routines from Intel Math Kernel Library 7.2.

a corresponding increase of computational time, while the discretization for QEA can stay the same (see Fig. 3.7).

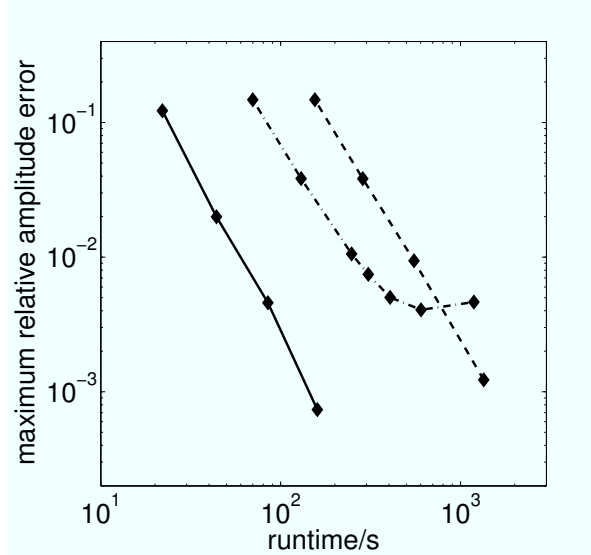


Figure 3.7: Maximum amplitude error vs. runtime ($a_0 = 0.12$) for constant N and varying τ for leap-frog with $N = 2^{13}$ (dashed), leap-frog with $N = 2^{12}$ (dash-dotted) and Gautschi + QEA with $N = 2^{11}$ (solid).

3.3.5 Effect of two-level approach

The benefit of the two-level approach suggested in Section 3.2.5 is illustrated in Fig. 3.8. The reference solution as well as the simulation results are shown at $t = 700 \cdot 2\pi$ for a plasma jump and $a_0 = 0.12$. It can be seen that in this case it is possible to work on a coarse grid ($N = 2^{11}$) in the major part of the simulation but it is not possible to do the whole simulation on the coarse grid. In the transition we interpolated to 2^{13} grid points.

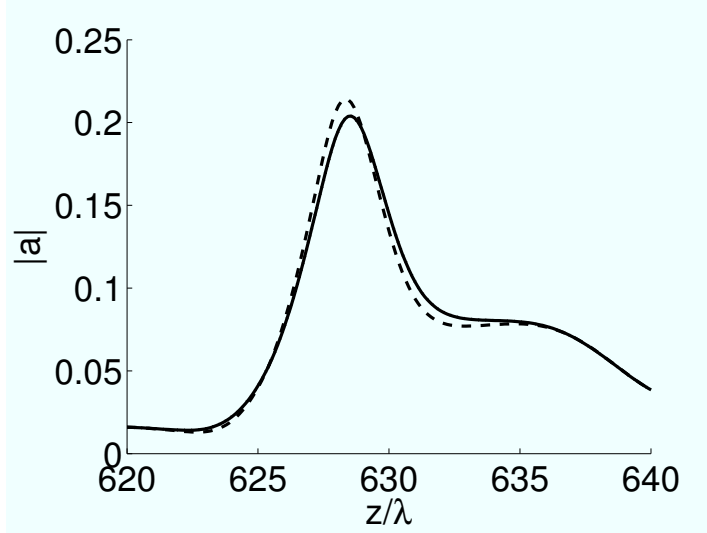


Figure 3.8: Results of simulations using the two-level approach compared to a one-level simulation on the (same) coarse grid only. Solid: reference solution, dashed: solution computed on a coarse grid only, dotted: two-level approach (curve coincides with the solid one).

3.3.6 Comparison with PIC

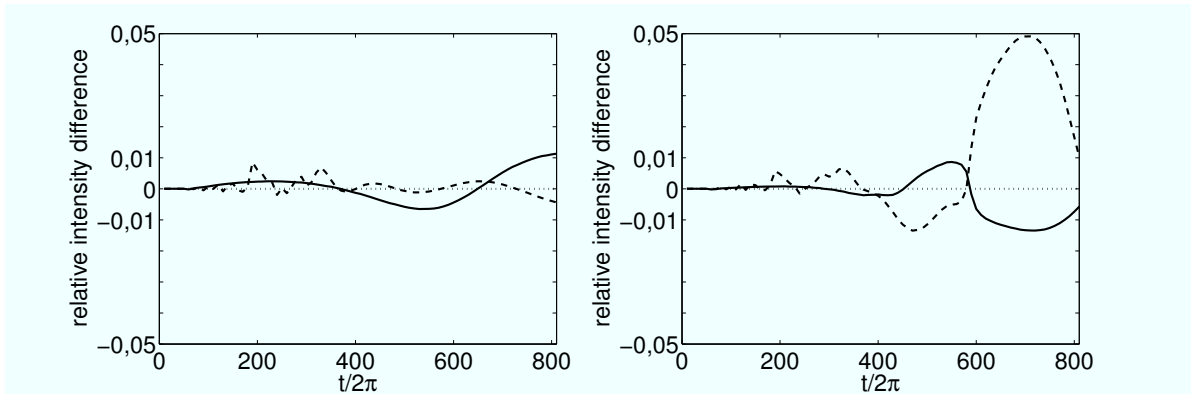


Figure 3.9: Relative difference in intensity to the reference solution of the reduced model for $a_0 = 0.1$ (left) and $a_0 = 0.12$ (right). Gautschi+QEA (see table 3.1, solid) and PIC (dashed) with $N = 2 \cdot 10^5$, $\tau = dz(N)$ and 3 particles per cell, runtime around 5 : 30 h.

Finally, we compare with PIC simulations performed with VLPL [55]. Since PIC simulates \mathbf{E} and \mathbf{B} instead of \mathbf{A} , we base our comparison on intensities, calculated by

$$I = \frac{1}{2} (|\mathbf{E}|^2 + |\mathbf{B}|^2) = \frac{1}{2} \left(\left| \frac{\partial}{\partial t} \mathbf{A} \right|^2 + \left| \frac{\partial}{\partial z} \mathbf{A} \right|^2 \right).$$

For the Gautschi-type method, one has to use (3.18) for the time-derivative, and for QEA $\partial/\partial z \rightarrow \partial/\partial z + i\kappa$. The difference in amplitudes between the reference solution

3.3. Accuracy and efficiency of the numerical scheme

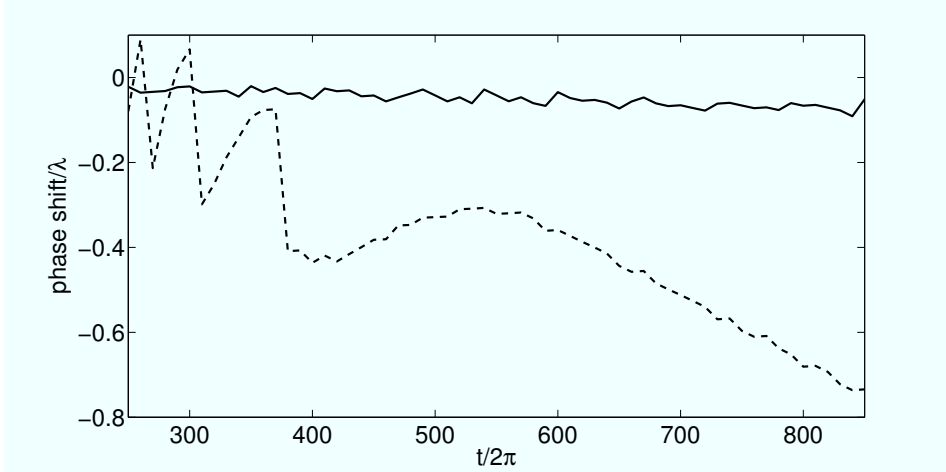


Figure 3.10: Phase-difference in terms of laser wavelength between the exact linear solution and PIC (dashed) and the exact linear solution and Gautschi+QEA (solid), both with $a_0 = 0.0001$.

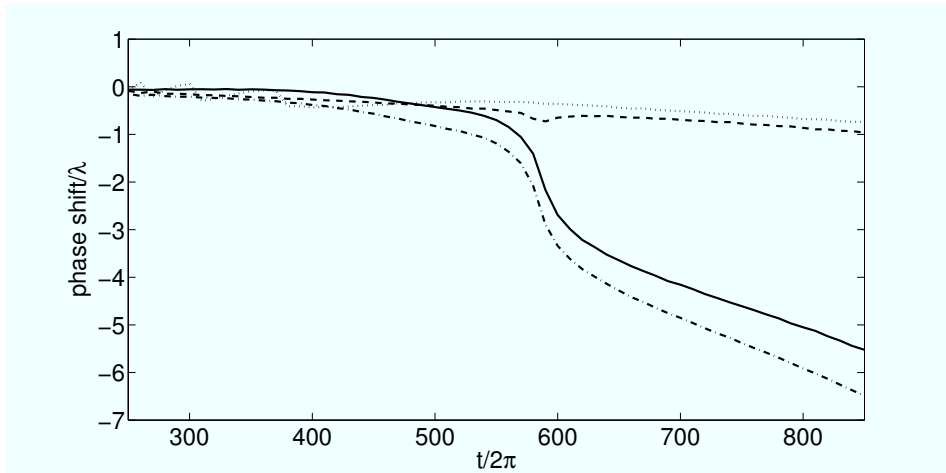


Figure 3.11: Phase-difference in terms of laser wavelength between the exact linear solution and PIC ($a_0 = 0.12$: dash-dotted and $a_0 = 0.0001$: dotted), exact linear solution and Gautschi+QEA ($a_0 = 0.12$, solid) and difference between PIC and Gautschi+QEA for $a_0 = 0.12$ (dashed).

for the reduced model and PIC (see Fig. 3.9) and the Gautschi-type method with QEA for the parameters given in table 3.1 are of the same order. This implies that, even with a relatively coarse discretization, the error of the simulations with our fastest solver is within the accuracy of the reduced model, which seems to be at the border of applicability at $a_0 = 0.12$.

We also noticed that there is a systematic difference in group velocity between PIC solutions and ours. To understand whether this is due to numerical error in PIC and/or our solvers, we made simulations with both for a very small amplitude ($a_0 = 0.0001$).

3. Pulse compression in one dimension

The combination of small amplitude and a cold plasma allows to test the phase error of the numerical simulations against the known linear analytical solution. The results in Fig. 3.10 show that PIC (dashed) produces a slight error in group velocity even on a fine grid, whereas Gautschi+QEA (solid) with coarse discretization is close to the exact solution.

In Fig. 3.11 we compare the phase shift (with respect to the exact linear solution) of VLPL (dash-dotted) and the Gautschi+QEA simulation from table 3.1 (solid) in the nonlinear case ($a_0 = 0.12$). The difference between the two (dashed) is consistent with the linear phase error of PIC (dotted). This shows that the difference in phase between nonlinear PIC and Gautschi+QEA is mostly linear phase error of PIC, which could also influence the accuracy of the amplitude calculation.

3.4 Pulse dynamics in 1D

3.4.1 Self compression threshold

As we have already seen in the example problems of section 3.3, a pulse with sufficient energy can overcome the dispersion of the plasma medium and self compress. This happens due to the nonlinearity caused by the relativistic mass increase of the electrons oscillating with the laser field. The energy threshold for the self-compression can be calculated simply from the single soliton solution of the cubic nonlinear Schrödinger equation (cubic NLSE), which is also a soliton solution to the (cubic) nonlinear wave equation (see section B.1 of the appendix) for which we discussed an efficient numerical scheme above. This threshold can also be derived from the NLSE via the variation-of-action method (VAM) with

$$a(\tau, \zeta) = A(\zeta) \sqrt{\frac{T_0}{T(\zeta)}} e^{-i\phi(\zeta)} e^{i\eta(\zeta)\tau^2} \operatorname{sech}\left(\frac{\tau}{T(\zeta)}\right) \quad (3.21)$$

as the trial function. Here $\eta(\zeta)$ is the linear chirp of the pulse.

The Lagrange density for the cubic NLSE is

$$\mathcal{L} = i\beta(a\partial_\zeta a^* - a^*\partial_\zeta a) + \frac{1-\beta^2}{\beta^2}(\partial_\tau a)(\partial_\tau a^*) - \frac{1-\beta^2}{4}|a|^4. \quad (3.22)$$

Inserting the trial function and integrating over τ yields

$$L = \frac{2(1-\beta^2)}{\beta^2} \frac{A^2}{T^2} - (1-\beta^2)A^4 \frac{T_0}{T} + \pi^2 \frac{2(1-\beta^2)}{\beta^2} A^2 T^2 + \pi^2 \beta A^2 T^2 \eta' - 12\beta A^2 \phi'. \quad (3.23)$$

Varying L for η and T and combining the two resulting equations leads to the following ordinary differential equation for the temporal length $T(\zeta)$ of the pulse

$$T''(\zeta) = -\frac{4(1-\beta^2)^2}{\pi^2\beta^6} \frac{1}{T^3(\zeta)} \left\{ \frac{\beta^2 A_0^2 T_0 T(\zeta)}{4} - 1 \right\} \quad (3.24)$$

3.4. Pulse dynamics in 1D

with T_0 the initial pulse length.

From this we immediately get the threshold value for the self compression: if the expression inside the parenthesis is larger than zero, the second derivative of $T(\zeta)$ is negative and the length decreases. An initial pulse that fulfills

$$A_0 T_0 \beta > 2 \quad (3.25)$$

will thus compress. The group velocity β enters into the threshold, because the temporal length of the pulse increases with decreasing group velocity. For the wave equation where a spatial distribution is propagated in time, the threshold takes the following form

$$A_0 L_0 > 2 \quad (3.26)$$

where L_0 is the initial spatial length of the pulse.

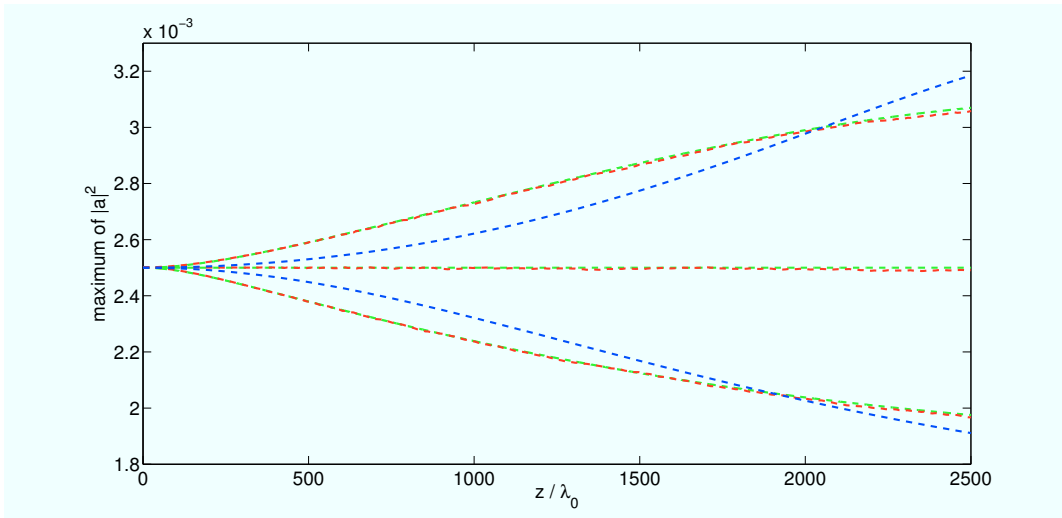


Figure 3.12: Amplitude evolution for solutions of the VAM model (blue), cubic NLSE (green) and cubic wave equation (red) for initial sech-pulses below, at, or above to the compression threshold. For VAM and NLSE the initial length are (from bottom to top) $T_0 = 7/\nu_0, 7.61/\nu_0, 8.2/\nu_0$ and for the cubic wave equation $L_0 = 5.857 \lambda_0, 6.37 \lambda_0, 6.86 \lambda_0$. Initial lengths are chosen according to (3.25) and (3.26) with $a_0 = 0.05$ and $n_0 = 0.3 n_c$.

As expected from true soliton solutions, the threshold values for both equations agree perfectly with numerics. The curves of intensity vs. propagation distance in Fig. 3.12 show that pulses directly at the threshold propagate unchanged. Slightly larger or smaller values compress or disperse respectively. But only slightly away from the threshold, the VAM model differs significantly from numerics. In part this is due to solutions of (3.24) being strictly periodic for $A_0 T_0 \beta > \sqrt{2}$ ¹. In reality a pulse with an energy between the one- and two-soliton state will over time radiate off the excess energy.

But also for a true periodic self compressing solution of the NLSE, the bound two-soliton state, there is no good agreement. A valid initial condition for the two-soliton

¹But with length of the period to infinity as $\sqrt{2}$ is approached.

3. Pulse compression in one dimension

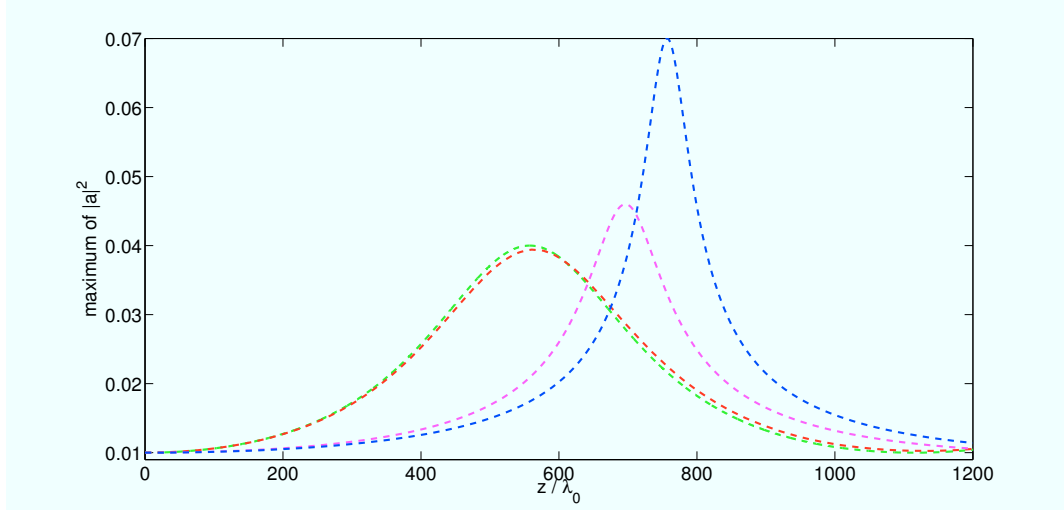


Figure 3.13: Amplitude evolution due to pulse compression for a two soliton state with $a_0 = 0.1$ and $n_0 = 0.3 n_e$. NLSE (green) with $T_0 = 7.61/\nu_0$, cubic wave equation (red) with $L_0 = 6.37 \lambda_0$ and VAM model with $T_0 = 6.37/\nu_0$ (magenta) and $T_0 = 7.61/\nu_0$ (blue).

state is simply a pulse with twice the single soliton amplitude. Simulation results and a comparison with the VAM prediction can be seen in Fig. 3.13. For the correctly chosen initial pulse length, the VAM model shows no agreement with the numerics for the NLSE and the nonlinear wave equation, neither with respect to the maximum amplitude, nor the position of the maximum.

An equivalent equation can be derived for a Gaussian-shaped initial pulse, which is closer to the pulse shape that is produced by real laser systems. Here we can not derive the threshold from a steady state solution, because a Gaussian pulse is not a time-independent solution of either the NLSE or nonlinear wave equation. For an initial condition for the NLSE of

$$a(\tau, \zeta) = A(\zeta) \sqrt{\frac{T_0}{T(\zeta)}} e^{-i\phi(\zeta)} e^{i\eta(\zeta)\tau^2} e^{-\frac{\tau^2}{T(\zeta)^2}} \quad (3.27)$$

we have

$$T'''(\zeta) = -\frac{4(1-\beta^2)^2}{\beta^6} \frac{1}{T^3(\zeta)} \left\{ \frac{\beta^2 A_0^2 T_0 T(\zeta)}{8\sqrt{2}} - 1 \right\} \quad (3.28)$$

as the evolution equation of the pulse length. It is equivalent to the equation derived in [56] and in [59] by means of the momentum method and also to the equation used to describe dispersion managed solitons in fiber optics [64]. It has the same form as (3.24) but differs in two respects. The factor outside the parenthesis is larger by a factor of π^2 , so both nonlinear and dispersive effects act on a shorter length scale. The threshold value is different, too

$$A_0 T_0 \beta = A_0 L_0 > \sqrt{8\sqrt{2}}. \quad (3.29)$$

The reason for this differences is on the one hand of course the different shape. But more importantly the two shapes have different half width for same value of the length

3.4. Pulse dynamics in 1D

parameter T_0 . The factor between T_0 and the half width for a Gaussian pulse is $\sqrt{\ln(2)} \approx 0.8$ while for a sech-shaped pulse it is $\text{sech}^{-1}(1/2) \approx 1.3$. For the same T_0 the half width of the two shapes thus differ by a factor of ≈ 1.582 which is close to the difference of the thresholds.

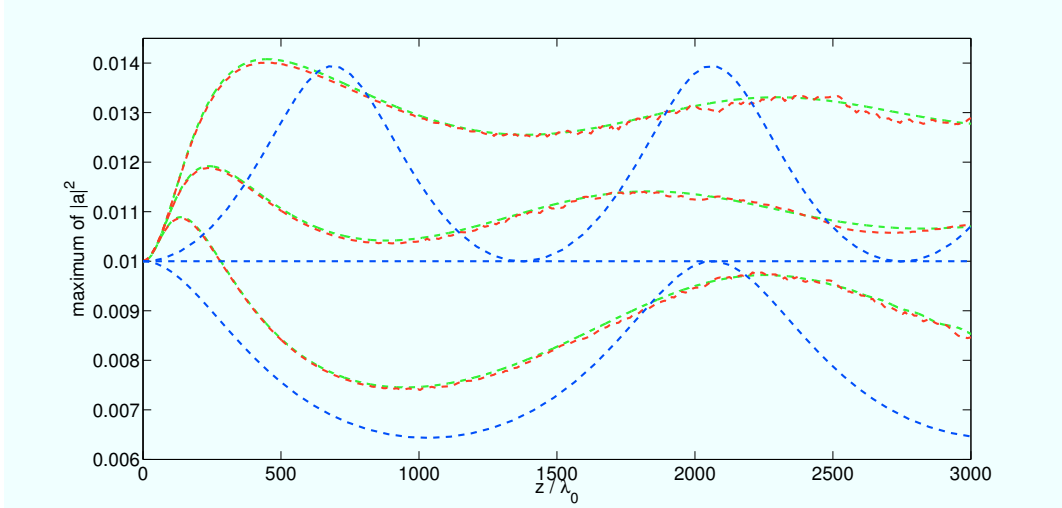


Figure 3.14: Amplitude evolution for solutions of the VAM model (blue), cubic NLSE (green) and cubic wave equation (red) for initial Gaussian pulses below, at, or above to the compression threshold. For VAM and NLSE the initial length are (from bottom to top) $T_0 = 5.8/\nu_0, 6.4/\nu_0, 7/\nu_0$ and for the cubic wave equation $L_0 = 4.85 \lambda_0, 5.35 \lambda_0, 5.86 \lambda_0$. Initial lengths are chosen according to (3.29) with $a_0 = 0.1$ and $n_0 = 0.3 n_c$.

Comparing the compression threshold with numerics for a Gaussian pulse yields not a result as clear as for the soliton shaped pulse discussed above. A pulse at the analytical compression threshold (3.29) does not propagate unchanged, because it will change its shape towards a soliton during propagation. The periodicity of the VAM solution vs. the non-periodicity of the numerical solutions is shown in Fig. 3.14. Still, the VAM derived threshold seems to predict sufficiently well if a pulse will show self compression or dispersion.

Considering again an initial condition with a (nearly) periodic behavior for this pulse shape, we conclude from Fig. 3.15 that, as in the case of the truly periodic two-soliton solution, the VAM model does not match the numerical results well. Only for the incorrect choice of $T_0 = L_0$ the maximum amplitudes are close. This choice also improves the agreement for the sech pulse shape, cf. the magenta curve in Fig. 3.13. The same parameters were used for the comparison in [59] to 1D PIC and good agreement was stated. In this comparison the pulse was initially in vacuum.

In conclusion the VAM model is useful to predict general compression vs. dispersion behavior of a pulse, but is unable to describe the dynamics correctly. This is in contrast to the very weakly nonlinear case for dispersion management in fiber optics, where the agreement is excellent. Including the full γ -nonlinearity and the n_e^1 -equation does not change the thresholds for low initial amplitudes.

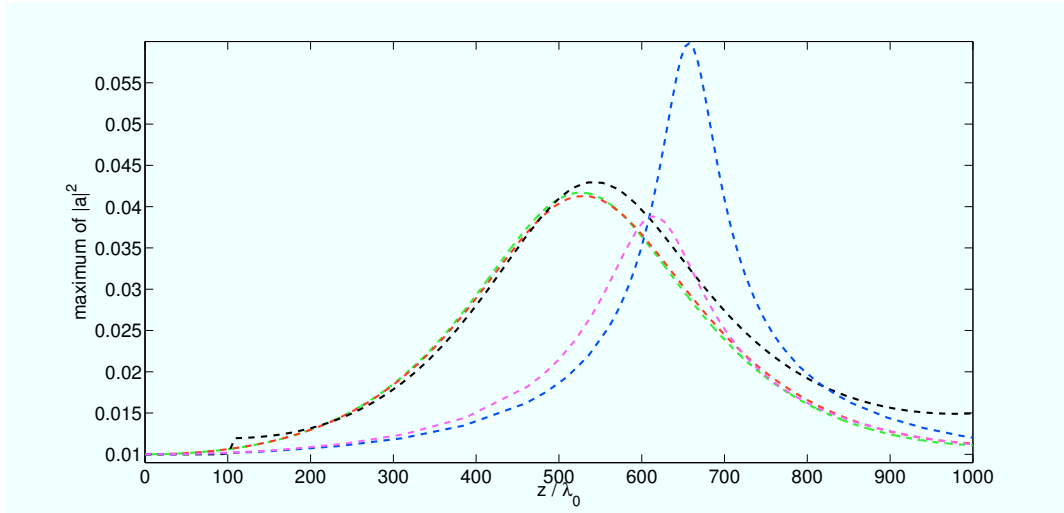


Figure 3.15: Amplitude evolution due to pulse compression for a Gaussian pulse close to a two soliton solution for $n_0 = 0.3n_c$ and $a_0 = 0.1$. NLSE (green) with $T_0 = 11.95/\nu_0$, cubic wave equation (red) with $L_0 = 10\lambda_0$, VAM model with $T_0 = 10/\nu_0$ (magenta) and $T_0 = 11.95/\nu_0$ (blue). Shown in black is a simulation of the cubic wave equation with the same parameters as used for the red curve, but including the transition of the pulse from vacuum to plasma.

3.4.2 Pulse amplitude vs. length

Above the compression threshold the strength and speed of the self compression varies with the initial amplitude and length of the pulse. First we consider pulses that have the same total energy with different initial amplitude and length, i.e. the same value of $a_0^2 L_0$. From (3.28) we immediately see that a larger initial length will lead to slower compression behavior that scales with L_0^2 [56]. The interesting question is whether they show the same amount of relative compression, i.e. that the length decreases by the same relative amount the amplitude increases. In Fig. 3.16 we can see on the left that initially longer pulses reach a higher maximum amplitude relative to a_0 , because the minimal length reached is nearly equal (right side of Fig. 3.16). This is even more clearly visible in Fig. 3.17 for pulses with the same initial amplitude, but different L_0 . A larger value of L_0 leads to a larger absolute value for the maximum amplitude. The minimum length reduces slightly with increasing initial length, but this effect quickly saturates. The same effect occurs for a constant initial length and increasing a_0 , as can be seen in Fig. 3.18. Higher values of a_0 lead to lower a minimum length, but this effect quickly saturates, too.

For the dynamics up to the first compression maximum, varying amplitude and length only change the time scale and maximum amplitude of the compression. The principal form of the amplitude evolution with time is unchanged (but see the next section about plasma density with respect to high amplitudes). After the first maximum of self-compression, the dynamics strongly depends on the ratio of pulse energy to single soliton energy. The same is true for the inclusion of the n_e^1 -equation. Up to the first maximum in intensity the compression changes only quantitatively not qualitatively,

3.4. Pulse dynamics in 1D

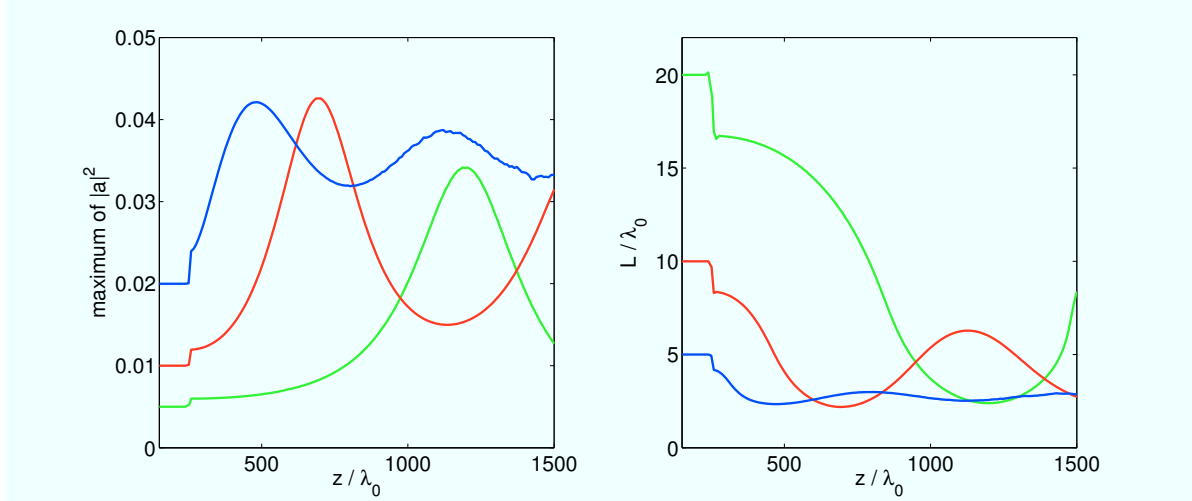


Figure 3.16: Amplitude evolution of wave equation simulations with γ -nonlinearity and $n_0 = 0.3 n_c$. Pulses with the same value of $a_0^2 L_0$. $a_0 = 0.1/\sqrt{2}$, $L_0 = 20 \lambda_0$ (green), $a_0 = 0.1$, $L_0 = 10 \lambda_0$ (red) and $a_0 = 0.1 \sqrt{2}$, $L_0 = 5 \lambda_0$ (blue).

Raman instability not considered. After the maximum, the dynamic differs in so far, that a true splitting of the pulse in several pulses that propagate with different velocities can occur. The difference in group velocity due to the relativistic nonlinearity alone is still too weak to drive pulses apart for the amplitudes considered here. For most amplitude / length combinations that have three or more times the single soliton energy, the pulse splits into a single short pulse with a high amplitude, and one or more smaller pulses. The the dominant short pulse then propagates over long distances with smaller and smaller oscillations in amplitude and thus seems to be close to a soliton, but with large energy loss to the plasma due to the large ponderomotive force it exerts.

3.4.3 Influence of plasma density

In the preceding sections we have used a plasma density of $n_0 = 0.3 n_c$ for the plasma background density as a standard value. In this section we will discuss why this is a sensible choice and what advantages and disadvantages other values for the background density have. We will also examine the influence of the equation for n_e^1 on simulation results depending on the background density. We will mostly restrict the discussion to density values larger than quarter critical.² The density range lower than quarter critical will be discussed in the section about Raman instability below.

Without a vacuum-plasma boundary and neglected density response, there is no change in the maximum amplitude reached by the self-compression when varying the

²Densities higher than $\frac{1}{4} \frac{n_0}{n_c}$ have been difficult to realize in experiments for $\sim 1 \mu\text{m}$ lasers, but are now routinely achieved through supersonic gas expansion, where a gas under high pressure (up to 100 bar) flows through a specially formed nozzle and expands in vacuum about 10 times and reaches velocities of about Mach 3 [54].

3. Pulse compression in one dimension

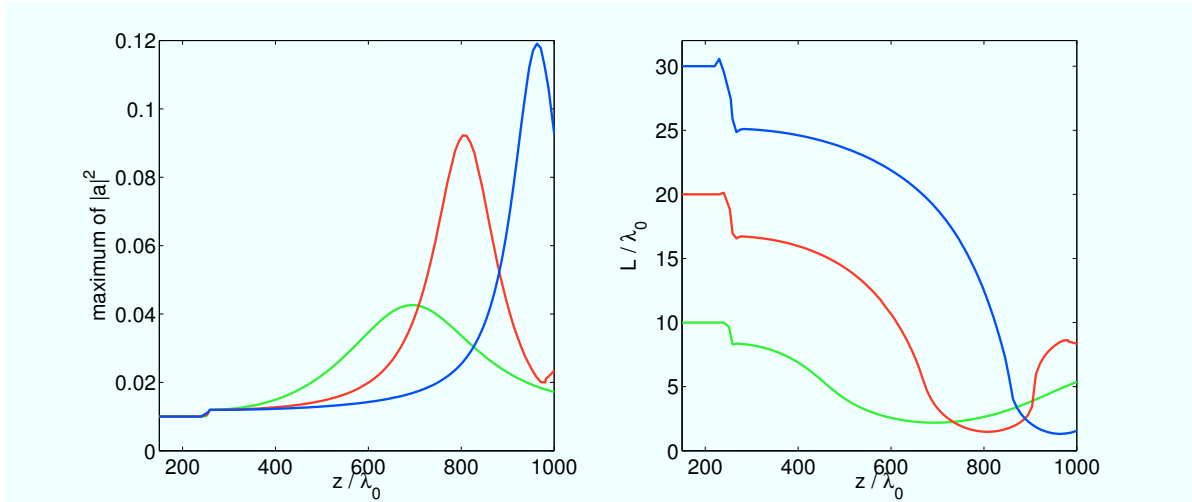


Figure 3.17: Amplitude evolution of wave equation simulations with γ -nonlinearity and $n_0 = 0.3 n_c$. Pulses with the same $a_0 = 0.1$ but different L_0 . $L_0 = 10 \lambda_0$ (green), $L_0 = 20 \lambda_0$ (red) and $L_0 = 30 \lambda_0$ (blue).

background density. Only the length (and time) scale over which the compression occurs changes proportional to $\sqrt{n_0/n_c}$, which can easily be seen by setting n_e^1 to zero in the wave equation and rescaling z and t . Numerical simulations confirm this density independent compression behavior. For the same reason the density value does not enter the soliton solution in appendix B.1.

Including the density response results in stronger compression and higher maximum amplitudes. Lower background densities show more gain than higher densities in this respect, thus the strength of the compression varies with the plasma density. We can understand this by neglecting the time derivative in the n_e^1 -equation and solving for n_e^1 . The local density perturbation then is the second space derivative of γ with a factor n_c/n_0 in front. Increasing the amplitude for a pulse with constant length shows that this effect reverses for higher amplitudes. At lower densities the wakefield excitation is stronger and thus more energy is transferred to the plasma which neglects the aforementioned effect. At a pulse length of $L_0 = 10 \lambda_0$ the breakeven for $n_0 = 0.3 n_c$ is around $a_0 = 0.14$. For low densities smaller than $0.25 n_c$ this is even the case for relatively low pulse energies. For higher energies Raman instability severely limits pulse compression.

If the pulse propagates from vacuum into the plasma, two additional effects become important. The part of the pulse spectrum below the plasma frequency can not propagate into the plasma. Even if reflections are suppressed by using a soft boundary with a linear increase over several λ_0 , this modes can not enter the plasma. Because the plasma frequency increases with density, this is a disadvantage for higher densities. But for most densities this is only visible at low amplitudes below $a_0 = 0.1$. Otherwise it is compensated by the relativistic mass increase that locally lowers ω_p , this is called self-transparency.

The other effect that occurs during the transition from vacuum to plasma is that the

3.4. Pulse dynamics in 1D

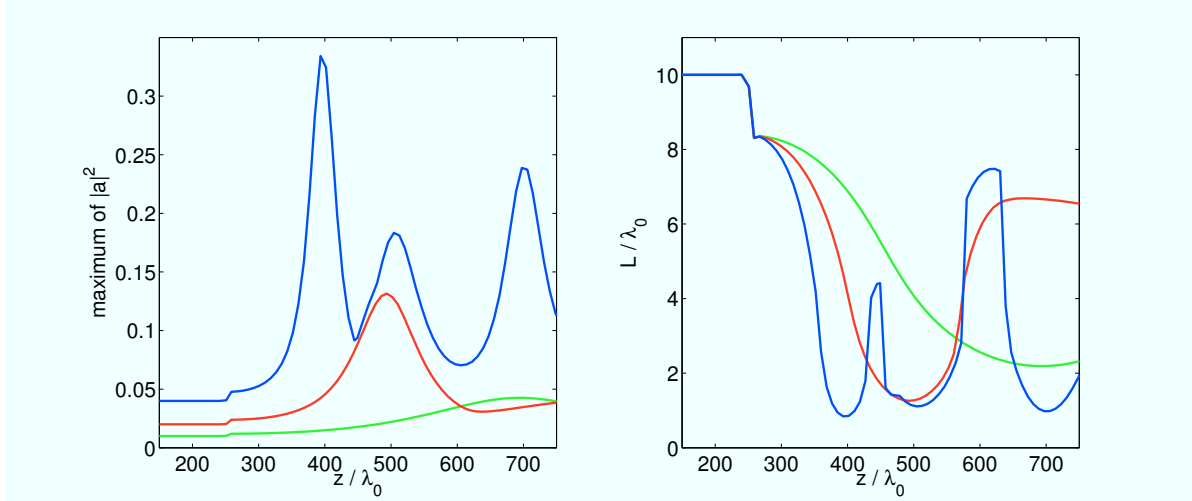


Figure 3.18: Amplitude evolution of wave equation simulations with γ -nonlinearity and $n_0 = 0.3 n_c$. Pulses of the same length $L_0 = 10 \lambda_0$, but different amplitude. $a_0 = 0.1$ (green), $a_0 = 0.14$ (red) and $a_0 = 0.2$ (blue).

carrier wavenumber is downshifted by a factor of β . Because the pulse is shortened, the amplitude increases accordingly, which in turn enhances the self compression, the more the higher the density. Combined with ponderomotive effects modelled by the n_e^1 -equation, this favors densities in the medium range. They also have the advantages that Raman instability is prohibited and the compression lengths are sufficiently long to be implementable in gasjet experiments. A disadvantage of this density range is that losses to the wakefield limit the initial intensity to lower values than possible for higher densities. At higher amplitudes, this can have a similar effect on the compression efficiency as Raman instability although no resonant unstable process occurs.

3.4.4 Relativistic intensities

In the last section we have seen that the density range just above quarter critical can only sustain efficient pulse compression for initial intensities below $a_0 \sim 0.2$. Can this problem be overcome by using higher densities (although the compression length would then be extremely small)? This question can not be answered with certainty by simulations of our model equations, because they are becoming invalid for large density oscillations caused by high pulse intensities. But it is interesting to test, if without strong density excitations, large initial amplitudes would become usable. As can be seen in Fig. 3.19 for a simulation with $a_0 = 0.5$ and without including the n_e^1 -equation, this is not the case. Because the nonlinearity is an order of magnitude larger than the dispersion, the pulse peak travels distinctly faster than the front and a shock forms. After the shock formation, the pulse filaments at the back due to relativistic self-phase modulation³,

³Self-phase modulation consists of two distinct effects, longitudinal bunching and photon acceleration (local increase of ω_0), see [50] for details.

3. Pulse compression in one dimension

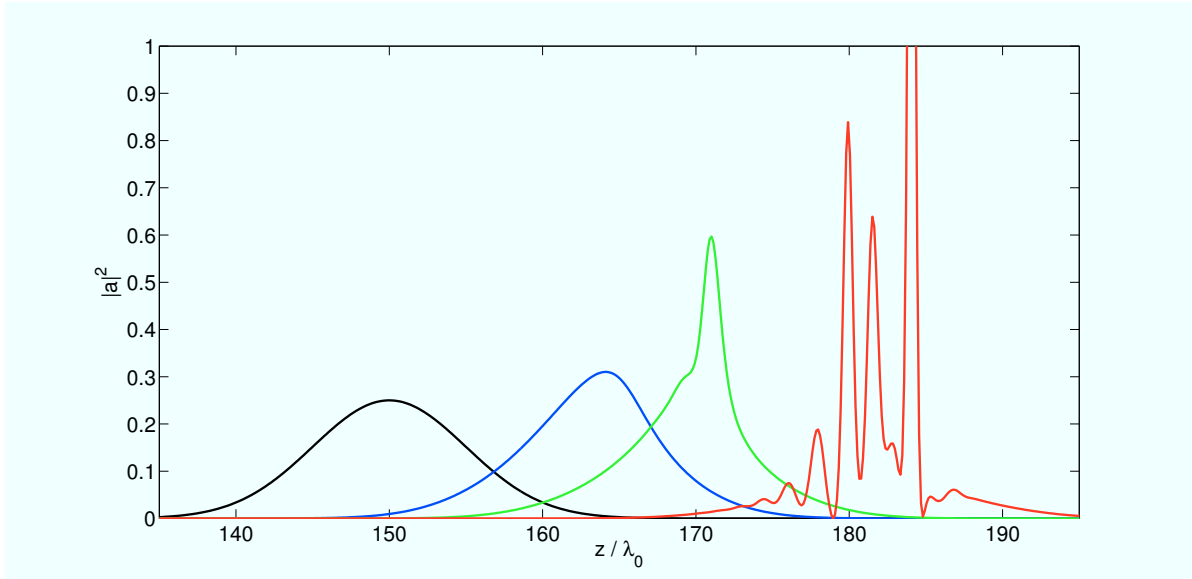


Figure 3.19: High amplitude ($a_0 = 0.5$) simulation with only γ -nonlinearity for a density of $n_0 = 0.6n_c$ and a pulse length of $10\lambda_0$. The initial pulse (black) was placed directly inside the plasma. Snapshots are taken at $t = 20/\nu_0$ (blue), $t = 30/\nu_0$ (green) and $t = 50/\nu_0$ (red).

which is only strong enough for relativistic amplitudes. Thus effective compression is prevented. With inclusion of the n_e^1 -equation, the system becomes unstable, because there is no saturation mechanism for the density oscillations. This instability is even more violent at high densities.

To answer the question, if there maybe nonlinear effects at higher intensities that keep the wakefield amplitude in control, we resort to PIC simulations with the 1D VLPL code. In Fig. 3.20 the result of such a simulation with $a_0 = 0.5$ and $n_0 = 0.6n_c$ shows that a part of the pulse are reflected, a part is trapped⁴ and only lower amplitude noise propagates through the plasma. Results for other densities above $n_0 = 0.25n_c$ or a higher a_0 equal or larger than unity show similar destruction of the pulse. The processes that are responsible for the fast destruction and depletion of short ultrarelativistic pulses are described in detail in [7]. Only at very low densities the pulse can propagate and compress slightly over some distance, but is then inevitably filamented by Raman instability.

So far the only known effect that allows stable propagation for high intensity pulses over a finite distance in all density regimes is bubble formation [20]. This is because of ultra relativistic self similarity, where the scale parameter of the system is no longer simply n_0/n_c , but $S = n_0/(a_0 n_c)$ [25]. Once the pulse has created a cavitation bubble free of electrons, it can propagate inside at c , while the front is still in plasma, propagating with the corresponding group velocity, thus compressing the pulse. No filamentation due to the wakefield is possible. But the cavitation process of course constantly transfers energy from the front of the pulse to the plasma. The most interesting consequence of

⁴This trapping occurs despite the plasma being underdense, this effect is described in [7].

3.4. Pulse dynamics in 1D

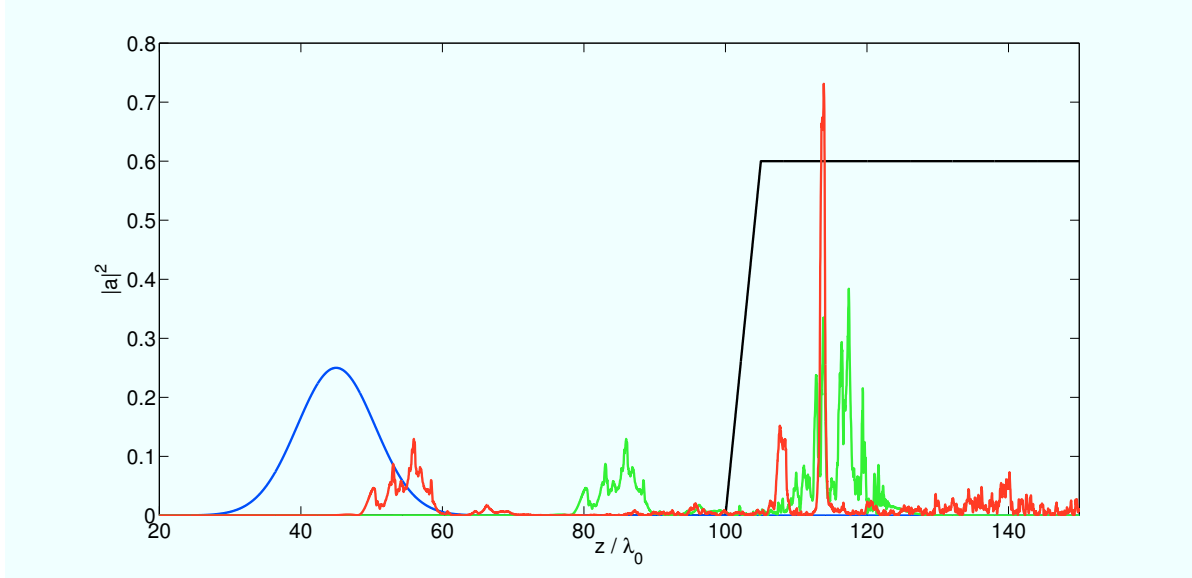


Figure 3.20: 1D PIC simulation using the VLPL code for $a_0 = 0.5$, $L_0 = 10 \lambda_0$ and $n_0 = 0.6 n_c$. The initial pulse (blue) is in vacuum and enters the plasma through a linear density ramp of $5 \lambda_0$ (density profile in black). Snapshots at $t = 90/\nu_0$ (green) and $t = 120/\nu_0$ (red).

this is the acceleration of electrons to high energies [19, 48]. Efficient pulse compression in the plasma is thus limited to weakly relativistic amplitudes, both initially and at the maximum of compression.

3.4.5 Wakefield generation and Raman instability

A short laser pulse exerts a very localized ponderomotive force on the plasma that leads to a density deprivation at the location of the pulse. The actual form of the density perturbation due to the pulse can be deduced from the equation for n_e^1 by neglecting the time derivative

$$n_e^1 = \frac{n_c}{n_0} \Delta \gamma \approx \frac{1}{2} \frac{n_c}{n_0} \Delta |a|^2 .$$

thus the shape of the perturbation simply is the second spatial derivative of the laser envelope. Behind the laser pulse the plasma oscillates at the plasma frequency. The pulse must fulfill a certain requirement [23, 45] to induce oscillations with a finite amplitude compared to the background density

$$k_p L \sim \mathcal{O}(1),$$

where k_p is the wavenumber of the plasma and L is the pulse length. Since the pulse that acts as the driver for the oscillations propagates through the plasma with the velocity $v_g = \sqrt{1 - n_0/n_c}$, the oscillations have v_g as their phase velocity and a wavelength of v_g/ω_p . This phenomenon is called the wakefield of the pulse and for a cold plasma it has zero group velocity.

3. Pulse compression in one dimension

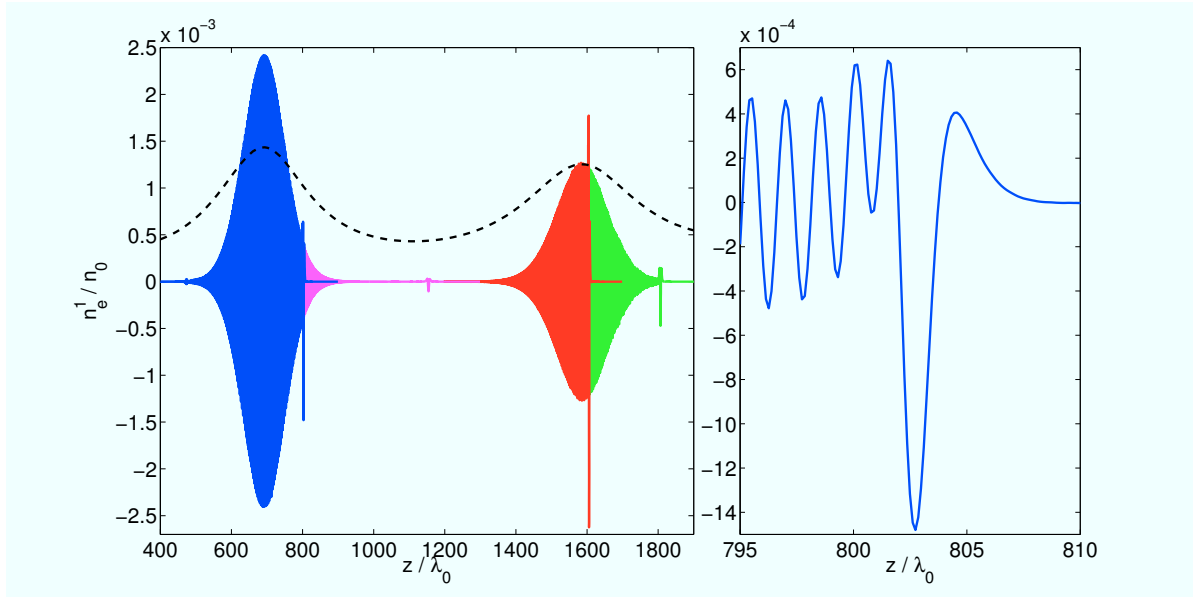


Figure 3.21: Wakefield for a Gaussian pulse with $a_0 = 0.1$ and $L_0 = 10 \lambda_0$ for $n_0 = 0.3 n_c$. The wakefield on the left hand side is pieced together from snapshots at different times. On the right hand side is a magnified section of the blue curve on the left.

A periodically compressing pulse can in this way produce a localized wakefield with the maximum amplitude of the oscillations at the maximum of compression, as shown in Fig. 3.21. If the intensity of the pulse is sufficient to induce a density cavity that partially traps the pulse and prevents the decompression, the wakefield becomes continuous until the pulse energy is depleted.

The most interesting application of wakefields is electron acceleration [18, 32, 21], also called laser wakefield acceleration (LWFA). Not included in our model equation for the electron density, is the breaking of the wakefield [11, 35, 45]. If the plasma wave breaks, the density gradients become infinite and particles start to overtake the wave. This can be used for self injection of electrons into the wakefield for acceleration purposes. Although relativistic wakefields will eventually break for any amplitude [45], for low relativistic amplitudes this will happen after many oscillations and thus occurs far behind the laser pulse without influence on the propagation of the pulse. In the 1D PIC simulations we performed for weakly relativistic amplitudes, we did not observe the generation of fast electrons.

Through stimulated Raman forward scattering (RFS) a resonant instability between the laser pulse and the wakefield can occur [2, 51, 49]. Forward scattering here means that the laser radiation scattered at a density perturbation still propagates in the same direction as the laser pulse as opposed to backward scattered radiation. Due to this scattering process, for a sinusoidal wakefield the laser energy lumps at the density minima. The laser radiation is scattered from the density maxima in front (sideband with

3.4. Pulse dynamics in 1D

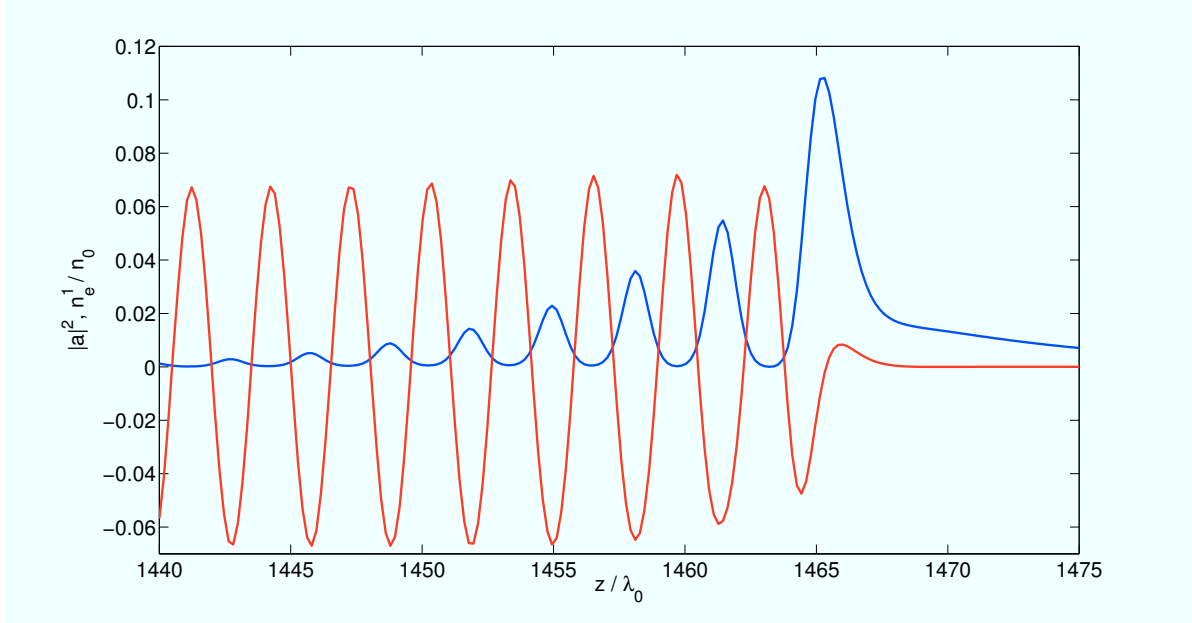


Figure 3.22: Pulse filamentation due to Raman instability for a laser pulse of $a_0 = 0.14$, $L_0 = 20 \lambda_0$ and $n_0 = 0.1 n_c$. $|a|^2$ in blue and n_e^1/n_0 in red.

$\omega_0 - \omega_p$) and behind a minimum towards the density minimum (sideband with $\omega_0 + \omega_p$).⁵ This results in a filamentation of the pulse, even for a short pulse as long as its length exceeds the wavelength of the wakefield. E.g. for a density of $n_0 = 0.1 n_c$ we have a wavelength of the wakefield of $3 \lambda_0$. The pulse in Fig. 3.22 with an initial length of $20 \lambda_0$ shows strong filamentation at its back. Because $\omega_0 - \omega_p > \omega_p$ to allow propagation of the lower sideband inside the plasma, the scattering process can only become resonant for $\omega_0 > 2\omega_p$. Thus the condition

$$\frac{\omega_p^2}{\omega_0^2} = \frac{n_0}{n_c} < \frac{1}{4}$$

for the plasma density to allow for this type of instability.

⁵In this picture it is also obvious why there is a phase shift of $\pi/2$ between the Raman filaments and the maxima of the density, as it is the case for every resonantly driven harmonic oscillator.

4 Pulse compression in two dimensions

In this chapter we will investigate transversal effects in the relativistic self-compression of laser pulses. We will first generalize the numerical methods discussed in chapter 3 to two dimensions. Since the numerical method used has very low noise, we can study pulse evolution without transversal filamentation, because noise at the unstable wavelengths is necessary to seed the instability. We discuss how the additional degree of freedom changes the pulse dynamics inside an infinite plasma slab depending on the transversal shape and spot size of the pulse vs. its length. This allows us to identify useful parameter ranges for 2D pulse compression. Because a real laser pulse will likely show transversal filamentation inside a plasma, we then examine in detail how the strength and spectrum of transversal perturbations influence the growth of this instability.

4.1 Numerical Methods

In chapter 3 we used a Gautschi-type exponential integrator for the time-integration of the one-dimensional problem and we presented comparisons which showed that such trigonometric integrators outperform the standard leap-frog method for this particular application. For the spatial discretization we introduced the so-called quasi-envelope approach (QEA) to reduce the number of spatial grid points significantly.

In the following sections, that are based on [40], we will generalize the numerical techniques to the two-dimensional case. This means we aim to solve the coupled equations (2.34) and (2.33) with a two dimensional Laplace operator in either a Cartesian geometry with z, x -parameterization or cylindrical geometry in z, r -parameterization. However, in contrast to the one-dimensional case, where a two-step implementation of the Gautschi-type exponential integrator with constant step size turned out to be sufficient, it is essential to enable changes of the time step-size for the two-dimensional case. We will therefore suggest use a one-step version of the Gautschi-type method [28, 29]. An error analysis for the whole family of these methods is given in [27]. In particular, it was shown that these methods are second order accurate independent of the highest frequencies arising in the system.

The main computational effort for one time step with an exponential integrator arises from the computation or approximation of the product of a matrix function with a vector. In the one-dimensional case, the proposed pseudospectral discretization enabled the use of fast Fourier transformation. This led to an implementation where the overhead compared to the leap-frog method was quite low. The situation changes completely in

two space dimensions. We therefore use the full two-dimensional Laplacian within the matrix functions only in vacuum, where huge time steps can be performed and higher costs pay off. During propagation in plasma, we split the Laplacian into a transversal and a longitudinal direction and use only the (one-dimensional) longitudinal direction with the matrix functions. This splitting is justified by physical properties of the solution.

Nevertheless, for large problems it can be necessary to parallelize the scheme. A key observation is that the parallelization has to be adapted to the different variations of the integrator being applied in different regions during the simulation (e.g. vacuum, plasma, and transition regions).

4.1.1 One step Gautschi-type exponential integrator for time discretization

After semi discretization in space (cf. Sec. 3.2.1), we obtain a system of second order ordinary differential equations of the form

$$\ddot{y}(t) = -\Omega^2 y(t) + F(y(t)) \quad (4.1)$$

where Ω^2 is a symmetric, positive semi-definite matrix and $\|F\|$, $\|F_y\|$, $\|F_{yy}\|$ and $\|y'\|^2 + \|\Omega y\|^2$ are bounded. For the solution we suggest to apply the following family of numerical schemes [30, 28]

$$y_{n+1} = \cos(h\Omega) y_n + h \operatorname{sinc}(h\Omega) \dot{y}_n + \frac{1}{2} h^2 \Psi F(\Phi y_n) \quad (4.2a)$$

$$\dot{y}_{n+1} = -\Omega \sin(h\Omega) y_n + \cos(h\Omega) \dot{y}_n + \frac{1}{2} h \left(\Psi_0 F(\Phi y_n) + \Psi_1 F(\Phi y_{n+1}) \right). \quad (4.2b)$$

Here,

$$\Phi = \phi(h\Omega), \quad \Psi = \psi(h\Omega), \quad \Psi_0 = \psi_0(h\Omega), \quad \Psi_1 = \psi_1(h\Omega),$$

where $\phi, \psi, \psi_0, \psi_1$ are even and analytical functions which are bounded on the non-negative real axis satisfying

$$\phi(0) = \psi(0) = \psi_0(0) = \psi_1(0) = 1.$$

To obtain a scheme with certain desirable properties imposes constraints on the choice of these functions. For instance, a scheme is symmetric if and only if

$$\psi(\xi) = \operatorname{sinc}(\xi) \psi_1(\xi) \quad \text{and} \quad \psi_0(\xi) = \cos(\xi) \psi_1(\xi)$$

and symplecticity is equivalent to

$$\psi(\xi) = \operatorname{sinc}(\xi) \phi(\xi).$$

Moreover, Hairer and Lubich [28] proved that for $\Omega = \omega I$, $\omega > 0$ and $F(y) = By$ with constant B , the energy is conserved up to $O(h)$ for all values of $h\omega$ if and only if

$$\psi(\xi) = \operatorname{sinc}^2(\xi) \phi(\xi) \quad (4.3)$$

4. Pulse compression in two dimensions

Thus, there is no scheme in this family, which is symplectic *and* gives good energy conservation.

In [27], Grimm and Hochbruck derived criteria, which guarantee second order accuracy independent of the eigenvalues of Ω . They suggested to choose

$$\psi(\xi) = \text{sinc}^3(\xi), \quad \phi(\xi) = \text{sinc}(\xi), \quad (4.4)$$

which results in a symmetric second order scheme satisfying (4.3). We use this choice of functions for our implementation.

Note that linear problems with $F \equiv 0$ are solved exactly by all these schemes. This allows to use arbitrarily large time steps for the propagation in vacuum. For the propagation inside of the plasma layers, smaller time steps have to be used to obtain the desired accuracy. This change of time steps would be much more complicated for the two-step method discussed in the preceding chapter. Moreover, the equivalent one-step variant of this scheme does not have the favorable energy conservation property.

4.1.2 Implementation of exponential integrators

For a Gautschi-type time integration scheme, the main effort per time step is the evaluation or approximation of the products of certain matrix functions of the discretized Laplacian Ω with vectors. It is indispensable to do this in an efficient way. The computational cost of each time step is thus closely related to the spatial discretization.

For one-dimensional problems with periodic boundary conditions, the method of choice is using spectral discretization, in which case the matrix Ω is diagonalizable via one-dimensional Fourier transformations.

It is not necessarily sensible to generalize this form of discretization to two space dimensions. Recall that a two-dimensional Fourier transformation on a grid consisting of $N_z \times N_x$ grid points can be evaluated using $O(N_z N_x (\log N_z + \log N_x))$ operations. For large grids, this may become too expensive. In addition, on parallel machines, such transformations become inefficient due to the large communication effort because of the non-locality of the Fourier transform.

In general, diagonalization of a large matrix Ω resulting from finite difference or finite element discretization is impossible. An alternative is to use Krylov subspace methods such as the symmetric Lanczos process [12, 33]. However, for the applications considered here such techniques are not competitive.

Therefore, we will use different spatial discretization in different regimes depending on physical properties of the solution. Moreover, we alter the splittings in (4.1) during the time integration, i.e. we move parts of the discretized Laplacian into the function F . This allows for an efficient evaluation of the matrix functions.

Cartesian coordinates in vacuum

In vacuum we only need to solve the linear wave equation

$$\frac{\partial^2}{\partial t^2} a = \frac{\partial^2}{\partial z^2} a + \frac{\partial^2}{\partial x^2} a . \quad (4.5)$$

4.1. Numerical Methods

For periodic boundary conditions the semi-discretization in space is done by a pseudo-spectral method with N_z Fourier modes on the interval $z \in z_0 + [-L_z, L_z]$ in propagation direction and N_x modes on the interval $x \in [-L_x, L_x]$ in perpendicular direction.

Let $a = a(t) \in \mathbb{C}^{N_z \times N_x}$ and $\dot{a} = \dot{a}(t) \in \mathbb{C}^{N_z \times N_x}$ be complex matrices containing approximations to the vector potential and its time derivative on the grid,

$$a_{i,j} \approx a(x_j, z_i, t), \quad \dot{a}_{i,j} \approx \frac{\partial}{\partial t} a(x_j, z_i, t).$$

The Laplacian is approximated by

$$\Delta a \approx \mathcal{F}_{N_z}^{-1} D_z^2 \mathcal{F}_{N_z} a + a \mathcal{F}_{N_x}^T D_x^2 \mathcal{F}_{N_x}^{-T}$$

where

$$D_k = \frac{2\pi i}{L_k} \text{diag} \left(-\frac{N_k}{2}, \dots, \frac{N_k}{2} - 1 \right), \quad k = x, z,$$

and \mathcal{F}_N denotes the discrete Fourier transform for N Fourier modes.

Formally, the matrices a and \dot{a} can be reorganized by writing them column wise into long vectors. Then the spatially discretized equation (4.5) can be written as a system of differential equations (4.1), where Ω is a matrix which can be diagonalized via two-dimensional fast Fourier transforms and $F \equiv 0$. However, for the implementation, the matrix notation is more efficient.

In the first time step, where the initial data is given in physical space, we start by performing a two-dimensional Fourier transform by applying fast (one-dimensional) Fourier transforms to all columns and rows of a and \dot{a} . Then we evaluate the functions arising in the Gautschi-type integrator at the diagonalized operator. The resulting operator can be applied to the matrices a and \dot{a} by pointwise multiplication. (If desired, subsequent time steps in vacuum can be computed in frequency space by diagonal operations only.) At times, where the solution is required in physical space, inverse Fourier transforms have to be applied to all rows and columns of a and \dot{a} again.

Due to the Gautschi-type integrator being exact in vacuum, in the best case we only have to compute one time step. The total cost amounts to two two-dimensional Fourier transforms and in addition four scalar multiplications per grid point. Storage is required for two arrays for a and \dot{a} plus four arrays for the diagonalized matrix functions of the same size. If a reduction of storage is necessary, the matrix functions can be computed on demand. From the computational point of view, this is a rather small overhead compared to the two-dimensional Fourier transforms.

Cartesian coordinates in plasma

In plasma layers we have to solve the full, nonlinear system of equations

$$\frac{\partial^2}{\partial t^2} a - \frac{\partial^2}{\partial z^2} a - \frac{\partial^2}{\partial x^2} a = -\frac{n_0}{n_c} \frac{n_e^0 + n_e^1}{\gamma} a \tag{4.6a}$$

$$\frac{\partial^2}{\partial t^2} n_e^1 + \frac{n_0}{n_c} n_e^0 n_e^1 = n_e^0 \Delta \gamma. \tag{4.6b}$$

4. Pulse compression in two dimensions

After space discretization, the linear part is represented by a 2×2 block diagonal matrix, whose upper diagonal block contains the discretized Laplacian and whose lower diagonal block contains the diagonal operator of the second equation. Hence, the matrix operators required for the time integration scheme can be computed separately for both equations. Note that due to the nonlinearity, we need to compute (and store) more matrix operators than in vacuum. The main costs of one time step in frequency domain amounts to two two-dimensional Fourier transformations.

Due to the nonlinearity, the time-integration scheme does not solve the the discretized system exactly anymore. However, the time step size is only limited by accuracy, not by stability. This is in contrast to the well known leap-frog method, where stability requires to use time steps proportional to the inverse of the largest eigenvalue of the linear part. This straightforward implementation turns out to be quite expensive with respect to computational cost and storage. Fortunately, it is possible to increase the efficiency considerably by exploiting properties of the solution.

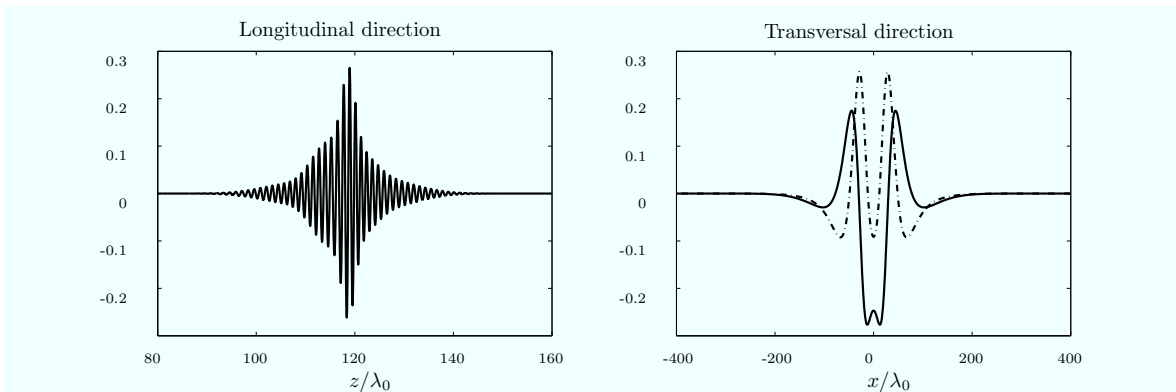


Figure 4.1: Left: The spatial distribution of the real part of the solution in longitudinal direction through the centroid of the pulse. Right: The spatial distribution of the real (solid) and imaginary (dashed) part of the solution in transversal direction through the centroid of the pulse.

In the left graph of Fig. 4.1 we show the longitudinal distribution of the real part of the vector potential a along the central axis of the pulse. On the right, we show the transversal distribution of the real (solid) and the imaginary (dashed) part of a at the point z , where the maximum of the pulse is attained. The transversal distribution is obviously much smoother than the longitudinal. Therefore, we can discretize the transversal direction on a much coarser grid. Moreover, it is possible to split the Laplacian and only treat the longitudinal part of it exactly ($\Omega \approx \Delta_{\parallel}$) whereas the transversal part is added to the nonlinearity $F(y)$. To avoid the expensive two-dimensional Fourier transformations, we propose to use fourth-order finite differences in this direction.

Due to this splitting, the longitudinal part of the Laplacian, can be diagonalized by one-dimensional Fourier transforms (of length N_z). Moreover, we only have to compute (and store) matrix operators of length N_z . For the computation we keep the vector potential and its derivative in Fourier space only in longitudinal direction. In transversal direction the arrays are not transformed.

4.1. Numerical Methods

For the density equation the application of the exponential integrator is straight forward in physical space. If the density profile only depends on z the storage requirements are again only of the order of vectors of length N_z . The inhomogeneity contains the Laplacian of the relativistic factor γ which depends on the absolute value of the vector potential. This is a smooth function for circular polarized laser beams. Thus it is sufficient to use fourth order finite differences in *both* directions to approximate the inhomogeneity of the density equation.

Cylindrical coordinates

For the equations in cylindrical coordinates

$$\frac{\partial^2}{\partial t^2} a = \frac{\partial^2}{\partial z^2} a + \frac{1}{r} \frac{\partial}{\partial r} \left(r \frac{\partial}{\partial r} a \right) - \frac{n_0}{n_c} \frac{n_e^0 + n_e^1}{\gamma} a \quad (4.7a)$$

$$\frac{\partial^2}{\partial t^2} n_e^1 = -\frac{n_0}{n_c} n_e^0 n_e^1 + n_e^0 \Delta \gamma \quad (4.7b)$$

we basically use the same ideas as for Cartesian coordinates in plasma regions, i.e., we use $\Omega \approx \Delta_{\parallel}$ and treat the transversal direction as part of the nonlinearity. For the longitudinal direction, we use pseudo-spectral discretization while for the transversal direction, we suggest to use second order finite differences.

Since in cylindrical coordinates it is hard to diagonalize the complete Laplacian in a fast and stable way we use the same implementation in vacuum as within the plasma. Methods for numerical Fourier-Bessel transforms that diagonalize the radial part of the Laplacian exist [8, 37, 60], but apparently there exist to date no fast transform on an equidistant grid with sufficient accuracy.

4.1.3 Adaptivity

For adaptivity of the integration scheme, we implement the methods discussed in 3.2.4 and 3.2.5. This is more important in two dimensions than in one dimension, because, as we will see in chapters 5 and 6, vacuum sections between the plasma layers strongly influence pulse propagation due to transversal effects. Using different grids and/or different values of κ for the QEA method in different parts of such a strongly inhomogeneous system can significantly increase accuracy and reduce computation time.

In order to apply all the different variations of our scheme at the appropriate time we have to determine the location of the pulse. This is done by physically motivated means. At the beginning we know the location of the maximum amplitude and the exact width of the pulse. Additionally we know the approximate group velocity of the pulse at any time. This allows to determine the approximate speed of the maximum of the pulse and to estimate the time when the pulse hits the next region of the simulation domain.

With this method we can switch between the different integration schemes in vacuum and plasma for Cartesian coordinates as well as adapt the values of κ for the QEA. The latter can be done by a simple shift in the position of the Fourier coefficients which also ensures periodicity of the shift function $e^{i\kappa z}$ with regard to the box length $2L_z$.

4. Pulse compression in two dimensions

Additionally we can change the spatial grid, which becomes necessary for very narrow pulses as they occur in the simulation of pulse compression. Also for hard plasma boundaries, where reflections are no longer negligible, it becomes necessary to interpolate to a finer grid and invert the QEA shift, as we have already shown for the one-dimensional case in section 3.3.5. For pseudo-spectral discretization this only requires a larger array in Fourier space where extra entries are filled with zeros. But the computation is much more expensive for the finer grid, thus interpolation is avoided unless absolutely necessary. Therefore, we also use a rather tight estimate for the pulse to be nonzero.

4.1.4 Moving simulation window

There are a lot of interesting applications, especially those with large amounts of vacuum, where the full simulation domain is very large and it is not at all feasible to use the complete spatial domain during the whole simulation. To avoid this we use a moving-window technique.

Using the group velocity as described above we estimate the time when the pulse comes close to the right boundary of the simulation box. For this purpose we slightly overestimate the domain on which we consider the pulse to be nonzero. This increases robustness while the computational cost is negligible.

The shift is implemented by transforming the vector potential to physical space, cutting off the left part and extrapolating to the right by adding zeros for a and n_e^1 . n_e^0 is calculated from the known profile function.

There are two difficulties to be mentioned in this context due to the periodic boundary conditions. First, if reflections occur at plasma boundaries we have to cut them off entirely when shifting the simulation box. Secondly, in vacuum this limits the time step size because otherwise the pulse would move periodically through the box instead of moving on continuously. This would result in spatial shifts of the solution.

4.1.5 Parallelization

Even though we already reduced computational costs significantly, for large problems it is useful to have a parallel version of the method. Here we have to tailor the means of parallelization to the different cases described above.

Vacuum

For Cartesian coordinates in vacuum we first distribute the columns of the arrays uniformly over the processors to perform the one-dimensional fast Fourier transforms for each column. We then do a parallel transposition of the array and distribute the rows over the processors for the second part of the two-dimensional Fourier transform¹. Of course the application of the matrix function is also spread over the processors involved.

¹We use the MPI based transpose routine from FFTW version 2 and serial FFT routines from FFTW 3.

Plasma

In plasma we basically use the same strategy for parallelization for both kinds of geometries. Here we again distribute all the columns of the arrays over the processors. But since we only need one-dimensional Fourier transforms we can avoid transposing the arrays and therefore save a lot of communication time between different processors.

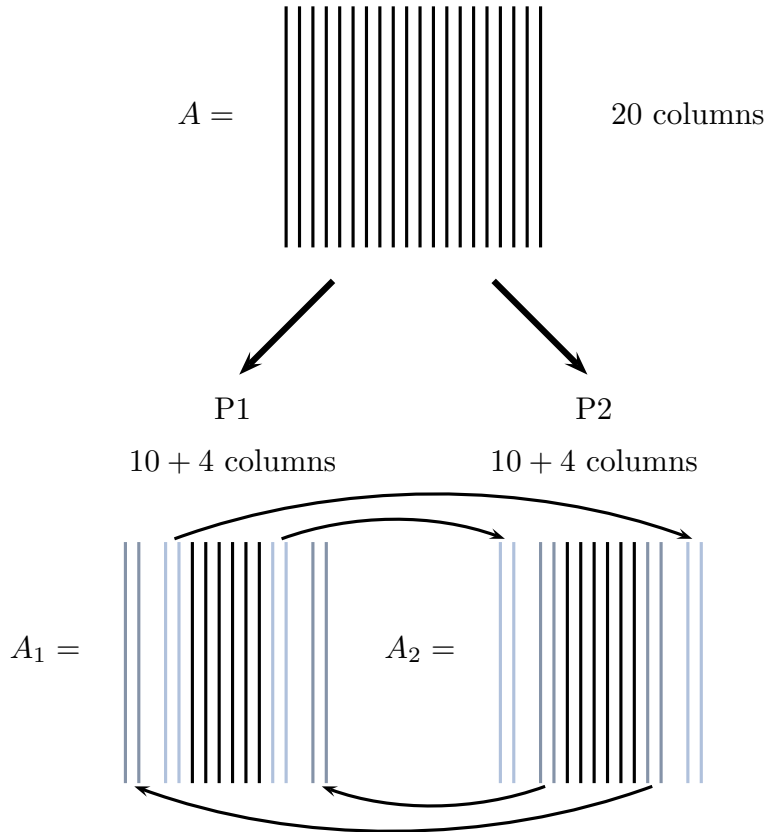


Figure 4.2: Example parallelization scheme for two processors, Cartesian coordinates in plasma, periodic boundary conditions and 20 grid points in transversal direction. The lighter colored columns have to be communicated between the processors for the evaluation of the transversal Laplacian with finite differences and are stored twice.

The only communication between processors is due to the transversal part of the Laplacian, which is discretized by fourth and second order finite differences in plasma for Cartesian and cylindrical coordinates, respectively. Thus we have to exchange at most two columns at each side of the distributed array slices. In Fig. 4.2 this is demonstrated for a matrix divided to two processors for Cartesian coordinates and periodic boundary conditions. In this case we have to store four extra columns per processor which are copied from the neighboring array.

Each processor first sends the boundary columns to the neighboring processors. Then the next time step is performed for the inner part of the array. At the end, the information sent from the neighboring arrays is used to calculate the finite difference

approximation at the boundaries. This results in a parallelization which hardly suffers from communication overhead between processors, because latencies and transmission times are almost completely hidden by the asynchronous communication.

4.2 Accuracy and efficiency of the over-all 2D scheme

4.2.1 Splitting of the Laplacian

In this section we will demonstrate that the error introduced by the splitting of the Laplacian is negligible. For this, we use a rather small example, where it is possible to have a high resolution reference solution to compare with. We also reduce the model and only consider the wave equation with constant density and cubic nonlinearity

$$\frac{\partial^2}{\partial t^2} a = \Delta a - \frac{n_0}{n_c} \left(1 - \frac{1}{2}|a|^2\right) a, \quad \frac{n_0}{n_c} = 0.3. \quad (4.8)$$

This is sufficient, since the splitting only affects the wave equation and does neither depend on the kind of nonlinearity nor on the density equation.

The initial conditions are chosen from

$$a(x, z, t) = a_0 e^{-\frac{(z-z_0-k_0t)^2}{L_0^2}} e^{-\frac{x^2}{W_0^2}} e^{i(k_0z-z_0-t)} \quad (4.9)$$

where $a_0 = 0.15$ is the initial amplitude, $z_0 = 35\lambda_0$ the initial pulse position in longitudinal direction, $W_0 = 10\lambda_0$ the length, $L_0 = 100\lambda_0$ the width of the pulse and $k_0 = \sqrt{1 - \frac{n_0}{n_c}}$ the plasma wave length.

This is solved for Cartesian coordinates $(x, z) \in [-300\lambda_0, 300\lambda_0] \times [0\lambda_0, 300\lambda_0]$ and $t \in [0/\nu_0, 300/\nu_0]$. We use 1024 grid points in z -direction and 512 grid points in x -direction. The time step size is chosen as $0.2 dz$. For the reference solution we use twice as many points in both spatial directions, whereas for the time discretization we choose a fourth of the original time step. For the error calculation we Fourier interpolate the solutions to the finer grid.

In Fig. 4.3 we can see the error in two different measures, in the upper picture the relative error in the maximum squared amplitude is shown and the lower one shows the absolute error of the position of the maximum in wave lengths. For each type of error there are three different curves. The circular marks show the error of the Gautschi-type method applied to the full Laplacian, discretized via Fourier spectral method in both directions. The square marks are the errors of the Gautschi-type method applied to the parallel Laplacian only and the transversal part treated as nonlinearity. Here we still use Fourier spectral methods for the discretization in both directions. The diamond marks represent the error of the splitted method, but this time with fourth order finite differences in transversal direction. We can see that the three error curves are nearly indistinguishable, which proves that the splitting does not degrade accuracy.

4.2. Accuracy and efficiency of the over-all 2D scheme

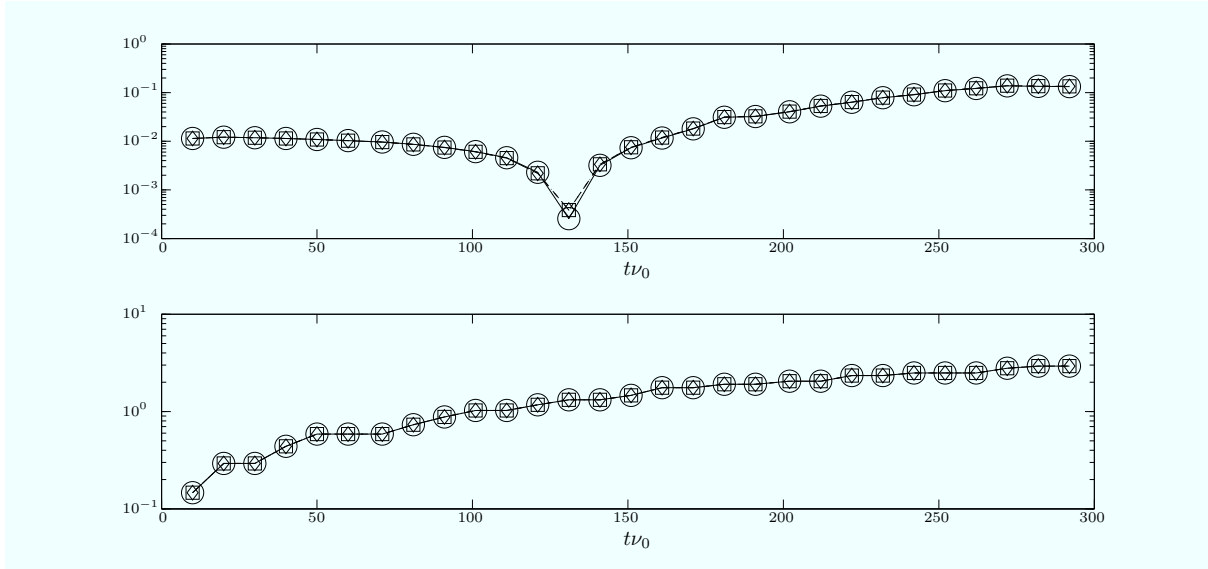


Figure 4.3: The relative error of the maximum squared amplitude is shown in the upper picture and the absolute error of the position of the maximum in wave lengths is drawn in the lower picture. The curves marked by circles are the errors of the Gautschi-type method applied to the full Laplacian, the squares are the errors of the splitted method with Fourier spectral discretization in both directions and the diamonds are those for the splitted method with finite differences in transversal direction.

4.2.2 Effect of different time-integration schemes

We next compare our implementation of the one-step Gautschi-type integrator with the leap-frog scheme. Here, we solve the full system of equations for the two-dimensional Cartesian case (4.6). The density layer starts at $250\lambda_0$ with a linear increase up to $\frac{n_0}{n_c} = 0.3$ over $5\lambda_0$, then it stays constant over $500\lambda_0$ until there is a linear decrease between $755\lambda_0$ and $760\lambda_0$ again.

The initial conditions are again taken from (4.9) with $a_0 = 0.12$, $z_0 = 150\lambda_0$ and $k_0 = 1$, since the pulse starts in vacuum. The remaining coefficients are the same as above. The simulation is run up to $t = 1240/\nu_0$, thus the pulse propagates through the plasma layer and travels through vacuum afterwards for some time. For the run time comparisons we used the moving window technique, since the simulation domain is quite long.

In vacuum there is no need to compare the leap-frog scheme with the exact solution which the Gautschi-type integrator computes, thus we include only the time steps done inside of the plasma in the run time comparison.

As a measure for the quality of the solution we choose the relative error of the maximum amplitude. As a sensible error threshold we use a value of 1%. Since the reference solution was computed on a finer grid, we interpolated the solution to the reference grid and then computed the maximum amplitude.

In Fig. 4.4 the amplitude error of the Gautschi-type method (circles) and the leap-frog method (squares) is plotted against computation time in plasma. The dashed line represents a coarse spatial discretization with 1024 grid points in longitudinal direction,

4. Pulse compression in two dimensions

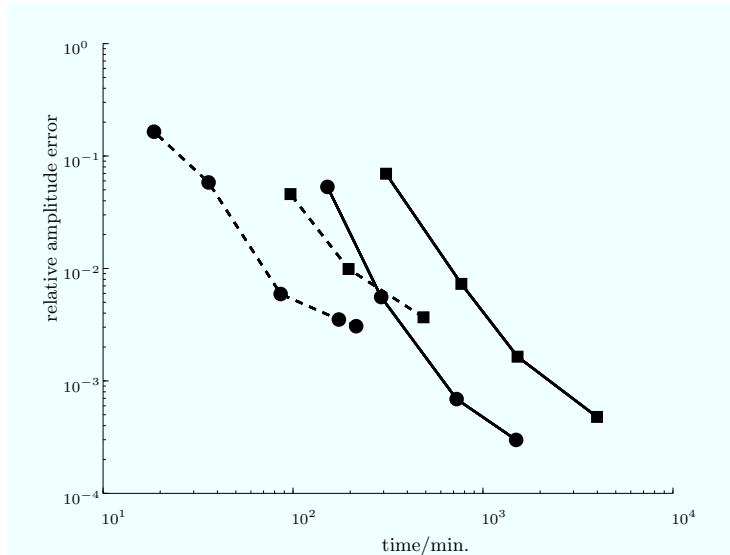


Figure 4.4: The relative error in the maximum amplitude is plotted over the run time in minutes. Circles: Gautschi-type integrator. Squares: leap-frog. Dashed: coarse spatial discretization. Line: fine spatial discretization. Along each curve the value of τ varies.

where dz is chosen to be $0.352\lambda_0$ and 400 grid points in transversal direction with $dx = 2\lambda_0$. The continuous line gives the errors for a fine spatial discretization with $N_z = 2048$, $dz = 0.176\lambda_0$, $N_x = 800$ and $dx = \lambda_0$. In both cases the resulting simulation box of approximately $360\lambda_0$ in longitudinal direction and $800\lambda_0$ in transversal direction is moved along with the solution.

For the same error the step size for the leap-frog method has to be about twice as small as for the Gautschi-type integrator. This is in agreement with the results in the one-dimensional case. But in the two-dimensional case the advantage of the leap-frog method in terms of computational time per time step is smaller than in the one dimensional case, because simulation times are more strongly affected by memory bandwidth limitations, see Fig. 4.5. Thus it is even more efficient to invest in a more sophisticated algorithm and benefit from the larger time steps.

4.2.3 Parallelization

To demonstrate the efficiency of the parallelized version of our code we simulated the same problem as for the run time comparison with one, two, four, six and eight processors on a cluster of single CPU P4 nodes with standard Gigabit Ethernet interconnects. We used the finer one of the two spatial discretizations.

In the upper three pictures of Fig. 4.6 full time (black), pure number crunching time (light gray), data receive time (dark gray) and synchronization time² (middle gray) per time step for two, four and eight processors, respectively, is shown. In each case we can distinguish between three different behaviors of the code. First of all there is the vacuum step region. Here, the crunching time is quite low, since we neither calculate

²The synchronization time is due to `MPI_Barrier()` calls after each time step.

4.2. Accuracy and efficiency of the over-all 2D scheme

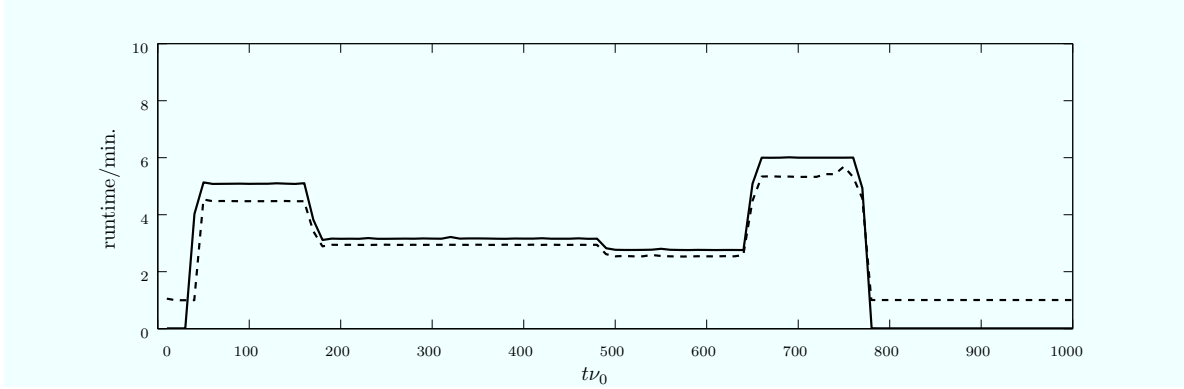


Figure 4.5: For the Gautschi-type method (solid) and the leap-frog method (dashed) the runtime between outputs (i.e. 228 timesteps, except for vacuum steps with the Gautschi-type method) is shown. The spatial *and* time discretization is the same for both schemes except in vacuum.

the nonlinearity nor the density equation. However, due to the matrix transpositions the communication time is rather long.

The other two cases are the plasma and transition regions. The only difference is the spatial resolution which is higher in the transition region. However in both cases the full equations are solved and the Laplace splitting is applied. The first results in higher crunching times whereas the latter reduces the communication time significantly.

Another nice property is the very short synchronization times given by the middle gray curves. Thus independent of the number of processors used, the work is evenly balanced over the processors.

In comparison we can see that a single vacuum time step takes longer than a single time step for the full equations, even with the higher spatial resolution in transition regions. This is compensated by the fact that the time steps in vacuum are 200 times larger than the time steps we use for solving the full set of equations. This is illustrated in the fourth picture of Fig. 4.6, where the accumulated full integration time is shown for a single processor and for two, four and eight parallel processors (curves from top to bottom). The strongest increase of computational time is in the transition region, where we use the higher spatial resolution directly followed by the plasma regions. We can also see that in comparison the integrator spends hardly any time in vacuum regions. Note that the length of the time steps in vacuum is only limited by points of data output and the shifting of the simulation box.

The run time per output step is shown in Fig. 4.7. Here again the different regions of the simulation are visible. The drop in simulation time towards the end of the plasma region is due to the remaining length of the plasma layer inside the simulation box, since the density equation is only solved on those grid points which lie inside the plasma.

Another point to emphasize is the good scaling of the accumulated full integration times with the number of processors used, even for this relatively small problem. Using two processors reduces the run time by a factor of 1.97. The run times for four, six and eight processors scale with 3.88, 5.73 and 7.19 respectively.

4. Pulse compression in two dimensions

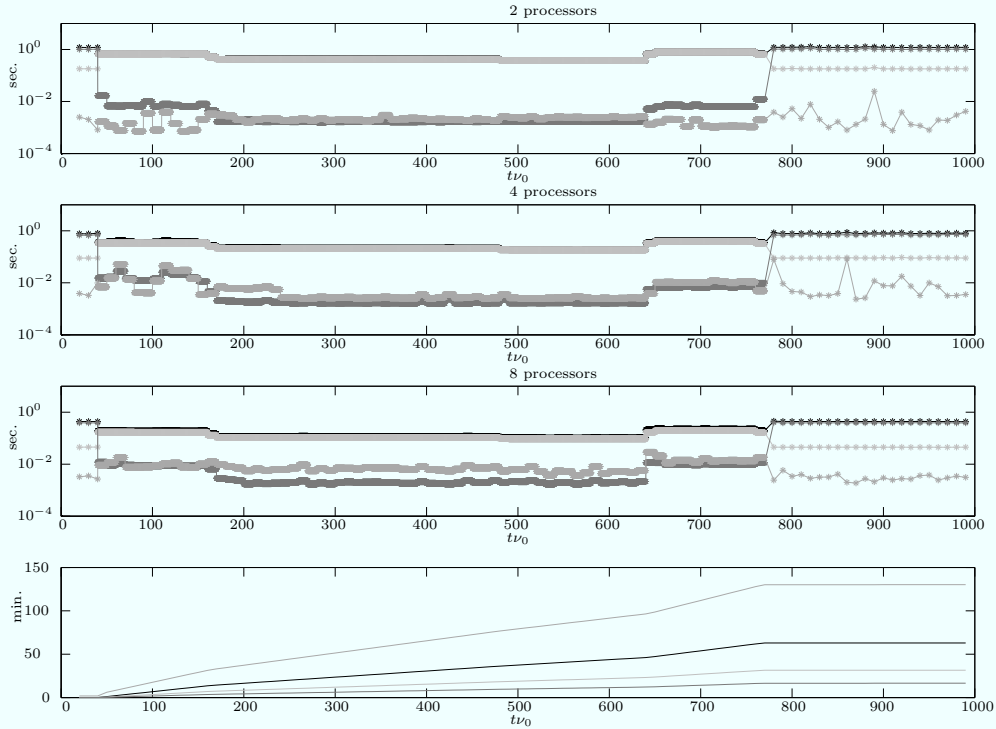


Figure 4.6: The upper three pictures show the full time (black), pure number crunching time (light gray), data receive time (dark gray) and synchronization time (middle gray) per time step for two, four and eight processors respectively. The fourth picture shows the accumulated full integration time for one, two, four and eight processors (curves from top to bottom).

4.3 Pulse dynamics in 2D

4.3.1 2D self-compression threshold

For a two dimensional pulse, we can derive equations for the temporal length and spatial width of the pulse by the same method as for one dimension in section 3.4.1. Since already in 1D the equation for the temporal length T of the pulse fails to describe the pulse dynamic well (see section 3.4.1), we expect this to be even more the case in 2D where there is a coupling between the dynamics of the two directions. Compression in one direction enhances the compression in the other, if for example the speed of compression in each individual direction deviates from the full model equations, the combined compression speed will deviate even more (and in a nonlinear way). Thus we are more interested in the values and the validity of the self-compression thresholds. In 1D the threshold can be easily shown to be exact for a soliton solution. The results were less conclusive for a Gaussian pulse, because a localized pulse with an arbitrary initial shape will start to change its shape towards the shape of a soliton. This leads to oscillations in pulse amplitude even at the threshold. Because we do not have an analytical soliton solution in 2D we restrict ourselves to examine the thresholds for Gaussian pulses, al-

4.3. Pulse dynamics in 2D

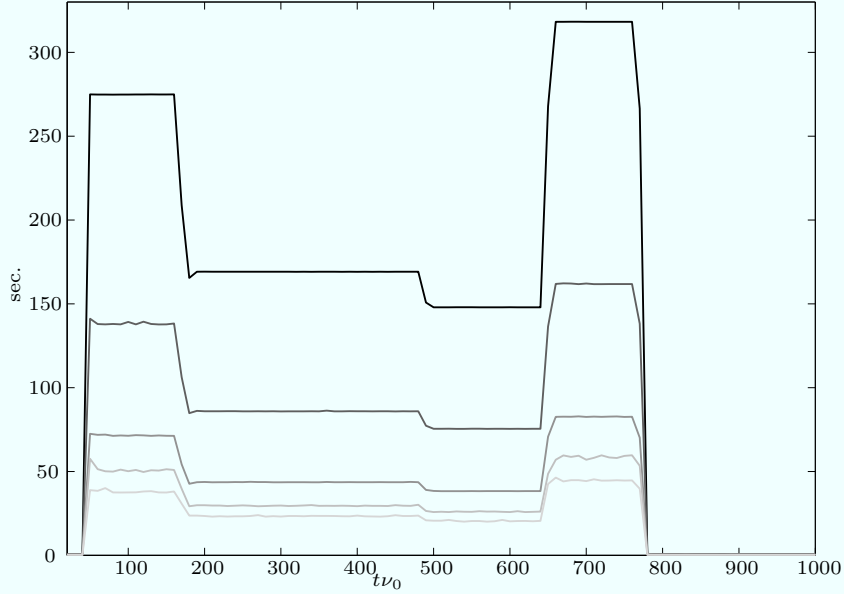


Figure 4.7: The run time per output step for two, four, six and eight processors (curves from dark to light gray) scales with 1.97, 3.88, 5.73 and 7.19 respectively compared to single processor run time (black).

though more general methods exist to derive the thresholds for arbitrary pulse shapes [10].

In a geometry which has cylindrical symmetry in the transversal direction, the variation-of-action method with a Gaussian trial function yields the equations

$$T'' = -\frac{4(1-\beta^2)^2}{\beta^6} \frac{1}{T^3} \left\{ \frac{\beta^2}{16\sqrt{2}} \frac{A_0^2 W_0^2 T_0 T}{W^2} - 1 \right\} \quad (4.10)$$

for the temporal length and

$$W'' = -\frac{4}{\beta^2} \frac{1}{W^3} \left\{ \frac{1-\beta^2}{16\sqrt{2}} \frac{A_0^2 W_0^2 T_0}{T} - 1 \right\} \quad (4.11)$$

for the spot size of the pulse. These equations were also derived in [56] for linear polarization and a different normalization.

In a 2D Cartesian geometry the equations are

$$T'' = -\frac{4(1-\beta^2)^2}{\beta^6} \frac{1}{T^3} \left\{ \frac{\beta^2}{16} \frac{A_0^2 W_0 T_0 T}{W} - 1 \right\} \quad (4.12)$$

and

$$W'' = -\frac{4}{\beta^2} \frac{1}{W^3} \left\{ \frac{1-\beta^2}{16} \frac{A_0^2 W_0 T_0 W}{T} - 1 \right\}. \quad (4.13)$$

The details of the derivation can be found in appendix A.

4. Pulse compression in two dimensions

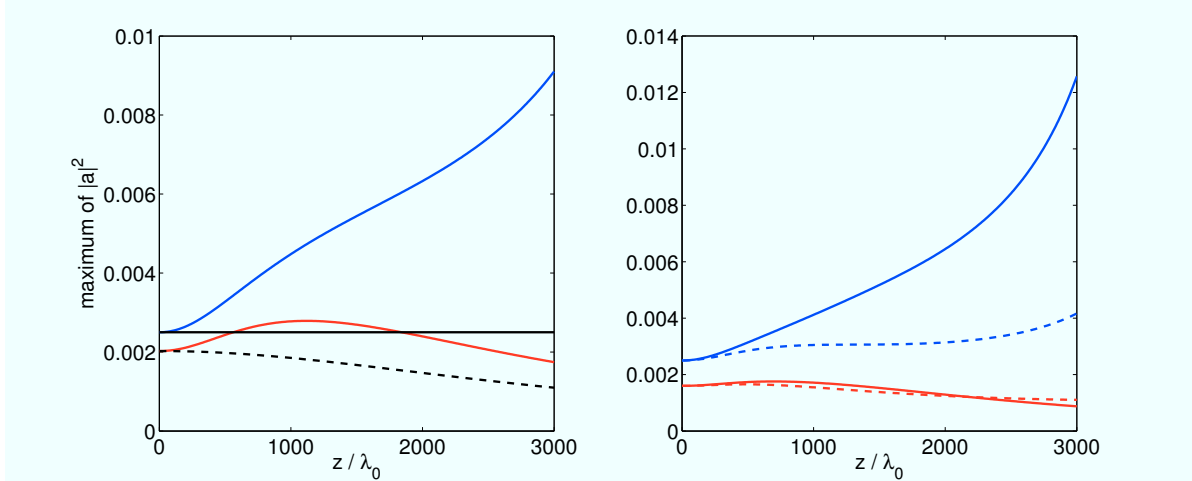


Figure 4.8: Amplitude evolution of initially Gaussian pulses at the 2D compression threshold in Cartesian geometry for $L_0 = \beta T_0 = 12.73 \lambda_0$, $W_0 = 23.25 \lambda_0$ and $n_0 = 0.3 n_c$. Left: 2D VAM model at (black, solid) and below the threshold (black, dashed), NLSE simulations at (blue) and below the threshold (red). Right: NLSE simulations for pulses that are at (blue) or below (red) the 1D compression in the longitudinal direction and above the 2D threshold in the transversal direction (solid: $W_0 = 30 \lambda_0$, dashed: $W_0 = 150 \lambda_0$). Pulses at the threshold have $a_0 = 0.045$ and pulses below have $a_0 = 0.045$.

From this equations we can directly read off the self-compression thresholds for the longitudinal direction

$$\beta^2 A_0^2 T_0^2 \geq P_c \quad (4.14)$$

and the transversal direction

$$(1 - \beta^2) A_0^2 W_0^2 \geq P_c, \quad (4.15)$$

where the critical power P_c here is either the pulse power in the longitudinal or transversal slice through the centroid of the pulse. Because the transversal and longitudinal threshold values are the same for a particular geometry, we do not distinguish between them. Every additional dimension increases the compression threshold by a factor of $\sqrt{2}$, from $8\sqrt{2}$ in 1D to 16 in 2D to $16\sqrt{2}$ in a cylindrical geometry, which is effectively 3D.

Amplitude evolution of initially Gaussian pulses at the 2D compression threshold in Cartesian geometry for $L_0 = \beta T_0 = 12.73 \lambda_0$, $W_0 = 23.25 \lambda_0$ and $n_0 = 0.3 n_c$. Left: 2D VAM model at (black, solid) and below the threshold (black, dashed), NLSE simulations at (blue) and below the threshold (red). Right: NLSE simulations for pulses that are at (blue) or below (red) the 1D compression in the longitudinal direction and above the 2D threshold in the transversal direction (solid: $W_0 = 30 \lambda_0$, dashed: $W_0 = 150 \lambda_0$). Pulses at the threshold have $a_0 = 0.045$ and pulses below have $a_0 = 0.045$.

The only difference between the longitudinal and transversal threshold relations is that for the longitudinal direction the group velocity β enters, while for the transversal

4.3. Pulse dynamics in 2D

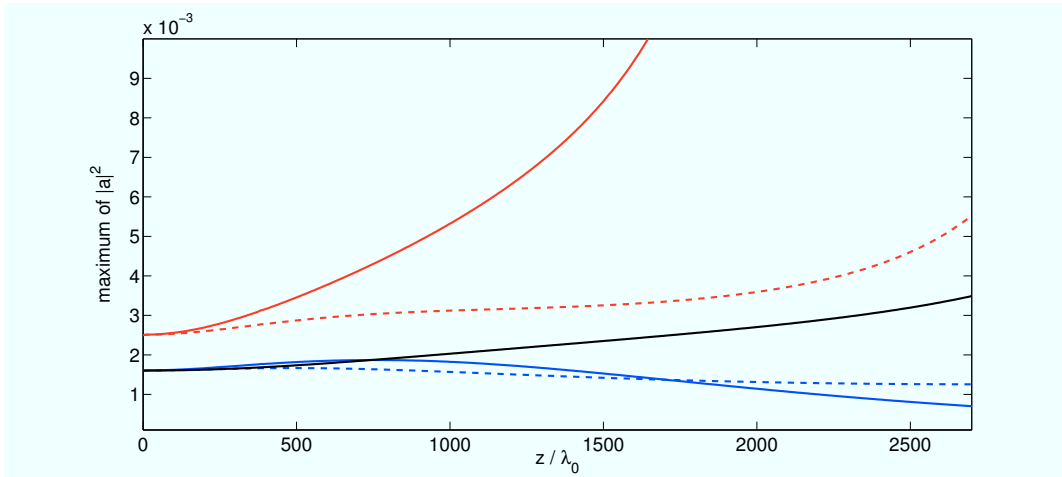


Figure 4.9: Amplitude evolution of initially Gaussian pulses at the compression threshold for 2D cylindrical geometry. Results from wave equation simulations for pulses that are at (blue, $a_0 = 0.05$) or below (red, $a_0 = 0.04$) the 1D threshold in the longitudinal direction ($L_0 = 10.71 \lambda_0$) and above the threshold for cylindrical geometry in the transversal direction (solid: $W_0 = 30 \lambda_0$, dashed: $W_0 = 150 \lambda_0$).

direction it is the plasma density parameter $\frac{n_0}{n_c} = 1 - \beta^2$. It is also noteworthy that the thresholds for the two directions are completely independent. The full energy of the pulse does not enter the relations although it enters the equations for T and W (cf. appendix A).

For a pulse that is at the threshold for both directions, we find that within the inaccuracy due to the expected amplitude oscillations of Gaussian pulses, the thresholds for both geometries are reasonably accurate. This is illustrated by the left hand side of Fig. 4.8. In 2D, we first checked this result with simulations of the NLSE and then confirmed it by simulations of the nonlinear wave equation. In cylindrical geometry we directly used wave equation based simulations.

To study the transition between 2D and 1D thresholds in the VAM model, we can fix the spot size or length of the pulse at a constant value T_0 or W_0 in the derivation of the T or W equation respectively. Unfortunately we get the nonsensical answer from the variation-of-action method that the threshold for the dynamical direction is unchanged from the case where both directions are dynamical. Thus the 1D threshold can not be recovered by letting the fixed length or spot size go to infinity. The reason is that the pulse shape we have prescribed has insufficient degrees of freedom to allow for a different strength of compression at different slices of the pulse. On axis for example, the longitudinal compression of a wide pulse should resemble one dimensional compression, while further from the axis the pulse should show weaker compression or defocusing if below the threshold.

Of special interest for the application of pulse compression, is the transition between the 2D threshold and the 1D threshold for the case when the spot size of the pulse is increased from a value calculated by using the 2D threshold. With increasing W_0 the deviation of the threshold value from the 2D threshold occurs rather quickly, illustrated

4. Pulse compression in two dimensions

by the right hand side of Fig. 4.8 and by Fig. 4.9. Like for longitudinal compression the speed of the transversal compression scales with W_0^2 [56]. Therefore the time scales of longitudinal and transversal compression will diverge quickly with increasing W_0/L_0 . Thus during the beginning of the longitudinal compression the spot size will stay nearly constant. This occurs both in Cartesian and cylindrical 2D geometry. A pulse with an energy at the threshold with $a_0 = 0.05$, $L_0 = \beta T_0 = 12.732 \lambda_0$, $W_0 = 23.246 \lambda_0$ for slab geometry and $L_0 = \beta T_0 = 15.1415 \lambda_0$ and $W_0 = 27.644 \lambda_0$ for cylindrical geometry, shows no compression at amplitudes slightly below the threshold. If the spot size is increased to $W_0 = 30 \lambda_0$, the pulse already shows compression at a length calculated from the longitudinal 1D threshold, and no compression below. This rapid shift from the 2D/3D threshold to the 1D threshold occurs in both Cartesian (Fig. 4.8) and cylindrical (Fig. 4.9) geometry.

4.3.2 Spot size vs. length of the pulse

As we have seen in chapter 3, a 1D pulse with parameters close to the bound two-soliton solution of the cubic nonlinear Schrödinger equation can compress and decompress periodically, as long as the amplitude is not too high and thus the density perturbations induced by the ponderomotive force of the pulse are not too large.

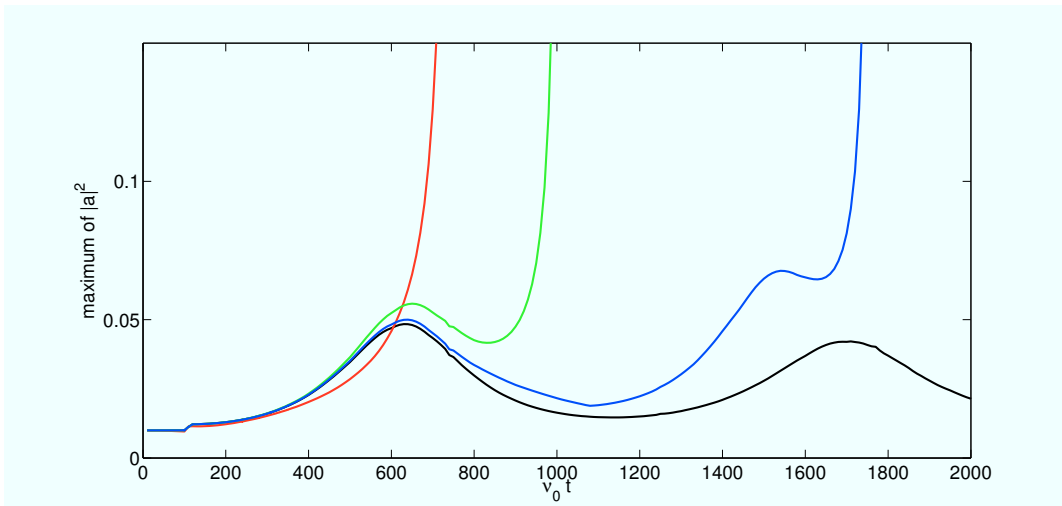


Figure 4.10: Comparison of 1D and 2D dynamics for different values of the initial spot size W_0 . 1D (black), $W_0 = 10$ (red), $W_0 = 100$ (green), $W_0 = 200 \lambda_0$ (blue) for $a_0 = 0.1$, $L_0 = 10 \lambda_0$ and $n_0 = 0.3 n_c$

We have also seen in the preceding section that the 2D dynamic deviates the more from the 1D dynamic the closer the ratio of the spot size to pulse length is to unity. For smaller initial spot sizes, the pulse starts to collapse after a shorter propagation distance (Fig. 4.10). A Gaussian pulse above the 1D self-compression threshold with $a_0 = 0.1$ and $L_0 = 10 \lambda_0$ and a spot size of $200 \lambda_0$ shows two compression and decompression cycles before collapse occurs. For the same pulse with a spot size of $100 \lambda_0$ the collapse occurs already after the first compression / decompression, while for a spot size of $10 \lambda_0$ the

4.3. Pulse dynamics in 2D

pulse starts to collapse directly. At this low initial intensity, the density perturbation only produces a slightly higher compression and does not change the pulse dynamics qualitatively (Fig. 4.11 and Fig. 4.12).

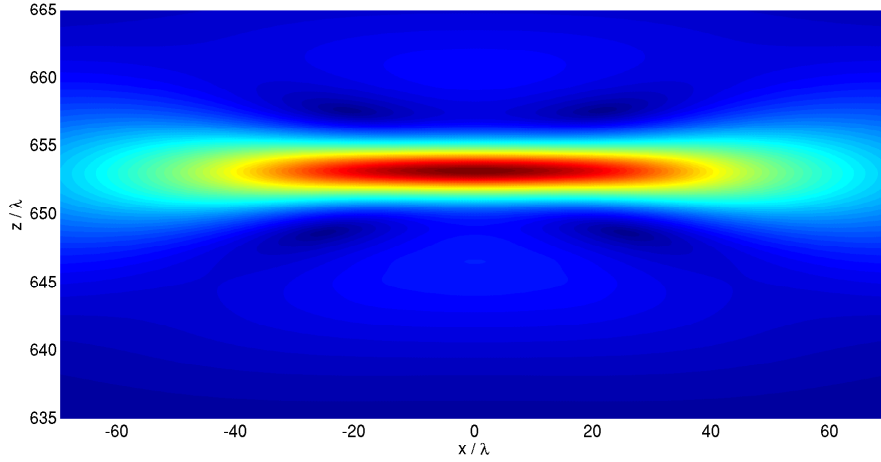


Figure 4.11: Color plot of $|a|^2$ for longitudinally compressed pulse at $t = 700/\nu_0$ with initial parameters of $a_0 = 0.1$, $L_0 = 10\lambda$, $W_0 = 100\lambda_0$ and a plasma density of $n_0 = 0.3n_c$. Intensity increases from blue to red.

The 2D wakefield in Fig. 4.12 is very similar to a 1D wakefield, modulated with the transversal pulse shape.

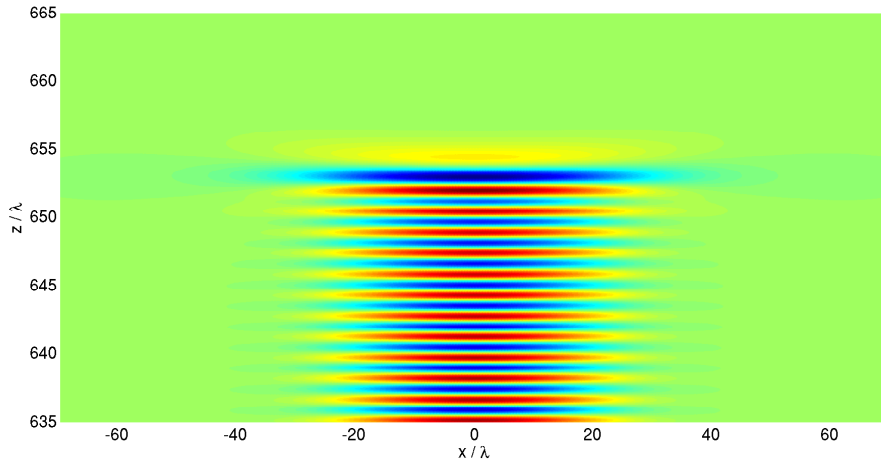


Figure 4.12: Color plot of the wakefield of the pulse in Fig. 4.11. Green for zero deviation from background density. Positive deviation are in red, negative in blue.

For an efficient pulse compression, the initial spot size of the pulse must be sufficiently large, so that at least one compression / decompression cycle can occur instead of direct collapse. This allows for a controlled compression of the pulse, because the amplitude changes only little around the maximum of compression and little fluctuations of the plasma length do not result in large changes of the maximum amplitude.

4. Pulse compression in two dimensions

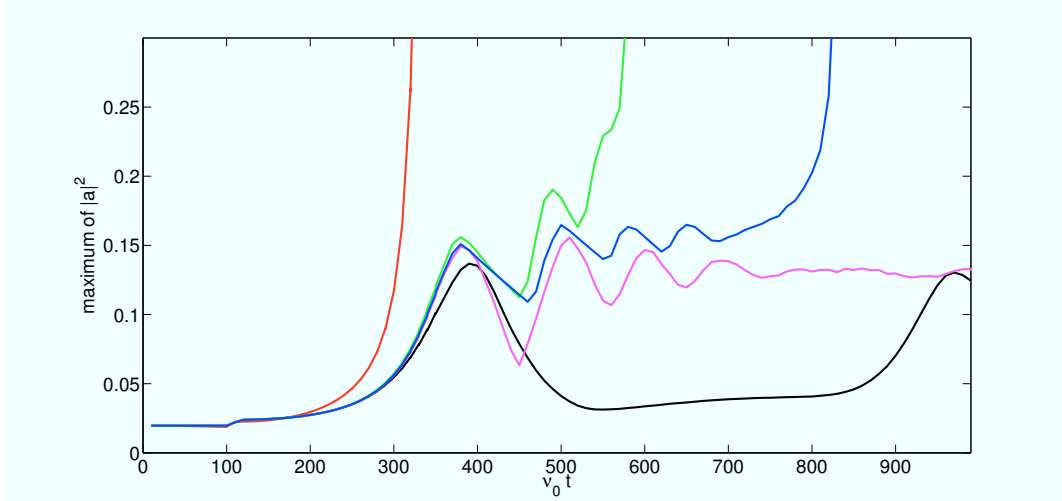


Figure 4.13: Comparison of the dynamics in 1D vs. 2D for a higher pulse amplitude and different initial spot sizes. 1D without density equation (black), 1D with density equation (magenta), $W_0 = 10 \lambda_0$ (red), $W_0 = 100 \lambda_0$ (green) and $W_0 = 200 \lambda_0$ (blue) for $a_0 = 0.14$, $L_0 = 10 \lambda_0$, $n_0/n_c = 0.3$

Higher amplitudes distinctly above the self-compression threshold lead to essentially the same effects as in 1D. With inclusion of the density response, the pulse decompresses only slightly after the first compression and starts to oscillate around a new stationary state (cf. Fig. 4.13). The ponderomotive force of the pulse is in this case sufficiently strong to produce a density cavity that traps the pulse and inhibits decompression.

This also reduces the local group velocity of the pulse, which leads to a curvature of the pulse as well as the wakefield. In Fig. 4.14 and Fig. 4.15 the corresponding curvature of pulse and wakefield is shown. This behavior occurs rather abruptly when for some initial pulse length the initial pulse amplitude is raised above a certain value. The threshold for this behavior is essentially the same as in 1D.

Like in 1D the pulse can split off a part of its energy surplus into a pre- or post-pulse to reach the new stationary state that is a 1D soliton. Although this effect is small compared to the transversal effects, it is clearly visible in simulations, e.g. in Fig. 4.16. But because of the compression in the transversal direction the pulse can not reach a truly stationary state and eventually starts to collapse. For the intended application it is only important that there is one cycle of compression and decompression before the collapse occurs to allow for a controlled decoupling of the pulse from the plasma.

4.3.3 Coupling between longitudinal and transversal compression

The amplitude evolution of the simulations in the last section seems to suggest that there is only a weak influence of the compression in the transversal direction on the compression in the longitudinal direction: the faster longitudinal direction (small initial length compared to the spot size) periodically compresses while the slower transversal direction seems to continuously compress and thus increase the pulse amplitude until

4.3. Pulse dynamics in 2D

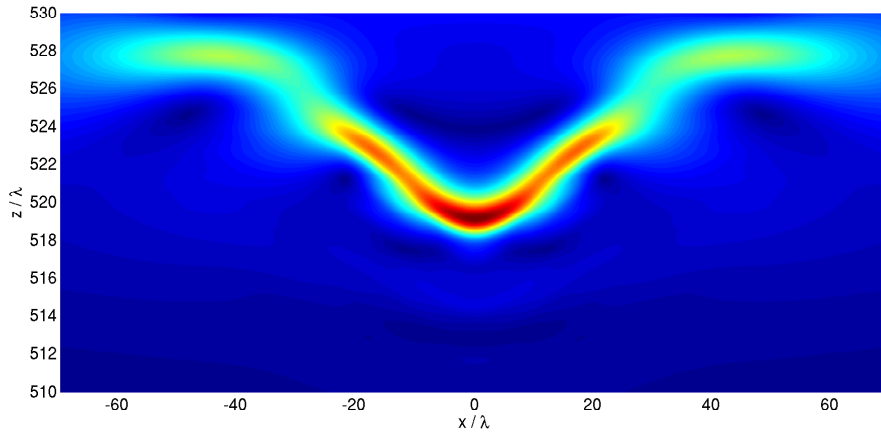


Figure 4.14: Color plot of $|a|^2$ for longitudinally compressed pulse at $t = 550/\nu_0$ with initial parameters of $a_0 = 0.14$, $L_0 = 10\lambda_0$, $W_0 = 100\lambda_0$ and a plasma density of $n_0 = 0.3n_c$.

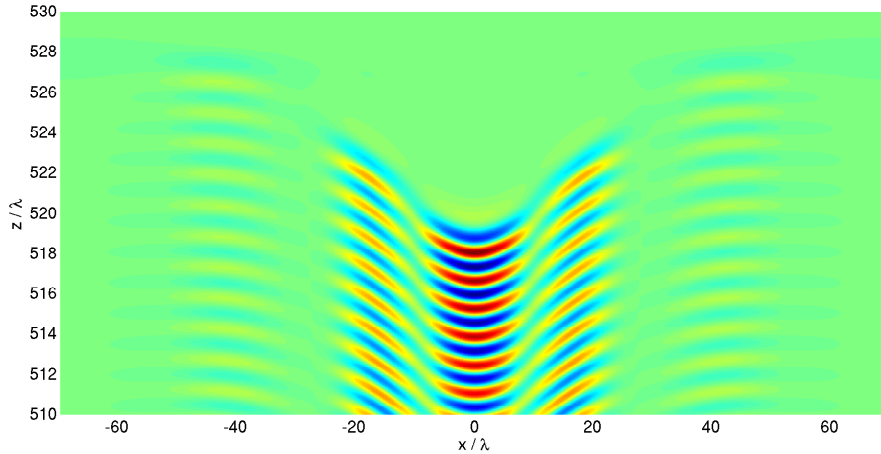


Figure 4.15: Color plot of the wakefield of the pulse in Fig. 4.14.

pulse collapse occurs. The collapse is the only point at which there is a strong coupling between the compression in both directions. This is further backed by the solutions of the VAM equations for T and W . Exactly this behavior can be seen in Fig. 4.17. The weaknesses in the quantitative predictions of these equations in 2D could be solely the result of the already weak quantitative predictions of the 1D VAM equation, while describing the qualitative dynamics in 2D correctly.

Surprisingly the actual length and spot size evolution from wave equation simulations show a very different behavior, as shown in Fig. 4.18. The faster compressing longitudinal direction “enslaves” the intrinsically slower transversal direction. Because of this enslavement the spot size shows minima at the same location as the pulse length and does not continuously decrease, but oscillates, too. Especially for wide initial spot sizes the pulse can defocus after the first minimum to nearly the initial spot size. This limits the possibility to reduce the spot size of short pulses inside the plasma severely.

4. Pulse compression in two dimensions

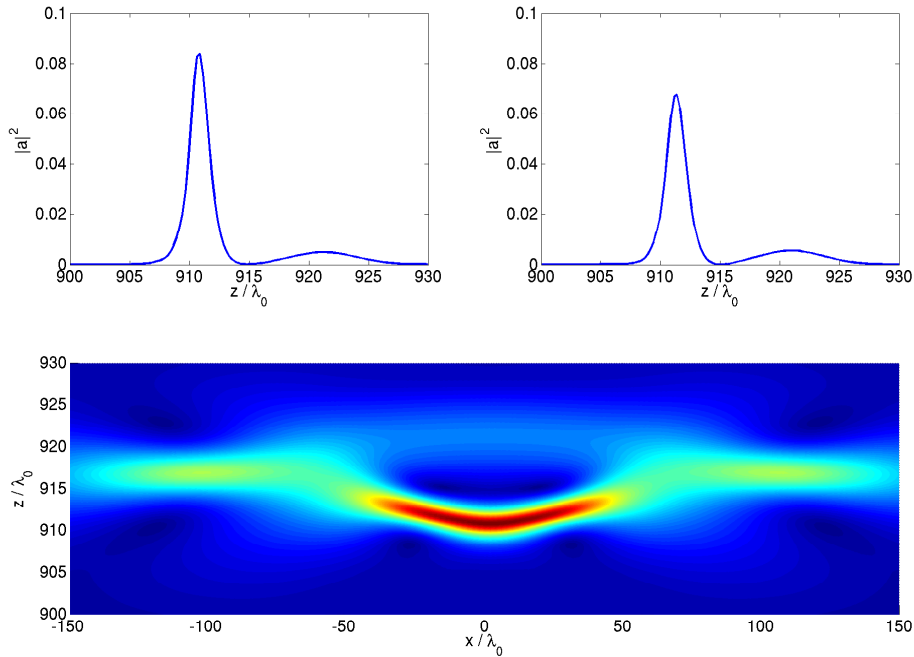


Figure 4.16: Comparison of on-axis intensity distribution in 1D vs. 2D. Simulations with $a_0 = 0.12$, $L_0 = 10 \lambda_0$, $W_0 = 200 \lambda_0$ and included density response. Top left: 2D on-axis cut. Top right: 1D. Bottom: 2D color plot.

4.4 Transversal filamentation instability

4.4.1 Pulses of constant length

Transversal instability of planar NLSE solitons, i.e. longitudinal 1D soliton solutions of the NLSE that are constant in the transversal direction, is a well understood phenomenon, both analytically and numerically [1, 5, 57, 66, 47, 41]. Harmonic perturbations in the transversal direction grow exponentially in time. Good analytical estimates exist for the growth rates. An example for the time evolution of this instability from a small initial perturbation to the full blown instability is shown in Fig. 4.19.

For the cubic NLSE the single soliton solution has the form

$$a(z, \tau) = 2 \eta \operatorname{sech}(\beta \eta \tau) e^{-i \frac{1-\beta^2}{2\beta} \eta^2 z}$$

with $\tau = z/\beta - t$ and $\beta = \sqrt{1 - n_0/n_c}$ the linear group velocity. The cubic nonlinear wave equation has a soliton solution of similar form, see appendix B.1 for the derivation. Perpendicular perturbations of this solution with (co)sine-modes below a certain cut-off wavenumber k_c are exponentially unstable with a growth rate of

$$\mu(k_\perp)^2 = \frac{n_0}{n_c} \eta^2 k_\perp^2 \left(1 - \frac{n_c}{n_0} \frac{k_\perp^2}{k_c^2}\right). \quad (4.16)$$

4.4. Transversal filamentation instability

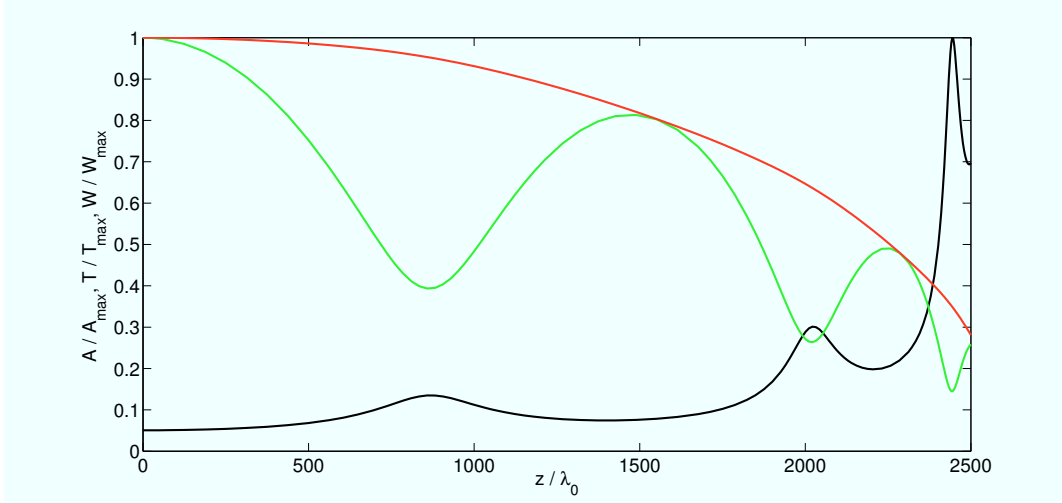


Figure 4.17: ODE solutions of the 2D VAM model for A , T and W with $a_0 = 0.1$, $\beta T_0 = 10 \lambda_0$, $W_0 = 100 \lambda_0$ and $n_0 = 0.3 n_c$ in Cartesian geometry. $T(z)/T_0$ in green, $W(z)/W_0$ in red and A^2/A_{\max}^2 in black.

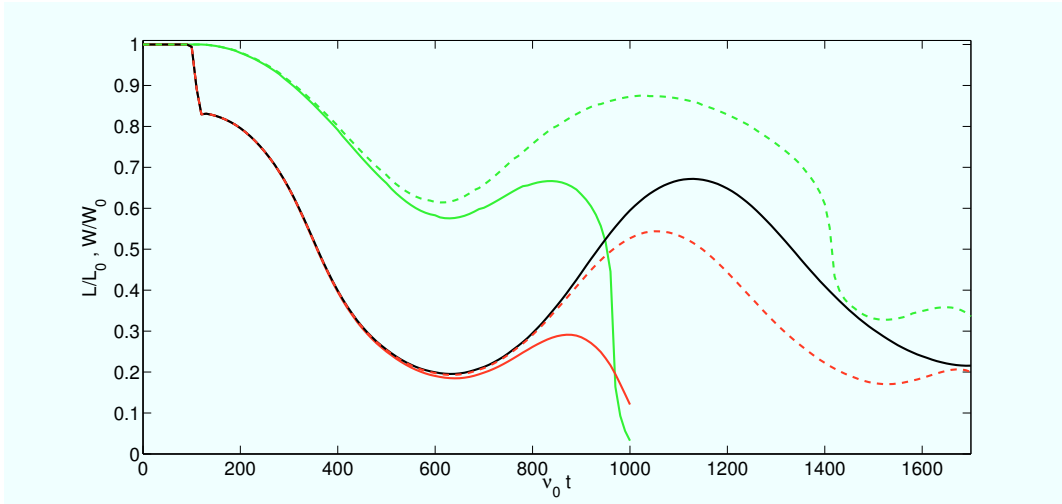


Figure 4.18: Length and spot size evolution of wave equation simulations for $a_0 = 0.1$ and $L_0 = 10 \lambda_0$ with $n_0 = 0.3 n_c$. Solid curves are for $W_0 = 100 \lambda_0$ and dashed curves for $W_0 = 200 \lambda_0$ with $L(t)/L_0$ in red, $W(t)/W_0$ in green. 1D reference curve of $L(t)/L_0$ in black.

The derivation can be found in appendix B.2. The same results were obtained by V.G. Makhankov in [47]. This growth rate is derived for the cubic NLSE, but also holds for the cubic nonlinear wave equation.

The VAM calculation yields the cut-off relation

$$k_c^2 = \frac{12 + \pi^2}{36} \eta^2. \quad (4.17)$$

We will see that this cut-off is not in good agreement with numerical simulations. A

4. Pulse compression in two dimensions

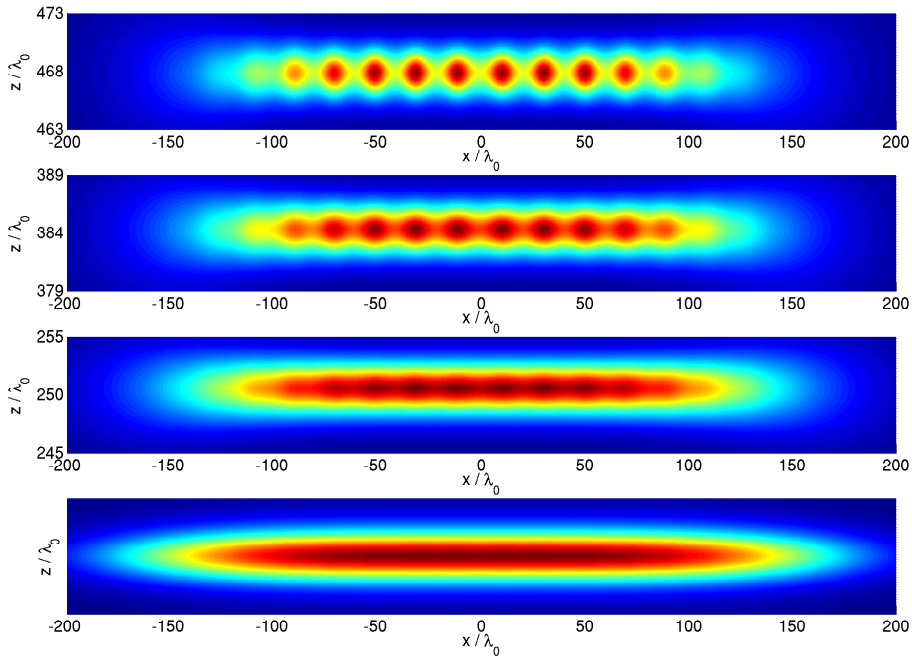


Figure 4.19: Color plot of $|a|^2$ for a simulation with cubic nonlinearity. Initial sech shape in the longitudinal direction and super-Gaussian shape in transversal direction. Initial pulse perturbation $10^{-3} a_0$ with a wavelength of $20 \lambda_0$. Bottom to top: $t = 0/\nu_0$, $t = 240/\nu_0$, $t = 400/\nu_0$, $t = 500/\nu_0$. The other simulation parameters are $n_0 = 0.3 n_c$, $a_0 = 0.16$, $L_0 = 2 \lambda_0$ and $W_0 = 200 \lambda_0$.

better estimate for the cut-off parameter is given by E.W. Laedke in [41]

$$k_c^2 = 3\eta^2 . \quad (4.18)$$

From equation (4.16) we can graphically determine the factor α in the relation

$$k_{\perp} = \alpha\eta$$

between the value of k_{\perp} with the maximum growth rate and the soliton parameter η by setting $\eta = 1$ (Fig. 4.20). This is sensible, since the position of the maximum scales linearly with η . For the different cut-offs (4.17) and (4.18) we have for $n_0 = 0.3 n_c$

$$\alpha_{0.3}^{\text{VAM}} \approx 0.497$$

and

$$\alpha_{0.3}^{\text{L}} \approx 0.671 .$$

For a short pulse of $2\lambda_0$ in length, this leads to a prediction for the most unstable wavelength via

$$\lambda_{\perp} = \frac{2\pi}{\alpha} L_0 \quad (4.19)$$

4.4. Transversal filamentation instability

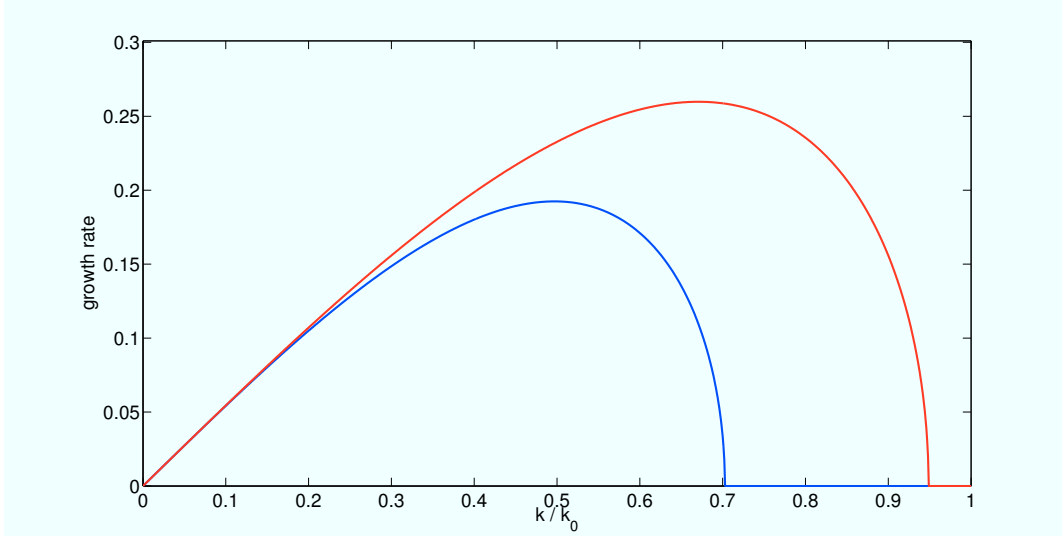


Figure 4.20: Growth rate (4.16) of the transversal instability for cut-off parameters (4.17) and (4.18) at a density of $n_0 = 0.3 n_c$.

of

$$\lambda_{0.3}^{\text{VAM}} \approx 25.15\lambda_0$$

and

$$\lambda_{0.3}^{\text{L}} \approx 18.63\lambda_0 .$$

NLSE simulations with these parameters³ clearly favor the modified cut-off value (4.18). Simulations of the cubic nonlinear wave equation with a non-constant transversal shape yield the same result. In Fig. 4.21 the results for a pulse with a super-Gaussian transversal shape with three different perturbation wavelengths are shown ($\lambda_{\perp} = 15\lambda_0$, $\lambda_{\perp} = 20\lambda_0$, $\lambda_{\perp} = 25\lambda_0$). The perturbation with $\lambda_{\perp} = 20\lambda_0$ shows the highest amplitude of instability, instead of $\lambda_{\perp} = 25\lambda_0$ which is predicted by (4.17).

Examining the time development of the transversal spectrum for these three wavelengths, we see that for a wide super-Gaussian the peak in the spectrum stays very narrow and is only slightly up- or down-shifted closer to k_{\perp}^{max} . For a Gaussian transversal shape the peak gets broader and the up/downshift is stronger. This is due to FWM between the perturbation mode and the main spectrum of the pulse. A Gaussian pulse is more localized for the same spot size. It has a broader spectrum and thus more FWM products of the pulse and the perturbation occur.

For a narrow initial pulse, especially with a Gaussian shape, another effect is superimposed. The faster transversal compression results in an upshift of the peak and thus the filaments move closer together (Fig. 4.22). This effect can be clearly distinguished from the up/downshift discussed above. It occurs later during the pulse evolution when the pulse is significantly compressed in the transversal direction (Fig. 4.23 and Fig. 4.24).

³The spatial length of the soliton is related to the temporal length by $L = \beta T$. An L_0 of $2\lambda_0$ is thus equal to a T_0 of about $2.38\lambda_0$. This has to be taken into account when comparing results from NLSE and wave equation simulations.

4. Pulse compression in two dimensions

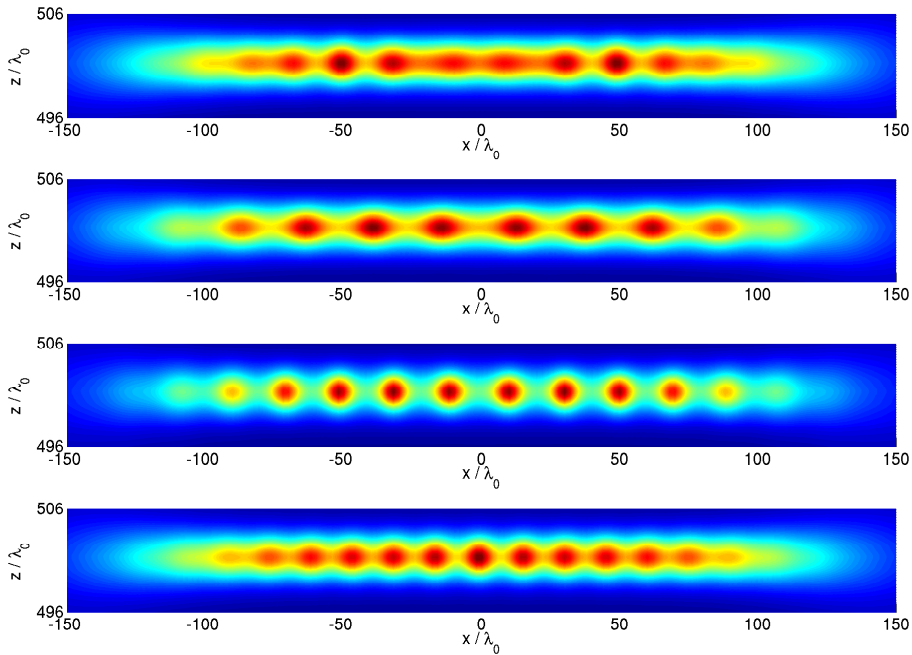


Figure 4.21: Color plot of $|a|^2$ for a simulation with cubic nonlinearity. Initial sech shape in the longitudinal direction and super-Gaussian shape in transversal direction. Bottom to top: pulses at $t = 540/\nu_0$ for an initial perturbation of $10^{-3} a_0$ with wavelengths of $15 \lambda_0$, $20 \lambda_0$, $25 \lambda_0$ and $10 \dots 30 \lambda_0$ (phase randomized). The other simulation parameters are $n_0 = 0.3 n_c$, $a_0 = 0.16$, $L_0 = 2 \lambda_0$ and $W_0 = 200 \lambda_0$.

Late in the evolution of the instability, additional peaks at higher integer multiples of the original k -value can also occur due to FWM (for details on four-wave-mixing, see [38]).

The agreement between numerics and analytics for the fastest growing mode is further confirmed by simulations with a perturbation that is a superposition of phase-randomized cosine-modes with wavelengths of $10 \dots 30 \lambda_0$, also shown in Fig. 4.21. Although the amplitude of the individual filaments is not as uniform as for a perturbation with a single wavelength, the dominant unstable wavelength is closely below $20 \lambda_0$ which matches the prediction of $18.63 \lambda_0$ by (4.18). This is the result for most drafts of random phases. But for some drafts the modes with the highest growth rates may have only small initial amplitudes, because, by adding the perturbation to the pulse, interference terms appear in $|a|^2$ that can suppress modes. The most unstable mode may still develop a high amplitude, but other modes that have a high initial amplitude can still have a large amplitude in the fully developed instability. It is even possible that they enslave modes with a higher growth rate, but smaller initial amplitude and become dominant.

For comparison with analytics, it is easier to use perturbations without this randomization, because the spectra of the instability are much simpler. Several features that occur during the development of the instability can be singled out this way. Modes

4.4. Transversal filamentation instability

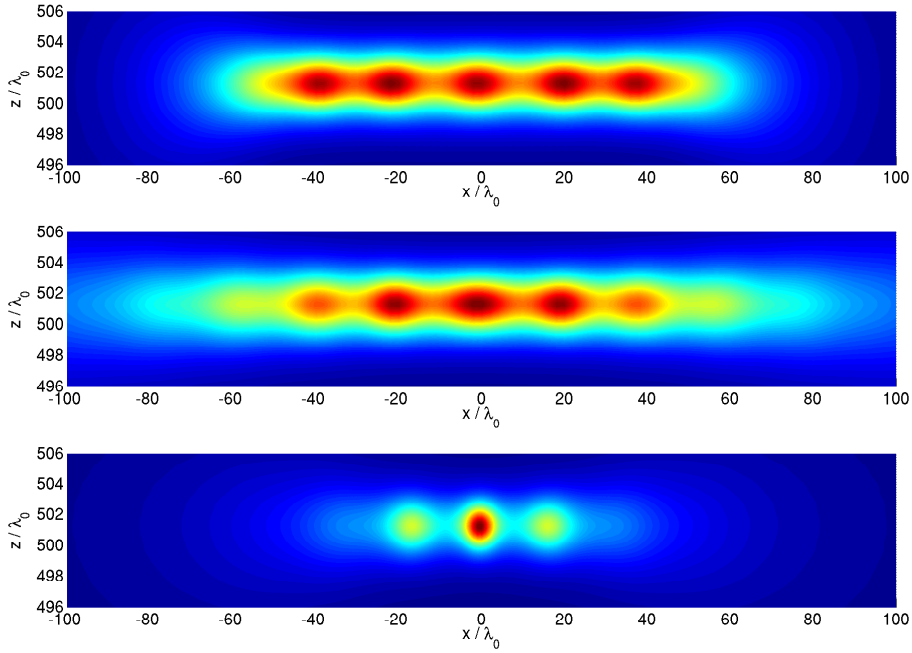


Figure 4.22: Color plots of initially Gaussian and super-Gaussian transversal shapes with different spot sizes at $t = 540/\nu_0$. Top to bottom: super-Gaussian with $W_0 = 100 \lambda_0$, Gaussian with $W_0 = 200 \lambda_0$, Gaussian with $W_0 = 100 \lambda_0$.

above the cut-off are damped as expected. But surprisingly, at first the smallest k -values show the largest growth, even for perturbation spectra that go down to $k = 2\pi/100\lambda_0$ (Fig. 4.25). For a super-Gaussian shape a distinct peak at the lower corner of the perturbation spectrum develops, probably due to the interaction with the sideband peaks in the spectrum of this function. The most unstable mode starts to show the highest growth only after the pulse has propagated for some time. The location of the peak in the spectrum is not dependent on the broadness of the perturbation spectrum, as shown in Fig. 4.26. This behavior can be explained in the following way: at first, low k -values can show the highest growth, because they are closer to the central $k = 0$ mode of the pulse and have a higher FWM efficiency. For the analytically predicted mode to show the highest growth, it is necessary that the pulse develops the matching longitudinal amplitude modulation of the transversal mode. After the pulse has changed its longitudinal shape accordingly, the growth rates behave as expected.

This effect can be circumvented by linearizing about the 1D soliton state and then iteratively “breeding” the longitudinal amplitude dependence for a given k_\perp . This method is well suited to examine the stability properties of soliton solutions where analytical statements are not possible [44]. But in our case the growth rate is already known analytically and this method would be very difficult to apply (if at all possible) for a spectrum of perturbations or compressing pulses.⁴ Instead we are interested in if

⁴In general we do not have analytical solutions for compressing pulses to linearize about. Even with

4. Pulse compression in two dimensions

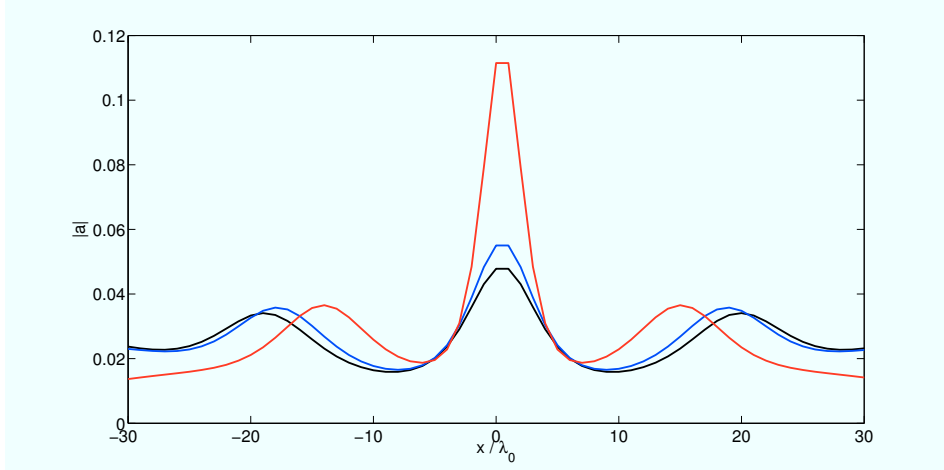


Figure 4.23: $|a|$ in transversal cuts for different initial shapes/spot sizes at $t = 350/\nu_0$. Black: super-Gaussian profile with $W_0 = 200 \lambda_0$, blue: Gaussian profile with $W_0 = 200 \lambda_0$, red: Gaussian profile with $W_0 = 100 \lambda_0$

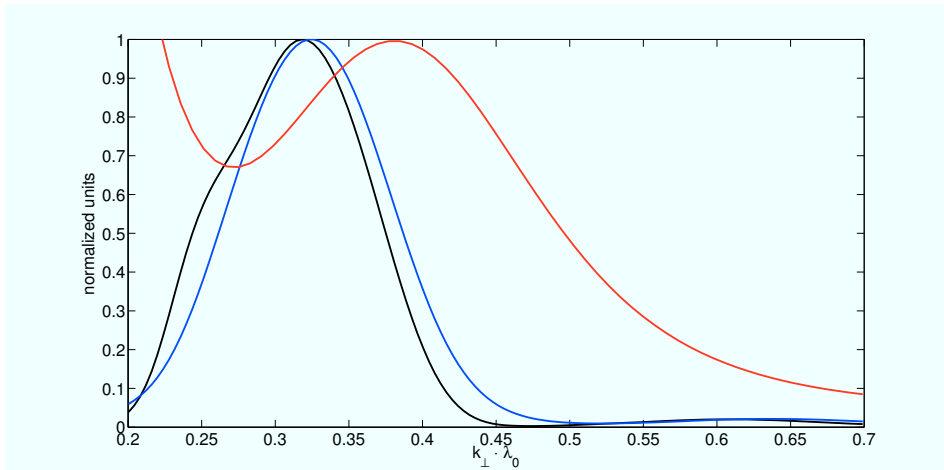


Figure 4.24: Transversal amplitude spectrum for different shapes/spot sizes at $t = 350/\nu_0$. black: super-Gaussian profile ($W_0 = 200 \lambda_0$), blue: Gaussian profile ($W_0 = 200 \lambda_0$), red: Gaussian profile ($W_0 = 100 \lambda_0$)

and how a pulse without a strong component of the matching longitudinal dependence develops the instability.

For most simulations in the next chapters, we will use phase randomized perturbation spectra. They model real physical systems better, and the phase randomization furthermore guarantees that the perturbation covers the full width of the pulse. Without it the perturbation would become the more localized in space, the broader its spectrum is. Randomization of the amplitude of the modes alone would not have this effect, while randomization of the phase yields a weakly localized perturbation with a random amplitude of the Fourier component.

such a solution, using this method would be very difficult, because the unperturbed state would be non-stationary.

4.4. Transversal filamentation instability

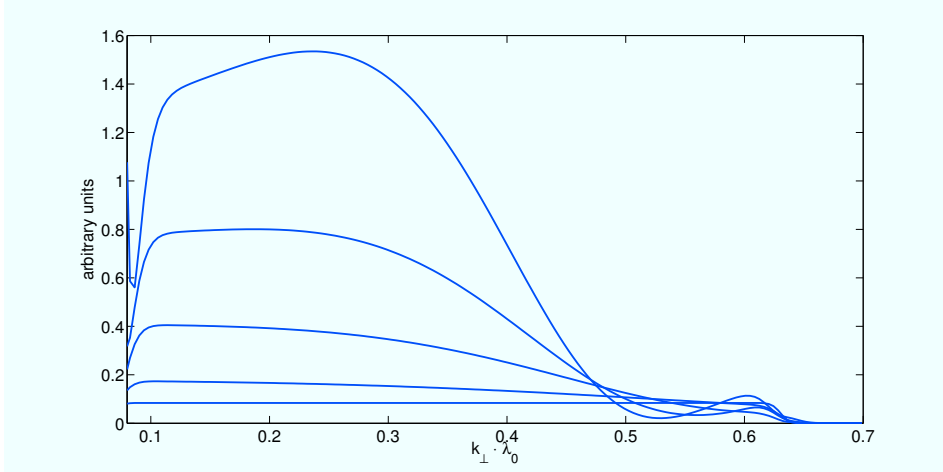


Figure 4.25: Time development of the transversal amplitude perturbation spectrum for an initial perturbation with wavelengths of $10 \dots 100 \lambda_0$ of equal amplitude. 1D soliton with a Gaussian initial shape in the transversal direction ($L_0 = 2 \lambda_0$, $W_0 = 200 \lambda_0$, $n_0 = 0.3 n_c$).

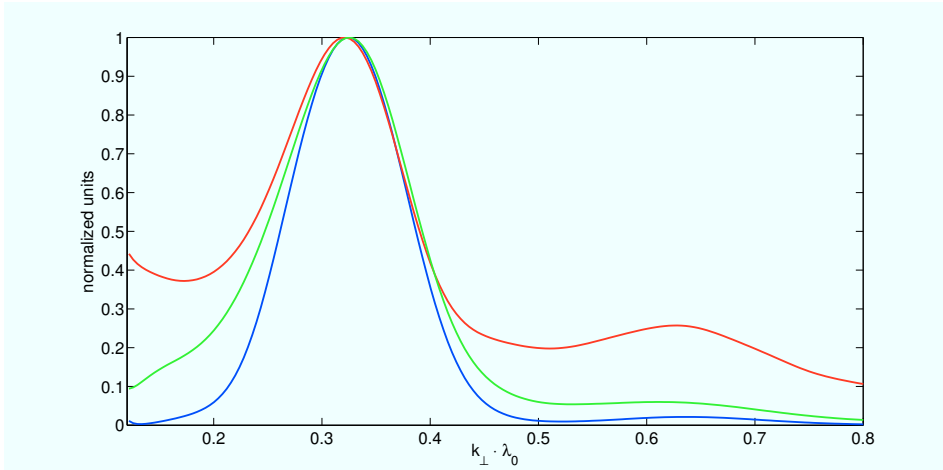


Figure 4.26: Transversal amplitude spectrum at $t = 700/\nu_0$ for different initial perturbation spectra. Blue: $10 \dots 30 \lambda_0$, red: $7 \dots 50 \lambda_0$, green: $10 \dots 100 \lambda_0$. Initially Gaussian transversal shape with $W_0 = 200 \lambda_0$.

Several different phase-randomized drafts for the transversal perturbation can be seen in Fig. 4.27. The resulting instability that evolves out of this initial perturbations is shown in Fig. 4.28. The correspondence between the initial amplitudes of the individual modes and the spectrum of the fully developed instability can be clearly seen. For the draft plotted in black, there is sufficient initial amplitude in the most unstable range of $k \approx 0.325/\lambda_0$ and no peaks at other locations with much higher amplitude. This results in a broad peak around this value at the later time. The blue draft has the largest initial amplitude at around $k \approx 0.26/\lambda_0$, which still is the largest at $t = 600/\nu_0$. But due to a higher growth rate a second peak that initially had a lower amplitude could grow to nearly the same value. For the red draft the situation is reversed. The

4. Pulse compression in two dimensions

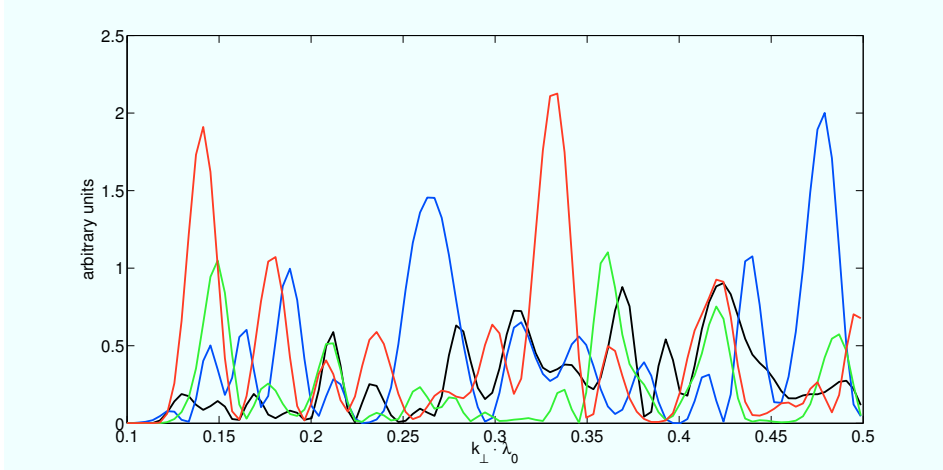


Figure 4.27: Initial spectra for different phase-randomized transversal perturbations with wavelengths of $7 \dots 50 \lambda_0$.

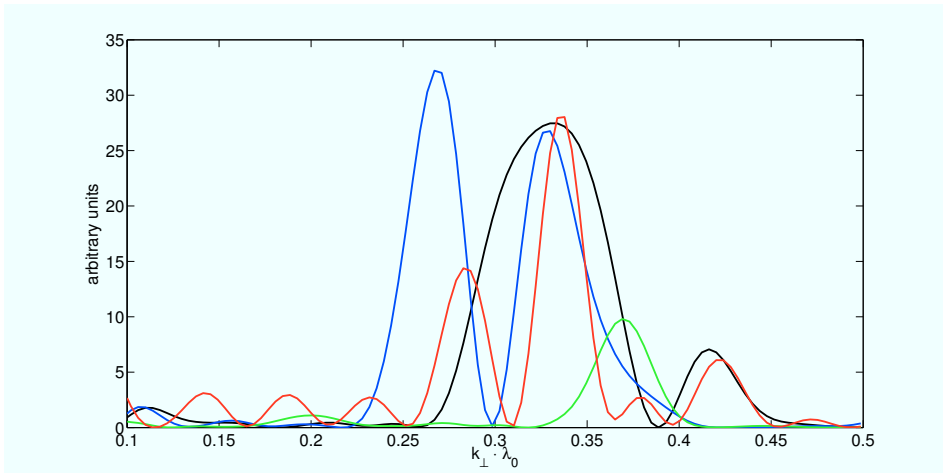


Figure 4.28: Spectra of the initial perturbations shown in Fig. 4.27 at $t = 600/\nu_0$.

peak with the largest initial value also has the largest growth rate and the largest final amplitude, but a second peak at a lower k -value could still develop. The green draft is an example that the mode with the largest growth rate will not necessarily develop a large amplitude. Initially there is small but finite amplitude between $k = 0.3$ and $k = 0.35$ but at $t = 600/\nu_0$ there is only a single peak with a maximum at $k = 0.37$, which also had the largest initial amplitude.

The long term behavior of the transversal instability is different from e.g. the modulation instability of the 1D plane wave. Modulation instability eventually saturates into a new stable state that is a train of 1D solitons. In 2D, soliton solutions of the cubic NLSE are only marginally stable, and collapse for a slightly higher amplitude into a singularity. The collapse of the individual filaments for a simulation of the cubic nonlinear wave equation is shown in Fig. 4.29.

In reality a laser pulse does of course not collapse into a singularity, because the cubic nonlinearity $(1 - \frac{1}{2}|a|^2)a$ is only a series expansion for small amplitudes of the correct

4.4. Transversal filamentation instability

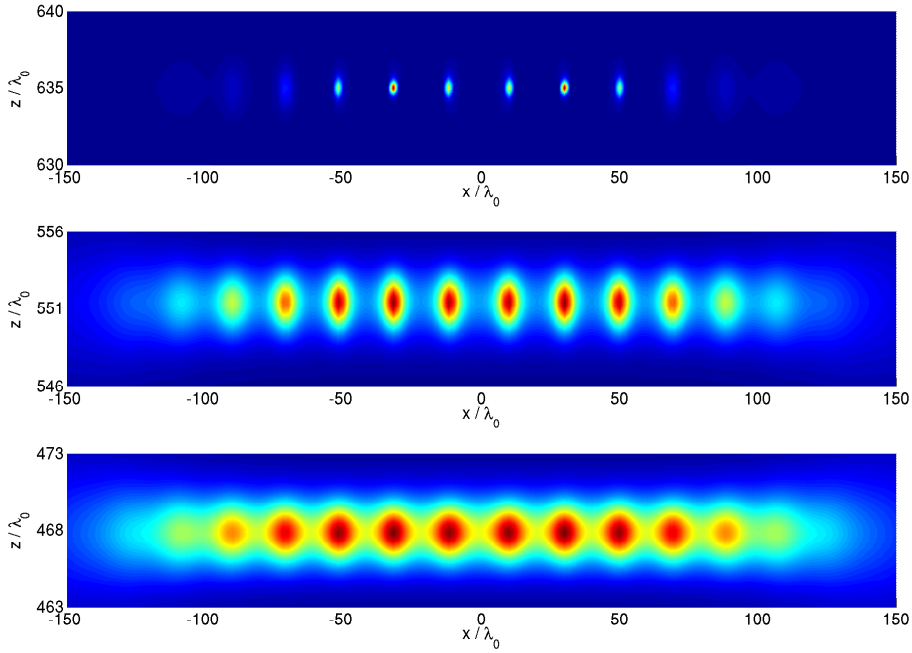


Figure 4.29: Color plots of $|a|^2$ at different times for a simulation with cubic nonlinearity. Initial sech pulse shape in the longitudinal direction and super-Gaussian in the transversal direction. Initial pulse perturbation with $10^{-3} a_0$ and a wavelength of $20 \lambda_0$. Bottom to top: $t = 500/\nu_0$, $t = 600/\nu_0$, $t = 700/\nu_0$. Other simulation parameters are $n_0 = 0.3 n_c$, $a_0 = 0.16$, $L_0 = 2 \lambda_0$ and $W_0 = 200 \lambda_0$.

relativistic mass factor of $\gamma = \sqrt{1 + |a|^2}$. The correct nonlinearity saturates for higher amplitudes and thus the growth of the instability is slowed. For higher amplitudes, density effects have to be taken into account, too. In the simplified model equations we use, the density perturbation at first accelerates the growth of the instability, because the collapsing filaments produce cavities in the electron density by pushing the electrons outwards through the ponderomotive force. This leads to a stronger trapping of the filaments which compensates for the saturation of the γ -nonlinearity, as shown in Fig. 4.30. But the more the filaments collapse, the stronger the wakefield that they generate becomes and the more energy is transferred to the plasma.

Within our model equations, it still happens that in simulations the filaments collapse to point-like structures and that density oscillations become larger than the background density. To fully avoid this problems, the heating of the plasma through kinetic effects has to be taken into account. Since parameter ranges for which high energy transfer between laser pulse and plasma occurs are not interesting for efficient pulse compression, density perturbations of the order of the background density will simply be taken as signs that the simulated parameters are not suitable for the intended application.

4. Pulse compression in two dimensions

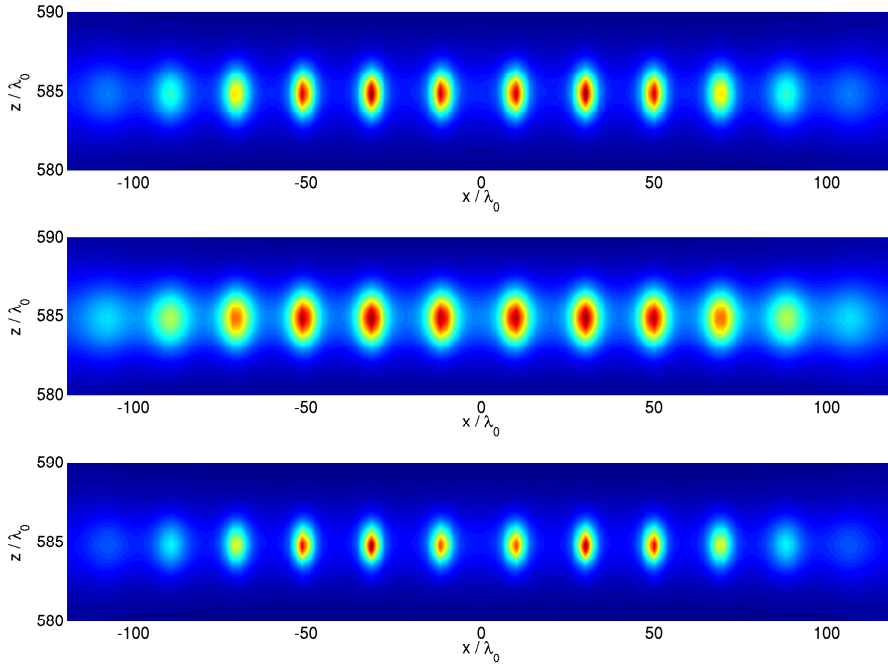


Figure 4.30: Influence of different nonlinearities in the wave equation on the transversal instability. From top to bottom: cubic nonlinearity (maximum $|a| = 0.28$), γ -nonlinearity (maximum $|a| = 0.24$), γ -nonlinearity and density response (maximum $|a| = 0.32$) at $t = 640/\nu_0$. Otherwise same parameters as in Fig. 4.29.

4.4.2 Longitudinally compressing pulses

For a pulse that compresses in the longitudinal direction, the behavior of the transversal instability is more complex. As an example we consider a pulse that has the same longitudinal shape as a soliton, but several times its amplitude. The mode that grows to the largest amplitude is not anymore independent of the width of the perturbation spectrum, although this effect is small (Fig. 4.31). During the pulse compression, shorter and shorter wavelengths can become unstable, so it is not necessarily a single mode that dominates. For pulses with the same initial spot size, but different amplitudes (higher amplitude equals faster compression) the spectrum of modes that show instability gets broader for higher amplitudes, as shown in Fig. 4.32. The spectra have to be compared at times where the pulse lengths and pulse widths are nearly the same for different initial amplitudes. If an unstable mode has sufficient time to grow before shorter wavelengths become unstable, it can even enslave the shorter modes and prevent their growth.

Since the pulse changes its longitudinal shape during the compression, it is unclear if the relationship between pulse length and most unstable transversal mode is the same as in the stationary case. In Fig. 4.32 we see that the peaks of the spectrum are generally lower than expected for a stationary pulse of the corresponding length. But for an initial pulse of four times the single soliton amplitude, it is actually at a k -value expected for a

4.4. Transversal filamentation instability

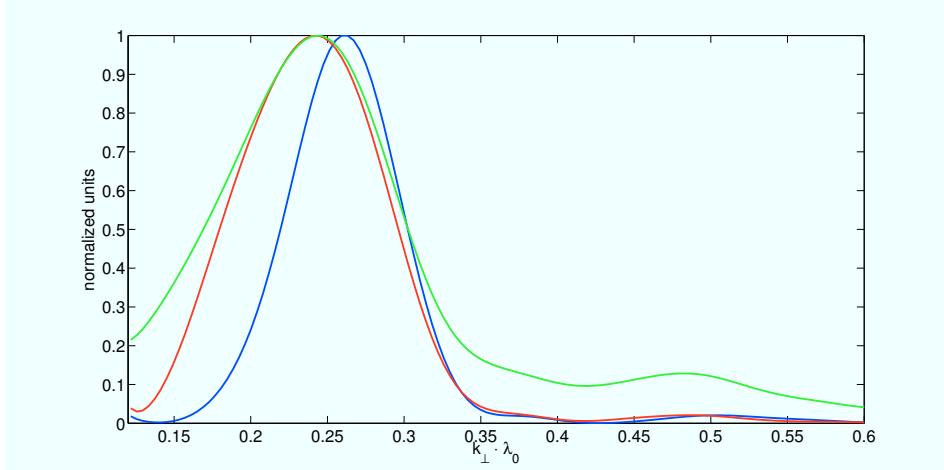


Figure 4.31: Transversal amplitude perturbation spectrum at $t = 380/\nu_0$ for a 1D soliton with an initially Gaussian shape in the transversal direction. Initial perturbation spectra of $10 \dots 30 \lambda_0$ (blue), $7 \dots 50 \lambda_0$ (red) and $10 \dots 100 \lambda_0$ (green). Other simulation parameters are $L_0 = 2 \lambda_0$, $W_0 = 200 \lambda_0$ and $n_0 = 0.3 n_c$.

pulse of length $L = 2.3\lambda_0$. This might occur, because the pulse rise and falloff becomes very steep during the compression and thus is very far from the shape of the soliton.

Another interesting question is how the initial longitudinal shape influences the instability. Especially important would be any difference between a sech-shaped pulse and a Gaussian pulse, because this is the pulse shape mostly used in experiments. The interesting result is that only the initial longitudinal half width needs to be equal.⁵ The transversal spectra will then be nearly equal at equal times, although the evolution of length and width is different. The graphs of length and spot size vs. time can be scaled to nearly match by multiplying the time axis by some factor to compensate the slower compression of the Gaussian pulse. This scaling factor does not seem to depend on plasma density or the width of the pulse. It only depends on the number N that gives the amplitude of the pulse relative to the single soliton amplitude and thus determines how fast the pulse compresses. It is reasonable to assume that this difference is due to the lower energy the Gaussian pulse has compared to a sech-shaped pulse at the same half width, due to the different asymptotic fall off. Note that at points in time where both pulse shapes have the same length and spot size, the spectra of their instability are different! An example is shown in Fig. 4.33.

Another important difference to the case of stationary pulse length we have discussed above is, that a pulse with parameters in a realistic range for pulse compression will have a much smaller ratio between its initial spot size and length, than the very short and wide pulses we considered in the previous section for comparison with analytics. If we take the analytical results for solitons as a guide, the range of wavelengths below the cut-off that will initially fit on such a pulse is very small. If we take a pulse with a length of $L_0 = 10 \lambda_0$, a spot size of $W_0 = 100 \lambda_0$ and a Gaussian transversal profile,

⁵But remember the difference between the length parameter L_0 and the actually measured half width. This leads to a factor of 1.58183 between L_0 for a Gaussian pulse and a soliton.

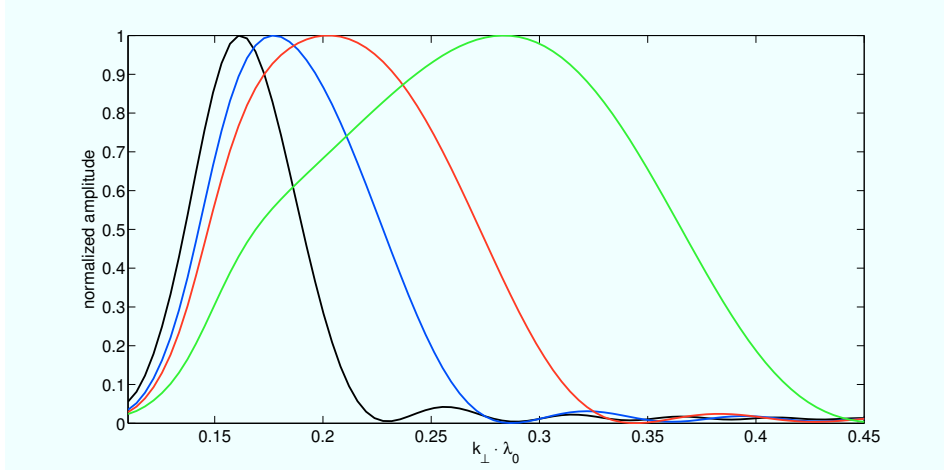


Figure 4.32: Transversal amplitude perturbation spectrum for initially $\text{sech}(z/L_0)$ -shaped pulses ($L_0 = 10\lambda_0$) with an amplitude of N -times the single soliton amplitude. The spectra are at a different times for each value of N such that each pulse has a length of $L = 3.16\lambda_0$ at that particular time. Black: $N = 2$, blue: $N = 2.5$, red: $N = 3$, green: $N = 4$.

the most unstable mode has a wavelength $\approx 94\lambda_0$ and the cut-off wavelength is $\approx 66\lambda_0$. Examining the transversal Fourier-spectrum of the pulse, we see that the modes up to the cut-off are close to, or already part of, the modes that determine the shape of the pulse. Through the broadening of the spectrum due to transversal compression, they become part of the core spectrum of the pulse in a short time. The dynamics of these modes is thus dominated by the dynamics of the main pulse and not by the transversal instability.

Only modes that are short compared to the wavelengths of the unperturbed pulse spectrum can effectively destroy the pulse and prevent efficient compression. For experimentally interesting parameter regimes, it is only possible for those modes to become unstable after sufficient longitudinal compression. This suggests that for a compressing pulse the transversal instability has only a finite time window to develop. This time window starts at the point where the pulse has become sufficiently short that the unstable wavelength are short compared to the spot size and ends at the point where the pulse is maximally compressed (where the plasma layer should end). If the initial pulse has a very clean spectrum with little noise, or the plasma produces no noise in the unstable range of wavelengths, no instability can develop.

4.5 Other 2D / 3D instabilities

Besides transversal filamentation there are other genuinely two or three dimensional instabilities of a laser pulse that can occur inside of the plasma. These can either be related to Raman instability and occur due to a resonance between the laser pulse and the plasma wakefield, or be driven by the relativistic mass nonlinearity and are only enhanced by the wakefield. The first type can only occur at densities below $0.25n_c$ and

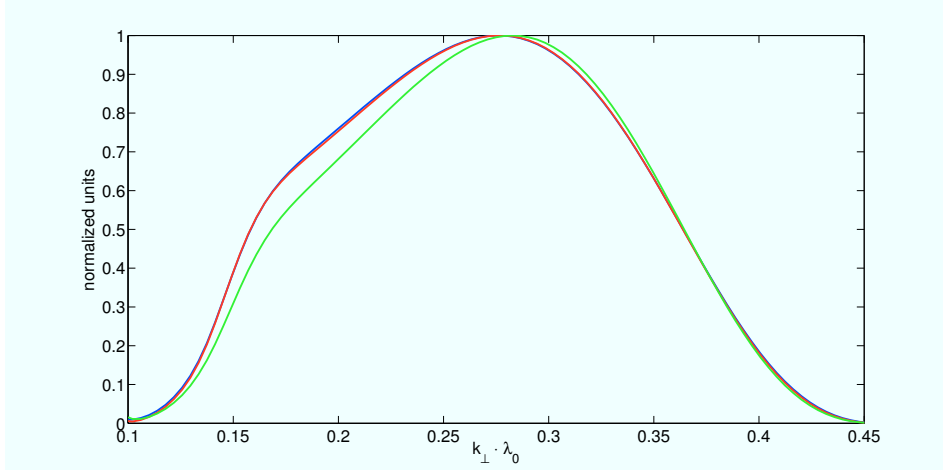


Figure 4.33: Comparison of transversal amplitude spectra for an initial $\text{sech}(z/L_s)$ pulse and an initial Gaussian pulse of length L_g . $L_s = 10 \lambda_0$ and L_g is chosen such that the measured longitudinal half width are initially equal. a_0 is $N = 4$ times the single soliton amplitude. Blue: sech pulse at $t = 330/\nu_0$. Red: Gaussian pulse at $t = 330/\nu_0$, Green: Gaussian pulse at $t = 360/\nu_0$ (same length and spot size as the sech pulse at $t = 330/\nu_0$).

is in the short wavelength range. The second type can also cause instability at higher densities and has a longer wavelength. Here short vs. long wavelength is relative to ω_p/c . The actual wavelength for a long wavelength instability at high density can thus be shorter than the plasma wavelength at low densities.

Three types of instability for a linear polarized laser beam are discussed in [14] by means of the variation-of-action method and linear stability analysis. These are hosing as well as symmetric and antisymmetric self-modulation instability. These instabilities can be derived from a nonlinear Schrödinger equation coupled to an equation for the plasma potential ϕ

$$\left(\nabla_{\perp}^2 - 2i\beta \frac{\partial}{\partial \zeta} \right) a = (1 - \phi)a \quad (4.20)$$

$$\frac{\partial^2}{\partial \tau^2} \phi + \phi = \frac{|a|^2}{2} . \quad (4.21)$$

Details of the calculation for circular polarization can be found in appendix C.

The stationary solution for which the linear stability is examined is a laser beam of infinite longitudinal length and a finite spot size (with Gaussian profile) that is at the threshold of transversal self focusing. Of course in the end we are interested in the behavior of the instabilities above the threshold, but as long as the growth of the instabilities is faster than the self-focusing process, the analysis should be approximately valid. The case where the beam focusses faster than the instability can grow is of no interest, because the instability then is of no physical relevance. The threshold can be calculated as

$$a_0^2 W_0^2 = P_0 \geq P_c = 16 .$$

4. Pulse compression in two dimensions

The threshold is ($P_c = 32$) for linear polarization. Otherwise the linearized equations for the instabilities are identical for both kinds of polarization. The general form of these equations is

$$\begin{aligned} (\partial_\zeta^2 + \Gamma_1) f &= \Gamma_2 h \\ (\partial_\tau^2 + 1) h &= \Gamma_3 f, \end{aligned} \tag{4.22}$$

where f and h are two of the collective coordinates used to describe the pulse shape and/or the shape of the plasma potential.

From these two coupled equations we can derive some general properties of the instabilities. Fourier analysis yields a dispersion relation and thus a growth rate dependent on the wave number of the perturbation. Plotting the growth rate $\text{Im}(g)$ against k , we can see that the general form is linear growth of $\text{Im}(g)$ with k for small values of k and a distinct peak around $k = \omega_p/c$ where a resonance with the wakefield wavelength occurs.⁶ Above the peak a sharp cut-off occurs at

$$k = \sqrt{\frac{\Gamma_1 - \Gamma_2\Gamma_3}{\Gamma_1}}.$$

At the resonance $k = \omega_p/c$ the growth rate is

$$g = \left(\frac{\Gamma_2\Gamma_3}{2}\right)^{\frac{1}{3}} \frac{-1 \pm \sqrt{3}i}{2}.$$

This describes the short wavelength type of the instabilities dominant at densities lower $k = \omega_p/c$.

For the long wavelength type instabilities to occur the condition that

$$\Gamma_2\Gamma_3 \geq \Gamma_1$$

has to be fulfilled.

The growth rate for small values of k then is

$$g = i\sqrt{\Gamma_1}k.$$

Important to understand the relevance of these instabilities is that Γ_1 and $\Gamma_2\Gamma_3$ are inversely proportional to the square of the Rayleigh length $z_R = \beta W_0^2/2$. This implies that the growth rates rapidly decrease with the spot size. For wide pulses these instabilities are thus not relevant. They could only become important after very strong transversal compression, but then still unlikely if the pulse is sufficiently short.

4.5.1 Hosing instability

The centroid of the laser beam can be unstable to perturbations and show sinusoidal oscillations like a winding snake or water hose, hence the name hosing instability. In

⁶Because the NLSE used is derived for a frame comoving at c instead of v_g , the wakefield wavelength is $2\pi c\omega_p$ instead of $2\pi v_g/\omega_p$. This is only a good approximation at low densities.

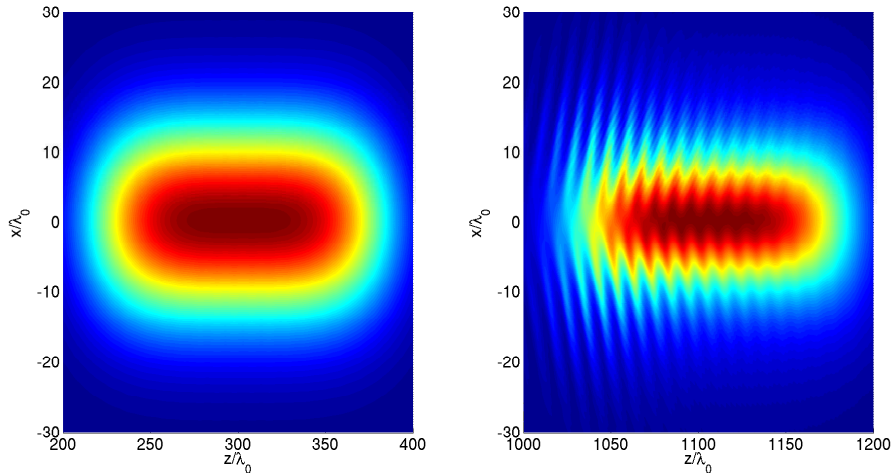


Figure 4.34: Left: initial pulse of longitudinally super-Gaussian ($L_0 = 100 \lambda_0$) and transversally Gaussian shape ($W_0 = 20 \lambda_0$) with $a_0 = 0.3$. Sinusoidal initial perturbation of $0.01 W_0$ for short wavelength hosing with $k = \omega_p/c$. Right: Pulse at $t = 820/\nu_0$ after propagation through plasma of $n_0 = 0.01 n_c$.

(4.22) the quantities f and g for this instability are the centroids x_a and x_ϕ of the laser and the plasma potential respectively and the constants are $\Gamma_1 = \Gamma_2 = \frac{P_0}{P_c} \frac{1}{z_R^2}$ and $\Gamma_3 = 1$.

In the short wavelength regime at low densities, hosing leads to an alternating shifting of the Raman filaments against the central axis. The wavelength can become longer, if a saturated Raman instability heats the plasma sufficiently [13]. Fig. 4.34 shows an example for short wavelength hosing, before Raman instability has fully developed. It is clearly visible that the amplitude of instability increases from the front to the back of the pulse, because the resonance between pulse and wakefield has more time to develop.

At higher densities only the nonresonant form of the instability can occur for which the growth rate increases with the background density.⁷ Since the instability is mostly due to the relativistic mass nonlinearity, it is more uniform along the pulse. The only exception are the parts right at the beginning and end of the pulse. But even for a high density like $n_0 = 0.6 n_c$ and a very narrow pulse of $W_0 = 10 \lambda_0$ the growth of the instability is comparatively slow (see Fig. 4.35). Only after $300 \lambda_0$ of plasma the instability has grown to a significant amplitude.

4.5.2 Symmetric self-modulation instability

A small sinusoidal amplitude modulation in the longitudinal direction of a long and narrow pulse can lead to an uneven focusing along the pulse. This is called symmetric self-focusing instability. Slices of the pulse can collapse while other slices are still only weakly focused or (if the beam is at the self-compression threshold) even defocused. This effect is enhanced by the density oscillations of the plasma. Regions with higher than background density have a defocusing effect, while regions with lower than background

⁷The density dependence is only implicit, due to the normalization of lengths and times with ω_p .

4. Pulse compression in two dimensions

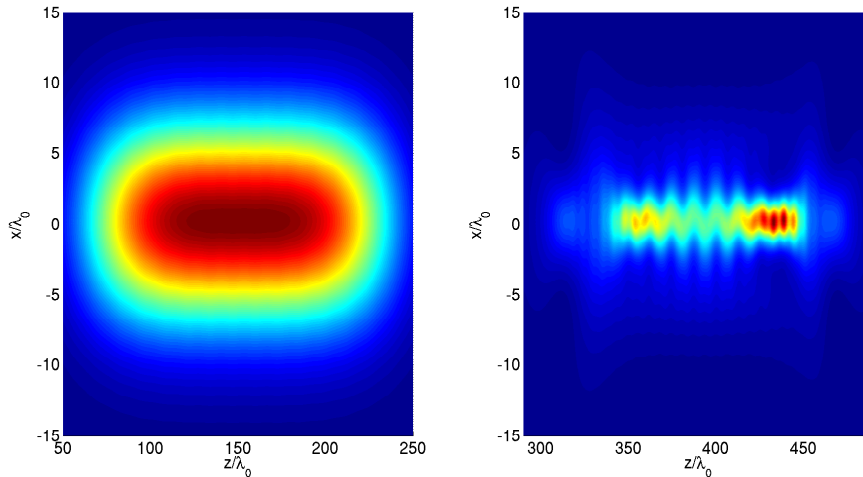


Figure 4.35: Left: initial pulse of longitudinally super-Gaussian ($L_0 = 100 \lambda_0$) and transversally Gaussian shape ($W_0 = 10 \lambda_0$) with $a_0 = 0.15$. Sinusoidal initial perturbation of $0.02 W_0$ for short wavelength hosing with $k = 0.1 \omega_p/c$. Right: Pulse at $t = 250/\nu_0$ after propagation through plasma of $n_0 = 0.6 n_c$.

density focus the beam. At $n_0 < 0.25 n_c$ this process can be resonant with the wakefield, but only modulates filaments induced by Raman instability to yield the typical inverse D shape [50] that can be seen in Fig. 4.36.

The relevant quantities for (4.22) are \bar{w}_a and \bar{w}_ϕ , the averages of the spot sizes in x - and y -direction of a and ϕ . For the exact definition see appendix C. The constants are $\Gamma_1 = \Gamma_2 = \frac{P_0}{P_c} \frac{1}{z_R^2}$ and $\Gamma_3 = 1$. For $n_0 > 0.25 n_c$ the density oscillations can only enhance the instability, but are not in resonance with the wakefield. The main difference between Raman instability and self-modulation can be seen in Fig. 4.37. Raman forward scattering redistributes pulse energy along the propagation direction and leads to a lumping of the energy. Low amplitude regions thus also have a narrow spot size. Symmetric self-modulation instead transversally focuses the pulse power, while the power in each transversal slice remains constant. This leads to a narrow spot size for slices with a high amplitude and a wide spot size for slices of low amplitude (Fig. 4.37).

4.5.3 Antisymmetric self-modulation instability

Related to the symmetric self-modulation is an asymmetric unstable mode, where a decreasing spot size in one transversal direction leads to an increasing spot size in the other. The unstable quantities for (4.22) are Δw_a and Δw_ϕ , the differences between the spot sizes in x - and y -direction of a and ϕ respectively. Antisymmetric self-modulation is the only true 3D instability of the instabilities we have discussed. Fortunately its growth rate decreases rapidly with the spot size as for the other two instabilities. Otherwise full 3D simulations would be necessary. For this instability $\Gamma_1 = \frac{3}{z_R^2}$, $\Gamma_2 = \frac{1}{z_R^2} \frac{P_0}{P_c}$ and $\Gamma_3 = 1$. Thus as long as $P_0 \leq 3 P_c$ no long wavelength regime exists. But this threshold is already crossed for a pulse with $a_0 \gtrsim 1.7 a_c$. Most pulses we will use for simulations

4.5. Other 2D / 3D instabilities

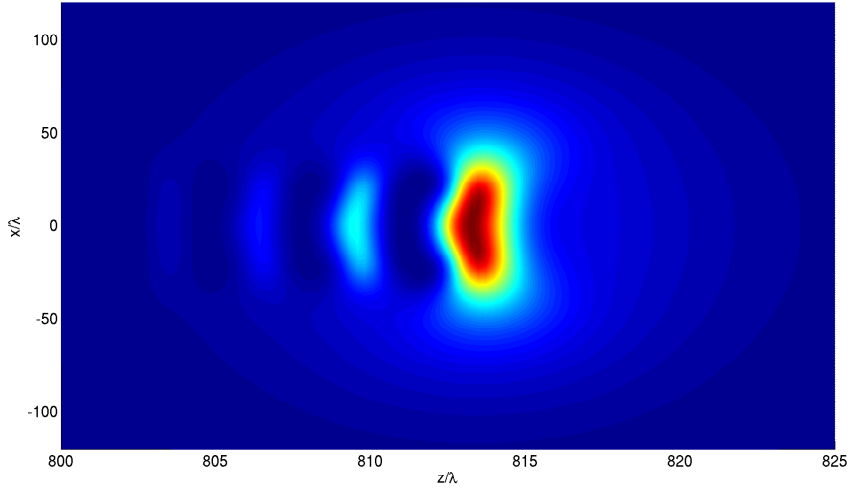


Figure 4.36: Color plot of 2D filaments induced by Raman instability for a simulation with $n_0/n_c = 0.1$, $a_0 = 0.16$, $L_0 = 10 \lambda$ and $W_0 = 100 \lambda$.

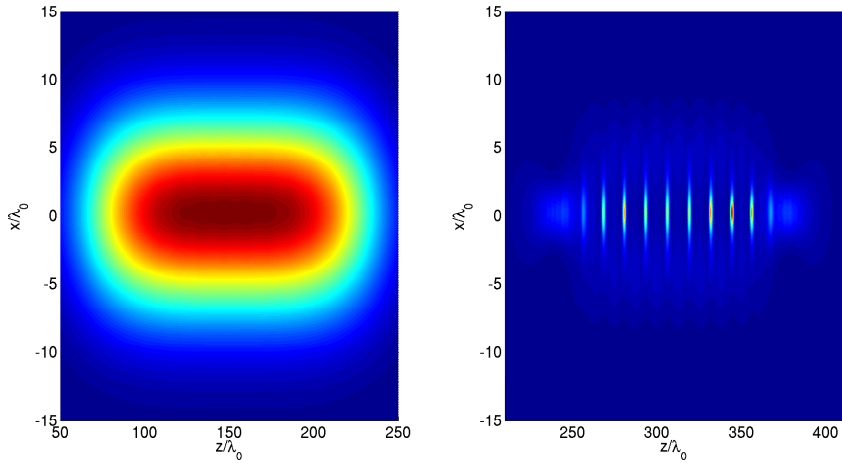


Figure 4.37: Left: initial pulse of longitudinally super-Gaussian ($L_0 = 100 \lambda_0$) and transversally Gaussian shape ($W_0 = 10 \lambda_0$) with $a_0 = 0.15$. Sinusoidal initial perturbation of $0.02 W_0$ for short wavelength symmetric self-modulation with $k = 0.1 \omega_p/c$. Right: Pulse at $t = 250/\nu_0$ after propagation through plasma of $n_0 = 0.6 n_c$.

of self-compression will be at least a factor of two above the compression threshold. Accordingly we have to use sufficiently wide initial pulses to avoid this instability and the necessity of 3D simulations.

5 Transversal focusing with plasma layers

To evaluate the pulse compression potential of plasmas, it is necessary to include the propagation in vacuum after the pulse has left the plasma. In 2D/3D geometry a plasma layer can act as a lens with a certain focal length. This increases the intensity of the pulse through a decrease in spot size. In this chapter we will first study the focusing properties of such a plasma lens and also compare (semi-)analytical descriptions of the plasma-vacuum transition and pulse focusing to full wave equation simulations. In the second part of the chapter, we investigate the propagation of transversal modes from filamentation instability in relation to the propagation of the main pulse. The results from both parts motivate the idea to use a layered plasma-vacuum structure for pulse compression. This will be detailed in the next chapter.

5.1 Focusing properties of plasma layers

The propagation of electromagnetic radiation in vacuum in 1D is very different from the 2D/3D case. In 1D an electromagnetic pulse propagates unchanged in vacuum. In 2D the pulse can either focus or defocus in the direction transversal to the propagation. A beam or pulse that at first focuses, will start to defocus after it reached a certain minimal spot size, called the beam waist. This behavior can be modelled with a homogeneous Schrödinger equation, which can be derived from the homogeneous wave equation by the so called paraxial approximation [61]

$$i\frac{\partial}{\partial z}a + \frac{1}{2}\frac{\partial^2}{\partial x^2}a = 0 \quad (5.1)$$

The approximation holds for beam waists that are large compared to the laser wavelength. Non-paraxial effects are for example discussed in [16].

The well known solution of this equation is the Gaussian beam [61]

$$u(z, x) = \frac{1}{W(z)}e^{i\phi(z)}e^{-x^2/W(z)^2 - ik_0\frac{x^2}{2R(z)}} \quad (5.2)$$

with the spot size

$$W(z) = W_0 \sqrt{1 + \frac{z^2}{z_R^2}} \quad (5.3)$$

5.1. Focusing properties of plasma layers

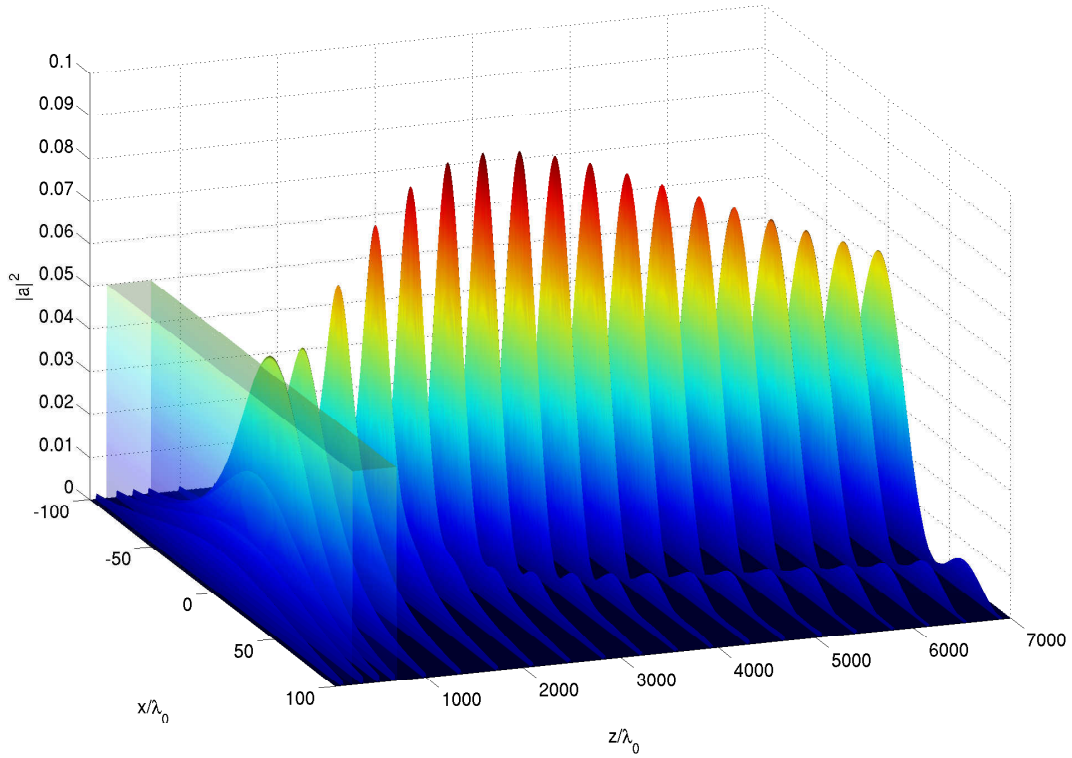


Figure 5.1: Time evolution of $|a|^2$ for a simulation of a $450\lambda_0$ thick plasma lens with $n_0/n_c = 0.3$, $a_0 = 0.1$, $L_0 = 10\lambda_0$ and $W_0 = 100\lambda_0$. The density profile is shown semi-transparent.

where W_0 is the waist spot size. The radius of curvature of the phase front is

$$R(z) = z + \frac{z_R^2}{z}. \quad (5.4)$$

The Rayleigh length

$$z_R = \pi \frac{W_0^2}{\lambda_0} \quad (5.5)$$

is the length of propagation where the pulse changes its diameter by a factor of $\sqrt{2}$.

Due to the missing time derivatives in equation 5.1, its solution can be modulated in time by an arbitrary time dependent function $v(t)$ to obtain a localized pulse $a(z, x, t) = v(t) \times u(z, x)$. Any initial condition $a(z = z_0, x, t)$ of this form will keep its longitudinal half width. In the derivation of (5.1) the mixed derivative $\frac{\partial^2}{\partial t \partial z}$ was neglected, which results in the conservation of power in each transversal slice

$$P(z) = A(z)^2 W(z) = A_0^2 W_0 = \text{const.} \quad (5.6)$$

Thus no power is transferred on-axis in the comoving frame.

For a negative curvature $R(z)$ the pulse will focus until its spot size reaches W_0 at the focal point. By letting a highly intense laser pulse pass through a plasma layer, the

5. Transversal focusing with plasma layers

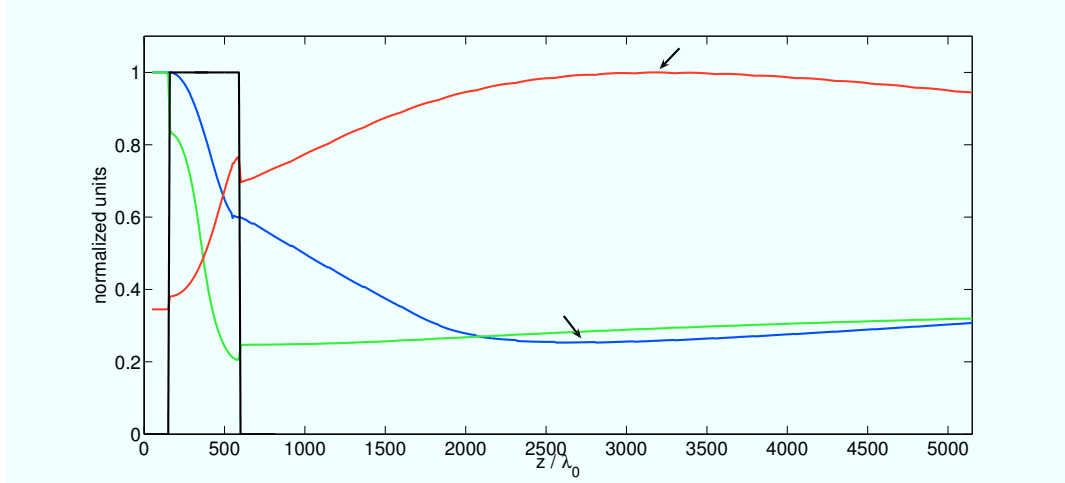


Figure 5.2: Evolution of pulse parameters for the simulation in Fig. 5.1 in normalized units. Density profile (black), amplitude $|a|$ (red), length L (green), spot size W (blue). The arrows mark the position of the maximum amplitude and minimum spot size.

relativistic nonlinearity produces such a curvature of the phase front of the pulse. This results in the transversal focusing of the pulse after it has left the plasma and propagates in vacuum. A plasma layer can thus be used as a focusing lens for laser intensities where a classical lens would be damaged. The focusing effect is shown in Fig. 5.1.

For pulses that interacted nonlinearly with a plasma layer before propagation in vacuum, the simple formulas for a Gaussian beam are only approximately valid. Compared to a Gaussian beam, the focusing behind a plasma layer can be highly asymmetric relative to the focal plane. The focusing occurs on a much shorter scale than the defocusing. Surprisingly the minimum of the spot size and the maximum of the amplitude need not (and in general do not) coincide as can be seen in Fig. 5.2, the amplitude reaches its maximum further away from the plasma.

The length evolution shows an at first unexpected effect, too. Compared to the Schrödinger model in vacuum the wave equation of course allows the pulse to change its length. But the effect should be very small for the parameters in our example and not as large as seen in Fig. 5.2. A Schrödinger simulation shows nearly the same length evolution, although the dispersion parameter in front of the time derivative is zero in vacuum.

We can understand this by realizing an important difference between a pulse of the form $a(z, x, t) = v(t) \times u(z, x)$ that propagates only in vacuum and a pulse that has propagated through a nonlinear medium. Due to the nonlinearity the pulse can have a different transversal spectrum for each value of the time coordinate. Each transversal slice can thus focus and defocus on a different time scale. The lower amplitude tails of the pulse will thus change its amplitude more slowly than the higher amplitude core, because there the nonlinearity produced a broader spectrum. In Fig. 5.3 the faster focusing and defocusing of the transversal slices with higher amplitude can be clearly seen. For a pulse that has maximally compressed in plasma the length always increases in vacuum, while pulses that are far from maximum compression shorten and then

5.1. Focusing properties of plasma layers

W_0	L_P	A_{PV}	A_{\max}	F_W	W_{\min}	W_{PV}	$\frac{W_{\min}}{W_{PV}}$	$W(F_W)$	$\frac{W(F_W)}{W_{PV}}$
100	200	0.126	0.149	5780	55	85	0.65	65	0.76
	320	0.172	0.216	3170	38	66	0.57	46	0.70
	460	0.214	0.318	1615	22	58	0.38	32	0.55
150	200	0.125	0.149	13190	83	128	0.65	97	0.76
	320	0.170	0.214	7720	57	101	0.56	72	0.71
	460	0.204	0.310	4490	35	93	0.38	54	0.58
200	200	0.125	0.149	23590	111	171	0.65	130	0.76
	320	0.169	0.214	13870	77	136	0.56	96	0.70
	460	0.201	0.307	8355	48	126	0.38	73	0.58
250	200	0.125	0.149	36840	139	214	0.65	163	0.76
	320	0.169	0.213	21920	96	171	0.56	120	0.70
	460	0.199	0.306	13430	61	159	0.38	93	0.59
300	200	0.125	0.149	53540	167	257	0.65	196	0.76
	320	0.169	0.213	32420	115	206	0.56	146	0.71
	460	0.199	0.305	19480	73	192	0.38	112	0.59

Table 5.1: Characteristic quantities of transversal focusing in Cartesian 2D geometry, dependent on the initial spot size W_0 and the plasma length L_P . A_{PV} : amplitude after plasma-vacuum transition, A_{\max} : maximum amplitude, F_W : focal point with minimum spot size, W_{\min} : minimum spot size, W_{PV} : spot size after plasma-vacuum transition. $W(F_W)$: spot size a Gaussian beam of minimum spot size W_{\min} would have at a distance of F_W away from the focus (this can be compared to the real spot size W_{PV} at that distance). The other simulation parameters are $a_0 = 0.1$, $L_0 = 10 \lambda_0$ and $n_0 = 0.3 n_c$.

Pulse parameters	L_P	W_{\min}/W_{PV}	$W(F_W)/W_{PV}$
$a_0 = 0.1, L_0 = 10 \lambda_0$	200	0.65	0.76
	320	0.56 - 0.57	0.70 - 0.71
	460	0.38 - 0.39	0.55 - 0.59
$a_0 = 0.1, L_0 = 20 \lambda_0$	200	0.65	0.76
	350	0.47 - 0.48	0.64 - 0.65
	530	0.33 - 0.38	0.51 - 0.58
$a_0 = 0.14, L_0 = 10 \lambda_0$	140	0.56	0.70
	180	0.54 - 0.55	0.70 - 0.71
	230	0.34 - 0.35	0.54 - 0.56

Table 5.2: Focusing properties of plasma layers in Cartesian 2D geometry. The ranges for the characteristic focusing quantities are for spot sizes between $W_0 = 100 \lambda_0$ and $300 \lambda_0$. For abbreviations and other simulation parameters, see table 5.1.

5. Transversal focusing with plasma layers

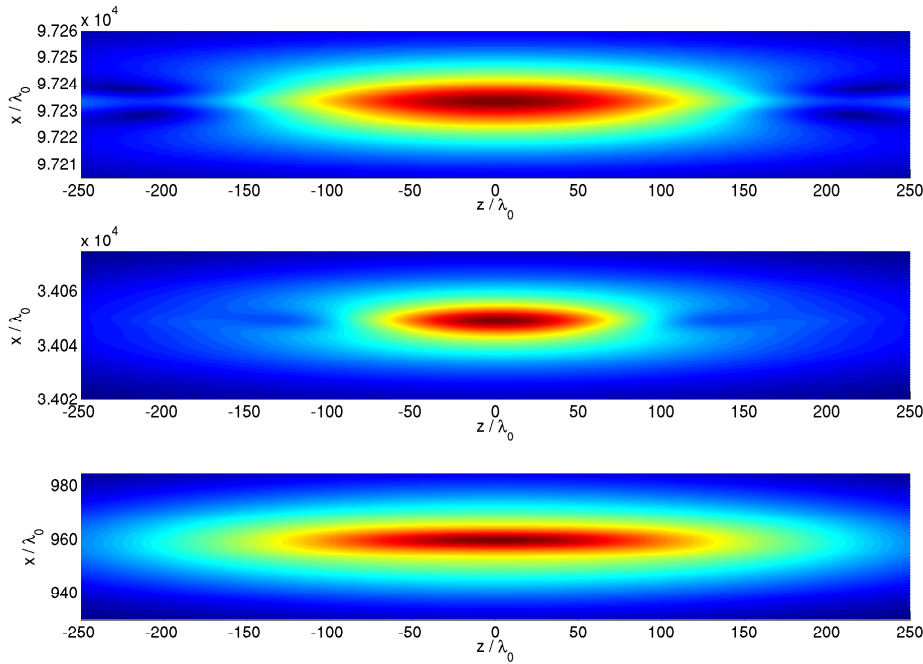


Figure 5.3: Color plots of $|a|^2$ for the pulse propagation in vacuum behind a plasma lens with $n_0 = 0.3 n_c$ and a length of $350\lambda_0$. Pulse parameters are $a_0 = 0.1$, $L_0 = 20\lambda_0$, $W_0 = 250\lambda_0$. From bottom to top: pulse directly behind the plasma lens, at the focal plane and far behind the focal plane.

lengthen again.

To study the focusing properties of a plasma lens more thoroughly, we made a large number of simulation runs with a systematic variation of pulse and plasma layer parameters. For three different combinations of pulse amplitude and length, the spot size of the pulse and the thickness of the plasma layer was varied. The initial spot size was between $100\lambda_0$ and $300\lambda_0$. For the length of the plasma layer three different values were used, where the largest length is given by the optimal value for longitudinal pulse compression. We used Cartesian 2D geometry for this parameter study, because the focal length for pulses with large initial spot sizes is very large. This is especially the case if the pulse is only weakly focused by a short layer. This can make it necessary to simulate the propagation in vacuum for well over $10^5\lambda_0$. Without the possibility to use very large steps in vacuum, the computational cost of such simulations would be prohibitive. The qualitative results should still carry over to cylindrical or full three dimensional geometry.

The results from the parameter study are given in tables 5.1 and 5.2. In table 5.1 detailed results for $a_0 = 0.1$ and $L_0 = 10\lambda_0$ are given. The most important quantities are the ratio of the minimum spot size W_{\min} to the spot size W_{PV} directly behind the plasma layer and the ratio of $W(F_W)$ to W_{PV} . The quantity $W(F_W)$ is the spot size a Gaussian beam with minimum spot size W_{\min} would have at the distance F_W from the

5.2. Boundaries between vacuum and plasma

focal point. This can be calculated from (5.3) and can be compared to the real spot size W_{PV} of the pulse at that distance. The two ratios thus quantify the relative reduction in spot size from behind the length to the focal spot and the strength of the focusing compared to a Gaussian beam. From table 5.1 we see that the scaling of the focusing with the length of the plasma layer is mostly independent of initial spot size.¹ It only depends on the length of the layer and is stronger than for a Gaussian beam. For a layer of optimal length for longitudinal pulse compression it is nearly twice as strong and the spot size can be reduced to about 25% of the initial value W_0 . This result is valid for other pulse parameters, too. Table 5.2 contains the summarized results for the two spot size ratios for three different pulse amplitude / length combinations. The ranges that are given in the Table, are for the different initial spot sizes and show a very low variance. Knowing this ratios allows the effective prediction of the focusing behavior of a very wide pulse by simulating a much more narrow pulse, which decreases the computational cost significantly because of the much smaller focusing length of the narrow pulse.

5.2 Boundaries between vacuum and plasma

To model the focusing effect of a plasma lens correctly, it is important to also model the boundaries between the vacuum and plasma regions to match the experimental situation of a gas jet experiment. It is especially important to understand the difference between hard and soft transitions to the plasma layer. The basic process that happens at a hard boundary is known from linear electrodynamics. A plane wave of wave number k and frequency ω is in part reflected and in part transmitted if $\omega > \omega_p$. Modes with $\omega < \omega_p$ have a reflection coefficient of unity and decrease exponentially inside the plasma, this is called skin effect. The length over which the amplitude drops by a factor of e is called the skin length. The transmission and reflection coefficients are given by the so called Fresnel formulas. For a thin layer the behavior is more complicated, because the reflection and transmission at both boundaries influence each other and skin modes do contribute to the energy transfer through the layer. For sufficiently long layers these effects are small and can be neglected. The transition of a localized pulse from vacuum to plasma or vice versa can be calculated by decomposing it into Fourier modes and multiplying the modes with their respective Fresnel factors. Through this method, boundaries can be included in NLSE simulations, since they are not treated selfconsistently in this equation. In 2D the transformation formulas of the vector potential for a plasma with $\mu_r = 1$ are

$$A_x(\mathbf{k}) = \frac{2}{1 + \eta \frac{\cos(\alpha'')}{\cos(\alpha)}} A_x(\mathbf{k}) \text{ and } A_y(\mathbf{k}) = \frac{2}{1 + \eta \frac{\cos(\alpha)}{\cos(\alpha')}} A_y(\mathbf{k}) , \quad (5.7)$$

where α is the incident angle measured relative to the normal vector of the plasma surface and α'' is the corresponding angle behind the surface. The angles are given by

¹This is only valid if the initial spot size is sufficiently larger than the spot size range where direct collapse of the pulse would occur.

5. Transversal focusing with plasma layers

the relations

$$\sin(\alpha) = \frac{k_x}{\sqrt{k_x^2 + k_z^2}} \text{ and } \sin(\alpha'') = \frac{\sin(\alpha)}{\eta}.$$

The index of refraction η can be taken in zeroth order from the linear plasma dispersion relation. In our units it is then equal to the linear group velocity. Relativistic corrections have to be included for higher intensities, in [17] several different are given for different parameter regimes. For a derivation of the 2D Fresnel formulas for the vector potential \mathbf{A} see e.g. [15].

When entering the plasma a localized pulse will get a higher vector potential amplitude and a smaller spatial length.² Heuristically this can be understood by remembering that the carrier wavelength of the pulse is shorter in plasma than in vacuum, as described by the linear dispersion relation. The effect is the larger the higher the plasma density and thus the lower the linear group velocity is. The width stays nearly unchanged for pulses wider than a few laser wavelengths. For long pulses the temporal length of the pulse is nearly unchanged, too. The pulse propagates more slowly inside the plasma by a factor $v_g \equiv \eta$, which is close to the factor the pulse is shorter spatially.

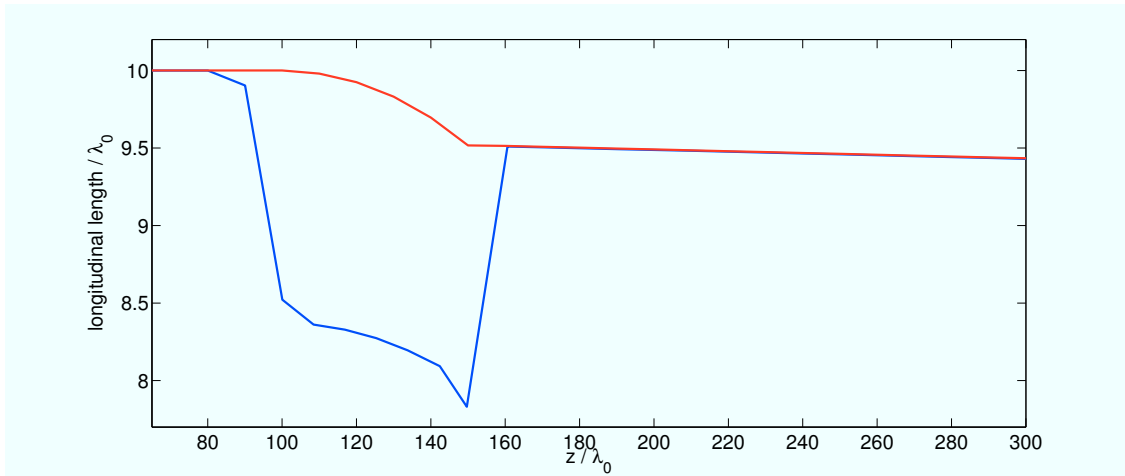


Figure 5.4: Comparison of the length evolution between NLSE (temporal pulse length) and wave equation (spatial pulse length) simulations. Plasma layer of $50 \lambda_0$ length and a density of $0.3 n_c$. Pulse parameters are $a_0 = 0.15$. $L_0 = 10 \lambda_0$ and $W_0 = 100 \lambda_0$.

To examine how well the physics at the plasma boundary is captured by the Fresnel formulas, we compare simulations of the nonlinear wave equation and nonlinear Schrödinger equation. All simulations were done using cubic nonlinearity and include no density response. In NLSE simulations a temporal initial distribution is propagated in z up to the boundary of the plasma layer. Then the field distribution is transformed using the Fresnel formulas for each Fourier mode and the resulting field is then propagated through the plasma. At the end of the plasma layer the same procedure is applied.

²If the density is close to the critical density and the pulse is short (i.e. has a broad frequency spectrum), the amplitude can instead decrease, because a large fraction of the pulse can not enter the plasma.

5.2. Boundaries between vacuum and plasma

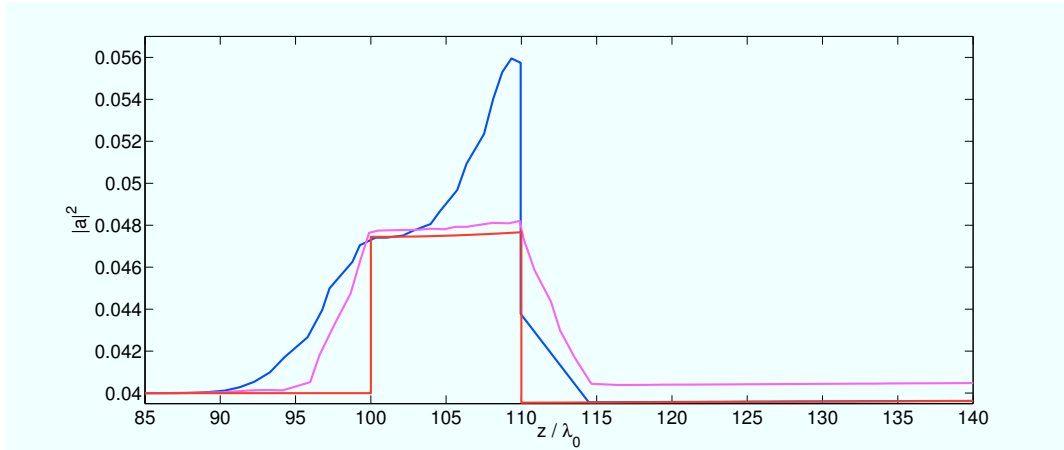


Figure 5.5: Comparison of amplitude evolution between NLSE and wave equation simulations. Plasma layer of $10 \lambda_0$ length and density of $0.3 n_c$. Pulse parameters are $a_0 = 0.2$, $L_0 = 10 \lambda_0$, $W_0 = 50 \lambda_0$. red : cubic NLSE + Fresnel formulas, blue: cubic nonlinear wave equation (hard boundaries), magenta : cubic nonlinear wave equation (soft boundaries, $5 \lambda_0$)

Only for pulses with a very small spot size, the 2D Fresnel formulas yield a different result than the 1D formulas ($\alpha \equiv 0$), because only very narrow pulses of $5 \lambda_0$ or less have k_\perp values that are not small compared to the k_0 of the laser carrier. Simulations based on the wave equation consistently show a slight increase in transversal width from vacuum to plasma and a decrease from plasma to vacuum, although this has little influence on the maximum intensity of the pulse.

The very different behavior at the plasma boundaries of the temporal length in NLSE and the spatial length in wave equation simulations respectively does not lead to differences in length when the pulse is again in vacuum (cf. Fig. 5.4). The effect on the amplitude for $n_0 = 0.3 n_c$ at the vacuum-plasma boundary is already quite large at around 9% for $|a|$. This jump in the amplitude is only this large for the vector potential. The intensity, calculated from \mathbf{E} and \mathbf{B} , changes much less. Although the reflection at the plasma-vacuum boundary leads to a higher maximum amplitude at the boundary to vacuum, the nonlinear interaction with the reflected pulse has little influence on the transmitted pulse. At least this is the case for pulses up to $20 \lambda_0$ length and weakly relativistic amplitudes.

For the weakly relativistic regime the Fresnel formulas thus describe the vacuum-plasma transition surprisingly good and allow the simulation of stratified plasmas with the NLSE, cf. Fig. 5.5. For higher amplitudes they can be modified by correcting the density used to calculate the index of refraction. The γ -factor can simply be evaluated for maximum pulse intensity. This correction reduces the increase of amplitude inside of the plasma (Fig. 5.6 on the left). It is also computationally much less intensive than a simulation of a hard boundary with the wave equation. Since reflected waves become important, the QEA method can not be used while the pulse propagates through the boundary and the grid discretization has to be further reduced than for a soft transition to ensure accurate results. For a realistic plasma boundary this Fresnel transformation

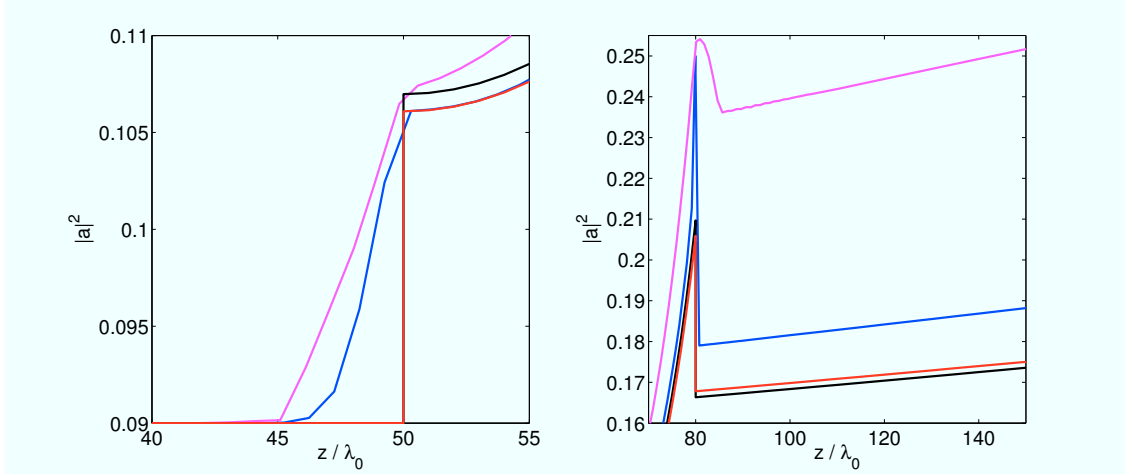


Figure 5.6: Comparison of amplitude evolution between NLSE and wave equation simulations at the vacuum-plasma (on the left) and plasma-vacuum boundary (on the right). Plasma layer of $30\lambda_0$ length and a density of $0.3n_c$. Pulse parameters are $a_0 = 0.3$, $L_0 = 4\lambda_0$ and $W_0 = 50\lambda_0$. Black : cubic NLSE + Fresnel formulas, red : cubic NLSE + relativistically corrected Fresnel formulas, blue: cubic nonlinear wave equation (hard boundaries), magenta : cubic nonlinear wave equation (soft boundaries, $5\lambda_0$).

would have to be modified though, because a hard density jump is not achievable with a gas jet and a smooth transition of only a few λ_0 length reduces reflection to nearly zero, see the magenta curve in Fig. 5.5. This might be accommodated by decomposing the density increase or decrease into small steps with Fresnel transformations in between. There are two main arguments against using the NLSE combined with the Fresnel formulas, though, for the simulation of plasma lenses. If the density response has to be included, it becomes difficult to solve the coupled equations for a and n_e^1 , because a has to be integrated in z while the density has to be integrated in time (cf. section 2.3). For short pulses of less than four cycles length, the envelope approximation starts to break down. This leads to large differences in amplitude after the pulse has propagated through the plasma layer (see Fig. 5.6).

5.3 Propagation of short vs. long wavelength transversal modes in vacuum

When a pulse that has developed transversal filamentation instability leaves the plasma and enters vacuum, the growth of the instability obviously stops. As we have seen in the preceding section, in vacuum the pulse as a whole will at first focus and then defocus with a typical length scale of one half to one Rayleigh length. This behavior can be understood from the Fourier decomposition of the pulse. The smaller the beam waist, the broader the spectrum of transversal Fourier modes becomes. From the vacuum dispersion relation

$$\omega(\mathbf{k}) = c \sqrt{k_{\parallel}^2 + k_{\perp}^2}$$

5.3. Propagation of short vs. long wavelength transversal modes in vacuum

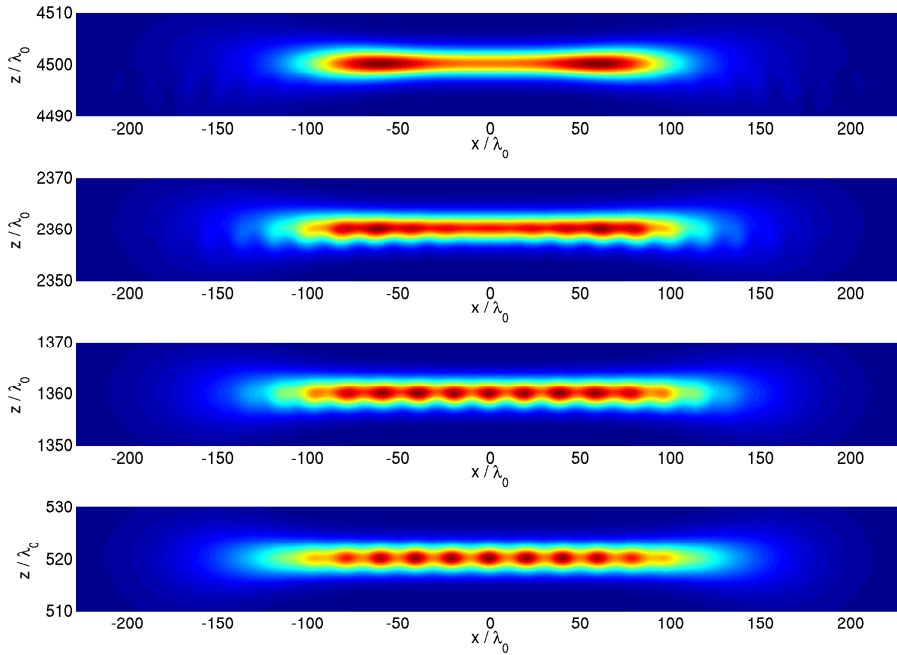


Figure 5.7: Color plot of $|a|^2$ for the propagation of a pulse in vacuum after propagation through a $500\lambda_0$ plasma layer with $n_0 = 0.3n_c$. The initial longitudinal sech shape and transversal super-Gaussian shape. Initial transversal pulse perturbation of $10^{-3} a_0$ with a wavelength of $20\lambda_0$. Bottom to top: pulse at $t = 560/\nu_0$, $t = 1400/\nu_0$, $t = 2400/\nu_0$ and $t = 4540/\nu_0$. The other simulation parameters are $a_0 = 0.16$, $L_0 = 2\lambda$ and $W_0 = 200\lambda$.

follows the group velocity of a transversal Fourier mode with a certain value of k_\perp

$$v_\perp(k_\perp, \omega) = \frac{\partial \omega(\mathbf{k})}{\partial k_\perp} = c \frac{k_\perp}{|\mathbf{k}|} = c^2 \frac{k_\perp}{\omega}. \quad (5.8)$$

For a wide pulse we can use the carrier wave number $k_0 = \omega_0/c$ for the value of k_\parallel and thus $\omega \approx \omega_0$.

Since for a symmetric beam the spectrum is symmetric, too, the wave numbers in the spectrum come in pairs of k_\perp , $-k_\perp$ that propagate in opposite directions. Combined with the higher group velocity of modes with higher absolute k -values, this implies that a pulse focuses or defocuses the faster the smaller its waist size is. This can be seen, too, from the Rayleigh length (5.5).

For a longitudinally localized pulse, this can influence the longitudinal propagation. The constancy of the speed of light leads to a lower parallel velocity the higher the perpendicular velocity of a mode $e^{i\mathbf{k}\cdot\mathbf{r}-i\omega_0 t}$ is. In contrast to 1D, this can lead to a change of the longitudinal pulse shape in vacuum. For the pulse parameters we are considering, the transversal k -values of the pulse will be small compared to k_0 and this effect will be small, too. This changes if the pulse develops transversal filamentation. The transversal k -modes due to the instability are not small compared to k_0 . These

5. Transversal focusing with plasma layers

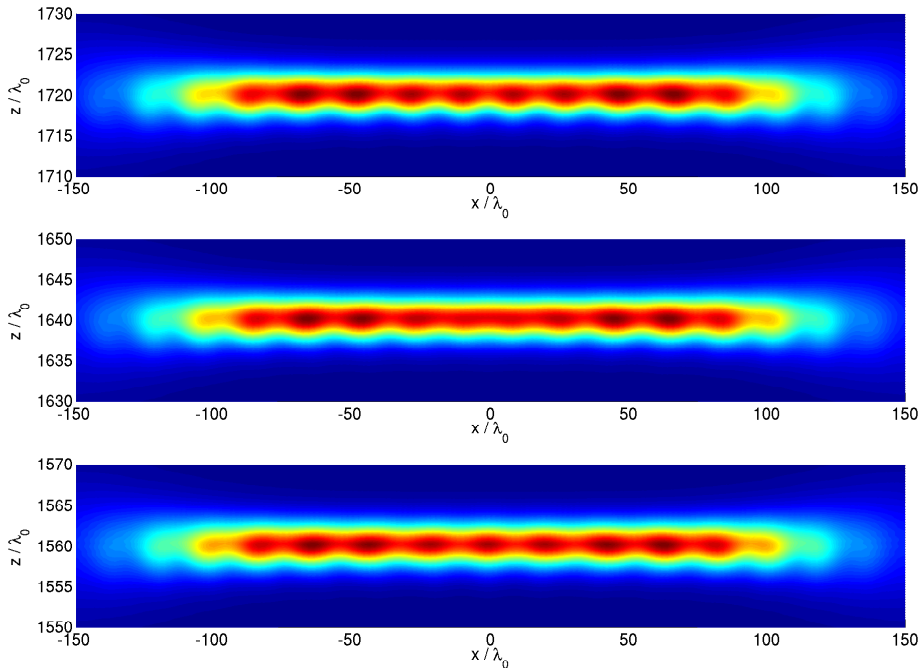


Figure 5.8: Same as Fig. 5.7, but for $t = 1600/\nu_0$, $t = 1680/\nu_0$ and $t = 1760/\nu_0$ (again from bottom to top).

unstable modes will thus propagate more slowly in the longitudinal direction than the main pulse and will also disperse faster in the transversal direction.

In Fig. 5.7 snapshots of the time evolution in vacuum can be seen for a pulse with a super-Gaussian shape in the transversal direction with only a single transversal mode as a perturbation. This simplifies the comparison with the analytically expected behavior. At first, after the pulse has left the plasma, the filaments of the instability are still located centrally on the pulse. But because of their slower longitudinal propagation, they soon begin to lag the main pulse. The resulting longitudinal asymmetry is the first sign that the unstable modes propagate differently from the main pulse. Although they travel in the transversal direction, too, the center of the pulse at first does not clear from the filamentation. The filaments seem to behave like two combs that move relative to each other. In this way we can explain the effect in Fig. 5.8 that peaks vanish for a short time and then reappear. This happens several times until the oppositely propagating filament combs do not overlap anymore and the center of the pulse clears from the instability.

The wavelength of the initial perturbation can still be identified for the parts of the instability that have already left the main pulse and their speed matches the expected value from the vacuum dispersion relation for this wavelength. They do not accumulate in one lump directly behind the pulse as stated in [59], because they have a considerable velocity component in the transversal direction.

After sufficiently long propagation in vacuum the pulse has shed all the unstable

5.3. Propagation of short vs. long wavelength transversal modes in vacuum

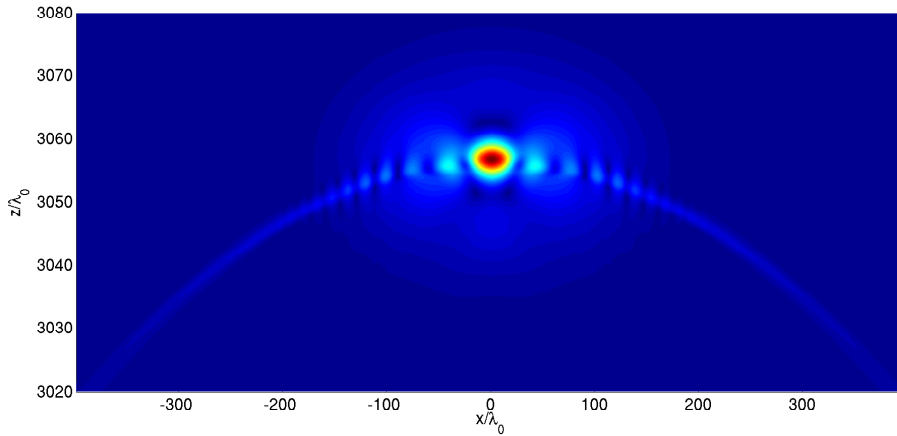


Figure 5.9: Color plot of $|a|$ showing a spherical radiation front after long propagation in vacuum. Note that $|a|$ is shown (not $|a|^2$) for better visibility of the lower amplitude parts of the pulse.

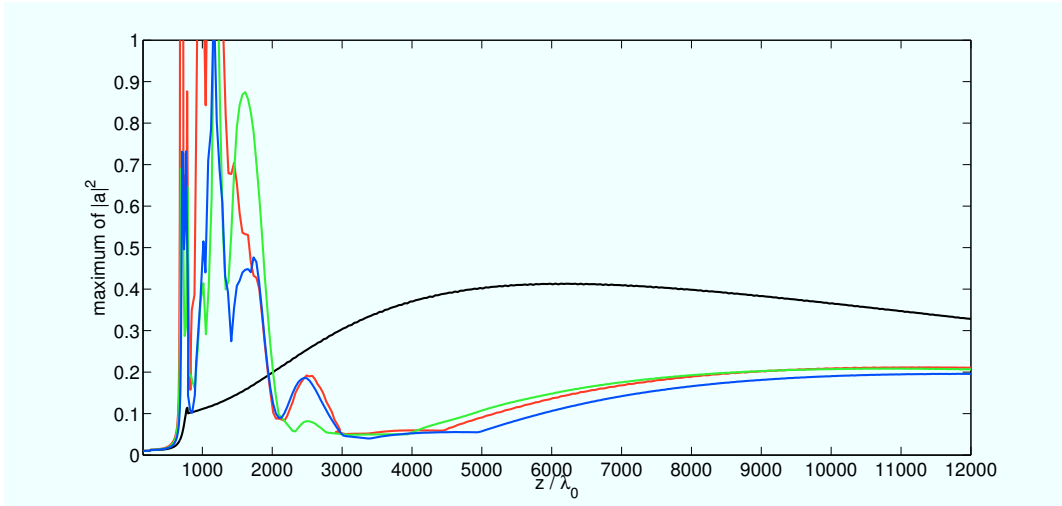


Figure 5.10: Amplitude evolution of a pulse in cylindrical geometry ($a_0 = 0.1$, $L_0 = 20 \lambda_0$, $W_0 = 200 \lambda_0$) with different phase randomized initial perturbations of $0.01 a_0$. Propagation through a plasma layer of $530 \lambda_0$ with a density $n_0 = 0.3n_c$.

modes that propagate on a spherically shaped surface, see for example Fig. 5.9. The remaining main pulse has the same shape as it would have had without filamentation instability, but with a lower amplitude. The amount of amplitude reduction depends on the strength of the instability.

In Fig. 5.10 the evolution of maximum amplitude for three phase-randomized initial perturbations of $0.01 a_0$ is shown for a simulation in cylindrical geometry. In this geometry, which is effectively 3D, the effects of the instability are stronger due to an increasing intensity of the collapse with an increasing number of dimensions. 2D is critical dimensionality for the collapse to occur [62].

The shedding of short wavelength transversal modes in vacuum thus prevents the de-

5. Transversal focusing with plasma layers

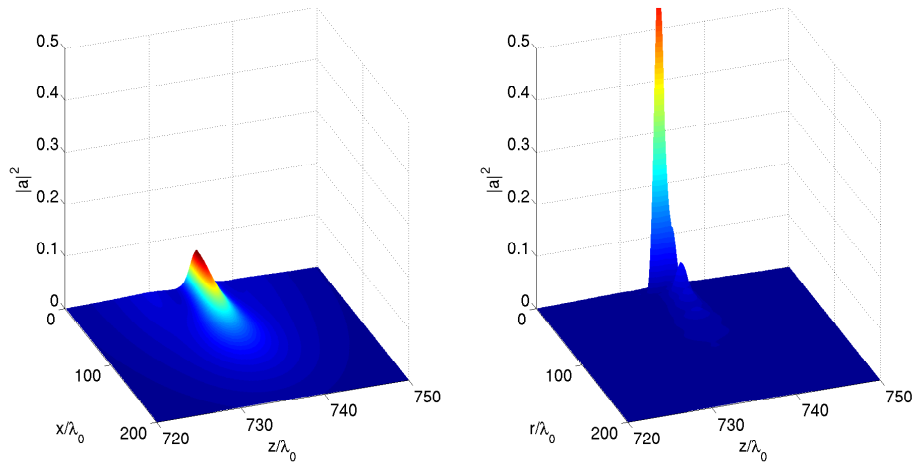


Figure 5.11: $|a|^2$ of pulses with (on the right) and without an initial perturbation (on the left) after propagation through a plasma layer. Same parameters as Fig. 5.10

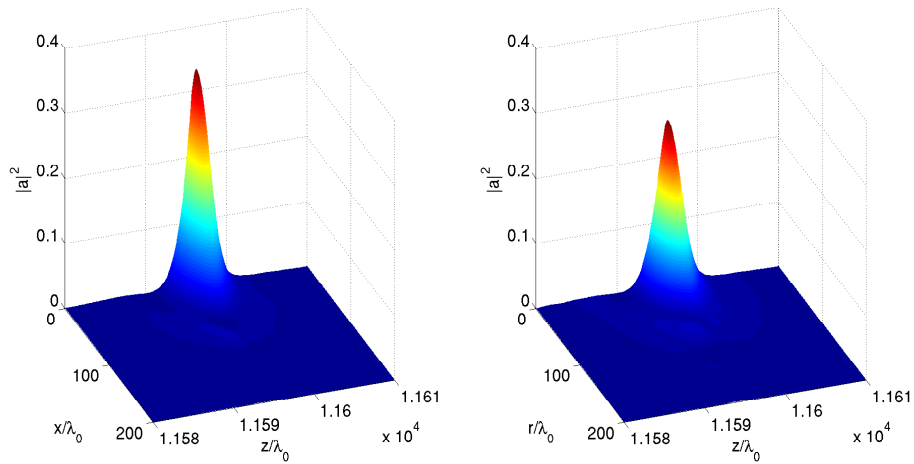


Figure 5.12: Same as Fig. 5.11 after propagation through $\sim 10000 \lambda_0$ of vacuum. Note that at this location only the initially perturbed pulse has its maximum intensity, *not* the unperturbed pulse. See Fig. 5.10 to compare maximum amplitudes.

tection of the filamentation in some distance behind the plasma (Fig. 5.11 and Fig. 5.12). After only a few millimeters in vacuum the pulse has nearly regained its unperturbed shape. This means that the data about the strength of the instability has to come from measurements inside the plasma, e.g. by means of shadowgraphy.

6 Stratified plasma-vacuum systems

In this chapter we will combine the ideas discussed in the preceding chapters by using layered plasma-vacuum structures instead of single layers for pulse compression. The advantage of this approach twofold. It allows to use the transversal focusing potential of a pulse more effectively, and thus increase the intensity of the compressed pulse. It also offers the possibility to control the transversal filamentation instability. By dividing the plasma layer into several shorter layers with vacuum in between, the transversal dispersion of the short unstable modes in vacuum is exploited to clean the pulse before this modes can grow to significant amplitude. Particular attention is given to plasma configurations that are experimentally achievable.

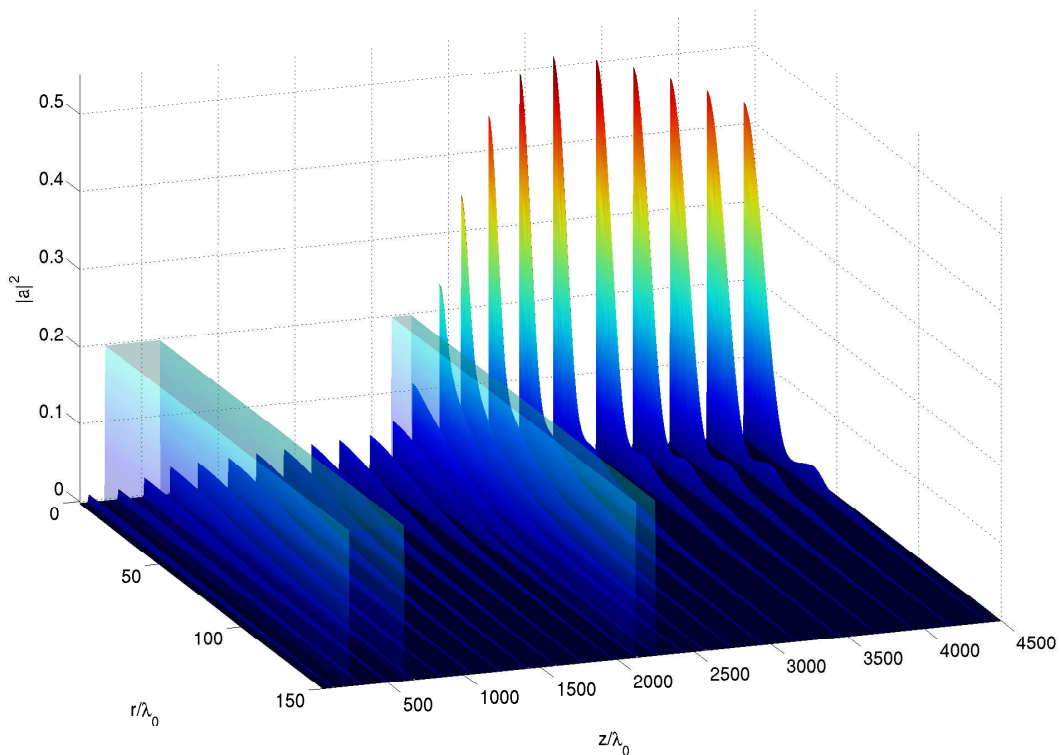


Figure 6.1: $|a|^2$ of a Gaussian pulse with $a_0 = 0.1$, $L_0 = 10 \lambda_0$ and $W_0 = 150 \lambda_0$ propagating through two plasma layers of density $n_0 = 0.3 n_c$. The first layer is $330 \lambda_0$ and the second is $125 \lambda_0$ long with $1500 \lambda_0$ vacuum in between.

6.1 Advantages of multiple plasma layers

6.1.1 Enhanced transversal focusing

For a controlled and efficient longitudinal compression, the initial laser amplitude has to be weakly relativistic, i.e. $a_0^2 \ll 1$ and stay subrelativistic during the compression. Otherwise the energy loss inside the plasma would become too large. Moreover, the spot size has to be much larger than the pulse length, otherwise the pulse would directly collapse inside of the plasma. This implies that a high power laser pulse can only be weakly focused into the plasma to be in the right amplitude and spot size range. Inside the plasma the pulse then is longitudinally compressed from its initial length to just one or two cycles. Thus to reach high subrelativistic or even relativistic intensities, the pulse has to be strongly transversally compressed. Because of the strong coupling between longitudinal and transversal compression, as discussed in section 4.3.3, it is not possible to realize the full transversal compression potential of the pulse purely inside the plasma. But the focusing can be enhanced by slicing a plasma layer of optimal length for longitudinal compression into multiple shorter layers with vacuum sections in between. During the propagation in vacuum the transversal and longitudinal dynamic is (mostly) decoupled. The pulse focuses in the transversal direction, due to the negative curvature of the phase front induced by the plasma, while its length stays nearly unchanged. When it reaches the next plasma layer, it has a higher intensity than without propagation in the vacuum between the layers. This increases the strength of the compression inside the next layer. Using two or more layers should in this way allow to produce pulses with much higher intensities and much reduced spot sizes.

An example of a two layer configuration is shown in Fig. 6.1. Such a vacuum-plasma configuration has several free parameters for which the optimal values are difficult to determine analytically. These are the number of plasma layers, the relative length of the layers and the amount of vacuum between the layers. We will study the influence of this parameters in the following sections.

6.1.2 Control of transversal filamentation

One result presented in the last chapter was that a pulse that is strongly filamented in the transversal direction can regain a smooth transversal shape after propagation through a sufficient amount of vacuum. How well a pulse is able to shed the unstable modes, can be estimated by comparing the Rayleigh lengths of the unfilamented pulse with the Rayleigh length of the individual filaments. A pulse can only lose the unstable modes if the Rayleigh length of the full pulse is several times larger than that of the filaments. This is already fulfilled if the pulse is a few times wider than the filaments, because of the quadratic dependency of z_R on the spot size. The pulse has to travel a few times the Rayleigh length of the filaments to shed the unstable modes. The obvious question is, if the pulse could shed its unstable modes before they can grow to large amplitudes, at the cost of the amplitude of the main pulse. A proposal for such a method was made by Shorokhov et. al. in [59]. The pulse propagates in plasma only for a short amount of

6.1. Advantages of multiple plasma layers

time and then propagates sufficiently long in vacuum for the unstable modes to get out of step with the main pulse. Then it enters another short plasma layer followed again by vacuum and so on until the maximum longitudinal compression is achieved.

The general plasma-vacuum configuration is thus similar to the configuration for enhanced transversal focusing, but the criteria for choosing the parameters are different. The length of the individual layers is limited by the filamentation length of the pulse. This length depends critically on two quantities. The longitudinal pulse length determines the most unstable transversal mode. The shorter this mode becomes, the higher its growth rate and thus the shorter the filamentation length. The other quantity is the noisiness of the system. This includes both perturbations of the pulse shape and fluctuations of the plasma density that act as a seed for the instability. The more noise the system exhibits, the shorter the filamentation length will be. Since the strength of the fluctuations depends on the intensity of the driving pulse, more intense pulses will have a shorter filamentation length. This suggests that the plasma layers have to become increasingly short as the pulse length decreases and its amplitude increases during the compression.

The length of the vacuum sections, too, depends on the wavelengths of the unstable transversal modes. Shorter wavelengths need less propagation vacuum to get out of step with the main pulse. We can make a simple analytical estimation for the necessary amount of vacuum for a certain pulse length. For this we assume that the main pulse travels at c in the longitudinal direction and has no transversal velocity component (i.e. the pulse shows no transversal dispersion). This is approximately valid, if the previously mentioned ratio of the Rayleigh lengths is large. From the expressions for the longitudinal and transversal velocity components of an $e^{i\mathbf{k}\cdot\mathbf{r}-i\omega_0 t}$ mode

$$v_{\parallel,\perp} = c^2 \frac{k_{\parallel,\perp}}{\omega_0}$$

and $c^2 = v_{\parallel}^2 + v_{\perp}^2$, we get for the parallel velocity component

$$\frac{v_{\parallel}}{c} = \sqrt{1 - \frac{v_{\perp}^2}{c^2}}. \quad (6.1)$$

This allows us to calculate after how many λ_0 of vacuum a mode with a certain k_{\perp} will lag the main pulse by the half width of the pulse. If we take for example a pulse that compresses down to $2\lambda_0$ in length and we take the value of the most unstable mode for a soliton of this length as a guide ($\approx 19\lambda_0$), we get a group velocity difference of $\Delta v_g \approx 0.0021c$ and vacuum length of $\approx 1400\lambda_0$ for a lag of one half width. This is consistent with the simulations in section 5.3. Since the growth rate of the instability depends only on $|\mathbf{k}_{\perp}|$ irrespective of the number of dimensions of \mathbf{k}_{\perp} the same formula can also be used to calculate the vacuum length for simulations in 3D Cartesian or cylindrical geometry. For the parameters in [59], the pulse compresses down to a single wavelength which results in $\lambda_{\perp} \approx 6.6\lambda_0$ for $n_0 = 0.6n_c$. The vacuum for a lag of a single wavelength is in this case approximately $90\lambda_0$, which is in very good agreement with the value of $100\lambda_0$ that was used as the vacuum length between the four plasma layers for a total vacuum length of $300\lambda_0$.

Of course there are constraints from the transversal focusing of the pulse. A strongly focused pulse is much more susceptible to collapse caused by the instability, but reducing the length of the vacuum sections to reduce focusing can result in an insufficient amount of vacuum for the control of the instability. The requirements for enhanced focusing and filamentation control have thus to be balanced against each other and the pulse, layer and vacuum parameters have to be chosen to meet both.

6.2 Optimization of transversal focusing

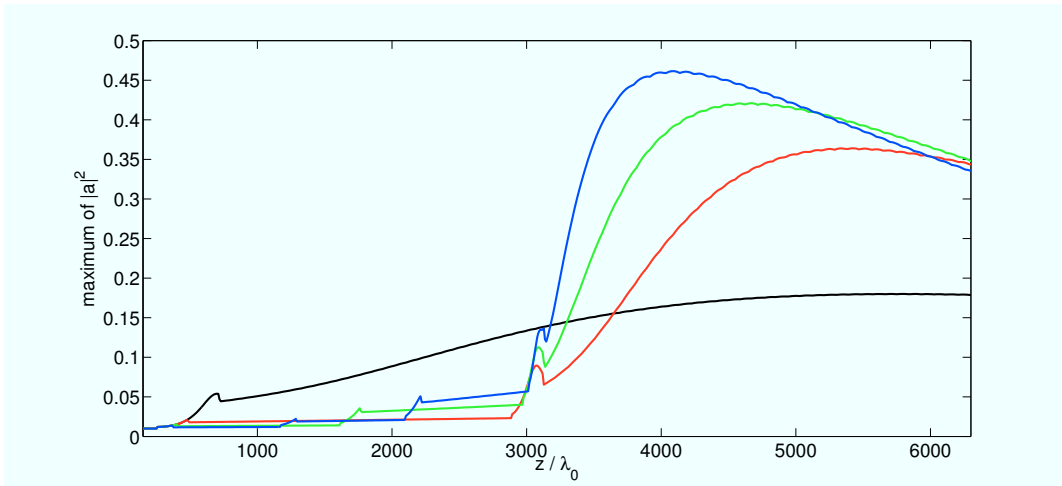


Figure 6.2: Amplitude evolution for $a_0 = 0.1$, $L_0 = 10 \lambda_0$, $W_0 = 150 \lambda_0$ for 1–4 plasma layers ($n_0 = 0.3 n_c$) of comparable total length. One layer of $460 \lambda_0$ (black), two layers of $227 \lambda_0$ (red), three layers of $150 \lambda_0$ (green), four layers of $112 \lambda_0$ (blue). Each layer has $5 \lambda_0$ transitions between vacuum and plasma on both sides. For each additional layer the total plasma length is reduced by $3 \lambda_0$ to account for the additional amount of plasma in the transition regions. Total amount of vacuum between layers is $2400 \lambda_0$, divided equally.

In the following we will examine the influence of different layer parameters, such as the number of plasma layers and the amount of vacuum between the layers, on the resulting amplitude, length and spot size of the pulse. Most of the simulations in the preceding sections were done in 2D Cartesian geometry, because we were only interested in qualitative results, or the results were independent of the transversal geometry. In this way we were able to take advantage of the fast simulation times in vacuum of the Gautschi-type integrator. This allowed us for example, to study the focusing behavior of very wide pulses with very large Rayleigh length. This is not possible when using more than a single plasma layer. In 3D the amplitude increase in vacuum due to transversal focusing is around two times larger than in 2D, due to the additional direction in which focusing occurs. Thus the propagation in the next plasma layer will be very different in 2D and 3D and we have to use a cylindrical geometry to perform realistic simulations. This increases simulation runtimes compared to Cartesian 2D simulations, not only

6.2. Optimization of transversal focusing

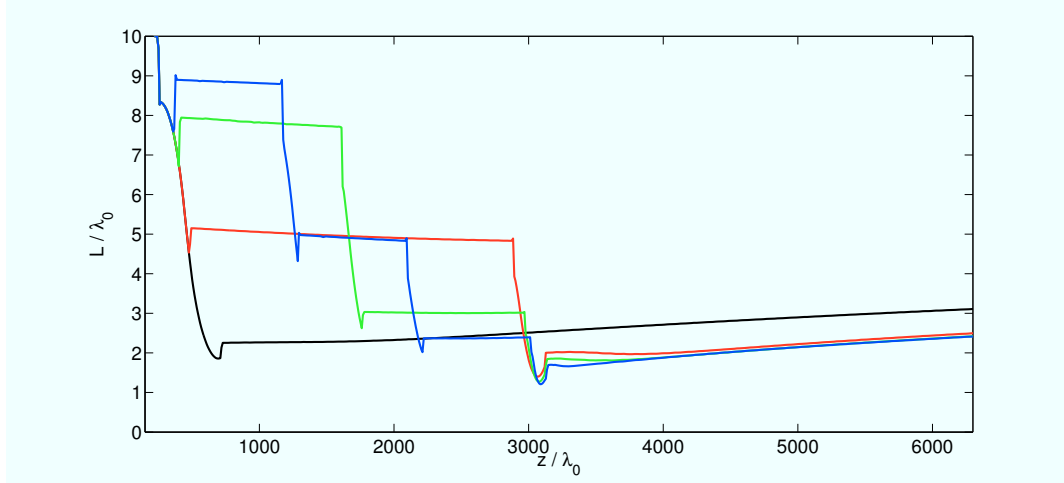


Figure 6.3: Pulse length evolution for the simulations shown in Fig. 6.2.

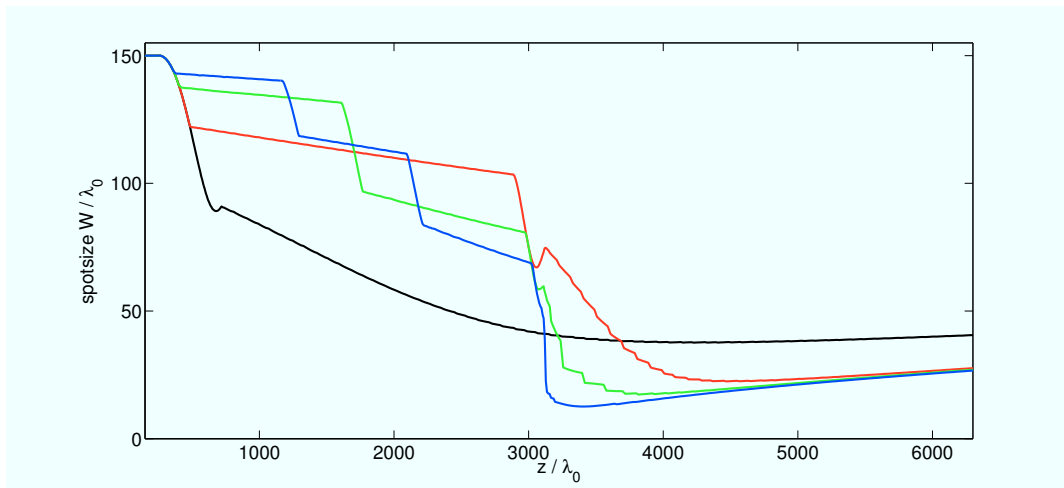


Figure 6.4: Spotsize evolution for the simulations shown in Fig. 6.2.

because small time steps have to be used in vacuum. They are also increased, because in cylindrical geometry the initial minimum spot size for that no direct collapse occurs is larger by a factor of about $\sqrt{2}$. This can be partially compensated by using a coarser transversal discretization, although the spot sizes at the focal point are not necessarily a factor $\sqrt{2}$ larger. For the simulations with a transversal perturbation the discretization is limited by the requirement to resolve the wavelengths of the instability.

6.2.1 Number of plasma layers

First we will examine how different numbers of plasma layers influence pulse compression and focusing. We take the length of a single layer that is needed to fully compress a pulse with certain parameters, split it into two, three or four layers of equal length and add linear transitions between vacuum and plasma of $5\lambda_0$ length. To compensate for the added length due to the linear transitions, we reduce the length of each layer by

6. Stratified plasma-vacuum systems

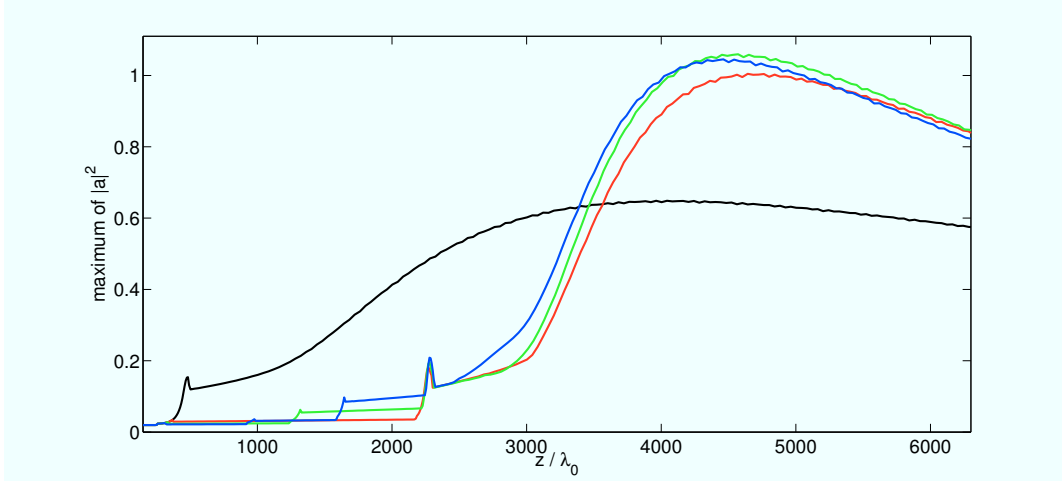


Figure 6.5: Amplitude evolution for $a_0 = 0.14$, $L_0 = 10 \lambda_0$, $W_0 = 150 \lambda_0$ for 1–4 plasma layers ($n_0 = 0.3 n_c$) of comparable total length. One layer of $235 \lambda_0$ (black), two layers of $115 \lambda_0$ (red), three layers of $75 \lambda_0$ (green), four layers of $55 \lambda_0$ (blue). Total amount of vacuum between layers is $1800 \lambda_0$.

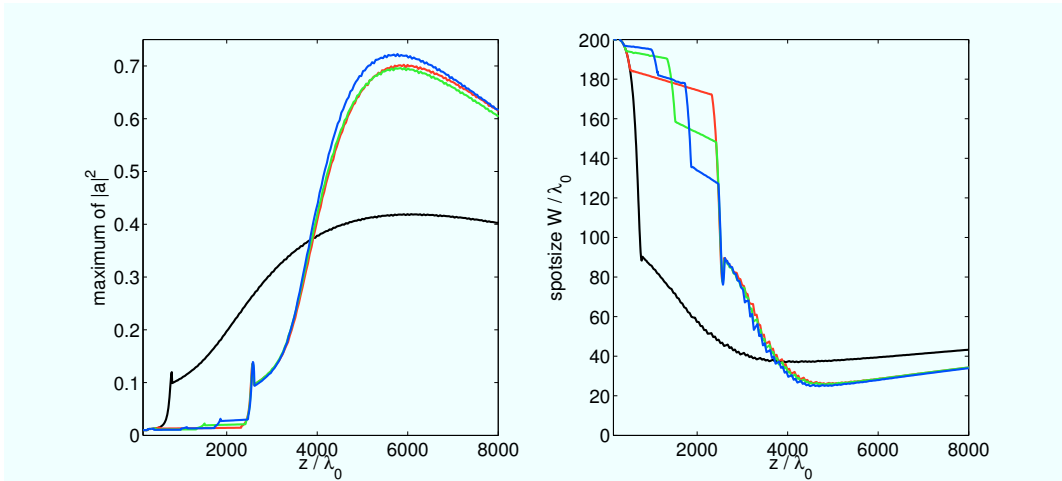


Figure 6.6: Amplitude (on the left) and spot size evolution (on the right) for $a_0 = 0.1$, $L_0 = 20 \lambda_0$, $W_0 = 200 \lambda_0$ for 1–4 plasma layers ($n_0 = 0.3 n_c$) of comparable total length. One layer of $530 \lambda_0$ (black), two layers of $262 \lambda_0$ (red), three layers of $174 \lambda_0$ (green), four layers of $130 \lambda_0$ (blue). Total amount of vacuum between layers is $1800 \lambda_0$.

$3 \lambda_0$. The total amount of vacuum between the layers is chosen to be the same for any number of layers, so that the length of the individual vacuum sections decreases with the number of layers.

In Fig. 6.2 the amplitude evolution for a pulse with $a_0 = 0.1$, $L_0 = 10 \lambda_0$ and $W_0 = 150 \lambda_0$ is shown for one to four layers layers of density $n_0 = 0.3 n_c$. The total length of the vacuum sections is $2400 \lambda_0$. The length and spot size evolution are shown in Fig. 6.3 and Fig. 6.4 respectively. For a single layer the pulse reaches the focal point after propagating $5450 \lambda_0$. With focal point we denote the z -position at which the maximum amplitude is reached. As we have seen in the last chapter, this point does not coincide

6.2. Optimization of transversal focusing

with the minimum spot size. The spot size at the focal point is $W = 39 \lambda_0$ and its length $L = 3 \lambda_0$. For more than one layer the focal point is already reached between $4100 \lambda_0$ to $4400 \lambda_0$. The spot size in focus for two layers is $W = 24 \lambda_0$ and the length $L = 2, \lambda_0$. For three and four layers the values are $W = 18 \lambda_0, L = 1.9, \lambda_0$ and $W = 16 \lambda_0, L = 1.9, \lambda_0$ respectively. The use of multiple layers can thus not only enhance transversal focusing but also increase the longitudinal compression. The decrease of spot size and length with the number of layers is directly proportional to the increase in intensity. Losses to the plasma are very low.

For $a_0 = 0.14$ and the same initial length and width and a total amount of $1800 \lambda_0$ the maximum amplitude also increases distinctly from one to two layers. But for three and four layers there is already a saturation in maximum amplitude visible in Fig. 6.5. This is not due to energy loss of the pulse to the plasma, but due to a saturation in both longitudinal and transversal compression. The spot size at the focal point (at $z = 4400 \dots 4700 \lambda_0$) for two to four layers ranges from about $19.5 \lambda_0$ to $21.4 \lambda_0$, the difference being less than $2 \lambda_0$. The pulse lengths are also very close at $1.42 \dots 1.5 \lambda_0$. The values for a single layer are $W = 31 \lambda_0$ and $L = 1.56 \lambda_0$ at $z = 4000 \lambda_0$. The same saturation effect can be seen for $a_0 = 0.1, L_0 = 20 \lambda_0$ and $W_0 = 200 \lambda_0$ in Fig. 6.6 where the spottsize evolution is shown, too. Here the focal point is for one layer at $z = 6000 \lambda_0$ with $W = 40 \lambda_0$ and $L = 1.9 \lambda_0$. For two to four layers the focal point is reached at $z = 5800 \dots 6000 \lambda_0$. The spot sizes are within less than a single laser wavelength around $W = 27.5 \lambda_0$ and the lengths are essentially the same at $L = 1.65 \lambda_0$.

6.2.2 Relative thickness of the plasma layers

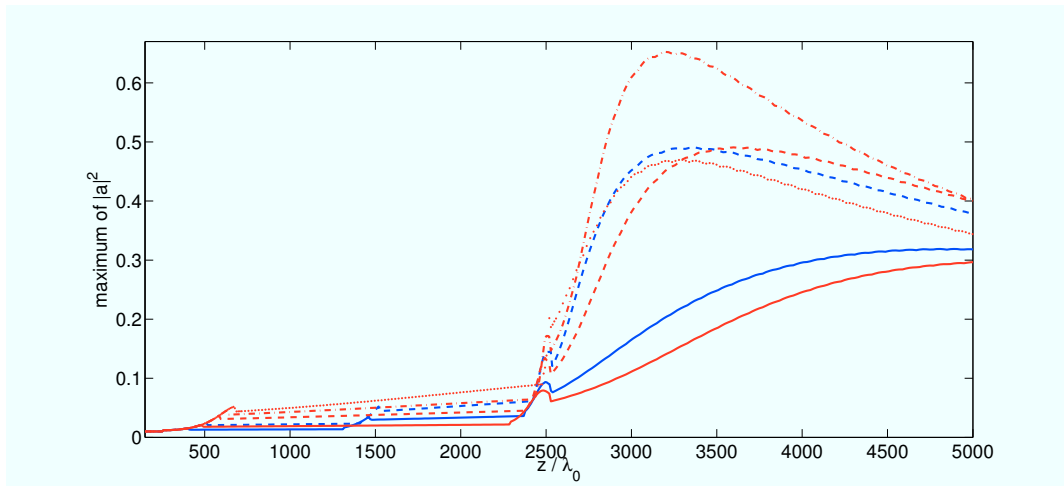


Figure 6.7: Amplitude evolution for $a_0 = 0.1, L_0 = 10 \lambda_0, W_0 = 150 \lambda_0$ for two and three plasma layers ($n_0 = 0.3 n_c$). Total length of the plasma is $455 \lambda_0$ for two layers and $450 \lambda_0$ for three layers respectively. Total amount of vacuum between layers is $1800 \lambda_0$. The partition for two layers is $227 \lambda_0/227 \lambda_0$ (red, solid), $330 \lambda_0/125 \lambda_0$ (red, dashed), $375 \lambda_0/80 \lambda_0$ (red, dash-dotted) and $420 \lambda_0/35 \lambda_0$ (red, dotted). For three layers the partition is $150 \lambda_0/150 \lambda_0/150 \lambda_0$ (blue, solid) and $250 \lambda_0/100 \lambda_0/100 \lambda_0$ (blue, dashed).

6. Stratified plasma-vacuum systems

Another parameter of the stratified plasma-vacuum system that can be varied, is the relative thickness of the plasma layers at a constant total amount of plasma. For the pulse parameters $a_0 = 0.1$, $L_0 = 10 \lambda_0$, $W_0 = 150 \lambda_0$ the result is shown in Fig. 6.7. Increasing the relative length of the first layer improves focusing and compression up to a certain optimal ratio above which the maximum amplitude decreases again. A longer first layer visibly increases transversal focusing and thus increases the intensity at the beginning of the second layer. But since the second layer is reduced accordingly in length, the second stage of longitudinal and transversal compression in plasma is weaker. If the length of the second layer goes to zero, the single layer result of course has to be recovered. At the optimal length ratio, the lowest minimum spot size and thus the strongest transversal focusing is reached, while other ratios for the length of the layers may have a lower minimum length. For three and four layers, increasing the length of the first layer yields the same result.

Again the effect is less pronounced for pulses with a higher initial amplitude or length. When the relative length of the first layer is increased, a saturation at which the spot size can not be reduced further sets in quickly.

6.2.3 Amount of vacuum between plasma layers

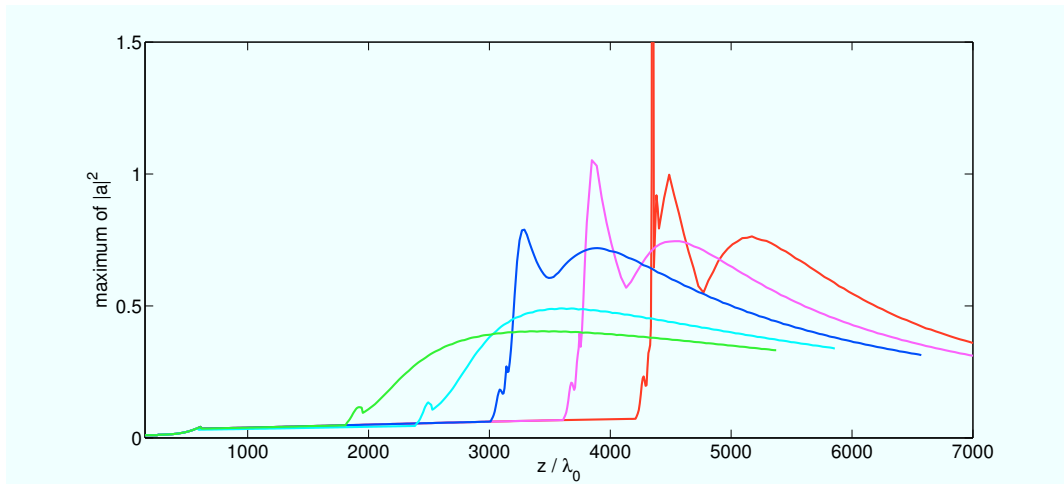


Figure 6.8: Amplitude evolution for $a_0 = 0.1$, $L_0 = 10 \lambda_0$, $W_0 = 150 \lambda_0$ for two plasma layers ($n_0 = 0.3 n_c$) and varying amount of vacuum between the layers. The plasma layers are $330 \lambda_0$ and $125 \lambda_0$ long respectively. The vacuum lengths are $1200 \lambda_0$ (green), $1800 \lambda_0$ (cyan), $2400 \lambda_0$ (blue), $3000 \lambda_0$ (magenta), $3600 \lambda_0$ (red).

The most important parameter for enhanced transversal focusing is the total amount of vacuum between the plasma layers. With a total amount of zero we arrive at the single layer again. Increasing the length of the vacuum leads to a pronounced increase of maximum amplitude and decrease of minimum spot size. But it is not possible, for example for two layers, to put the last layer at the focal distance of the first layer (or generally the layer before), because this would cause the pulse to collapse inside of the last layer. The distance to the last layer has thus to be either smaller or substantially

6.2. Optimization of transversal focusing

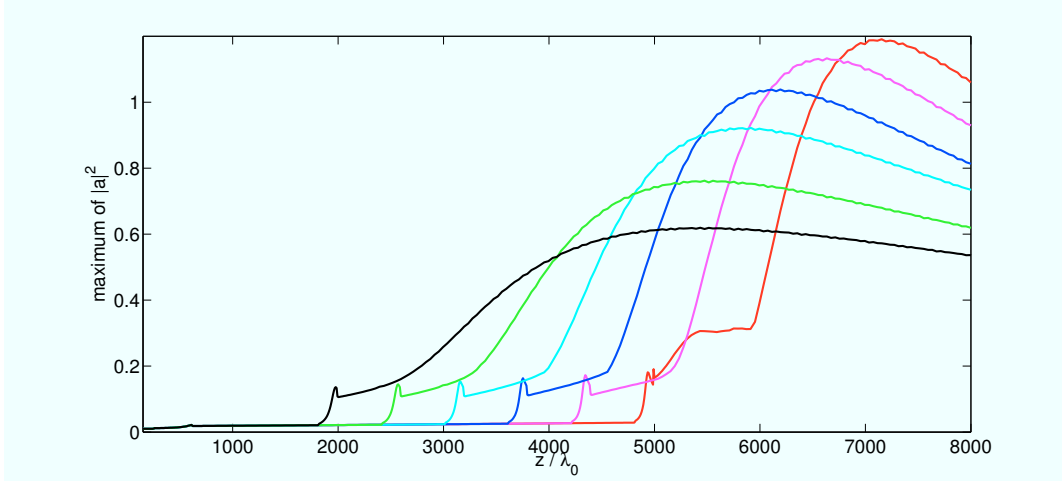


Figure 6.9: Amplitude evolution for $a_0 = 0.1$, $L_0 = 20 \lambda_0$, $W_0 = 200 \lambda_0$ for two plasma layers ($n_0 = 0.3 n_c$) and varying amount of vacuum between the layers. The plasma layers are $355 \lambda_0$ and $170 \lambda_0$ long respectively. The vacuum lengths are $1200 \lambda_0$ (black), $1800 \lambda_0$ (green), $2400 \lambda_0$ (cyan), $3000 \lambda_0$ (blue), $3600 \lambda_0$ (magenta) and $4200 \lambda_0$ (red).

larger than the focal distance. Otherwise the pulse will still be strongly deformed, which leads to oscillation of the pulse amplitude in vacuum (Fig. 6.8).

The stronger transversal focusing for a larger absolute amount of vacuum does not show saturation for a larger pulse amplitude or length (Fig. 6.9). This is different to the other variations of the plasma-vacuum structure, which where of a relative kind. This suggests that the achievable minimum spot size is fixed by the absolute amount of vacuum. A certain configuration may not reach the optimum spot size / amplitude, but no configuration can exceed this value. It also suggests that increasing the initial spot size of the pulse and the total amount of vacuum, is the best way to increase the intensity at the focal point. No saturation should occur in this way until the intensities become already relativistic inside of the plasma.

It is of course possible for more than two layers to vary the relative amount of vacuum between the layers. From the preceding two section we can already guess the result. Increasing the number of layers, or decreasing the thickness of the layers from the first to the last, effectively shifts plasma towards the beginning and vacuum to the end of the plasma-vacuum structure. We can thus expect to achieve a higher intensity by shortening the first vacuum section and lengthening the last (Fig. 6.10). Since this change is relative in nature, we also expect to see a saturation effect for the same pulse parameters as before (Fig. 6.11). The relative change in the vacuum distribution can of course be combined with a relative change in plasma distribution to further enhance the focusing (Fig. 6.12 and Fig. 6.13).

6.2.4 Currently feasible experimental configurations

All of the configurations discussed up to this point have steep transitions between vacuum and plasma. Some of them have very short plasma layers of less than $100 \lambda_0$

6. Stratified plasma-vacuum systems

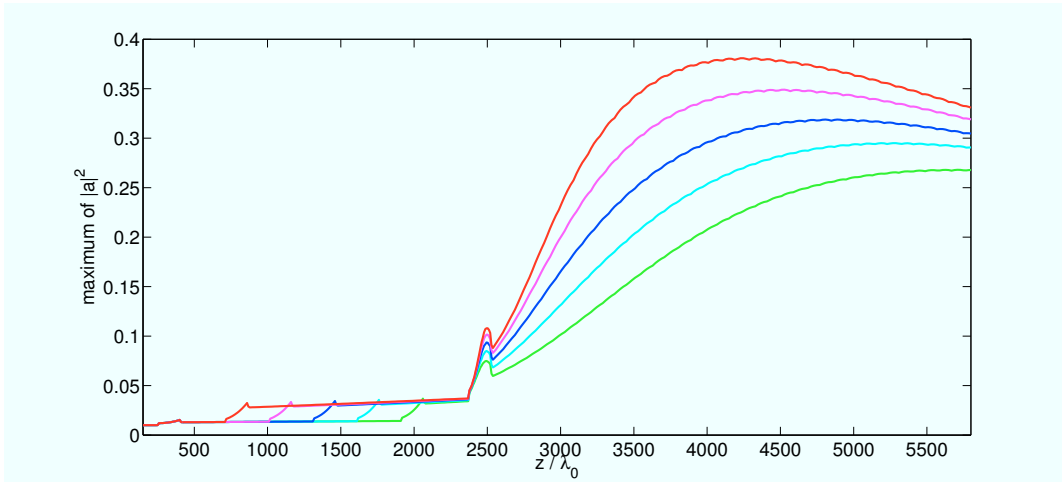


Figure 6.10: Amplitude evolution for $a_0 = 0.1$, $L_0 = 10 \lambda_0$, $W_0 = 150 \lambda_0$ for three plasma layers with $n_0 = 0.3 n_c$ and a total amount of $1800 \lambda_0$ vacuum between layers. Each plasma layer is $150 \lambda_0$ long. The partition of the vacuum is $1500 \lambda_0/300 \lambda_0$ (green), $1200 \lambda_0/600 \lambda_0$ (cyan), $900 \lambda_0/900 \lambda_0$ (blue), $600 \lambda_0/1200 \lambda_0$ (magenta) and $300 \lambda_0/1500 \lambda_0$ (red).

thickness. With gasjets of maximum densities larger $0.25 n_c$, produced through supersonic gas expansion, such parameters are currently not achievable. The current state of the art are a density plateau of about $200 \mu m$ at $n_0 = 0.3 n_c$ with a transition to vacuum of a length of also $\sim 200 \mu m$ around the core of the gasjet [54]. This reduces the number of plasma layers we can use to two. Even for only two layers such a configuration would be longer than the optimal length for a pulse with $a_0 = 0.1$ (or more) and $L_0 = 10 \lambda_0$ (or less).

Since increasing the spot size or decreasing the amount of vacuum between the two layers does only weakly change the length of plasma for which optimal longitudinal compression is achieved, we only have the initial pulse length and amplitude to effectively control the compression length. We are looking for a combination of pulse parameters which allows strong compression and focusing and is stable against slight variations in the thickness of the gasjets that can occur in experiments.

A parameter combination, which fulfills this requirements, is $a_0 = 0.08$, $L_0 = 20 \lambda_0$ and $W_0 = 250 \lambda_0$. The length of the density plateau can be varied between $200 \lambda_0$ and $280 \lambda_0$ with a distance between the gasjets of $3600 \lambda_0$ to $5000 \lambda_0$. The results for the intensity evolution for three different plasma-vacuum configurations can be seen in Fig. 6.14. It is possible with such configurations to reach a more than hundredfold increase in intensity from $I = 0.0064$ to $I = 0.69$. This is nearly as good as for the physically less realistic examples discussed above, although the absolute value of the maximum intensity is not as high. Still, the spot size can be decreased to less than $30 \lambda_0$ (Fig. 6.15) and the length to less than 2.5 laser cycles.

There are two interesting points to note. The first is that, although substantial parts of the two layers have a density of less than quarter critical, no Raman instability was visible in any of the simulations. The second is that the focal length of the last layer is

6.3. Controlling transversal filamentation

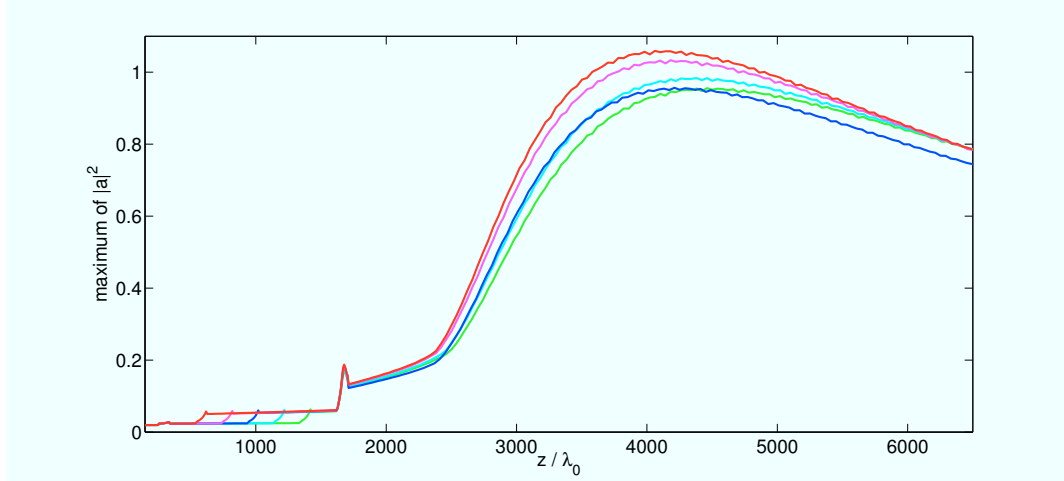


Figure 6.11: Amplitude evolution for $a_0 = 0.14$, $L_0 = 10 \lambda_0$, $W_0 = 150 \lambda_0$ for three plasma layers ($n_0 = 0.3 n_c$). Each plasma layer is $75 \lambda_0$ long. The total vacuum length is $1800 \lambda_0$. The partition of the vacuum is $1000 \lambda_0 / 200 \lambda_0$ (green), $800 \lambda_0 / 400 \lambda_0$ (cyan), $600 \lambda_0 / 600 \lambda_0$ (blue), $400 \lambda_0 / 800 \lambda_0$ (magenta) and $200 \lambda_0 / 1000 \lambda_0$ (red).

about $6000 \lambda_0$, much larger than for most of the other configurations discussed before. This can be explained by the large initial spot size and less extreme focusing.

6.3 Controlling transversal filamentation

We will now introduce pulse perturbations to the simulations to examine the stability of the pulse propagation through a layered plasma vacuum structure with respect to transversal filamentation. The aim is to find parameters that allow (nearly) optimal compression and minimize losses due to pulse filamentation. Compared to the transversal perturbations used in section 4.4, we here use a discrete spectrum of wavelengths. The amplitude parameter for the perturbation is for each wavelength and not for the superposed perturbation after phase randomization. For the longitudinal perturbation profile a super-Gaussian with two times the pulse length (full width at half maximum) is used that is shifted by half the pulse length towards the back of the pulse. A perturbation is applied to the pulse before each of the layers, where the local amplitude and length of the pulse is used to determine the amplitude of the perturbation and the length of the longitudinal perturbation profile instead of the initial values. Without a perturbation applied before each layer the shorter modes that can only grow in the last layer where the pulse is sufficiently short would have already dispersed before the pulse has propagated this far. The standard perturbation that is used, consists of 20 cosine or Bessel modes (depending on the transversal geometry) with wavelengths from $10 \lambda_0$ to $30 \lambda_0$ and an amplitude of either 0.01 or 0.005 times the pulse amplitude at the position where the perturbation is applied to the pulse.

Both perturbation amplitudes are sufficient to induce a strong instability if only a single long layer is used. For several shorter layers the lower amplitude of 0.005 seems

6. Stratified plasma-vacuum systems

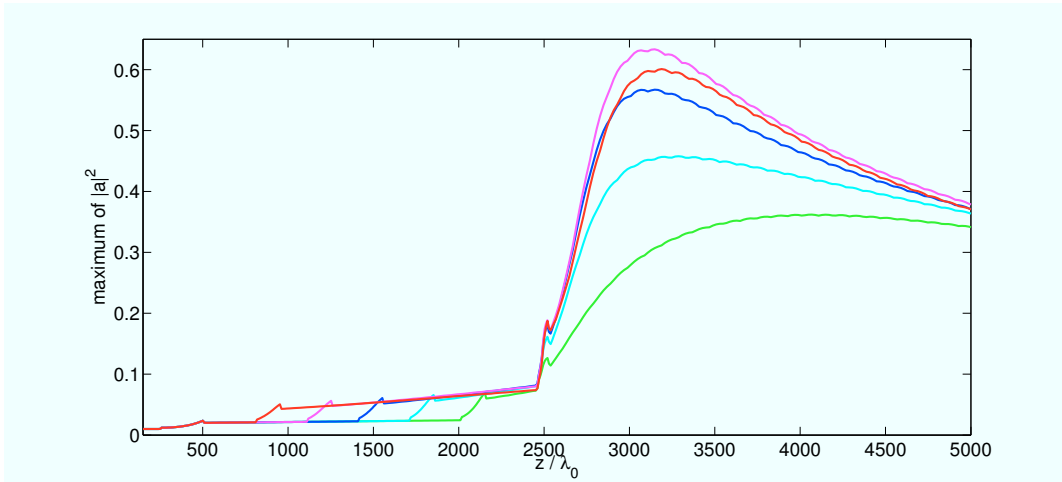


Figure 6.12: Amplitude evolution for $a_0 = 0.1$, $L_0 = 10 \lambda_0$, $W_0 = 150 \lambda_0$ for three plasma layers ($n_0 = 0.3 n_c$). The plasma layers are $250 \lambda_0$, $140 \lambda_0$ and $60 \lambda_0$ long respectively. Total amount of $1800 \lambda_0$ vacuum between layers. Partition of the vacuum is $1500 \lambda_0/300 \lambda_0$ (green), $1200 \lambda_0/600 \lambda_0$ (cyan), $900 \lambda_0/900 \lambda_0$ (blue), $600 \lambda_0/1200 \lambda_0$ (magenta) and $300 \lambda_0/1500 \lambda_0$ (red).

to favor the growth of short wavelength modes. The larger perturbation amplitude of 0.01 can lead to strong growth of long wavelength modes in the first layer that the pulse can not fully shed before reaching the next layer. Thus they can grow further and still dominate in the last layer. Due to the phase randomization used to produce a spatially uniform perturbation that can influence the strength of the instability, for each simulation run that shows successful control of the instability at least one additional run was made to verify the result.

The type and strength of the perturbations we use represents a worst case scenario. The four layer configuration in [59] simulated with a 3D PIC code shows strong instability in our simulations for the higher perturbation amplitude of 0.01 and is not stable for every run with the lower amplitude of 0.005, even with more than $100 \lambda_0$ vacuum between the layers. It is unknown how strong the filamentation will be in experiments, but possibly weaker than in PIC simulations due to their inherent noisiness. If we can find configurations that still allow stable pulse compression for these strong perturbations, we can be sufficiently sure that they will show stable behavior in experiments, too.

In the preceding section about enhanced transversal focusing, we optimized the plasma-vacuum configurations to reach the highest possible intensity for a certain combination of pulse parameters. We found these optimized configurations to be generally highly susceptible to transversal instability. We thus have to modify either the pulse parameters or the vacuum-plasma configuration to allow for stable pulse propagation again. Different strategies will be discussed in the following sections.

6.3. Controlling transversal filamentation

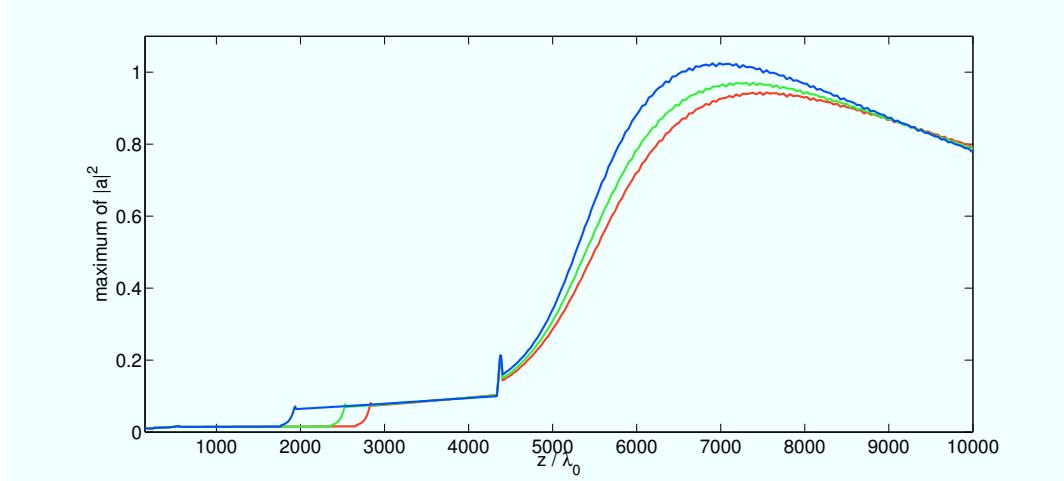


Figure 6.13: Amplitude evolution for $a_0 = 0.1$, $L_0 = 20 \lambda_0$, $W_0 = 250 \lambda_0$ for three plasma layers ($n_0 = 0.3 n_c$). The plasma layers are $300 \lambda_0$, $170 \lambda_0$ and $50 \lambda_0$ long respectively. Total amount of $3600 \lambda_0$ vacuum between layers. Partition of the vacuum is $2100 \lambda_0/1500 \lambda_0$ (red), $1800 \lambda_0/1800 \lambda_0$ (green) and $1200 \lambda_0/2400 \lambda_0$ (blue).

6.3.1 Very long vacuum sections

If the amount of the vacuum between the plasma layers is not sufficient to allow the shedding of the unstable modes, it is possible to increase the amount to a length much longer than the optimal length for focusing. This has the additional advantage that the amplitude of the pulse at the last layer is decreased, too, which further reduces the strength of the transversal instability. The disadvantage is of course that the maximum intensity after compression in the last layer is also reduced. Despite of this, high intensities can still be reached (Fig. 6.16). Because of the strongly asymmetric focusing behavior of plasma layers, the length of the vacuum may have to be increased to several times the focal distance of a single layer. For more than two layers the partition of the large amount of vacuum has to be chosen to prevent collapse in one of the layers. In most cases, this can not be achieved with an equal partition of the vacuum. The best strategy is to put most of the vacuum between the last two layers, as shown in Fig. 6.17. This yields a higher intensity than the same amount of vacuum between the first two layers. Additionally it allows a full shedding of unstable modes from previous layers before the pulse enters the last layer. From theoretical considerations it would seem that the longer vacuum section is more useful behind the first layer, where long wavelengths have become unstable that can not be fully shed in a short vacuum section. The simulation results clearly suggest otherwise. It seems that a complete shedding is most important before the pulse enters the last layer, because remaining short wavelength modes drive the pulse rapidly unstable.

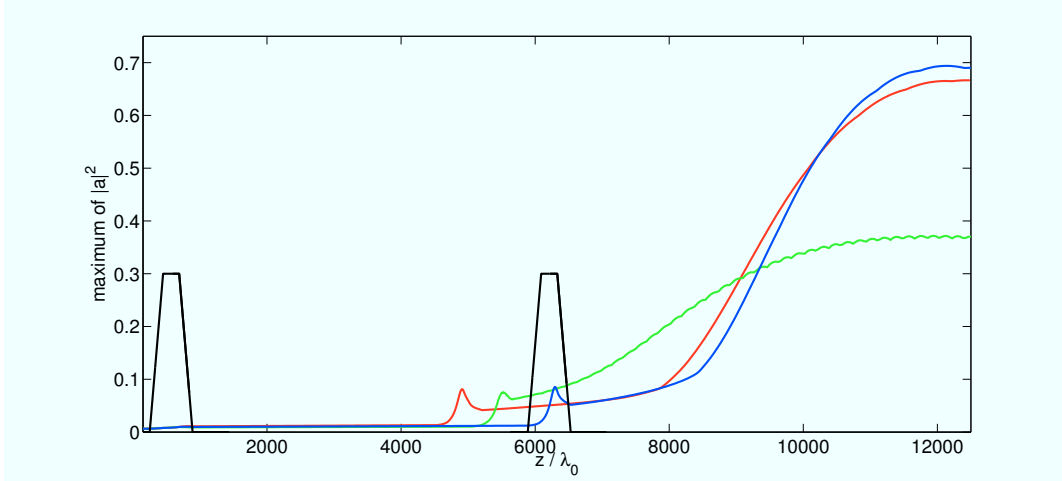


Figure 6.14: Amplitude evolution for $a_0 = 0.08$, $L_0 = 20 \lambda_0$, $W_0 = 250 \lambda_0$ and three different two-layer configurations. Each layer has two linear transition regions of $200 \lambda_0$ between vacuum and plasma. The density plateaus ($n_0 = 0.3 n_c$) are $200 \lambda_0$ (green), $240 \lambda_0$ (blue) and $280 \lambda_0$ (red) long with $4200 \lambda_0$, $5000 \lambda_0$ and $3600 \lambda_0$ of vacuum between the layers respectively. The density profile for the $240 \lambda_0$ long plateaus (blue curve) with $5000 \lambda_0$ between the layers is shown in black.

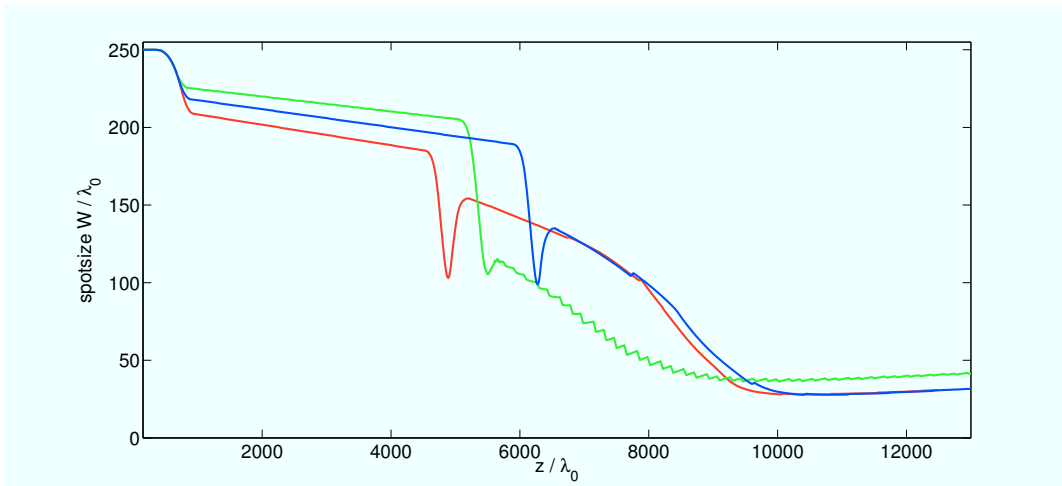


Figure 6.15: Spotsizes evolution for the simulations shown in Fig. 6.14.

6.3.2 Increasing the initial pulse spot size

Another strategy to allow for an easier control of the filamentation is to increase of the initial spot size. Without a corresponding increase in the amount of vacuum, a wider pulse is focused less strongly and is thus less close to collapse (Fig. 6.18). For a sufficiently large increase in spot size, the length of the vacuum sections can be increased, too, without being again close to the collapse of the pulse. This allows a more thorough shedding of the unstable modes and very good suppression of the instability (Fig. 6.19).

If the amplitude of the pulse is increased as well, e.g. to $a_0 = 0.14$, filamentation control becomes much more simple, because pulse amplitude and length determine the

6.3. Controlling transversal filamentation

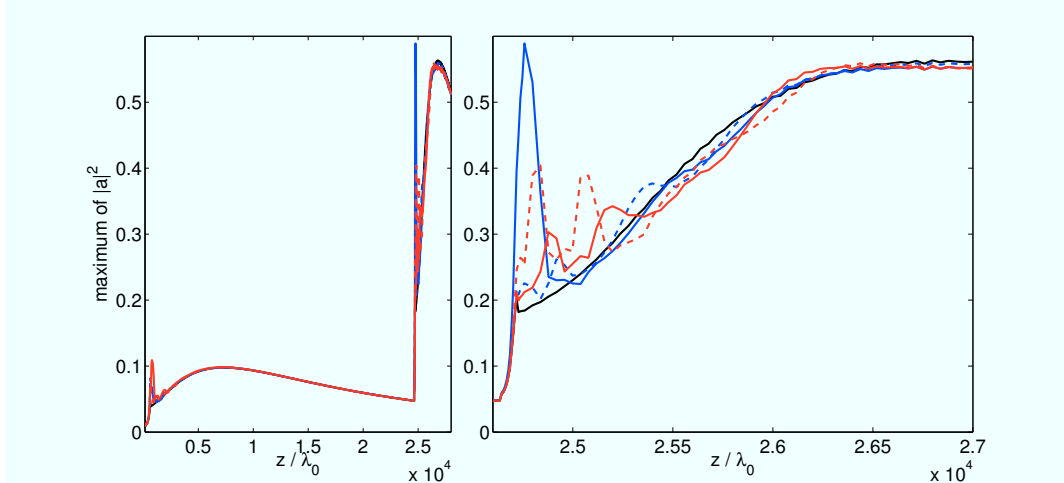


Figure 6.16: Amplitude evolution for $a_0 = 0.1$, $L_0 = 10 \lambda_0$, $W_0 = 150 \lambda_0$. Two layers ($n_0 = 0.3 n_c$) of $375 \lambda_0$ and $80 \lambda_0$ length respectively, with $24000 \lambda_0$ vacuum in between. Unperturbed simulation run in black, two runs with 0.5% perturbation (blue) and two runs with 1% perturbation (red), see text for details. Left: full simulation domain. Right: second layer only.

plasma length necessary for maximum longitudinal compression. If the layers are very short, the instability has only a short time to develop, too. Decreasing the pulse length can have the same effect (as long as the pulse power is above the compression threshold), but this reduces the achievable intensity and is limited by the laser hardware. For a short and intense pulse, e.g. $a_0 = 0.14$ and $L_0 = 10 \lambda_0$, which reaches full longitudinal compression after only $230 \lambda_0$ of plasma, a small increase in spot size from $W_0 = 150 \lambda_0$ to $W_0 = 180 \lambda_0$ is already sufficient for stable pulse propagation. For this parameters filamentation control is possible with only two layers (Fig. 6.20). Very high intensities of $|a|^2 \sim 1.5$ can be reached in this way. A spot size of $W_0 = 200 \lambda_0$ allows for enough vacuum to use three layers (Fig. 6.21). This reduces the strength of the instability in the first (now shorter) layer and results in an even higher maximum intensity.

Control of the filamentation becomes increasingly difficult for longer pulses. The individual layers are much longer and thus the instability has more time to develop. The amplitude of a long pulse can not be increased to compensate for this in the same way as it is possible for a shorter pulse. Intensities would become too large before the pulse length has decreased to the desired value and a large part of the pulse energy would be transferred to the plasma.¹ Even for a large initial spotsizes of $W_0 = 250 \lambda_0$ and a sufficient amount of vacuum between the layers, reliable filamentation control can not be achieved for a pulse of $a_0 = 0.1$ and $L_0 = 20 \lambda_0$ with three layers (Fig. 6.22 and Fig. 6.23), because the layers are too long for stable propagation. Increasing the number of layers to four would necessitate a much larger initial spotsize to accommodate for the additional vacuum section and/or using one very long vacuum section. Both measures increase the computational cost to a level that makes a parameter optimization of such

¹This consideration of course only applies if the aim is to generate a pulse that is as short as possible and not to simply maximize intensity.

6. Stratified plasma-vacuum systems

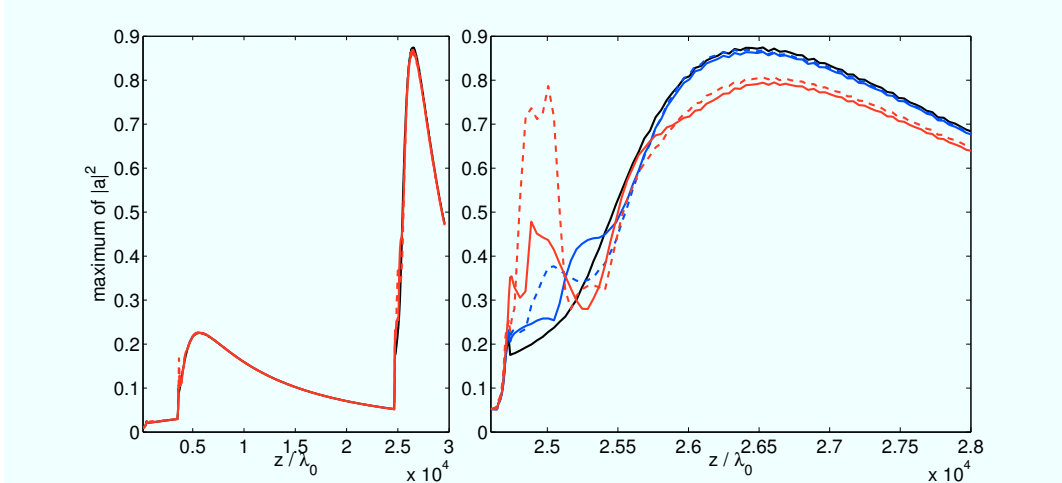


Figure 6.17: Amplitude evolution for $a_0 = 0.1$, $L_0 = 10 \lambda_0$, $W_0 = 150 \lambda_0$. Three layers ($n_0 = 0.3 n_c$) of $225 \lambda_0$, $120 \lambda_0$ and $80 \lambda_0$ respectively, with $2000 \lambda_0$ and $22000 \lambda_0$ vacuum in between. Unperturbed simulation run (black), two 0.5% perturbation runs (blue), two 1% perturbation runs (red). Left: full simulation domain. Right: third layer only.

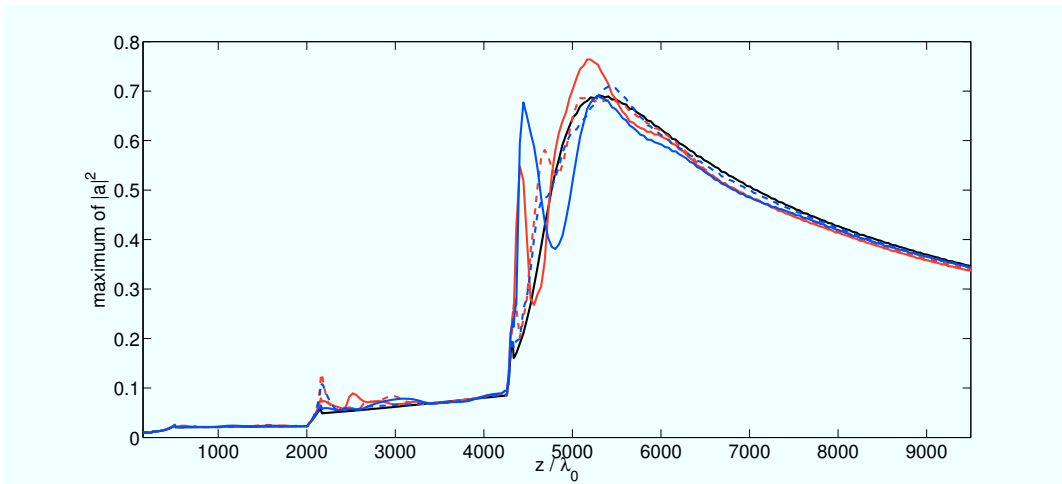


Figure 6.18: Amplitude evolution for $a_0 = 0.1$, $L_0 = 10 \lambda_0$, $W_0 = 200 \lambda_0$. Three layers ($n_0 = 0.3 n_c$) of $225 \lambda_0$, $140 \lambda_0$ and $60 \lambda_0$ respectively, with $1500 \lambda_0$ and $2100 \lambda_0$ vacuum in between. Unperturbed simulation run (black), two 0.5% perturbation runs (blue), two 1% perturbation runs (red).

a system unattractive as long as other options exist. Instead, the individual layers can be slightly shortened to reduce the strength of the pulse compression and also the time for the instability to develop. This comes at the price of a reduced maximum intensity (Fig. 6.24 and Fig. 6.25) and an increase of the minimum spotsize, but without a significant increase in the minimum pulse length.

6.3. Controlling transversal filamentation

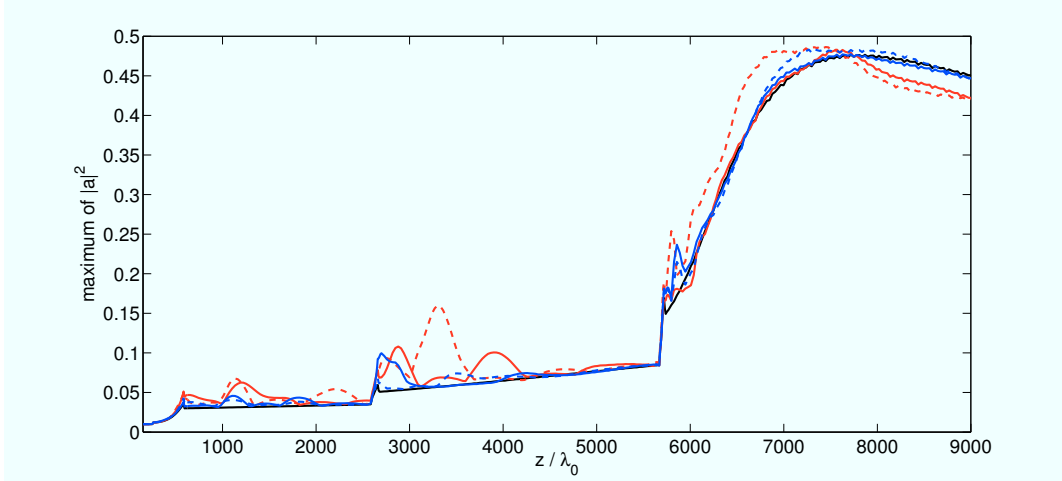


Figure 6.19: Amplitude evolution for $a_0 = 0.1$, $L_0 = 10 \lambda_0$, $W_0 = 250 \lambda_0$. Three layers ($n_0 = 0.3 n_c$) of $225 \lambda_0$, $140 \lambda_0$ and $60 \lambda_0$ respectively, with $2000 \lambda_0$ and $3000 \lambda_0$ vacuum in between. Unperturbed simulation run (black), two 0.5% perturbation runs (blue), two 1% perturbation runs (red).

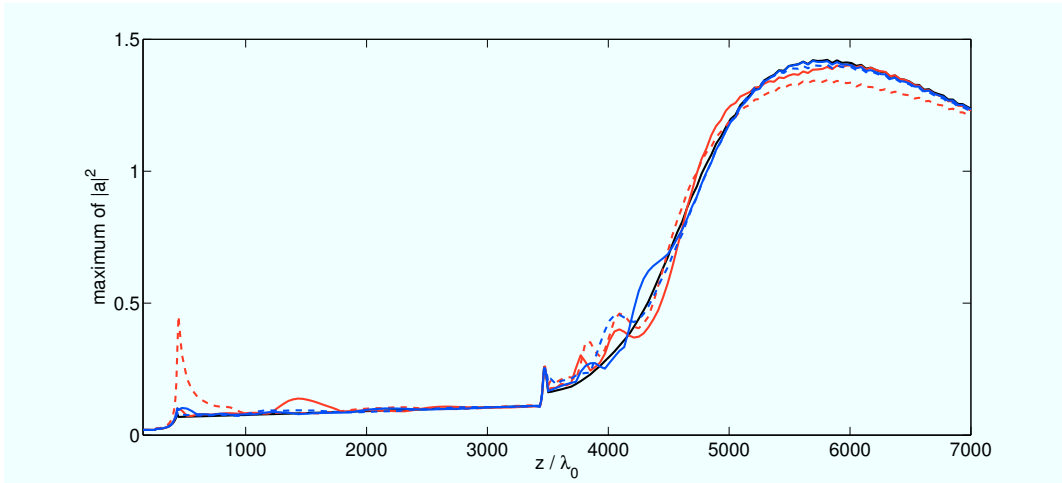


Figure 6.20: Amplitude evolution for $a_0 = 0.14$, $L_0 = 10 \lambda_0$, $W_0 = 180 \lambda_0$. Two layers ($n_0 = 0.3 n_c$) of $180 \lambda_0$ and $50 \lambda_0$ respectively, with $3000 \lambda_0$ vacuum in between. Unperturbed simulation run (black), two 0.5% perturbation runs (blue), two 1% perturbation runs (red).

6.3.3 Reducing the initial pulse amplitude

In experiments it might not be possible to reduce the length of the individual plasma layers below a certain value that is still too large for stable pulse propagation. In this case the strategies discussed above are not applicable. The only possibility might then be to reduce the initial pulse amplitude. For the simulations of two gasjets we already had to use a lower amplitude than for other plasma configurations, even without pulse perturbations. This improves control of the instability as well. For the gasjet configuration with density plateaus of $200 \lambda_0$, the filamentation is kept well in control (Fig. 6.26).

6. Stratified plasma-vacuum systems

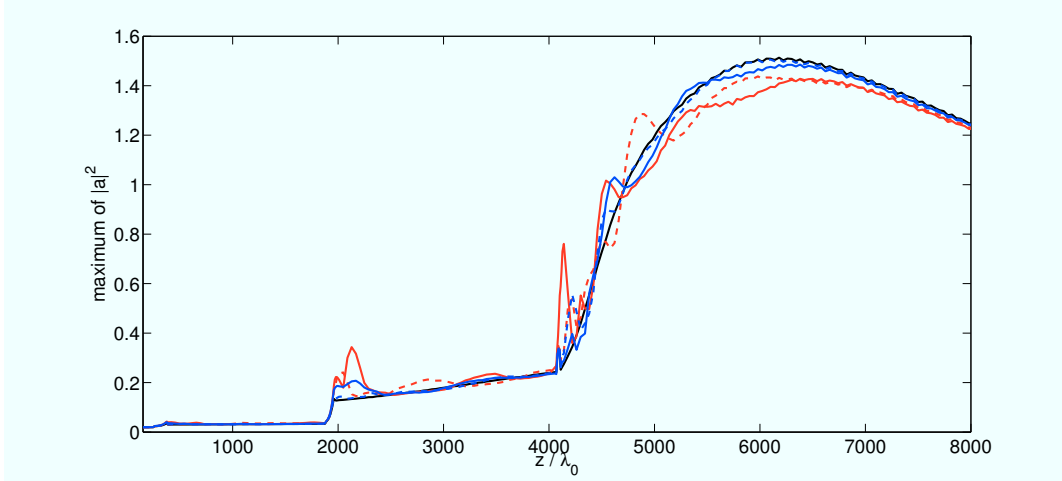


Figure 6.21: Amplitude evolution for $a_0 = 0.14$, $L_0 = 10 \lambda_0$, $W_0 = 200 \lambda_0$. Three layers ($n_0 = 0.3 n_c$) of $120 \lambda_0$, $80 \lambda_0$ and $30 \lambda_0$ respectively, with $1500 \lambda_0$ and $2100 \lambda_0$ vacuum in between. Unperturbed simulation run (black), two 0.5% perturbation runs (blue), two 1% perturbation runs (red).

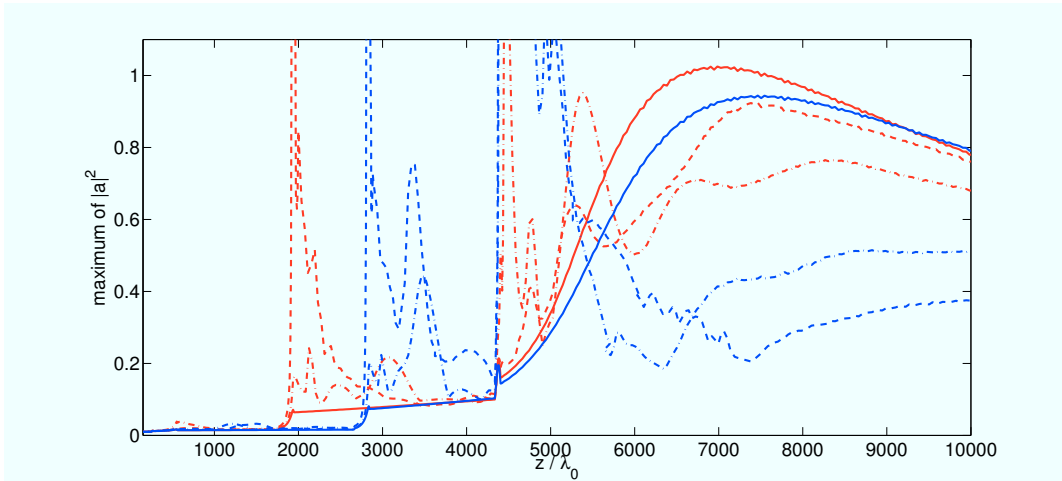


Figure 6.22: Amplitude evolution for $a_0 = 0.1$, $L_0 = 20 \lambda_0$, $W_0 = 250 \lambda_0$. Three layers ($n_0 = 0.3 n_c$) of $300 \lambda_0$, $170 \lambda_0$ and $50 \lambda_0$ length respectively. Two different vacuum configurations, $1200 \lambda_0 / 2400 \lambda_0$ in red and $2400 \lambda_0 / 1200 \lambda_0$ in blue. Solid curves for unperturbed simulation runs, dashed and dash-dotted curves for 1% perturbation runs.

Although there is a visible reduction in maximum intensity, the losses are still tolerable. In simulations with longer plateau sections of $240 \lambda_0$, where a higher maximum intensity is reached, the losses stay only in an acceptable range for the perturbation with a relative amplitude of 0.005 (Fig. 6.27 and Fig. 6.28).

6.3. Controlling transversal filamentation

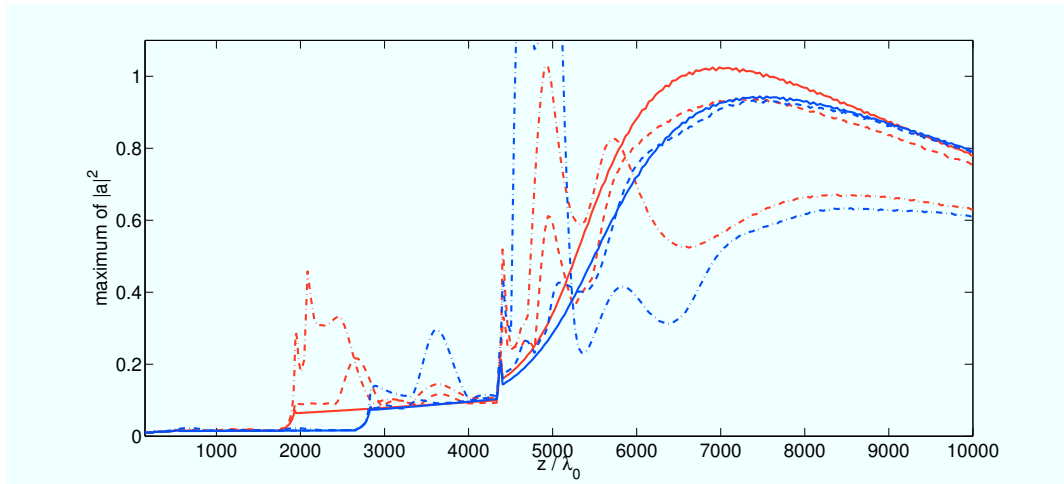


Figure 6.23: Same simulation parameters as shown in Fig. 6.22, but for 0.5% perturbation.

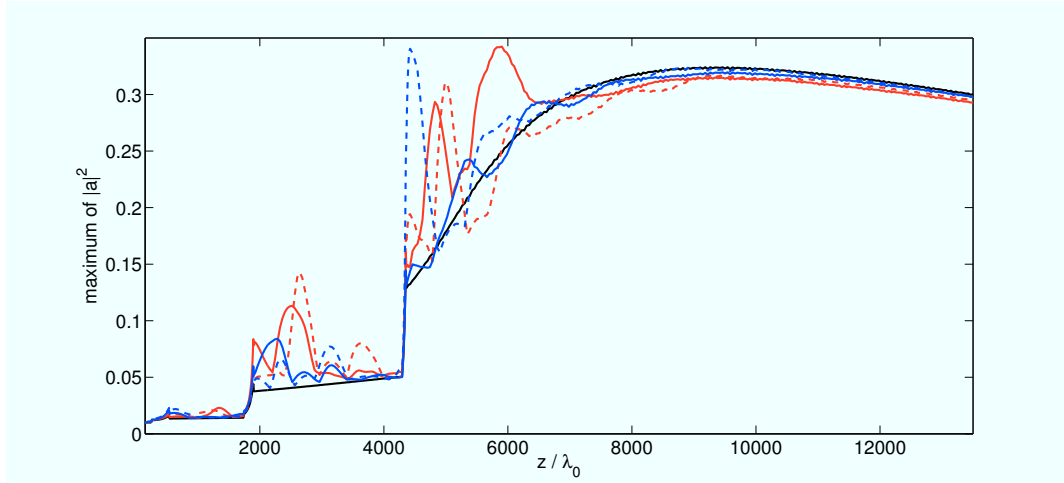


Figure 6.24: Amplitude evolution for $a_0 = 0.1$, $L_0 = 20 \lambda_0$, $W_0 = 250 \lambda_0$. Three layers ($n_0 = 0.3 n_c$) of $280 \lambda_0$, $150 \lambda_0$ and $50 \lambda_0$ respectively, with $1200 \lambda_0$ and $2400 \lambda_0$ vacuum in between. Unperturbed simulation run (black), two 0.5% perturbation runs (blue), two 1% perturbation runs (red).

6. Stratified plasma-vacuum systems

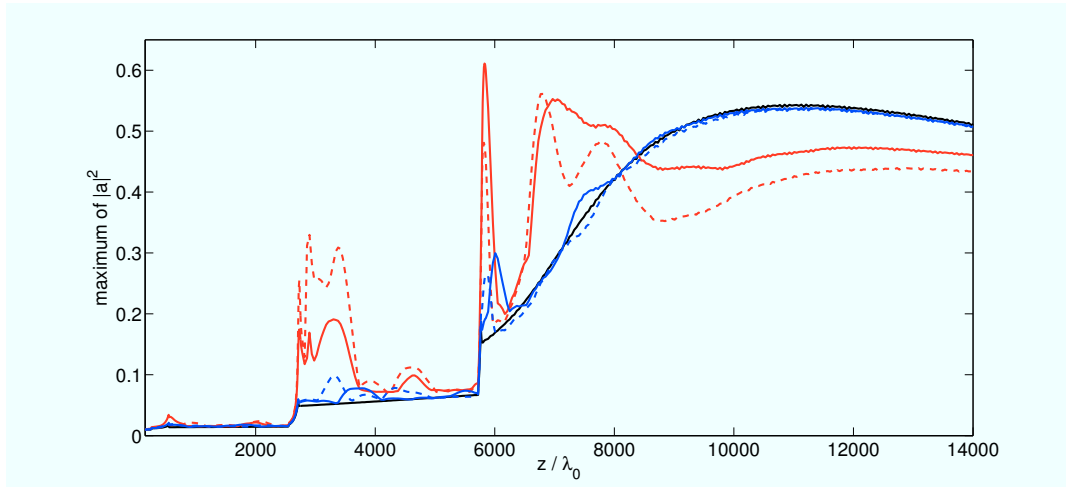


Figure 6.25: Amplitude evolution for $a_0 = 0.1$, $L_0 = 20 \lambda_0$, $W_0 = 300 \lambda_0$. Three layers ($n_0 = 0.3 n_c$) of $290 \lambda_0$, $160 \lambda_0$ and $50 \lambda_0$ respectively, with $2000 \lambda_0$ and $3000 \lambda_0$ vacuum in between. Unperturbed simulation run (black), two 0.5% perturbation runs (blue), two 1% perturbation runs (red).

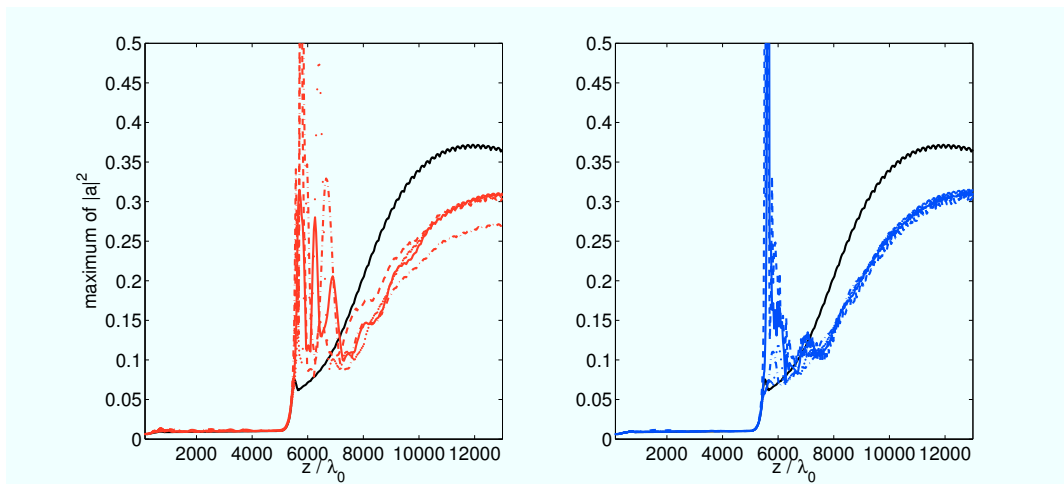


Figure 6.26: Amplitude evolution for two layers with linear transition regions of $200 \lambda_0$ and a plateau of also $200 \lambda_0$ ($n_0 = 0.3 n_c$) with $4200 \lambda_0$ vacuum between the layers. Pulse parameters are $a_0 = 0.08$, $L_0 = 20 \lambda_0$ and $W_0 = 250 \lambda_0$. Unperturbed simulation run in black. Left: four 1% perturbation runs (red). Right: four 0.5% perturbation runs (blue).

6.3. Controlling transversal filamentation

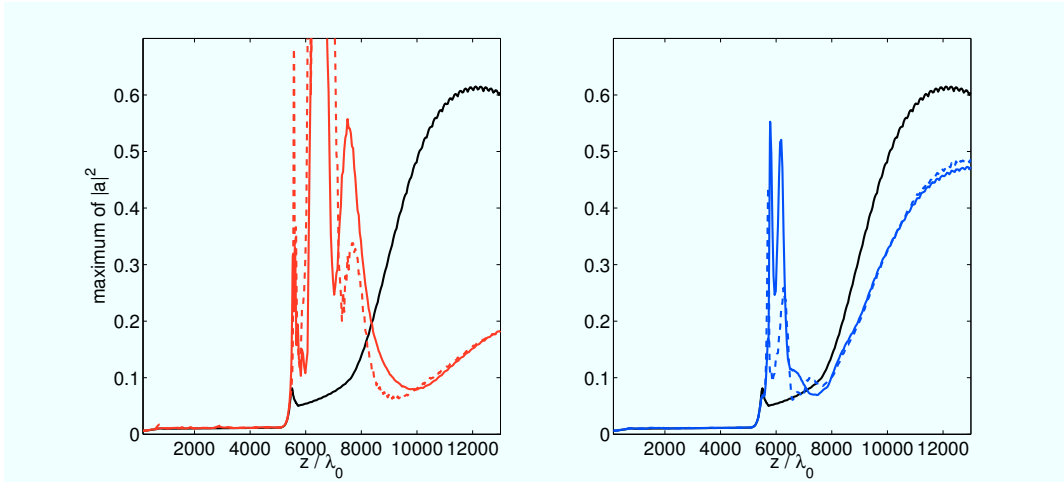


Figure 6.27: Amplitude evolution for two layers with linear transition regions of $200 \lambda_0$ and a plateau of $240 \lambda_0$ ($n_0 = 0.3 n_c$) with $4200 \lambda_0$ vacuum between the layers. Pulse parameters are $a_0 = 0.08$, $L_0 = 20 \lambda_0$ and $W_0 = 250 \lambda_0$. Unperturbed simulation run in black. Left: two 1% perturbation runs (red). Right: two 0.5% perturbation runs (blue).

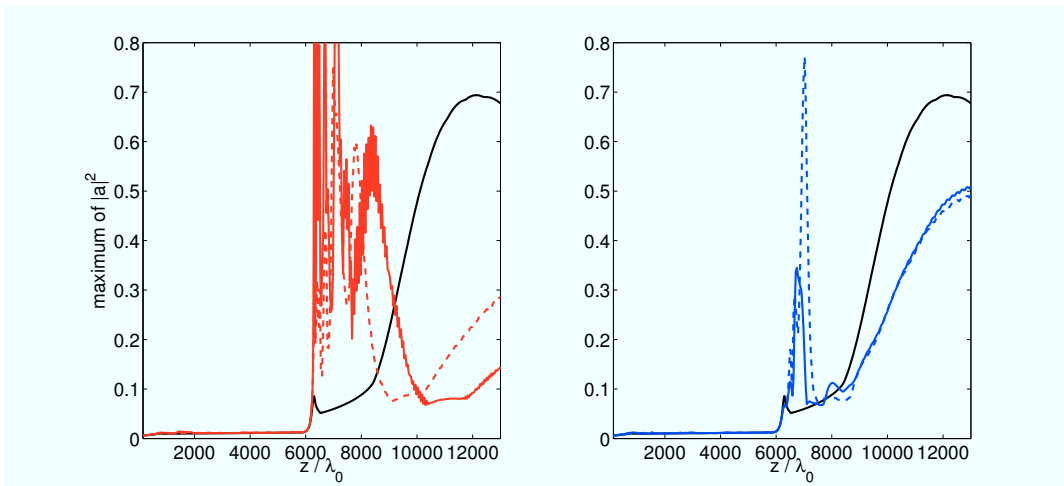


Figure 6.28: Amplitude evolution for two layers with linear transition regions of $200 \lambda_0$ and a plateau of $240 \lambda_0$ ($n_0 = 0.3 n_c$) with $5000 \lambda_0$ vacuum between the layers. Pulse parameters are $a_0 = 0.08$, $L_0 = 20 \lambda_0$ and $W_0 = 250 \lambda_0$. Unperturbed simulation run in black. Left: two 1% perturbation runs (red). Right: two 0.5% perturbation runs (blue).

7 Conclusion

In the present work we studied the question whether a laser pulse can be efficiently compressed in both the longitudinal and transversal directions by means of the relativistic nonlinear self-interaction inside of a plasma. For this purpose we derived two coupled equations for the vector potential of the laser and the electron density perturbation caused by the laser pulse. These equations are valid in the weakly relativistic parameter regime. Only for weakly relativistic intensities, efficient pulse compression with low energy losses is possible. With further assumptions the cubic nonlinear Schrödinger equation (NLSE) can be derived from these equations. Analytical models based on the NLSE allow to calculate the power thresholds for self-compression in the longitudinal and transversal direction, by means of the variation-of-action method (VAM). We conclusively showed that only pulses that are in both the longitudinal and the transversal direction directly at the 2D (or 3D) threshold, obey this threshold. Any pulse that for one direction is clearly above the threshold, obeys the 1D threshold for the other direction instead. We also showed that while the thresholds are sufficiently accurate, the pulse dynamic is not well described by a VAM that prescribes a Gaussian pulse shape. A distinct dependence of the transversal shape on the longitudinal coordinate and vice versa is visible in simulations both inside the plasma (stronger compression on axis, chapter 4) and after the pulse has left the plasma (stronger transversal focusing of the pulse center, chapter 5).

Thus it is indispensable to study the pulse dynamics by means of numerical simulations. We developed numerical schemes with high accuracy and efficiency for one (chapter 3) and two (chapter 4) dimensions. This was achieved by combining Gautschi-type exponential integrators with other means like splitting the linear operator of the wave equation and the quasi-envelope approach (QEA). With these methods, it is possible to handle the fast temporal and spatial dependence of the solutions effectively. Special attention was given to tailor the scheme to the different sections of the simulation domain, i.e. plasma and vacuum sections and transition regions. In 2D, the parallel implementation of this integrator scales well with the number of processors.

Numerical simulations were used to study the longitudinal pulse compression in 1D for a wide range of pulse and plasma parameters. This confirmed the result from [59] that efficient compression without high energy losses to the plasma is limited to weakly relativistic intensities and densities above $0.25 n_c$ to avoid Raman instability. In 2D the interaction between longitudinal and transversal compression and its dependence on the initial length and spot size of the pulse was examined. Here the result was that, for a controlled longitudinal compression, the spot size of the pulse has to be much larger than its length. Otherwise the pulse will directly start to collapse, a behavior which eventually occurs for wider spot sizes, too, but only after a much longer propagation

in plasma than needed for optimal longitudinal compression. We also showed that the compression in the longitudinal and transversal directions is strongly coupled even before the pulse starts to collapse. The faster direction (smaller initial length or width) essentially enslaves the compression dynamics of the slower direction (larger initial length or width).

Due to the additional degree of freedom in 2D, the pulse can develop new types of instabilities compared to 1D. These were discussed in chapter 4. Because of the low noise properties of the numerical methods we used, each instability could be triggered independently of the others by applying an appropriate initial perturbation to the pulse. The most important one, with respect to efficient pulse compression, is the transversal filamentation instability. Because a pulse which shows longitudinal compression and has a wide spot size is several times above the transversal self-compression threshold, individual filaments can self-focus and ultimately collapse. This leads to large energy losses due to strong plasma excitations and heating. Analytical results exist only for the transversal stability of soliton solutions and show a dependence of the filamentation wavelength on the pulse length. The analytical predictions for the most unstable wavelength were verified numerically. Additionally, for the first time the relation between the filamentation wavelength and pulse length was studied numerically for a longitudinally compressing pulse. During the compression the spectrum of the unstable modes shifts towards shorter wavelengths. The shortest possible filamentation wavelength given by the minimal pulse length is only reached for slowly compressing pulses. We also demonstrated that the shape and time evolution of the unstable spectrum is nearly the same for a soliton like and a Gaussian pulse shape, as long as their longitudinal half width is the same.

We also studied the propagation of the pulse from plasma to vacuum and how this transition can be described analytically, as well as the pulse propagation in vacuum. While in 1D the pulse shape stays unchanged during propagation in vacuum, in 2D the pulse can either focus or defocus. Because the plasma induces a negative curvature on the phase front of the pulse, the pulse focuses behind the plasma layer similar to a classical lens. This further increases the amplitude and reduces the spot size of the pulse. We showed that the focusing behavior differs from the well known Gaussian beam. The difference increases with the length of the plasma layer and reaches a maximum for the fully compressed pulse. We demonstrated that the focal length and minimum spot size of an initially very wide pulse can be predicted by the simulation of a pulse with a much smaller initial spot size. For pulses that developed transversal filamentation inside the plasma, detailed simulations of the propagation of unstable modes in vacuum relative to the main pulse were performed. The difference in propagation of short wavelength (belonging to the instability) and long wavelength transversal modes (belonging to the main pulse) is the key to control transversal filamentation.

Combining the results from pulse compression in plasma, transversal focusing, and shedding of unstable modes in vacuum, we demonstrated that a stratified plasma-vacuum structure can not only be used to control transversal filamentation, as in [59]. It can also significantly increase the maximum intensity of the compressed pulse through

7. Conclusion

enhanced transversal focusing. This was tested for a wide variety of pulse parameters and plasma configurations. The intensity can be increased hundredfold in this way, with excellent control of transversal filamentation. Relativistic intensities in the focal spot of the last layer are possible, while still being subrelativistic inside the plasma. For plasma configurations that are possible in current gasjet experiments, the peak intensities are less high and transversal filamentation is less well controlled. The results are still very encouraging as they show the real world applicability of layered pulse compression that will only increase with advances in experimental configurations.

A VAM model for pulse compression in 2D

The cubic nonlinear Schrödinger equation in cylindrical geometry is

$$i \frac{\partial}{\partial \zeta} a + \frac{1 - \beta^2}{2\beta^3} \frac{\partial^2}{\partial \tau^2} a + \frac{1}{2\beta} \frac{1}{r} \frac{\partial}{\partial r} r \frac{\partial}{\partial r} a + \frac{1 - \beta^2}{4\beta} |a|^2 a = 0 . \quad (\text{A.1})$$

The Lagrangian density of this equation is

$$\mathcal{L} = i \beta (a \partial_\zeta a^* - a^* \partial_\zeta a) + \frac{1 - \beta^2}{\beta^2} (\partial_\tau a)(\partial_\tau a^*) + (\partial_r a)(\partial_r a^*) - \frac{1 - \beta^2}{4} |a|^4 . \quad (\text{A.2})$$

As the ansatz for the trial function, we use

$$a(r, \tau, \zeta) = \frac{A(\zeta) W_0 \sqrt{T_0}}{W(\zeta) \sqrt{T(\zeta)}} e^{-i\phi(\zeta)} e^{i\eta(\zeta) \tau^2} e^{-\frac{\tau^2}{T(\zeta)^2}} e^{i\beta \frac{r^2}{2R(\zeta)^2}} e^{-\frac{r^2}{W(\zeta)^2}} , \quad (\text{A.3})$$

where η is the linear chirp and R the radius of transversal curvature. This is an exact solution to the linear version of (A.1), valid for a purely dispersive medium.

The Lagrangian is then defined as

$$L = \int_{\mathbb{R}^2} d\tau dr r \mathcal{L} . \quad (\text{A.4})$$

Note that to recover the Schrödinger equation from this Lagrangian density, the variation has to be done under the integral, to include the factor r from the Jacobian determinant. Inserting the test function and performing the integration in (A.4) results in

$$L = \frac{2(1 - \beta^2) E^2}{\beta^2} \frac{E^2}{T^2} - \frac{1 - \beta^2}{4\sqrt{2}} \frac{E^4}{T W^2} + \frac{2(1 - \beta^2)}{\beta^2} E^2 T^2 \eta^2 - \beta^2 \frac{E^2 W^2}{R^2} (R' - 1) + 4 \frac{E^2}{W^2} + \beta E^2 (T^2 \eta' - 4 \phi') , \quad (\text{A.5})$$

where $E(\zeta) = A(\zeta) W_0 \sqrt{T_0}$ is proportional to the pulse energy.

As all collective coordinates only depend on ζ , variation of the action with respect to them will yield ordinary differential equations. The variation with regard to one of the collective coordinates is defined as

$$\delta L[q, q_\zeta] = \partial_q L - \partial_\zeta \frac{\partial}{\partial q_\zeta} L \quad (\text{A.6})$$

A. VAM model for pulse compression in 2D

where q_ζ denotes the derivative of q with respect to ζ .

From varying for ϕ we get $E' = 0$, thus $E(\zeta) = E_0$ and

$$A(\zeta) = A_0 \quad (\text{A.7})$$

Varying L with respect to R gives the simple relation

$$W' = \frac{W}{R} \quad (\text{A.8})$$

Differentiating this relation with respect to ζ yields

$$R' - 1 = -\frac{R^2}{W} W'' \quad (\text{A.9})$$

Varying L with respect to R results in

$$R' - 1 = \frac{4}{\beta^2} \frac{R^2}{W^4} \left\{ \frac{1 - \beta^2}{16\sqrt{2}} \frac{E^2}{T} - 1 \right\} \quad (\text{A.10})$$

Combining the two equations for R' , we get

$$W'' = -\frac{4}{\beta^2} \frac{1}{W^3} \left\{ \frac{1 - \beta^2}{16\sqrt{2}} \frac{E^2}{T} - 1 \right\} \quad (\text{A.11})$$

Since W'' has to be negative for transversal compression, we immediately get the compression threshold

$$(1 - \beta^2) A_0^2 W_0^2 \geq 16\sqrt{2} . \quad (\text{A.12})$$

Varying L with respect to η results in

$$T' = \frac{1 - \beta^2}{\beta^3} T \eta \quad (\text{A.13})$$

Differentiating with respect to ζ and solving for η' yields

$$\eta' = \frac{\beta^2}{1 - \beta^2} \left\{ \frac{T''}{T} - \frac{(T')^2}{T^2} \right\} \quad (\text{A.14})$$

Varying L with respect to T gives a second equation for η'

$$\eta' = -\frac{2(1 - \beta^2)}{\beta^3} \eta^2 - \frac{2(1 - \beta^2)}{\beta^3} \frac{1}{T^4} \left\{ \frac{\beta^2}{16\sqrt{2}} \frac{E^2 T}{W^2} - 1 \right\} \quad (\text{A.15})$$

Both equations for η' combined yield

$$T'' = -\frac{4(1 - \beta^2)^2}{\beta^6} \frac{1}{T^3} \left\{ \frac{\beta^2}{16\sqrt{2}} \frac{E^2 T}{W^2} - 1 \right\} . \quad (\text{A.16})$$

This gives us a threshold for the longitudinal compression

$$\beta^2 A_0^2 T_0^2 \geq 16 \sqrt{2} , \quad (\text{A.17})$$

by the same argument as in the case of the transversal compression. To derive the same differential equations for T and W in a 2D Cartesian geometry, where the NLSE has the form

$$i \frac{\partial}{\partial \zeta} a + \frac{1 - \beta^2}{2\beta^3} \frac{\partial^2}{\partial \tau^2} a + \frac{1}{2\beta} \frac{\partial^2}{\partial x^2} a + \frac{1 - \beta^2}{4\beta} |a|^2 a = 0 , \quad (\text{A.18})$$

we use a similar test function

$$a(r, \tau, \zeta) = \frac{A(\zeta) \sqrt{W_0 T_0}}{\sqrt{W(\zeta) T(\zeta)}} e^{-i\phi(\zeta)} e^{i\eta(\zeta) \tau^2} e^{-\frac{\tau^2}{T(\zeta)^2}} e^{i\beta \frac{x^2}{2R(\zeta)^2}} e^{-\frac{x^2}{W(\zeta)^2}} , \quad (\text{A.19})$$

and a Lagrangian density of the same form as for cylindrical geometry, but with r substituted for x and

$$L = \int_{\mathbb{R}^2} d\tau dx \mathcal{L} . \quad (\text{A.20})$$

This yields

$$\begin{aligned} L = & \frac{2(1 - \beta^2) E^2}{\beta^2} \frac{E^2}{T^2} + \frac{2(1 - \beta^2)}{\beta^2} E^2 T^2 \eta^2 - \frac{\beta^2 E^2 W}{2 R^2} (R' - 1) \\ & - (1 - \beta^2) \frac{E^4}{4 T W} + \frac{2 E^2}{W^2} + \beta E^2 (T^2 \eta' - 4 \phi') . \end{aligned} \quad (\text{A.21})$$

In this case $E(\zeta) = A(\zeta) \sqrt{W_0 T_0}$.

Again from varying for ϕ we get $E(\zeta)' = A(\zeta)' \equiv 0$. The equations from varying for η and R are unchanged from the cylindrical case. Combined with the equations from variation of T and W respectively we have

$$T'' = -\frac{4(1 - \beta^2)^2}{\beta^6} \frac{1}{T^3} \left\{ \frac{\beta^2 E^2 T}{16 W} - 1 \right\} \quad (\text{A.22})$$

and

$$W'' = -\frac{4}{\beta^2} \frac{1}{W^3} \left\{ \frac{1 - \beta^2 E^2 W}{16 T} - 1 \right\} , \quad (\text{A.23})$$

which results in the same form of the thresholds (because here $E_0 = A_0 \sqrt{W_0 T_0}$), but a difference of factor $\sqrt{2}$ in the threshold values.

B Transversal filamentation instability

B.1 Stationary solution of the cubic nonlinear wave equation

We derive the stationary solution of the equation

$$\frac{\partial^2}{\partial t^2} a(z, t) - \frac{\partial^2}{\partial z^2} a(z, t) = -\frac{n_0}{n_c} \left(1 - \frac{1}{2} |a(z, t)|^2 \right) a(z, t), \quad (\text{B.1})$$

i.e. the solution that is constant in shape in the frame comoving with the group velocity.

We use the ansatz

$$a_s(z, t) = g(\zeta = z - v_s t) e^{i k_s z - i \omega_s t}. \quad (\text{B.2})$$

Inserting (B.2) in (B.1) and dividing by the phase factor results in

$$v_s^2 g'' + 2i\omega_s v_s g' - \omega_s^2 g - g'' - 2ik_s g' + k_s^2 g = -\frac{n_0}{n_c} \left(1 - \frac{1}{2} g^2 \right) g, \quad (\text{B.3})$$

where the prime denotes derivation with respect to the comoving coordinate $\zeta = z - v_s t$.

Assuming $k_s = v_s \omega_s$, which is consistent with the linear plasma dispersion relation for $v_s^2 = 1 - n_0/n_c$, simplifies this to

$$v_s^2 g'' - \omega_s^2 g - g'' + v_s^2 \omega_s^2 g = -\frac{n_0}{n_c} \left(1 - \frac{1}{2} g^2 \right) g. \quad (\text{B.4})$$

Using $n_0/n_c = 1 - v_s^2$ and the definition $\eta^2 = 1 - \omega_s^2$, (B.4) can be transformed into

$$\frac{n_0}{n_c} g'' - \frac{n_0}{n_c} \eta^2 g = -\frac{1}{2} \frac{n_0}{n_c} g^3. \quad (\text{B.5})$$

The substitution $\xi = \eta \zeta$ and a rescaling of the amplitude $g \rightarrow \eta g$ finally yields

$$g'' = \left(1 - \frac{1}{2} g^2 \right) g. \quad (\text{B.6})$$

It is easy to verify that this equation has a solution of the form

$$g_s(\zeta) = 2\eta \operatorname{sech}(\eta \zeta), \quad (\text{B.7})$$

where we reintroduced the factor η from the last substitutions.

By using the relation between k_s and ω_s , we arrive at the full time-dependent solution

$$a_s(\zeta) = 2\eta \operatorname{sech}(\eta \zeta) e^{i\sqrt{1-\eta^2}(v_s \zeta - (1-v_s^2)\tau)}. \quad (\text{B.8})$$

B.2 Growth rate of the instability

To investigate the growth rate of transversal perturbations for 1D soliton solution of the NLSE, we use the following ansatz function

$$a(z, x, \tau) = 2\eta(z, x)e^{-i\phi(z, x)}\text{sech}(\eta(z, x)\beta\tau) . \quad (\text{B.9})$$

The Lagrangian for the 2D NLSE in Cartesian coordinates consists of four parts. Insertion of the ansatz function into each part yields

$$\begin{aligned} \mathcal{L}_1 &= i\beta \left(a(z, x, \tau) \frac{\partial}{\partial z} a^*(z, x, \tau) - a^*(z, x, \tau) \frac{\partial}{\partial z} a(z, x, \tau) \right) \\ &= -8\beta\eta^2 \text{sech}(\eta\beta\tau)^2 \frac{\partial}{\partial z} \phi \\ \mathcal{L}_2 &= \frac{(1 - \beta^2)}{\beta^2} \left(\frac{\partial}{\partial \tau} a(z, x, \tau) \right) \left(\frac{\partial}{\partial \tau} a^*(z, x, \tau) \right) \\ &= 4\eta^4 (1 - \beta^2) \text{sech}(\eta\beta\tau)^2 \tanh(\eta\beta\tau)^2 \\ \mathcal{L}_3 &= \left(\frac{\partial}{\partial x} a(z, x, \tau) \right) \left(\frac{\partial}{\partial x} a^*(z, x, \tau) \right) \\ &= 4\text{sech}(\eta\beta\tau)^2 \left(\left(\frac{\partial}{\partial x} \eta \right)^2 + \eta^2 \left(\frac{\partial}{\partial x} \phi \right)^2 \right) \\ &\quad + 4\text{sech}(\eta\beta\tau)^2 \left(\tau^2 \beta^2 \eta^2 \tanh(\eta\beta\tau)^2 \frac{\partial}{\partial x} \eta^2 - 2\beta\tau\eta \tanh(\eta\beta\tau) \frac{\partial}{\partial x} \eta^2 \right) \\ \mathcal{L}_4 &= -\frac{1 - \beta^2}{4} a(z, x, \tau)^2 a^*(z, x, \tau)^2 \\ &= -4(1 - \beta^2) \eta^4 \text{sech}(\eta\beta\tau)^4 \end{aligned}$$

Integration over τ results in the shortened Lagrangian

$$\bar{\mathcal{L}} = -\frac{1}{3} (1 - \beta^2) \eta(z, x)^4 + \frac{12 + \pi^2}{36} \frac{\partial}{\partial x} \eta(t, y)^2 + \eta(z, x)^2 \left(\frac{\partial}{\partial x} \phi(t, y)^2 - 2\beta \frac{\partial}{\partial z} \phi(t, y) \right) . \quad (\text{B.10})$$

Varying for η

$$\frac{\partial}{\partial \eta} \bar{\mathcal{L}} - \frac{\partial}{\partial z} \left(\frac{\partial}{\partial \frac{\partial \eta}{\partial z}} \bar{\mathcal{L}} \right) - \frac{\partial}{\partial x} \left(\frac{\partial}{\partial \frac{\partial \eta}{\partial x}} \bar{\mathcal{L}} \right) = 0 \quad (\text{B.11})$$

yields

$$\left(\frac{\partial}{\partial x} \phi \right)^2 - 2\beta \frac{\partial}{\partial z} \phi = (1 - \beta^2) \eta^2 + \frac{12 + \pi^2}{36} \left[2 \frac{\partial_x^2 \eta}{\eta} - \frac{(\partial_x \eta)^2}{\eta^2} \right] , \quad (\text{B.12})$$

varying for ϕ

$$\frac{\partial}{\partial \phi} \bar{\mathcal{L}} - \frac{\partial}{\partial z} \left(\frac{\partial}{\partial \frac{\partial \phi}{\partial z}} \bar{\mathcal{L}} \right) - \frac{\partial}{\partial x} \left(\frac{\partial}{\partial \frac{\partial \phi}{\partial x}} \bar{\mathcal{L}} \right) = 0$$

B. Transversal filamentation instability

yields

$$\beta \frac{\partial}{\partial z} \eta = \frac{\partial}{\partial x} \left(\eta \frac{\partial}{\partial x} \phi \right). \quad (\text{B.13})$$

To study the transversal stability, we linearize around the 1D soliton with $\eta_0 = \text{const.}$ and $\phi_0 = \phi_0(z)$

$$\eta(z, x) = \eta_0 + \delta\eta(z, x) \quad (\text{B.14})$$

$$\phi(z, x) = \phi_0(z) + \delta\phi(z, x). \quad (\text{B.15})$$

From (B.12) we get the zeroth-order equation for ϕ

$$\frac{\partial}{\partial z} \phi_0(z) = -\frac{(1 - \beta^2)}{2\beta} \eta_0^2. \quad (\text{B.16})$$

The first-order equation is

$$\frac{\partial}{\partial z} \delta\phi = -\frac{(1 - \beta^2)}{\beta} \eta_0 \delta\eta - \frac{(12 + \pi^2)}{36\beta\eta_0} \frac{\partial^2}{\partial x^2} \delta\eta(z, x), \quad (\text{B.17})$$

where we already substituted $\partial_z \phi_0$ from (B.16).

From (B.13) we get an equation for $\delta\eta$

$$\beta \frac{\partial}{\partial z} \delta\eta = \eta_0 \frac{\partial^2}{\partial x^2} \delta\phi. \quad (\text{B.18})$$

Differentiating this equation with respect to z and substituting $\partial_z \delta\phi$ from (B.17) results in

$$\frac{\partial^2}{\partial z^2} \eta(z, x) = -\frac{(1 - \beta^2)}{\beta^2} \eta_0^2 \frac{\partial^2}{\partial x^2} \delta\eta(z, x) - \frac{(12 + \pi^2)}{36\beta^2} \frac{\partial^4}{\partial x^4} \delta\eta(z, x). \quad (\text{B.19})$$

By inserting $\delta\eta = e^{ik_x x - i\omega z/\beta}$ we get for the dispersion relation

$$\omega^2 = -\frac{n_0}{n_c} \eta_0^2 k_x^2 \left(1 - \frac{n_c}{n_0} \frac{(12 + \pi^2)}{36} \frac{k_x^2}{\eta_0^2} \right). \quad (\text{B.20})$$

This implies that we get instability for

$$k_x^2 < \frac{n_0}{n_c} \frac{36}{(12 + \pi^2)} \eta_0^2. \quad (\text{B.21})$$

Two transversal dimensions (x, y) change only the Laplace operator in (B.19) to $\frac{\partial^2}{\partial x^2} + \frac{\partial^2}{\partial y^2}$. Thus the dispersion relation has the same form as (B.20) with $k_\perp = \sqrt{k_x^2 + k_y^2}$ instead of only k_x .

In cylindrical geometry equation B.19 becomes

$$\frac{\partial^2}{\partial z^2} \eta = -\frac{(1 - \beta^2)}{\beta^2} \eta_0^2 \left(\frac{\partial^2}{\partial r^2} + \frac{1}{r} \frac{\partial}{\partial r} \right) \delta\eta - \frac{(12 + \pi^2)}{36\beta^2} \left(\frac{\partial^2}{\partial r^2} + \frac{1}{r} \frac{\partial}{\partial r} \right)^2 \delta\eta. \quad (\text{B.22})$$

The radial Laplace operator is diagonalized by Bessel functions of first kind and order zero with

$$\Delta_r J_0(k_r r) = \left(\frac{\partial^2}{\partial r^2} + \frac{1}{r} \frac{\partial}{\partial r} \right) J_0(k_r r) = -k_r^2 J_0(k_r r). \quad (\text{B.23})$$

For a transversal perturbation of this form the dispersion relation is again the same as in (B.20) with $k_\perp = k_r$.

C 3D instabilities

We here rederive for circular polarization the growth rates of the instabilities discussed in [14] for linear polarization. The nonlinear Schrödinger equation in a frame that comoves with c is

$$\left(\nabla_{\perp}^2 - 2i\beta \frac{\partial}{\partial \zeta} \right) a = (1 - \phi)a \quad (\text{C.1})$$

$$\left(\frac{\partial^2}{\partial \tau^2} + 1 \right) \phi = \frac{|a|^2}{2} \quad (\text{C.2})$$

coupled with the equation for the potential $\phi = n_e^1 - |a|^2/2$, where $n_e^1 = n_e - n_e^0$. Here ω_p and ω_p/c were used for time and space normalization. Note that this leads to an implicit dependence of lengths and times on the plasma density, compared to a normalization with ω_0 and ω_0/c where n_0/n_c is included explicitly.

The Lagrangian density for these equations is

$$\begin{aligned} \mathcal{L} = & \nabla_{\perp} a \cdot \nabla_{\perp} a^* - i\beta(a \partial_{\zeta} a^* - a^* \partial_{\zeta} a) \\ & - (\partial_{\tau} \phi)^2 + \phi^2 + (1 - \phi)|a|^2 \end{aligned} \quad (\text{C.3})$$

We define the shortened Lagrangian $\bar{\mathcal{L}}$ as the integral over the perpendicular coordinates

$$\bar{\mathcal{L}} = \int_{\mathbb{R}^2} d\mathbf{r}_{\perp} \mathcal{L} \quad (\text{C.4})$$

For the test functions the following ansatz is used

$$\begin{aligned} a(\tau, \zeta) = & A(\tau, \zeta) e^{i k_x(\tau, \zeta) \tilde{x}_a} e^{i k_y(\tau, \zeta) \tilde{y}_a} \\ & \times \exp \left(-[1 - i \alpha(\tau, \zeta)] \frac{\tilde{x}_a^2}{w_{xa}(\tau, \zeta)^2} \right) \\ & \times \exp \left(-[1 - i \alpha(\tau, \zeta)] \frac{\tilde{y}_a^2}{w_{ya}(\tau, \zeta)^2} \right) \end{aligned} \quad (\text{C.5})$$

$$\phi(\tau, \zeta) = \Phi(\tau, \zeta) \exp \left(-2 \frac{\tilde{x}_{\phi}^2}{w_{x\phi}(\tau, \zeta)^2} \right) \exp \left(-2 \frac{\tilde{y}_{\phi}^2}{w_{y\phi}(\tau, \zeta)^2} \right). \quad (\text{C.6})$$

with the definitions

$$\begin{aligned} \tilde{x}_a &= x - x_a(\tau, \zeta) \\ \tilde{y}_a &= y - y_a(\tau, \zeta) \\ \tilde{x}_{\phi} &= x - x_{\phi}(\tau, \zeta) \\ \tilde{y}_{\phi} &= y - y_{\phi}(\tau, \zeta) \\ A(\tau, \zeta) &= \sqrt{\xi(\tau, \zeta)} e^{i \chi(\tau, \zeta)} \end{aligned}$$

C. 3D instabilities

This ansatz includes variations in the amplitude A , shifts of the beam and wakefield centroids (x_a, y_a) and (x_ϕ, y_ϕ) as well as variations of the beam spot size.

The variation of $\bar{\mathcal{L}}$ is defined as

$$\delta\bar{\mathcal{L}}[q, q_\tau, q_\zeta] = \left\{ \partial_q - \partial_\tau \frac{\partial}{\partial q_\tau} - \partial_\zeta \frac{\partial}{\partial q_\zeta} \right\} \bar{\mathcal{L}} \quad (\text{C.7})$$

where the subscript of q denotes the corresponding derivative.

Varying $\bar{\mathcal{L}}$ with respect to $\alpha_x, \alpha_y, k_x, k_y, \chi$ yields the relations

$$\alpha_x = -\frac{\beta}{4} \partial_\zeta (w_{xa}^2) \quad (\text{C.8})$$

$$\alpha_y = -\frac{\beta}{4} \partial_\zeta (w_{ya}^2) \quad (\text{C.9})$$

$$k_x = -\beta \partial_\zeta x_a \quad (\text{C.10})$$

$$k_y = -\beta \partial_\zeta y_a \quad (\text{C.11})$$

$$\partial_\zeta P = 0 \quad (\text{C.12})$$

with $P = A^2 w_{xa} w_{ya}$. This relations reduce the number of variables by five.

To obtain an equilibrium solution for the linear stability analysis, we set $w_{xa} = w_{ya} \equiv w_a$, $w_{x\phi} = w_{y\phi} \equiv w_\phi$, $x_a = y_a = x_\phi = y_\phi \equiv 0$ and all derivatives with respect to τ to zero. This yields

$$w_a = w_\phi \quad (\text{C.13})$$

$$\Phi = \frac{P}{2w_a^2} \quad (\text{C.14})$$

$$\partial_\zeta^2 w_a = -\frac{4}{\beta^2 w_a^3} \left(\frac{P}{16} - 1 \right). \quad (\text{C.15})$$

From this follows the self compression threshold for the beam

$$A_0^2 w_0^2 = P_0 \geq P_c = 16 \quad (\text{C.16})$$

and the zeroth order solution

$$P_0 = P_c \quad (\text{C.17})$$

$$w_a = w_0 \quad (\text{C.18})$$

$$\Phi_0 = \frac{P_0}{2w_0} \quad (\text{C.19})$$

around which we will expand the Lagrangian. The threshold value is smaller by a factor of two than for linear polarization.

To simplify the resulting equations, we define

$$\bar{w}_a = \frac{w_{xa1} + w_{ya1}}{2} \quad (\text{C.20})$$

$$\bar{w}_\phi = \frac{w_{x\phi1} + w_{y\phi1}}{2} \quad (\text{C.21})$$

$$\Delta w_a = \frac{w_{xa1} + w_{ya1}}{2} \quad (\text{C.22})$$

$$\Delta w_\phi = \frac{w_{x\phi1} + w_{y\phi1}}{2} . \quad (\text{C.23})$$

We now vary the expanded $\bar{\mathcal{L}}$ with respect to the first order quantities. The expansion in the first order quantities $q_1 = q - q_0$ has to be done to second order in the perturbation parameter.

Varying with respect to x_{a1} and $x_{\phi1}$ results in the equations for the hosing instability

$$\partial_\zeta^2 x_{a1} + \frac{P}{P_c} \frac{1}{x_R^2} x_{a1} = \frac{P}{P_c} \frac{1}{x_R^2} x_{\phi1} \quad (\text{C.24})$$

$$(\partial_\tau^2 + 1) x_{\phi1} = x_{a1} \quad (\text{C.25})$$

The equations for y_{a1} and $y_{\phi1}$ are identical.

Varying for \bar{w}_a and Φ_1 yields

$$(\partial_\tau^2 + 1) \left(\Phi_1 + \frac{8}{w_0^3} \frac{P}{P_c} \bar{w}_\phi \right) = -\frac{8}{w_0^3} \frac{P}{P_c} \bar{w}_a \quad (\text{C.26})$$

$$(\partial_\tau^2 + 1) \left(\Phi_1 + \frac{16}{w_0^3} \frac{P}{P_c} \bar{w}_\phi \right) = 0 \quad (\text{C.27})$$

Varying for \bar{w}_ϕ and combining the equations from \bar{w}_a and Φ_1 leads to the equations for the symmetric self-modulation instability

$$\left[\partial_\zeta^2 + \frac{1}{x_R^2} \left(3 - \frac{P}{P_c} \right) \right] \bar{w}_a = -\frac{w_0^3}{8 x_R^2} \phi_1 \quad (\text{C.28})$$

$$(\partial_\tau^2 + 1) \phi_1 = -\frac{16}{w_0^3} \frac{P}{P_c} \bar{w}_a \quad (\text{C.29})$$

$$(\partial_\tau^2 + 1) \bar{w}_\phi = \bar{w}_a . \quad (\text{C.30})$$

The equation for \bar{w}_ϕ is decoupled from the other two equations and thus takes only passively part in the instability.

The equations for asymmetric spot size self-modulation result from varying with respect to Δw_a and Δw_ϕ

$$\left(\partial_\zeta^2 + \frac{3}{x_R^2} \right) \Delta w_a = \frac{P}{P_c} \frac{1}{x_R^2} \Delta w_\phi \quad (\text{C.31})$$

$$(\partial_\tau^2 + 1) \Delta w_\phi = \Delta w_a \quad (\text{C.32})$$

C. 3D instabilities

Despite using circular instead of linear polarization, and thus having a stronger nonlinearity for the same a_0 , these equations are identical to the equations in [14].

The general form of the the equations for the three types of instabilities is

$$(\partial_\zeta^2 + \Gamma_1) f = \Gamma_2 h \quad (\text{C.33})$$

$$(\partial_\tau^2 + 1) h = \Gamma_3 f , \quad (\text{C.34})$$

Fourier mode analysis with $f, g \sim e^{ik\zeta - i\omega\tau}$ and calculating the secular determinant yields the dispersion relation

$$\omega^2 k^2 + \Gamma_1(1 - \omega^2) - k^2 + \Gamma_1 - \Gamma_2\Gamma_3 = 0 . \quad (\text{C.35})$$

Since ω and k are measured in a comoving frame, we have to do the inverse transform to obtain the dispersion relation in the laboratory frame for $\omega' = \omega$ and $k' = \omega' + k$. If we further assume that the relation between k' and ω' is mostly linear with only small deviations, so that $\omega' = k' + g$ we get

$$g^4 + 2g^3 k' + g^2 k'^2 - \Gamma_1(g^2 + 2gk' + k'^2) - g^2 + \Gamma_1 - \Gamma_2\Gamma_3 = 0 , \quad (\text{C.36})$$

where k' is real and g is small and complex.

The maximum value for the growth rate $\text{Im}(\omega) = \text{Im}(g)$ is attained for $k' = 1$, because at this value the resonance with the plasma wake occurs. By setting $g = 0$ we get

$$k' = \sqrt{\frac{\Gamma_1 - \Gamma_2\Gamma_3}{\Gamma_1}} \quad (\text{C.37})$$

for the cut-off value, above which instabilities can not occur.

In [14] the growth rate for the short wavelength regime around $k' = 1$ is argued to be

$$g = \left(\frac{\Gamma_2\Gamma_3}{2}\right)^{\frac{1}{3}} \frac{-1 \pm \sqrt{3}i}{2} \quad (\text{C.38})$$

by considering $\Gamma_1 \sim \Gamma_2\Gamma_3 \sim \frac{1}{x_R^2} = \varepsilon^2$ and $g \sim \varepsilon$. For $k' = 1$ the constant term in (C.36) of order ε^2 then has to be balanced by the lowest order terms that contain g . Inconsistently they neglect $2\gamma_1 g \sim \varepsilon^3$ and only use the term that is cubic in g to calculate the growth rate (although the correction due to the linear term should be small).

For the long wavelength regime, that is not driven by the resonance with the wakefield, but instead mostly by the relativistic mass nonlinearity alone, we have $k' \sim \varepsilon$. The balancing then is between the constant term and the term quadratic in g

$$g = i\sqrt{\Gamma_2\Gamma_3 - \Gamma_1} . \quad (\text{C.39})$$

This only gives us a condition for the occurrence of the long wavelength regime, namely that $\Gamma_2\Gamma_3 \geq \Gamma_1$, but not the desired relation between g and k' . By plotting the full dispersion relation, we see that for long wavelength the relation is nearly linear. The only possibility then is

$$g = i\sqrt{\Gamma_1} k' . \quad (\text{C.40})$$

Bibliography

- [1] D. Anderson, A. Bondeson, and M. Lisak, *Transverse instability of soliton solutions to nonlinear Schrödinger equations*, J. Plasma Physics **21** (1979) 259–266.
- [2] T. Antonsen and P. Mora, *Self-focusing and Raman scattering of laser pulses in tenuous plasmas*, Phys. Rev. Lett. **69**(15) (1992) 2204–2207.
- [3] T. Baeva, S. Gordienko, and A. Pukhov, *Theory of high-order harmonic generation in relativistic laser interaction with overdense plasma*, Phys. Rev. E **74** (2006) 046404.
- [4] V. I. Berezhiani, D. P. Garuchava, S. V. Mikeladze, K. I. Sigua, N. L. Tsintsadze, S. M. Mahajan, Y. Kishimoto, and K. Nishikawa, *Fluid-Maxwell simulation of laser pulse dynamics in overdense plasma*, Physics of Plasmas **12**(6) (2005) 062308.
- [5] T. J. Bridges, *On the susceptibility of bright nonlinear Schrödinger solitons to long-wave transverse instability*, Proc. R. Soc. Lond. A **460** (2004) 2605–2615.
- [6] S. V. Bulanov, F. Califano, G. I. Dudnikova, T. Z. Esirkepov, I. N. Inovenkov, F. F. Kamenets, T. V. Liseikina, M. Lontano, K. Mima, N. M. Naumova, K. Nishihara, F. Pegoraro, H. Ruhl, A. S. Sakharov, Y. Sentoku, V. A. Vshivkov, and V. V. Zhakhovskii, *Reviews of Plasma Physics*, volume 22, chapter Relativistic Interaction of Laser Pulses with Plasmas, pages 227–335, Kluwer Academic/Plenum Publishers, 2001.
- [7] S. V. Bulanov, I. N. Inovenkov, V. I. Kirsanov, N. M. Naumova, and A. S. Sakharov, *Nonlinear depletion of ultrashort and relativistically strong laser pulses in an underdense plasma*, Phys. Fluids B **7** (1992) 1935–1942.
- [8] S. M. Candel, *An Algorithm for the Fourier-Bessel transform*, Comp. Phys. Comm. **23** (1981) 343–353.
- [9] X. L. Chen and R. N. Sudan, *Two-dimensional self-focusing of short intense laser pulse in underdense plasma*, Phys. Fluids B **5**(4) (1992) 1336–1348.
- [10] X. L. Chen and R. N. Sudan, *Necessary and Sufficient Conditions for Self-Focusing of Short Ultraintense Laser Pulse in Underdense Plasma*, Phys. Rev. Lett. **70**(14) (1993) 2082–2085.
- [11] J. M. Dawson, *Nonlinear electron oscillations in a cold plasma*, Phys. Rev. **113** (1959) 383.

Bibliography

- [12] V. Druskin and L. Knizherman, *Krylov subspace approximation of eigenpairs and matrix functions in exact and computer arithmetic*, Numer. Linear Algebra Appl. **2**(3) (1995) 205–217.
- [13] B. J. Duda, R. G. Hemker, K. C. Tzeng, and W. Mori, *A Long-Wavelength Hosing Instability in Laser-Plasma Interactions*, Phys. Rev. Lett. **83**(10) (1999) 1978–1981.
- [14] B. J. Duda and W. B. Mori, *Variational principle approach to short-pulse laser-plasma interactions in three dimensions*, Phys. Rev. E **61**(2) (2000) 1925–1939.
- [15] G. Eder, *Elektrodynamik*, chapter 10.8, pages 177–182, B.I. Hochschultaschenbücher, 1967.
- [16] E. Esarey, C. B. Schroeder, B. A. Shadwick, J. S. Wurtele, and W. P. Leemans, *Nonlinear Theory of Nonparaxial Laser Pulse Propagation in Plasma Channels*, Phys. Rev. Lett. **84**(14) (2000) 3081–3084.
- [17] E. Esarey, P. Sprangle, J. Krall, and A. Ting, *Self-Focusing and Guiding of Short Laser Pulses in Ionizing Gases and Plasmas*, IEEE J. of Quantum Electronics **33**(11) (1997) 1879–1914.
- [18] J. Faure, Y. Glinec, A. Pukhov, S. Kiselev, S. Gordienko, E. Lefebvre, J.-P. Rousseau, F. Burgy, and V. Malka, *A laser-plasma accelerator producing monoenergetic electron beams*, Nature **43** (2004) 541–544.
- [19] J. Faure, Y. Glinec, A. Pukhov, S. Kiselev, S. Gordienko, E. Lefebvre, J.-P. Rousseau, F. Burgy, and V. Malka, *A laser-plasma accelerator producing monoenergetic electron beams*, Nature **431** (2004) 541–544.
- [20] J. Faure, Y. Glinec, J. J. Santos, F. Ewald, J.-P. Rousseau, S. Kiselev, A. Pukhov, T. Hosokai, and V. Malka, *Observation of Laser-Pulse Shortening in Nonlinear Plasma Waves*, Phys. Rev. Lett. **95**(20) (2005) 205003.
- [21] J. Fuchs, C. A. Cecchetti, M. Borghesi, T. Grismayer, E. d’Humieres, P. Antici, S. Atzeni, P. Mora, A. Pipahl, L. Romagnani, A. Schiavi, Y. Sentoku, T. Toncian, P. Audebert, and O. Willi, *Laser-Foil Acceleration of high-energy protons in small-scale plasma gradients*, Phys. Rev. Lett. **99** (2007).
- [22] W. Gautschi, *Numerical integration of ordinary differential equations based on trigonometric polynomials*, Numer. Math. **3** (1961) 381–397.
- [23] L. M. Gorbunov and V. I. Kirsanov, *Excitation of plasma waves by an electromagnetic wave packet*, Zh. Eksp. Teor. Fiz. **93** (1987) 509.
- [24] S. Gordienko, T. Baeva, and A. Pukhov, *Focusing of laser-generated ion beams by a plasma cylinder: Similarity theory and the thick lens formula*, Physics of Plasmas **13** (2006) 063103.

Bibliography

- [25] S. Gordienko and A. Pukhov, *Scalings for ultrarelativistic laser plasma and quasi-monoenergetic electrons*, Physics of Plasmas **12** (2005) 043109.
- [26] S. Gordienko, A. Pukhov, O. Shokorov, and T. Baeva, *Relativistic Doppler Effect: Universal Spectra and Zeptosecond Pulses*, Phys. Rev. Lett. **93** (2004) 135002.
- [27] V. Grimm and M. Hochbruck, *Error analysis of exponential integrators for oscillatory second-order differential equations*, J. Phys. A: Math. Gen. **39** (2006) 5495–5507.
- [28] E. Hairer and C. Lubich, *Long-Time Energy Conservation of Numerical Methods for Oscillatory Differential Equations*, SIAM Journal on Numerical Analysis **38**(2) (2000) 414–441.
- [29] E. Hairer, C. Lubich, and G. Wanner, *Geometric Numerical Integration. Structure-Preserving Algorithms for Ordinary Differential Equations*, Springer, Berlin, 2002.
- [30] E. Hairer, C. Lubich, and G. Wanner, *Geometric numerical integration illustrated by the Störmer/Verlet method*, Acta Numerica (2003) 1–51.
- [31] B. M. Hegelich, B. J. Albrightand, J. Cobble, K. Flippo, S. Letzring, M. Paffett, H. Ruhl, J. Schreiber, R. K. Schulze, and J. C. Fernandez, *Laser acceleration of quasi-monoenergetic MeV ion beams*, Nature **439** (2006) 441.
- [32] B. Hidding, K.-U. Amthor, B. Liesfeld, H. Schwöerer, S. Karsch, M. Geissler, L. Veisz, K. Schmid, J. G. Gallacher, S. P. Jamison, D. Jaroszynski, G. Pretzler, and R. Sauerbrey, *Generation of Quasi-monoenergetic Electron Bunches with 80-fs Laser Pulses*, Phys. Rev. Lett. **96** (2006) 105004.
- [33] M. Hochbruck and C. Lubich, *On Krylov Subspace Approximations to the Matrix Exponential Operator*, SIAM Journal on Numerical Analysis **34**(5) (1997) 1911–1925.
- [34] M. Hochbruck and C. Lubich, *A Gautschi-type method for oscillatory second-order differential equations.*, Numer. Math. **83** (1999) 403–426.
- [35] E. Infeld and G. Rowlands, *Relativistic bursts*, Phys. Rev. Lett. **62**(10) (1989) 1122–1125.
- [36] P. B. J and D. L. Book, *Flux Corrected Transport. I. SHASTA, A Fluid Transport Algorithm That Works*, J. Comp. Phys. **11** (1973) 38–69.
- [37] H. F. Johnson, *An improved method for computing a discrete Hankel transform*, Comp. Phys. Comm. **43** (1987) 181–202.
- [38] C. Karle, *Simulation der Ausbreitung nichtlinearer Pulse unter Berücksichtigung von WDM*, Diplomarbeit, Heinrich-Heine-Universität Düsseldorf, 2001.

Bibliography

- [39] C. Karle, J. Schweitzer, M. Hochbruck, E. W. Laedke, and K. H. Spatschek, *Numerical solution of nonlinear wave equations in stratified dispersive media*, J. Comp. Phys. **216** (2006) 138–152.
- [40] C. Karle, J. Schweitzer, M. Hochbruck, and K. H. Spatschek, *A parallel implementation of a two-dimensional fluid laser-plasma integrator for stratified plasma-vacuum systems*, submitted to J. Comp. Phys. (2007).
- [41] E. W. Laedke, *Zur nichtlinearen Stabilität solitärer Wellen in Plasmen*, Dissertation, Universität Essen, 1978.
- [42] W. P. Leemans, B. Nagler, A. J. Gonsalves, C. Toth, K. Nakamura, C. G. R. Geddes, E. Esarey, C. B. Schroeder, and S. M. Hooker, *GeV electron beams from a centimetre-scale accelerator*, Nature Physics **2**(10) (2006) 696–699.
- [43] G. Lehmann, *Private communications*, 2006.
- [44] G. Lehmann, E. W. Laedke, and K. H. Spatschek, *Stability and evolution of one-dimensional relativistic solitons on the ion time scale*, Physics of Plasmas **13**(9) (2006) 092302.
- [45] G. Lehmann, E. W. Laedke, and K. H. Spatschek, *Localized wake-field excitation and relativistic wave-breaking*, Physics of Plasmas **14**(10) (2007) 103109.
- [46] R. LeVeque, *Numerical Methods for Conservation Laws*, Birkhäuser, 1992.
- [47] V. G. Makhankov, *Dynamics of classical solitons (in non-integrable systems)*, Phys. Rep. (Sect. C of Phys. Lett.) **35** (1978) 1–128.
- [48] V. Malka, J. Faure, Y. Glinec, A. Pukhov, and J. P. Rousseau, *Monoenergetic electron beam optimization in the bubble regime*, Physics of Plasmas **12**(5) (2005) 056702.
- [49] K. Mima, M. S. Jovanovic, Y. Sentoku, Z.-M. Sheng, M. M. Skoric, and T. Sato, *Stimulated photon cascade and condensate in a relativistic laser-plasma interaction*, Physics of Plasmas **8**(5) (2001) 2349–2356.
- [50] W. B. Mori, *The Physics of the Nonlinear Optics of Plasmas at Relativistic Intensities for Short-Pulse Lasers*, IEEE Journal of Quant. Electronics **33**(11) (1997) 1942–1953.
- [51] W. B. Mori, C. D. Decker, D. E. Hinkel, and T. Katsouleas, *Raman Forward Scattering of Short-Pulse High-Intensity Lasers*, Phys. Rev. Lett. **72**(10) (1994) 1482–1485.
- [52] G. A. Mourou, T. Tajima, and S. V. Bulanov, *Optics in the relativistic regime*, Rev. Mod. Phys. **78** (2006) 309–371.

Bibliography

- [53] C. Nieter and J. R. Cary, *VORPAL: a versatile plasma simulation code*, J. Comp. Phys. **196** (2004) 448–473.
- [54] C. Peth and W. Viöl, *Characterization of gas targets for laser produced extreme ultraviolet plasmas with a Hartmann-Shack sensor*, Rev. Sci. Instrum. **69**(11) (2004) 3288–3293.
- [55] A. Pukhov, *Three-dimensional electromagnetic relativistic particle-in-cell code VLPL (virtual laser plasma lab)*, J. Plasma Phys. **61** (1999) 425.
- [56] C. Ren, B. J. Duda, R. G. Hemker, W. B. Mori, T. Katsouleas, T. M. Antonsen, and P. Mora, *Compressing and focusing a short laser pulse by a thin plasma lens*, Phys. Rev. E **63** (2001) 026411.
- [57] G. Schmidt, *Stability of Envelope Solitons*, Phys. Rev. Lett **34**(12) (1975) 724–726.
- [58] H. Schworer, S. Pfotenhauer, O. Jäckel, K.-U. Amthor, B. Liesfeld, W. Ziegler, R. Sauerbrey, K. W. D. Ledingham, and T. Esirkepov, *Laser-plasma acceleration of quasi-monoenergetic protons from microstructured targets*, Nature **439** (2006) 445.
- [59] O. Shorokhov, A. Pukhov, and I. Kostyukov, *Self-Compression of Laser Pulses in Plasma*, Phys. Rev. Lett. **91** (2003).
- [60] A. E. Siegman, *Quasi fast Hankel transform*, Opt. Lett. **1**(1) (1977) 13–15.
- [61] A. E. Siegman, *Lasers*, Univ. Science Books, 1986.
- [62] K. H. Spatschek, *Theoretische Plasmaphysik*, Teubner, 1990.
- [63] T. Toncian, M. Borghesi, J. Fuchs, E. d’Humières, P. Antici, P. Audebert, E. Brambrink, C. A. Cecchetti, A. Pipahl, L. Romagnani, and O. Willi, *Ultrafast Laser-Driven Microlens to Focus and Energy-Select Mega-Electron Volt Protons*, Science **312** (2006).
- [64] S. Turitsyn, T. Schäfer, K. Spatschek, and V. Mezentsev, *Path-averaged chirped optical soliton in dispersion-managed fiber communication lines*, Opt. Comm. **163** (1999) 122–158.
- [65] D. Umstadter, *Einsteins’s impact on optics at the frontier*, Phys. Lett. A **347** (2005) 121–132.
- [66] N. Yajima, *Stability of Envelope Solitons*, Prog. Theor. Phys. **52** (1974) 1066–1067.
- [67] S. T. Zalesak, *Fully Multidimensional Flux-Corrected Transport Algorithms for Fluids*, J. Comp. Phys. **31** (1979) 335–362.

Danksagung

An dieser Stelle möchte ich mich bei allen bedanken, die zum Gelingen dieser Dissertation beigetragen haben.

Herrn Prof. Dr. K. H. Spatschek danke ich für die interessante Themenstellung und die Betreuung dieser Arbeit, sowie Frau Prof. Dr. M. Hochbruck für die Übernahme des Korreferats. Ihr und insbesondere Dipl. Math. Julia Schweitzer möchte ich außerdem für die ausgesprochen angenehme und ergiebige Zusammenarbeit danken. Mein Dank gilt ebenfalls Herrn Dr. E. W. Laedke für die Mitbetreuung meiner Dissertation.

Herrn Prof. Dr. A. Pukhov danke ich für das zur Verfügung stellen des 1D VLPL Codes, sowie Oleg Shorokhov und Sergei Kiselev für die Hilfe bei der Durchführung der benötigten Simulationen.

Frau Elvira Gröters gilt mein Dank für die stets unkomplizierte Regelung administrativer Fragen. Ebenfalls dankbar bin ich Herrn Dr. Herbert Wenk und Herrn Eckhard Zügge für die Administration des Computernetzwerks und die schnelle Behebung von Hardwareproblemen.

Anteil am Gelingen dieser Arbeit hatten auch meine Kollegen Alexander Posth, Götz Lehmann, Marcus Neuer, Andreas Wingen sowie natürlich Daniel an der Brügge, Naveen Kumar und Anupam Karmakar. Sie alle haben wesentlich zur angenehmen Arbeitsatmosphäre an unserem Institut beigetragen und das Diskutieren mit ihnen war stets hilfreich.

Erklärung

Hiermit erkläre ich, vorliegende Dissertation selbstständig verfaßt, keine anderen als die angegebenen Quellen und Hilfsmittel benutzt, sowie Zitate kenntlich gemacht zu haben.

Düsseldorf, den